Effects of Integrin Binding Peptides and Low Level Laser Therapy on Scaffold Free Vascularized Bone Microtissue Regeneration

Submitted to the Graduate School of Natural and Applied Sciences in partial fulfillment of the requirements for the degree of

Doctor of Philosophy

in Biomedical Technologies

by

Ziyşan Buse ÇEVİK

ORCID 0000-0002-9371-6424

September, 2022

This is to certify that we have read the thesis **Effects of Integrin Binding Peptides and Low Level Laser Therapy on Scaffold Free Vascularized Bone Microtissue Regeneration** submitted by **Ziyşan Buse ÇEVİK**, and it has been judged to be successful, in scope and in quality, at the defense exam and accepted by our jury as a DOCTORAL THESIS.

APPROVED BY:

Advisor : **Assoc. Prof. Dr. Ozan KARAMAN** ……………….
İzmir Kâtip Çelebi University

Committee Members :

Prof. Dr. Bahattin TANYOLAÇ ………………..
Ege University

Assoc. Prof. Dr. Haşim Özgür TABAKOĞLU ………………..
İzmir Bakırçay University

Assoc. Prof. Dr. Mustafa ŞEN ………………..
İzmir Kâtip Çelebi University

Assist. Prof. Dr. Nermin TOPALOĞLU AVŞAR ………………..
İzmir Kâtip Çelebi University

Date of Defense : 21 September, 2022

Declaration of Authorship

I, Ziyşan Buse ÇEVİK, declare that this thesis titled Effects of Integrin Binding Peptides and Low Level Laser Therapy on Scaffold Free Vascularized Bone Microtissue Regeneration and the work presented in it are my own. I confirm that:

- This work was done wholly or mainly while in candidature for the Doctoral degree at this university.
- Where any part of this thesis has previously been submitted for a degree or any other qualification at this university or any other institution, this has been clearly stated.
- Where I have consulted the published work of others, this is always clearly attributed.
- Where I have quoted from the work of others, the source is always given. This thesis is entirely my own work, with the exception of such quotations.
- I have acknowledged all major sources of assistance.
- Where the thesis is based on work done by myself jointly with others, I have made clear exactly what was done by others and what I have contributed myself.

Date: 21.09.2022

Effects of Integrin Binding Peptides and Low Level Laser Therapy on Scaffold Free Vascularized Bone Microtissue Regeneration

Abstract

Bone tissue engineering (BTE) targets to develop bone regeneration capacity in case of bone damages and fractures. Although traditional monolayer cell culture is a widely used technique for investigation of precursor studies of BTE strategy, it may be insufficient to measure cellular responses and regeneration capacities. Scaffold free microtissues (3D SFMs) have been developed to overcome these disadvantages. The platform mimics in vivo conditions in terms of arrangement of cell-cell or extracellular matrix (ECM) and contribute to maximum cell-cell interaction in co-culture formation. Considering all these, the first part of the study aimed to create a vascularized bone-like structure by coculture with human bone mesenchymal stem cells (hBMSC) and human umbilical vein endothelial cells (HUVEC). The cell proliferation and viability of SFMs were verified by diameter measurement, live and dead staining. The vascular potential of SFMs was analysed by Ve-cadherin, PECAM and VEGF mRNA gene expressions in qPCR and VEGF immunofluorescence staining. It was found that the coculture of hBMSC:HUVEC increased the proliferation, viability of hBMSC and HUVECs, and supported vascularization potential of bone like SFMs. In the second part of the study, the effect and osteogenic potential of integrin-binding peptides (IKVAV, RGD and YIGSR) on vascularized bone SFMs were investigated. The effects of different concentrations (0.5 mM, 1 mM, and 2 mM) of integrin binding peptides were examined through diameter and viability analysis, osteogenic differentiation analysis (DNA, ALP Activity and Calcium amount) and osteogenic marker expressions (ALP, collagen and osteopontin gene expressions) in qPCR. It was found that 1 mM RGD peptide supported higher proliferation, viability, and osteogenic differentiation than the IKVAV and YIGSR groups and 0.5 mM and 2 mM concentrations of RGD. In the third part, a plot study, the optimal light parameters in low level laser therapy (LLLT) (1, 3 and 5 J/cm^2 energy densities at 655 nm and 808 nm of wavelength) were investigated to induce osteogenic differentiation in hBMSC:HUVEC monolayer coculture through scratch assay, ROS and ATP synthesis, NO release, temperature monitoring, and osteogenic differentiation analyses. LLLT-dependent NO release and ATP synthesis were observed in monolayer culture. 5 J/cm^2 energy density at 655 nm and 808 nm of wavelength showed the highest osteogenic differentiation. In the fourth chapter, cell viability, diameter measurements, ROS and ATP synthesis, NO release, temperature measurement, osteogenic differentiation analyses and osteogenic marker expressions of SFMs were analysed within the same LLLT parameters (1, 3, and 5 J/cm^2 energy densities at 655 nm and 808 nm of wavelength). 1 J/cm^2 energy density at 655 nm of wavelength and 5 J/cm^2 energy density at 808 nm of wavelength exhibited higher osteogenic potential than the other experimental groups through ROS production, ATP synthesis and NO releasing. In the last part, cell viability, diameter measurements, ROS production and ATP synthesis, NO release analysis, osteogenic differentiation and osteogenic gene expression analysis were performed by combining the groups with the highest regenerative capacity of peptides (1 mM RGD) and LLLT application (1 J/cm^2 energy density at 655 nm of wavelength and 5 J/cm^2 energy density at 808 nm of wavelength). The combination therapy (particularly 1 mM of RGD and 1 J/cm^2 energy density at 655 nm of wavelength) improved regenerative capacity of SFMs rather than only RGD or only LLLT groups. Both peptide and LLLT applications in SFMs regulated and promoted stem cell behaviours such as proliferation, viability and differentiation due to the similarity to in vivo. However, the combined therapy provided higher bone regeneration rather than only peptide and only light applications. It is predicted that the combination of 1 mM RGD and 1 J/cm^2 energy density at 655 nm of wavelength group will be a potential application that can be used in the clinical trials.

Keywords: Scaffold Free Microtissues (SFMs), Vascularized Bone Microtissue, Integrin Binding Peptides, Low Level Laser Therapy (LLLT), The Combined Therapy with Peptide and LLLT, Osteogenic Differentiation, Bone Regeneration.

İntegrin Bağlayici Peptidlerin ve Düşük Seviyeli Lazer Terapisinin Doku İskelesiz Vaskülerize Kemik Mikrodoku Rejenerasyonuna Etkisi

Öz

Kemik doku mühendisliği (BTE) kemiğin hasar görmesi ve kırılması durumunda kemik rejenerasyon kapasitesini geliştirmeyi amaçlamaktadır. Geleneksel tek tabakalı hücre kültürü, BTE stratejilerinin öncül çalışmalarının araştırılması için hala yaygın olarak kullanılan bir teknik olmasına rağmen hücresel tepkilerin ve rejenerasyon kapasitelerinin ölçülmesinde yetersiz olabilmektedir. Bu dezavantajların üstesinden gelmek için doku iskelesi içermeyen mikro dokular (3D SFM'ler) geliştirilmiştir. Bu platform, hücre-hücre veya hücre-hücre dışı matriksin (ECM) düzenlenmesi açısından in vivo koşulları taklit etmekte ve ortak kültür oluşumunda maksimum hücre-hücre etkileşimine katkıda bulunmaktadır. Bunlar göz önüne alındığında, çalışmanın ilk bölümü insan kemik mezenkimal kök hücresi (hBMSC) ve insan göbek kordonu damar endotel hücresi (HUVEC) ile kokültür yapılarak vaskülarize kemik benzeri yapının oluşturulmasını amaçlamıştır. Çap ölçümü, canlı&ölü boyama yapılarak SFM 'lerin hücre çoğalması ve canlılığı doğrulanmıştır. Vasküler potansiyeli ise qPCR da Ve-cadherin, PECAM ve VEGF gen ifadeleriyle ve VEGF immünofloresan boyamasıyla analiz edilmiştir. hBMSC:HUVEC kokültürünün, hBMSC ve HUVEC'lerin proliferasyonunu, canlılığını arttırdığı ve kemik benzeri SFM'lerin vaskülarizasyonunu desteklediği bulunmuştur. İkinci kısmda, integrin bağlayıcı peptitlerin (IKVAV, RGD ve YIGSR) vaskülarize kemik SFM'lerindeki etkileri ve osteojenik potansiyelleri incelenmiştir. İntegrin bağlayıcı peptidlerin farklı konsantrasyonlarının (0.5 mM, 1 mM, and 2 mM) etkileri çap ve canlılık analizi, osteojenik farklılaşma analizi (DNA, ALP Aktivitesi ve Kalsiyum miktarı) ve qPCR'da osteojenik belirteç ifadelerinin analizi (ALP, kollajen ve osteopontin mRNA gen ifadeleri) ile ölçülmüştür. 1 mM RGD peptidinin, IKVAV ve YIGSR gruplarına ve RGD'nin 0.5 mM ve 2 mM konsantrasyonlarına göre proliferasyonu, canlılığı, ve osteojenik farklılaşmayı daha fazla desteklediği bulunmuştur. Üçüncü kısım, rehber

niteliğinde bir çalışma, düşük seviyeli lazer tedavisinde (LLLT) (655 nm ve 808 nm dalga boyunda ve 1, 3 ve 5 J/cm^2 enerji yoğunluklarında) osteojenik farklılaşmayı indüklemek için, yara modeli, ROS ve ATP sentezi, NO salınımı, sıcaklık ölçümü ve osteojenik farklılaşma analizleriyle hBMSC:HUVEC tek tabakalı hücre kültüründe optimal ışık parametreleri araştırılmıştır. Tek tabakalı kültürde LLLT 'ye bağlı NO salınımı ve ATP sentezi gözlemlenmiştir. En yüksek osteojenik farklılaşmayı 655 nm ve 808 nm dalga boylarının 5 J/cm^2 enerji yoğunluğu göstermiştir. Dördüncü bölümde, SFM 'lerin hücre canlılığı, çap ölçümleri, ROS ve ATP sentezi, NO salınımı, sıcaklık ölçümü, osteojenik farklılaşma analizleri ve osteojenik marker ifadeleri aynı LLLT parametreleri (655 nm ve 808 nm dalga boyunda ve 1, 3 ve 5 J/cm^2 enerji yoğunluklarında) ile analiz edilmiştir. 655 nm dalga boyunda 1 J/cm^2 enerji yoğunluğu ve 808 nm dalga boyunda 5 J/cm^2 enerji yoğunluğu, ROS ve ATP üretimi ve NO salınımıyla diğer deney gruplarına göre daha yüksek osteojenik potansiyel sergilemiştir. Son kısımda, peptitlerin (1 mM RGD) ve LLLT uygulamasının (655 nm dalga boyunda 1 J/cm^2 enerji yoğunluğu ve 808 nm dalga boyunda 5 J/cm^2 enerji yoğunluğu) en yüksek rejeneratif kapasitiye sahip grupları kombine edilerek hücre canlılığı, çap ölçümleri, ROS ve ATP sentezi, NO salınımı analizleri, osteojenik farklılaşma ve osteojenik gen ekspresyon analizleri yapılmıştır. Kombinasyon terapi (özellikle 1 mM RGD ve 655 nm dalga boyunun 1 J/cm^2 enerji yoğunluğu), sadece RGD veya sadece LLLT gruplarına göre SFM'lerin rejenerasyonunu arttırmıştır. SFM'lerdeki hem peptit hem de LLLT uygulamaları, in vivo benzerliği nedeniyle çoğalma, canlılık ve farklılaşma gibi kök hücre davranışlarını düzenlemiş ve arttırmıştır. Bununla birlikte, kombine terapi, sadece peptit ve sadece LLLT uygulamalarına göre daha yüksek kemik rejenerasyonu sağlamıştır.1 mM RGD ve 655 nm dalga boyunun 1 J/cm^2 enerji yoğunluğunun kombinasyonunun klinik deneylerde kullanılabilecek potansiyel bir uygulama olacağı öngörülmektedir.

Anahtar Kelimeler: Doku iskelesiz Mikrodokular (SFM), Vaskülerize Kemik Mikrodokusu, İntegrin Bağlayıcı Peptitler, Düşük Seviyeli Lazer Tedavisi (LLLT), Peptit ve LLLT ile Kombine Tedavi, Osteojenik Farklılaşma, Kemik Rejenerasyonu.

To my family

Acknowledgement

I would like to thank TÜBİTAK for “Project No. 220S280. The Investigation Biostimulative and Differentiation Efficacy of Red and Near Infrared Wavelength on Bone like Microtissues” named project support.

I am deeply and sincerely grateful to my advisor dear Assoc. Prof. Dr. Ozan KARAMAN. I appreciate all his support in providing me with ideas, patience, and funding to carry out my research.

I would like to express my sincerely thanks to Dear Assist. Prof. Dr. Nermin TOPALOĞLU AVŞAR for her contributions to the progression. I want to thank to the thesis advisory committee members, Dear Prof. Dr. Bahattin Tanyolaç, Assoc. Prof. Dr. Mustafa Şen and Assoc. Prof. Dr. Haşim Özgür TABAKOĞLU.

I would like to thank my office mate, Dilek Kaya for her friendship and support. I want to thank KARAMAN lab members, Sümeyra Arslan, Aylin Korkmaz, Gülşah Sunal and Günnur Pulat, the biophotonic lab research group members and Emel Bakay.

I specially thank my friends, Serap Akdeniz and Seda Yavuz for providing me with support, friendship, and motivation.

I especially thank my family for providing me with support and encouragement; my dear mother İlknur Yaralı, my father Sedat Yaralı, my sister Zülal Beril Yaralı and my brother Sedat Efe Yaralı, whose motivate me.

Finally, I want to special thanks to my husband Dr. Ali Çevik for his patience, big support, and understanding. I would not be successful without his encouragement and presence.

21 September 2022

Ziyşan Buse ÇEVİK

Table of Contents

Page

List of Figures

List of Tables

List of Abbreviations

2D : Two-Dimensional

3D : Three-Dimensional

ALP : Alkaline Phosphatase

ATP : Adenosine triphosphate

BMP : Bone Matrix Proteins

BTE : Bone Tissue Engineering

Ca^{+2} : Calcium

cm^2 : Centimeter

CCO : Cytochrome c Oxidase

COL : Collagen Type-I

COOH : Carboxyl

DCM : Dichloromethane

DIEA : N, N-Diisopropylethylamine

DMEM : Dulbeccos Modified Eagle Medium

ECM : Extracellular Matrix

EO : Endochondral ossification

FBS : Fetal Bovine Serum

Fmoc : 9-fluorenylmethyloxycarbonyl

g : Gram

GAPDH : Glyceraldehyde 3-Phosphate Dehydrogenase

hBMSC : Human Bone Marrow Stem Cells

HBTU : 2-(1H-benzotriazol-1-yl)-1,1,3,3-tetramethyluronium hexafluorophosphate

HOBt : Hydroxybenzotriazole

HUVECs	: Human Umbilical Vein Endothelial Cells
IO	: Intramembranous ossification
J	: Joule
LLLT	: Low Level Laser Therapy
MBHA	: 4-Methylbenzhydrylamine
ml	: mililiter
mM	: miliMolar
MSCs	: Mesenchymal Stem Cells
mW	: milliwatt
NH2	: Amine
nm	: Nanometer
NO	: Nitric Oxide
OD	: Optical Density
OPN	: Osteopontin
PBM	: Photobiomodulation
PECAM	: Platelet Endothelial Cell Adhesion Molecule
ROS	: Reactive Oxygen Species
SFM	: Scaffold Free Microtissue
TFA	: Trifluoroacetic Acid
TIPS	: Triisopropylsilane
Ve-cadherin	: Vascular Endothelial Cadherin
VEGF	: Vascular Endothelial Growth Factor
W	: Watt

List of Symbols

µl : microliter

ºC : Degree celcius

Chapter 1

1. INTRODUCTION

1.1 Bone

Human body is principally shaped by four major critically important tissues: nervous, epithelial, muscle tissue, and connective tissue. Bone is one of the critically important mineralized connective tissue for the adult human body [1]. Protection, strength, mineral deposition, homeostasis, supporting and movement tasks of the body are ensured by bone which plays an essential role in the interaction of the other part of the body, as a component of the skeletal system [2]. The architecture of bone in the human body is related with mechanical and biological functions of bone. Adult human body includes 213 bones which can be classified into five groups according to morphology: short, flat, irregular, long, and sesamoid [3, 4]. The shape and internal structures of bone, which are impacted by load and various stimuli and pressures, are important factors in defining bone specific properties [5].

1.1.1 Hierarchical Structure and Function of Bone

Bone tissue has a hierarchical arrangement that includes contents ranging from macro to nanoscale that communicate with the organs and tissues of the body (see Figure 1.1). Histologically, bone is classified into two types: primary (woven) bone and secondary (lamellar) bone [1]. Woven bone constructs the early stage skeleton [1, 2]. It barely endures in the adult skeleton, despite the fact that the primary form of bone forms in growth plates and the early stages of fracture callus. Woven bone is described as an irregular organization with random collagen fibrils and mineralization, which makes it adaptable but nearly weak. On the other hand, lamellar bone is characterized well organized and tightly packed collagen fibrils with regular distribution of osteocytes and matrix. Lamellar bone turns into the woven bone during growth and healing. The organization of lamellar bone supports rigidity and strength. Lamellar bone mostly consists of osteons units.

Structurally, bone is categorized at the macroscopic level as compact (cortical) and cancellous (spongy or trabecular) filled with bone marrow [4]. Whereas the compact part of bone constructs outside, the cancellous part of bone covers the inside. The recognition of both bone parts depends on their porosities and densities. The compact part is denser than the cancellous part. Bending, torsional, and shear stresses are all resistant to the compact bone architecture. The essential function of cancellous bone is the absorption of load and interruption of deformation. Cancellous bone, which is located in the bone marrow as 3 Dimensional (3D) network, is encloses in a relatively thin layer of compact bone that is mostly found at surrounding joints and inside of the skeleton. The weight of the mature skeleton comprises of 80% compact bone which has porosity of 5 to 10% and 20% cancellous bone which has porosity of 50 to 90% [1]. The cancellous bone is made out of osteocytes within a honeycomb shaped lacuna organization of trabecular plate rods sprinkled in the bone marrow. The lacuna spaces within the permeable design consist of red bone marrow into which mesenchymal stem cells (MSCs) are delivered [6]. Compact bone is covered by an external periosteal surface (periosteum), which is a fibrous connective tissue sheath surrounding the external compact surface of the bone.

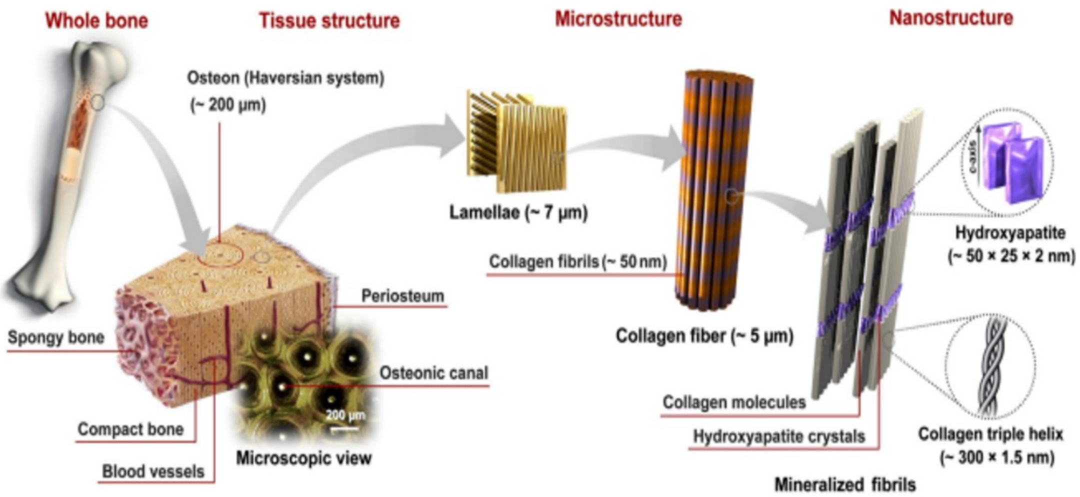

Figure 1.1: Structure of the bone from macroscale to nanoscale [7].

The periosteum plays a significant role in the healing, development, growth, and formation of bone. It also contains bone cells (such as osteoblast, and osteocytes), Haversian channel packaged with osteons and nerve filaments. Osteons are the main structural part of cancellous bone [2]. They are shaped from concentric lamellae surrounding Haversian canals, which lay down endosteal cells and include blood vessels, and nerves. The Haversian channel is a round and hollow shape, framed by osteogenic channels. The channel is covered by lamellae and lacunae which is the space between the osteocytes. Additionally, the channel includes blood vessels that provide metabolic enhancements, for example, oxygen, and glucose that can arrive at the bone surface [8]. Endosteum is a surface that covers the internal surface of all bones and encompasses the blood vessels (Volkmann's canals) [7]. The bone marrow is a reservoir of bone and stem cells, and the blood vessels within the marrow play a prominent role in the blood circulation of the bone. Cancellous bone has a higher metabolic activity than compact bone [1]. It shows remodeling and more quick responses to mechanical signals because primary bone cells are located on the surface and are closer to circulating growth factors and cytokines.

1.1.2 Bone Cell Types

One of the major components of bone is bone cells which have critically important role in bone formation, healing, and regeneration (see Figure 1.2) Remodeling of bone tissue in case of needed repair old and fractured consistently gets through a physiological cycle to adjust to environmental changes [9]. The process is resulted by the activity of special cells which are firmly managed and controlled through biochemical pathways. The major cell types of bone tissue are osteoprogenitors, osteoblasts, osteoclasts, and osteocytes [10]. In vivo remodeling of bone mainly consists of four following stages: mononuclear progenitor cell activation, mature osteoclasts resorption in the organic and inorganic matrix, matrix deposition, and new bone formation by osteoblasts.

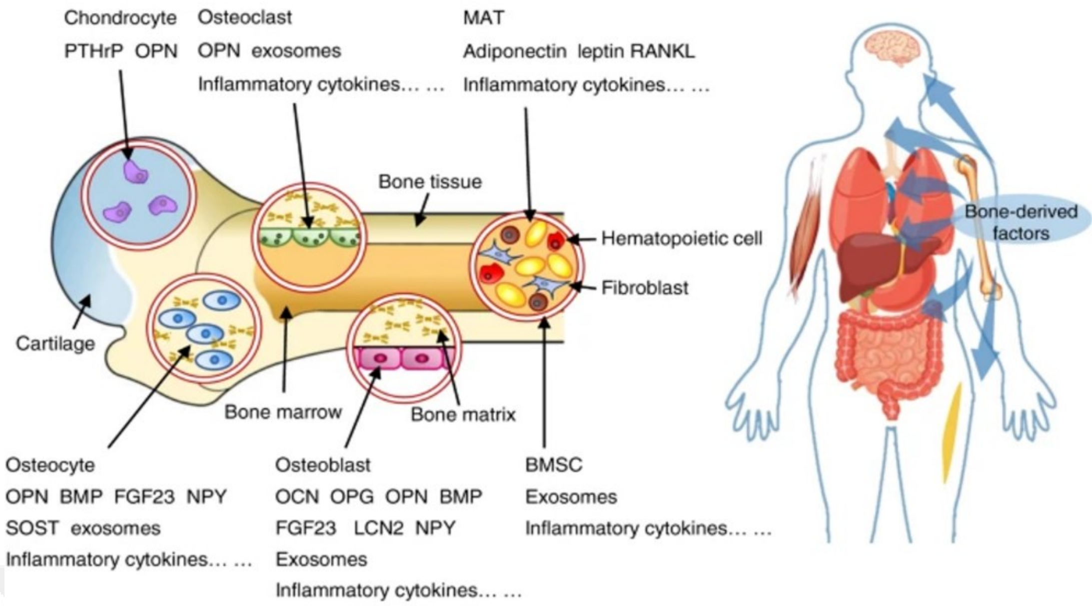

Figure 1.2: Primary cells in bone structure [11].

Osteoprogenitors: Osteoprogenitor cells, otherwise called osteogenic cells are MSCs that have a crucial role in the replacement and development of bone [2, 12]. The properties of osteoprogenitor cells are self-renewable and self-proliferative [13]. They are located within the endosteum, the cellular layer of the periosteum, and also the lining of the other osteogenic cells. In the osteogenic period, they are attributed as inactive osteoblasts. In case of bone growth, fracture, healing, and regeneration, MSCs differentiate into osteoblasts [2, 12].

Osteoblasts: Osteoblasts are cuboidal cells and unique differentiated MSCs. Osteoblasts secrete bone morphogenic proteins (BMP) and promote bone resorption and formation. Bone matrix is also formed by osteoblasts in two steps: matrix deposition and mineralization [4]. The initial step requires secreting collagen, predominantly type I collagen protein, non-collagen proteins (osteocalcin, osteonectin, bone sialoprotein II and osteopontin), and proteoglycans. This recently formed non-mineralized bone is called as osteoid. Then, the mineralization process occurs through hydroxyapatite crystals. Resistance to the pressure and homeostasis of bone are supported by osteoblast [10]. They produce bone extracellular matrix (ECM) composed of primarily collagen type I (COL) [9], alkaline phosphatase (ALP), osteopontin (OPN), and osteocalcin (OCN) [10, 14]. The mature forms of osteocytes are osteoblasts [10, 12, 14].

Osteocytes: Osteocytes are differentiated osteoblasts that is structure 95% of the cell part of the bone; in this manner, they are the most plentiful bone cell type [6, 10]. They have a major role in the bone forming process. Osteoblasts are inserted in the mineralized ECM, declined their volume, and turned stellar like shape with long cycles which constitute an organization with their near cells on the bone surface [14]. Osteocytes coordinate the bone formation and resorption activities by interpreting mechanical loading into biochemical signals [9, 10, 14].

Osteoclasts: Osteoclasts are final differentiated multinuclear cells of monocyte/macrophage which are differentiated by hematopoietic stem cells. These cells are located in the bone marrow and assembled with peripheral blood [6, 9]. Neighboring stromal cells and osteoblasts can regulate the differentiation and activation of osteoclasts. Osteoclasts break down the inorganic matrix [6] and secrete acids and lytic enzymes to degrade ECM proteins [9, 14]. During bone formation, osteoclasts are settled on the surfaces of the trabeculae or the inner surfaces of the compact parts and initiate dissolve them so they make new bone tissue [2]. In this way, the bone tissue has the opportunity to extend and expand, and to remove the aging and replacement.

1.1.3 Bone Matrix

The major bone component is matrix aside from bone cells. The matrix (which makes up 90% of bone) comprises four significant units: inorganic or mineral unit (65%), organic unit (20%), and lipids and water (less than 15%) [1, 3]. The inorganic bone matrix, which is called mineral phase, accounts for 99% of the storage of calcium in human body, 85% of the phosphorous, and 40% to 60% of the magnesium [2], sodium, and potassium [4]. Inorganic matrix is fundamental as hydroxyapatite which occurs with the chemical reaction of calcium and phosphate [4]. These ions constitute osteocalcium phosphate crystals (Brushite). While the rigidity of bone is regulated by hydroxyapatite crystals, the strength of bone is regulated by collagen [2]. These crystals are stored in a network of collagen fibrils and are surrounded by a layer of water and ions. The layer helps provision of calcium and phosphorus from the bone tissue to the blood in case of unsupplied these minerals in the body. The structure supports mainly bone strength, rigidity, and protection from compressive powers.

Additionally, bone can turn to soft, malleable, and spongy form in case of bone removal.

The tensile strength is provided by organic unit of bone [4]. The organic part, mostly type I collagen (nearly 90%) along with type V and XII, is produced by osteoblasts [1, 3]. The other 10% part of organic unit of the bone comprises of specific proteoglycans for bone and non-collagenous glycoproteins. Type I collagen with specific aminoacid substance is recognized by different collagens. It is framed of a triple helix of two α1 chains and one α2 chain. Each triple helix polypeptide chain of collagen is needed glycine, which is the smallest aminoacid, to create main structure of (Gly-X-Y)n sequence. The glycine is in the primary position, the X and Y position frequently followed by proline and hydroxyproline [4]. The type I collagen has relatively huge diameter fibrils so it provides large tensile loads in tissues including tendon and ligament. Bone specific proteoglycans are made out of glycosaminoglycane protein heterocomplex, for example, decorin and biglycan [4, 14]. They play critical role incollagen fiber association and growth factor binding. Non-collagenous proteins regulate the adjustment of the mineralization, and behaviours of cells. These proteins are osteocalcin, osteopontin (bone cell binding protein), osteonectin, and bone sialoprotein. Additionally, natural bone matrix has some growth factors such as IGF-1, IGF-2, bone morphogenic proteins (BMP), IL-1, IL-6 and platelet-derived growth factors that play an active role in the regulation of bone function [1, 3, 4].

1.1.4 Bone Formation

Bone formation is also called ossification or osteogenesis which occurs with two different steps: endochondral (Intracartilaginous) and intramembranous (Mesenchymal) ossification [15, 16]. In both of them, the developing first bone is the primary bone. The primary bone replaces with the secondary bone. During development of bone formation, primary and secondary bone and also resorption areas are found side by side [2]. Endochondral ossification (EO) is mostly realized in long bone formation [1]. Except for skull bones, the majority of the mammalian skeleton is formed by EO, which occurs when cartilage is replaced by bone tissue. The EO is triggered by the proliferation of chondrocytes into five zoned hyaline cartilage structure (see Figure 1.3). The construction of a cartilage model, growth of the cartilage model, development of the main ossification center (clustered osteoblasts are called ossification center), development of the secondary ossification center, and production of articular cartilage and epiphyseal plate are all followed processes in EO [15-17]. Briefly, the process of EO performed these following steps [1]: The resting zone mostly contains typical chondrocytes. When the chondrocytes proliferate in the proliferative zone, they show hypertrophy in zone 3 and delivery Alkaline Phosphatase (ALP), which ultimately results in chondrocyte apoptosis and arrival of angiogenic factors containing Vascular Endothelial Growth Factor (VEGF). Barren matrix is created by dead chondrocytes in calcification zone which supports migration of osteoprogenitor cells and capillary ingrowth. Then, osteoprogenitor cells generate osteoblasts.

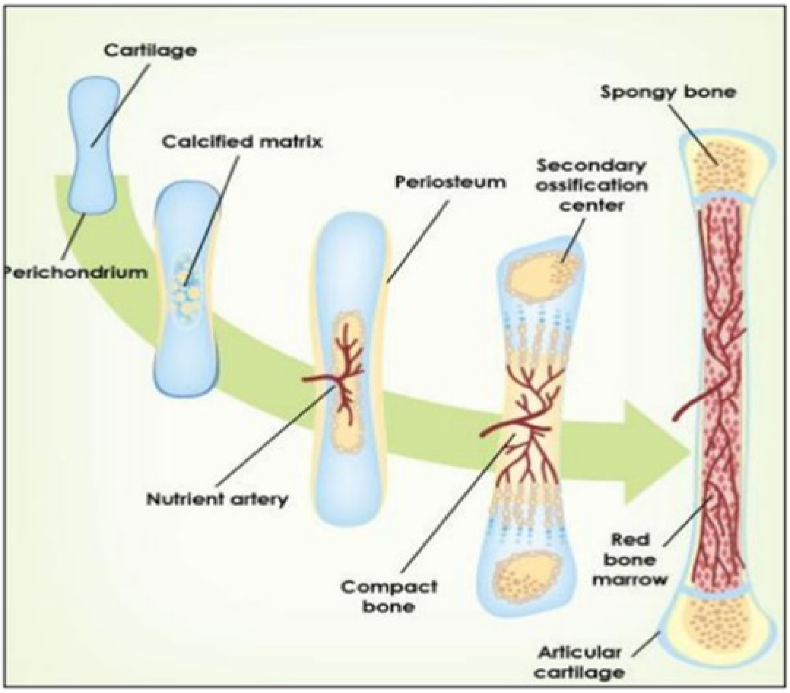

Figure 1.3: Endochondral bone formation [17].

The intramembranous ossification (IO) spontaneously occurs without EO. The process develops during the flat bone formation, primary bone healing, and distraction osteogenesis. MSCs in the embryonic skeleton differentiate into osteoblasts and capillary cells. The osteoblastic cells take place ossification centres (see Figure 1.4) [2, 15].

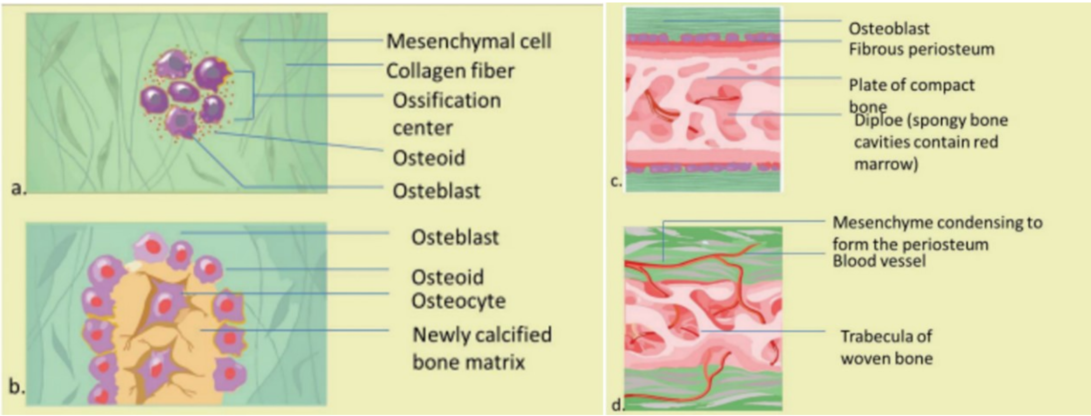

Figure 1.4: Intramembranous Bone Formation [15].

IO take places via spontaneously improvement of ossification center [1, 2, 15]. Osteoid tissue (bone matrix) is created by osteoblast which is settled into the lacunae. After a few days, the osteoid tissue shows mineralization. Then, osteoblasts produce osteocytes. Primary cancellous bone and periosteum are shaped. Encapsulated cells and blood vessel formation are formed. Deposition of osteoid is followed by osteoblasts, the encased cells form into osteocytes. Accumulating osteoid is set down between embryonic blood veins, which structure a random organization of trabecular (instead of lamellae). Additionally, vascularized mesenchyme consolidates on external face of the woven bone and turns into the periosteum. Osteocytes lose their capacity to contribute to expansion of bone size. However, osteoblasts on the periosteum surface produce more osteoid tissue that thickens the tissue layer on the current bone surface. Shaped woven bone that subsequently turns into mature cancellous bone. Cancellous bone, consisting of distinct trabeculae, persists internally and vascular part of cancellous bone becomes red marrow. The cancellous bone is shaped by the fusion of many ossification centres. Bone mineralization makes bone moderately impermeable for supplements and metabolic waste. Compact bone is newly formed and thickens on the trabeculae. During bone formation, veins and surrounding connective tissue are compressed. Additionally, the Haversian canals are modelled in bone structure.

1.1.4.1 Vascular Supply for Bone Formation

Bone is a dynamic and vascularized tissue going through consistent remodelling [16, 18]. Long bones especially contain diaphyseal nutrient artery and periosteal veins that penetrate the bone and interface to the encompassing vascular supply of tissue [15]. Tiny blood veins support nutrients and removals of waste for osteocytes in the complex bone. The structure carries oxygen and supplements to osteocytes implanted inside the concentric mineralized lamellae and the fundamental multicellular unit including endothelial cells, osteoblasts and osteoclasts [18]. While vascular cells can regulate bone cells activity, bone cells can also regulate the activity of vascular cells [19, 20]. Vascular structure basically consists of endothelial and mural (or perivascular) cells. The perivascular cells can be classified as pericytes and vascular smooth muscle cells. Endothelial cells are functional cell types in blood vessel formation process. Angiogenesis or vasculogenesis processes contribute formation of blood vessels.

Growth of new capillaries happens from pre-existing blood in angiogenesis [21, 22]. The process is mainly defined as followed steps: endothelial cell activation and matrix degradation, cell proliferation, vasculogenic assembly, vessel sprouting, formation of lumen and vascular structure remodelling [22]. Similar to angiogenesis, vasculogenesis is also new vessel formation process. Vasculogenesis depicts the improvement of fresh blood vessels from in situ separating endothelial cells [23]. Vasculogenesis is characterized as the differentiation of endothelial precursors, or angioblasts, into endothelial cells during the early development of embryo and de novo constitution of a primitive vascular organization [21]. Mesenchymal cells and smooth muscle cells are necessary for vascular regeneration, stabilization, growth, and maturation. In addition, vasculogenesis can be regulated by internal signals. The internal signals are directed by special molecular markers of endothelial cells. Since bone is a highly complex and vascularized tissue, these directions are also crucial for bone vascularization process.

1.2 Bone Tissue Engineering

Bone tissue is a programmed organized tissue which has repair and regeneration capacity. However, bone disorders are daily problem with striking health, social and economic consequences. Bone health can be also deteriorated by age, damage, fractures and diseases. More than 20 million people are faced with bone loss [24, 25]. Bone has naturally the capacity to heal uninterruptedly in the event of injury throughout adult life as a requirement of the skeletal system. Bone recovery contains a perfectly tuned series of organic occasions of bone acceptance and conduction, including various cell types and intracellular and extracellular signalling pathways, with the end goal to upgrade skeletal fix and establish skeletal capacity [13]. However, natural regeneration capacity of long bone fractures may be insufficient [26]. Thus, organ grafts (such as autograft, allograft, and xenograft) are used to effort these fractures. Autograft is a type of grafts which is taken from a person and transferred to same person [27]. It doesn’t have any rejection risk and disease transmission challenge even though harvest sites limitation, additional operations and amount of graft material cause patients to hesitate. Allograft is transplanted from cadavers to a recipient [28] but it carries risks of contamination and immune rejection [29]. Xenograft is harvested from animals. Moreover, nearly 60% of grafts fail for osteointegration to bone units and repair fractures [30]. To overcome those disadvantages, new strategies such as bone tissue engineering (BTE) are welcomed approach to recover bone fractures.

BTE is a multidisciplinary field that aims to regenerate and repair damaged bone tissue by using physiological pathways, biological process, bioactive materials and cell therapies [29, 31, 32]. BTE primarily aims to understand natural structure of bone, mimic the structure in vitro conditions and improve regeneration capacity of bone. Thus, the field benefits from stem cells, growth factor/signal molecules and scaffolds based or scaffold free systems to create engineered tissue (see Figure 1.5) [29-31, 33]. These combinations target cell attachment, growth, viability, proliferation, high quality matrix interaction, osteogenic differentiation and vascular ingrowth [32].

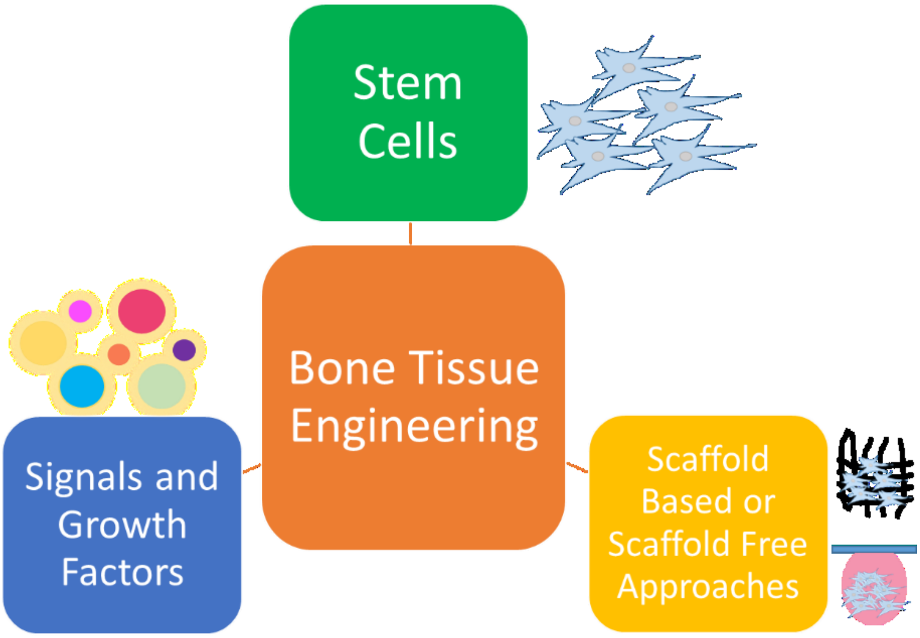

Figure 1.5: Bone tissue engineering strategies for regeneration.

1.2.1 Stem Cells

One cell type of hematopoietic tissue derived [34] is progenitor cells, which are initiator cells for regeneration, have therapeutic potential for bone repair mechanism [32]. For BTE, especially mesenchymal stem cells (MSCs) are precious sources to create bone architecture. Under the appropriate physiological conditions, stem cells can migrate to damaged area and differentiate into several tissues such as cartilage, bone, neuronal tissue, muscle, tendon, and adipogenic tissue [35].

Human MSCs are recognized one of multipotent stem cell that can be promptly obtained from different grown-up tissues including the bone marrow, adipogenic tissue and blood [9, 30, 32]. Human bone marrow stem cell (hBMSC) is one of the most suitable cell type because of wide accessibility, high proliferation and migration capacity [30, 36], low risk profile and minimally invasive isolation process [37]. hBMSC is a viable alternative source for autologous bone transplants [30].

hBMSCs closely get in the contact with endothelial cells in natural bone structure because the combination of stem cell and endothelial cell promoted the vascularization of bone tissue. As vascularization is critically important process for bone formation, stem cells in bone regeneration are needed vascular cells. One of the differentiated human endothelial progenitor cells is human umbilical vein endothelial cells (HUVECs) which promote vascularization of bone [38]. The coculture of hBMSCs and HUVECs increases cell viability in vitro conditions [18, 38]. Moreover, vascular endothelial growth factor (VEGF), which is released by HUVECs, improves to osteogenesis [18, 38] and regulates vasculogenesis [20]. Furthermore, bone morphogenic proteins (BMPs), which are also induced by VEGF, support osteogenic differentiation of hBMSCs [18]. Consequently, the coculture of stem cells and endothelial cells are critically important for expression osteogenic markers and also osteogenesis.

1.2.2 Growth Factors/Signal Molecules

Understanding biochemical environment of bone supports to easily creating natural bone structure [39]. Biomimetic agents (growth factors and signal molecules) are specific components that are used as BTE strategy to promote differentiation of stem cells and to increase regeneration capacity of bone. Differentiation of hBMSCs is also triggered by the microenvironment. The microenvironment including the agents transfers signal molecules for stem cell differentiation and provides faster regeneration. As physiological, growth factors play fundamental role in bone ECM [30]. After injury, growth factors are actively synthesized and delivered for remedy of damaged bone. The factors also promoted proliferation, migration, differentiation of cells and also ECM synthesis. Bone morphogenetic proteins (BMPs), changing growth factors -β1 (TGF-β1), vascular endothelial growth factors (VEGF), and insulin-like growth factors 1 (IGF-1) can significantly regulate bone repair. Growth factors such as VEGF and BMP permit to accelerated bone and vascularization [33]. In similar, bioactive signal molecules (hormones, antibodies, and nucleic acids) are also effective agents for bone healing process [40]. They can regulate bone regeneration by promoting cell proliferation and producing ECM.

1.2.3 Scaffold Based Approach

Scaffold based materials aim to regenerate bone unions in case of restricted accessibility or morbidity of donor [29]. Many different biomaterials (natural scaffolds, ceramics, polymers, metals, and composites) can be utilized for the development of the platforms that better mimic bone organization and repair damaged bone structure [29, 41]. The major properties of biomaterials in BTE are biocompatibility, bioactivity, biodegradability, reproducibility, ability three dimensional (3D) structure, high porosity, and no potential of immune rejection [26, 29].

Natural scaffolds such as alginate, collagen, fibrins, gelatine and etc. can mimic natural environment of tissue [26, 29, 30]. They have porous 3D structure and available and biocompatible properties [29] but they have low mechanical properties. Thus, their structures are also brittle. Ceramics comprise inorganic oxides and salts such as calcium phosphates, which is one of the major bone components [31, 42]. Bioceramics can provide osteoinductivity (enrolment of immature cells and development of preosteoblasts) and osteoconductivity (bone growth on the surface) for bone tissue [43]. Biomimetic scaffolds with bioceramics exhibit great mechanical strength and adjustment capacity. Although they are degradable materials, slow motion degradation and brittle properties are disadvantages of those scaffolds [44]. Polymers are biomaterials which remodel bone tissue and permit to tissue growth [30, 42]. Synthetic polymers (polycaprolactone (PCL), polylactic acid (PLA), poly(glycolic acid) (PGA) and etc.) can be hold under the control so they are open source for the surface modification [26, 29]. A critical unfavourable properties of polymers are their lower ability in terms of interaction with cells [26], poor cell adhesion and compression strength [44]. Metals (for example: titanium, stainless steel, cobalt) have superior mechanical features such as great strength, formability and hardness [41, 42]. Nonetheless, they have many limitations such as toxic corrosion products, low long term functionality and lack of inherent bioactivity [42]. Composites are created by combination of two or more different biomaterials [29]. They have biocompatible properties and great degradation rate for bone tissue. Moreover, they are also osteoconductive materials [44]. However, composites are fabricated to eliminate disadvantages of the other biomaterials [29], the fabrication procedures can be complex [44].

The regeneration of bone may occur with scaffold based approach because of their natural 3D shapes and possibility of cell growth, viability and differentiation of hBMSC rather than 2D systems. However, the using scaffold based approach presents some challenges addition to special disadvantages of scaffold types. For example, inhomogeneous cell distribution in porous scaffolds and low initial density for large constructs [45]. Synthetic scaffolds are particularly required biofunctionalization process [46]. Scaffold based approach, which is not static, exhibits insufficient nutrients diffusion and wastes removal of cells. It does not permit self ECM production [45]. These challenges move from lab benchtop to clinical relevance has been credited to biomaterials (limited known compounds, regulations and functionalities) and complexity (too complicated large scale production and reproducible fabrication) impediments [32]. To overcome these challenges, scaffold free approach is an alternative way for bone regeneration in BTE.

1.2.4 Scaffold Free Approach

Scaffold free approach, which is a bottom up technique, is set up self-assembly systems [45]. It doesn't have any solid support by allowing cell growth within own ECM [47]. On the other hand, it relies on self-aggregation and organization properties of cells to produce 3D spheroids or organoids [48]. The approach presents simulation of complex bone structure because it permits to natural cell to cell connection and cell to matrix interaction [49]. Unique design of microenvironment in tissue can be utilized to enhance proliferation rate, ECM production, stem cell differentiation and migration [49, 50]. Since natural ECM components are directly synthesized by cells, it is easy to lead to enhance cell to cell contact and communication and also follow signalling pathways [51, 52]. In addition, the approach provides to control culture conditions via growth factors or additional biomaterials. When scaffold free approach also presents in vivo, it also permits to growth factor and signal molecule diffusion on in vitro condition in absence of the scaffold networks [53]. It is possible to come together multiple cells so it gives more similar results to in vivo systems rather than monolayer culture [51, 52, 54]. Gene and protein expressions of stem cells and endothelial cells in scaffold free approach are also identical with in vivo systems [55, 56]. Thus, scaffold free approach supports to mimic natural bone structure in vitro conditions.

Scaffold free approach, which contributes to the perfect cellular connection and cell matrix interaction, helps to understand in vivo conditions for cellular development. Thus, 3D scaffold free systems have been gained a trend in recent years. Researches about scaffold free approach sharply increased between 2016 and 2019 according to study of Lee, SJ and Lee, HA in nonclinical testing (57). The reason of the dramatically tend to use of scaffold free approach may depend on having high applicable technology for many different tissues and cell types such as brain, heart, muscles, lung, liver, kidney, cancer, blood, and stem cells [50, 57-59]. Since these different cell types has enabled in scaffold free approach, the approach can be practiced in many fields such as precision medicine, toxicology, drug discovery, host and microbe interactions, gene editing, phylogenetic studies, development biology, disease remodelling (tumor ingrowth) and regenerative medicine [58, 59].

Scaffold free approach has many different fabrication techniques such as pellet culture, hanging drops, bioreactors, cell sheets, microfluidics, magnetic levitation, and low attachment plates [45, 46, 48, 49, 53, 55, 60, 61].

Pellet culture: The technique is get together by centrifugal force. Cells are adhered into each other on deep of the tube [55]. After cell pellet is removed, it is resuspended to form spheroids or microtissues. It can be used in signalling pathway researches. Moreover, it can be used many different biomedical application such as differentiation of stem cells.

Hanging drops: The technique employs specific hanging drop plates with a bottomless well where the media droplet develops [46]. Aggregates within the tiny droplet of culture medium form the microtissues. Coculture can be accomplished by adding cells during the initial distribution or by increasing cells sequentially. Additionally, it is moderately easy and productive. Moreover, it is applicable for different cell lines without toxicity tests and drug discovery. On the other hand, the technique has an advantage in terms of reproducibility with persistent size of spheroids.

Bioreactors: Cells are cultured into spinner or rotating wall vessels. They are durable suspended state in containers. The critical point of the technique is stirring rate because high speed may be detrimental for cells [55].

Cell sheets: The technique, which doesn't use any scaffold to produce microtissue, uses only tiered cells layer by layer [49]. Basically, cell sheets are constructed in monolayer culture flasks where are covered by thermoresponsive polymer [45]. They are harvested depending on thermal parameters [62]. They can be applied for prevasculogenesis, corneal tissue, dentistry and also BTE [45, 62].

Microfluidics: The miniaturize device is constructed by many interconnected microwells to loading chamber through with microchannel that has more dynamic environment [46, 61]. Microfluidics allow for accurate control of low amounts of fluid through hollow tubes as small as 1 μm diameter. Spheroids, which have uniform size, may be manufactured at high throughput and are applicable for both monocultures and cocultures. Microfluidics, which are cost effective platforms, remodel to test efficacy and toxicity of the growth factors or signal molecules because they contribute examination of gradient of oxygen, nutrients or chemical concentration [61]. Organ on chip based microfluidics center on mimicking the healthy tissue functions or disease responses. The property allows to investigate disease phenotypes and pharmacological responses that are clinically relevant and provides more accurate predictions of treatment efficacy.

Magnetic levitation: Spheroids are formed through magnetic nanoparticles [46, 60, 61]. Magnetic nanoparticles are attached into cells during a day. After magnetic field is applied into cells, spheroids are fabricated without continuous magnetic field.

Low attachment plates: The surface of low adhesion plates, which has wells, inhibits cell adherence into surfaces and encourages cell aggregation [46]. The coating material which may be poly-2-hydroxyethyl methacrylate (HEMA) or agarose [60, 61]. Agarose is a really successful substance for preventing cell attachment. It outperforms in terms of non-adherent characteristics compared with the poly-HEMA. Cells grow depending on microgravity on agarose and release self ECM proteins [55].

Agarose, is specifically used material in 3D petri plate which is one of the low attachment plates fabrication technique, can be preferable for tissue modelling [54, 63, 64]. In agarose, cells spontaneously form scaffold free microtissues (SFM) by boosting cell to cell adhesion and cell to self-synthesized matrix protein connection. It is ideally suited for multicellular culture due to their huge capacity. Since it is a non-toxic compound, it is commonly utilized for BTE applicaitons. Moreover, the technique has high throughput screening and mass production properties [61].

SFMs, which are fabricated in low attachment plates, construct a diffusion gradient for nutrients, oxygens, carbondioxide, biological or chemical compounds [60, 61]. They also create a proliferation zone and permit to follow proliferative effects of biomaterials, growth factors and signal molecules (see Figure 1.6) [60, 65].

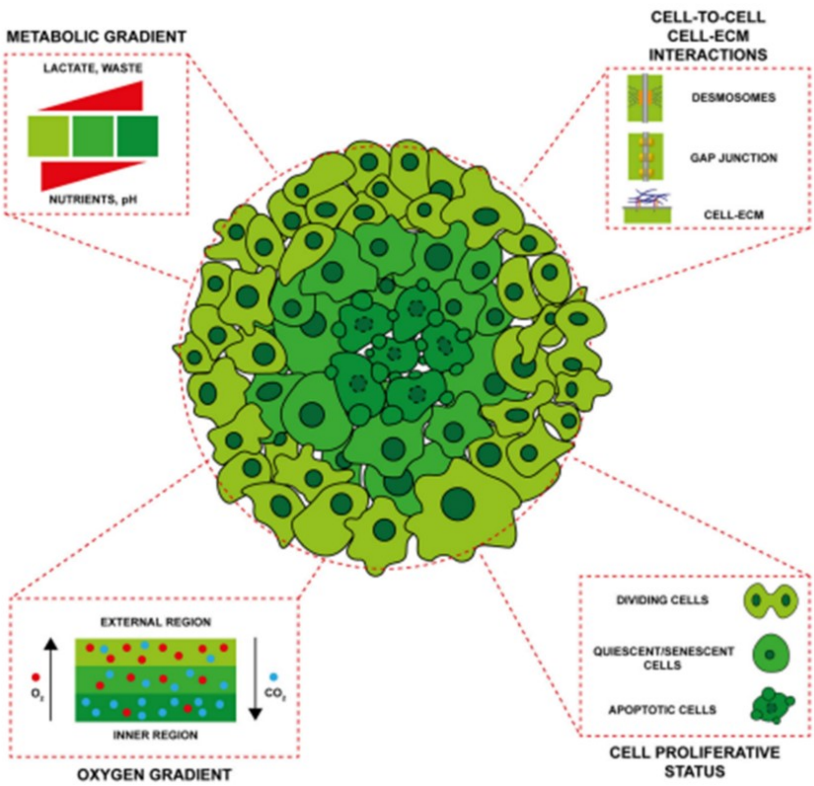

Figure 1.6: Zones of Microtissue [65].

The proliferative zone is shaped on outside of SFMs [65, 66]. The middle layer is quiescent zone where receive less oxygen molecules than proliferative zone [65, 67]. Hence, the layer develops slowly compared with outside of SFMs. The inner layer of SFMs includes necrotic cells which are constructed necrotic zone. Metabolic products such as CO_2 level, lactate and waste increase from proliferative zone to necrotic zone [65]. Controversy, oxygen level, pH and nutrients decrease from proliferative zone to necrotic zone [65, 66]. SFMs exhibit maximum cell to cell interaction and cell matrix communication [65]. Especially, desmosome structure which is intercellular junctions, plays a crucial role in cell behaviour [68]. The structure is responsible for context-dependent signals and regulation of cell behaviours such as migration, adhesion, differentiation, and tissue specific expression even tissue regeneration. Additionally, cell to cell interaction is occurred by gap junction which is intercellular connection [69]. The interaction improves the transduction of cellular signals which includes proliferation, angiogenesis, survival, differentiation, and even responses to treatments [55, 70]. Similar to desmosomes, gap junctions also regulate bone tissue development, MSC differentiation, remodelling.

Since SFMs have the high capacity of cell to cell and to matrix, they model in vivo conditions in terms of proliferation, migration, adhesion, differentiation of MSC, and tissue regeneration. Thus, bioactive molecules, particularly peptides, can be examined by using more complex systems such as SFMs. SFMs could serve more realistic response in terms of sensitivity and resistance to bioactive molecules because they are platforms that have a tissue deep [63, 64, 71]. SFMs mimicking in vivo conditions might permit more precise characterization of varieties in cells, gene, protein, and bioactive molecules, and ingredients. Therefore, SFMs have great advantages in bone regeneration particularly bioactive peptide researches [63, 72].

1.3 Biofunctional Peptide Application for Bone Regeneration

Proteins are small constitutes of cells that are primary constructed by peptide chains [73]. All proteins have bioactive chains which carry out the activation process of proteins [73, 74]. The active sites interact with specific binding target which is peptide sequence. Peptides are small molecule chains and consisted of 2-20 aminoacids [74-76]. Due to diversity of their biofunctionality, peptides have received increasing attention from the pharmaceutical and cosmetic perspectives as well as the scientific community [76]. Peptides have voluminous advantages so peptide therapies make for a large percentage of the pharmacological industry, with global sales exceeding $70 billion in 2019, indicating a more than two-fold jump over 2013 [77, 78]. Peptides are obtained from natural sources such as milk, fish, meat etc. as well as synthesized in the laboratory conditions.

1.3.1 Chemistry of Peptide Synthesis

Peptide synthesis process basically covers two major methodologies which are liquid phase peptide synthesis and solid phase peptide synthesis (SPPS) under laboratory conditions [79]. Classical liquid phase peptide synthesis supports large scale products but it causes low purification yields, only small sequences and optimization problems. Moreover, liquid phase synthesis is also time consuming and laboratory intensive technique [77, 80, 81]. Products of liquid phase peptide synthesis show less purity.

To overcome these disadvantages of liquid phase peptide synthesis, SPPS has been developed by Merrifield in 1963 [77, 81, 82]. Basically, synthesis of SPPS is made up of a cycle that involves the carboxylic group of amino acids being coupled to a solid polymeric resin and the amine group being released from the protection group (see Figure 1.7) [77, 82, 83]. SPPS follows these fundamental steps: 1. binding the first aminoacid into resin, 2. deprotection of side chain protecting groups, 3. coupling new aminoacid with previous aminoacid, 4. repeat 2. and 3. steps until the end of the sequences, 5. cleavage peptide sequences from the resin [83]. The amine group and the side chains of the amino acids are frequently protected by distinct chemical groups during synthesis, which reduces the purity of peptides [83].

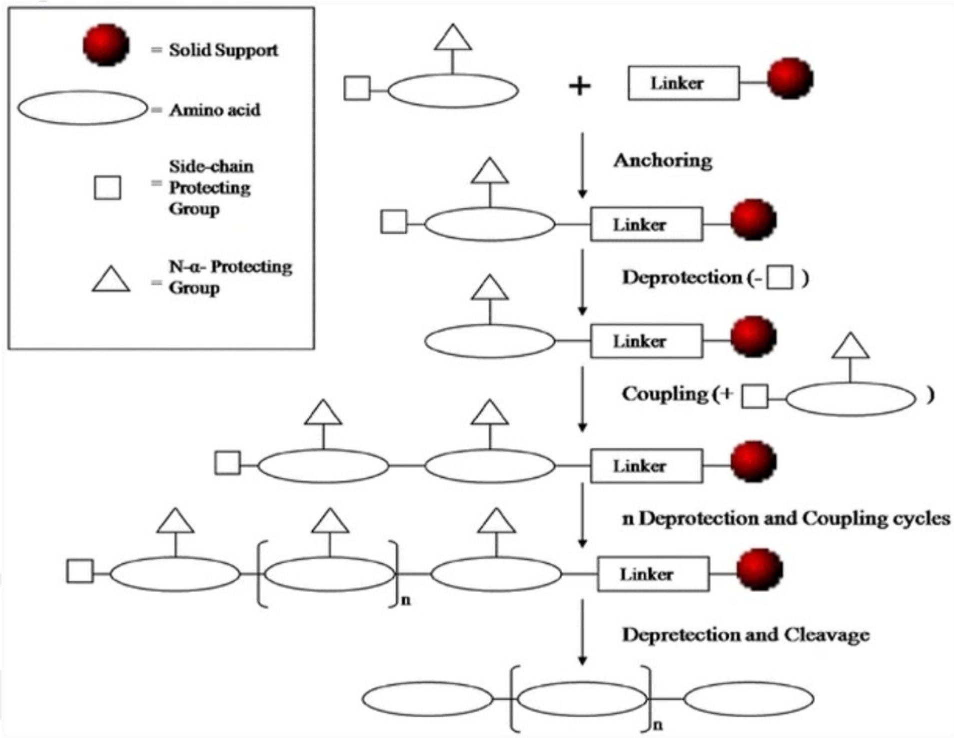

Figure 1.7: Schematic of SPPS steps [83].

SPPS uses either Bmoc or Fmoc chemistry as protection groups [77, 80]. Fmoc chemistry became the most popular because it includes less toxic compound than Bmoc in terms of purification and separation process of protection group [80]. Since Fmoc chemistry has less side reaction and also more safety than Bmoc chemistry, the Fmoc is more preferable for SPPS.

It is possible to attain stabile biofunctional peptides that can be produced by Fmoc-SPPS methodology in laboratory conditions. Previous studies have been shown that chemically synthesized peptides are able to exhibit properties of natural peptide and protein sources [63, 64, 81].

1.3.2 Biomimetic Peptides

Biomimetic peptide may probably initiate physical and biological pathways [73, 75, 76, 84, 85]. They tend to a wide range of biological functions, including immunomodulatory, antimicrobial, mineral binding, antioxidative, and regenerative properties [73, 75, 76]. The usage of biofunctional peptide fragments supports to low toxicity, high biological and chemical diversity, immunogenicity, high selectivity, great efficacy, low accumulation in biological systems, and a variety of specific targets [86].

Biomimetic peptides comprising signalling domains interact with receptors on the ECM proteins and surfaces of cell membrane [87-89]. Diversity of ECM related peptides has been investigated for bone regeneration. They use sources of ECM proteins and send signal molecules for bone cell attachment, migration, proliferation, and differentiation [84, 87, 88]. Moreover, they also upregulate ECM products and expressions of osteogenic gene markers. One of the ECM related biomimetic peptides is integrin binding peptides [87].

1.3.2.1 Integrin Binding Peptides

Adhesion is a dynamic process, with cells constantly are on the alert for their environments. Since cells have a highly sensitive receptor, they react immediately altering their orientation and differentiation [90, 91]. Integrins, which are adhesion molecules of cells, moderate cell to cell and cell to ECM interactions in a wide range of physiological process, along with adhesion and migration, differentiation, proliferation, mechanotransduction (Mechanical stimuli are sensed and responded by cells which turn them into biochemical signals that activate specific cellular responses) organ development and tissue regeneration [90, 92-94].

Moreover, integrins are heterodimeric membrane proteins made up of α and β subunits that are an essential component of integrin-adhesion complexes in focal adhesions in terms of outside to inside signalling [88, 92, 95, 96]. These orientation, proliferation and differentiation are possible with regulation of α and β subunits of integrin. The subunits, which are linked each other as covalent and construct heterodimer structure, consist of type I transmembrane protein which links with ECM and cytoplasma membrane [92]. Human and mice have 18 integrin α subunits and 8 integrin β subunits, resulting in at least 24 distinct integrin αβ heterodimers [90, 92, 93]. The heterodimer complex transmits transmembrane signals as bidirectional by conformational changes. The extracellular domains undergo widespread conformational changes, resulting in a fast increase in ligand-binding affinity [92, 96, 97]. Integrin receptors have many binding capacity of ligand receptors. The activation of these receptor is modulated by ECM and surface adhesion molecules [90, 92].

The ligand and ECM interaction induces the stabilization of high affinity conformations that maintain signalling to the cytoplasm, consequently altering cellular processes such as proliferation, metabolism, and migration [92]. Thus, integrin mediated cellular behaviours play a critical role in proliferation, migration, adhesion and differentiation of stem cells, even regeneration capacity of bone [9, 87, 96]. Since most of cell to ECM interactions are mainly regulated by universally expressed integrins, integrin binding sequences such as Arg-Gly-Asp (RGD), Ile-Lys-Val-Ala-Val (IKVAV), and Tyr-Ile-Gly-Ser-Asp (YIGSR) have crucial role in regulation of bone regeneration [95, 98-102]. These subunits adhere to bone matrix proteins such as (collagen, osteopontin, laminin, fibronectin, vitronectin, etc.) and upregulate osteogenic genes and protein expression [87, 88, 99-101, 103].

RGD: RGD is one of the most well-known small peptides in BTE. RGD targets specific plasma membrane glycoproteins, allowing the classification of ECM protein receptors, many of which are α and β heterodimers of the integrin family [90, 104]. RGD is a short peptide which is found in ECM proteins such as fibronectin, laminin, vitronectin or bone sialoprotein [95]. RGD unit of fibronectin, which is one of the ECM protein, is recognized by five different integrin subunit (mostly $\alpha5\beta1$) [96, 104]. It binds to integrins to improve cell adhesion, proliferation and differentiation. Literature has been reported that small RGD units can augment attachment and differentiation of MSCs [95, 105]. RGD sequence directly enhances osteoblast survive [96]. Additionally, RGD contributes to bone ECM deposition and intracellular bridges [105]. Thus, RGD may be effective sequence to ensure bone regeneration.

IKVAV: One of peptides of laminin protein structure, which is located within ECM, is IKVAV sequence [97]. The IKVAV sequence consists of Isoleucine, Lysine, Valine, Alanine and Valine aminoacids, respectively. Laminin protein is one of the main proteins in ECM of bone marrow [106]. Especially, α subunit of laminin is mostly accountable for integrins binding receptor. Although laminin expression is mostly observed in endothelial cells, the relation of laminin and integrin supports cell viability, adhesion, proliferation, migration, and differentiation of stem cells [104, 106-112]. The peptide may lead bone regeneration in case of stem cell and endothelial cell combination.

YIGSR: Similar to IKVAV, YIGSR is also found in β1 unit of laminin [88, 102, 113]. YIGSR may also regulate integrin mediated signalling molecules just as RGD and IKVAV [102]. YIGSR supports attachment, spreading, proliferation, and migration of cells [88, 102]. Additionally, it improves cell to matrix interaction [114, 115]. YIGSR peptide may affect stem cell adhesion and environment [115]. The adhesion of stem cell forces integrin protein interaction so stem cells attached into bone ECM. Additionally, the attachment of matrix in stem cells contributes to differentiation and regeneration of them. Li L. et. al. showed that scaffolds including YIGSR sequence may enhance bone regeneration capacity [114].

1.4 Low Level Laser Therapy (LLLT) or Photobiomodulation (PBM)

Low level laser therapy (LLLT) is another application of BTE. LLLT can be used to improve regeneration capacity of bone. Historically, Nils Finsen won the Nobel Prize by using lamps in recovery of tuberculosis research in 1904 [116]. However, discovery of LLLT dates back into the late 1960s by Endre Mester. The term of LLLT replaced with Photobiomodulation (PBM) which is mostly used in nowadays [116-119]. Many different fields such as targeting inflammation, sport injuries, ophthalmology, dermatology, autoimmune disease, lung disease, enhancements of performance, skin and bone healing [116, 119] benefit from LLLT or PBM.

LLLT can be provided by low level lights or light emitting diodes (LEDs) at visible (400-700 nm) and at near infrared spectrum (700-1000 nm) (see Figure 1.8) [116, 120]. Clinical trial benefits from spectra between 600 and 1000 nm, which is called as therapeutic window, addition to blue, green, yellow, and infrared spectra in visible light [121, 122]. Since the visible light is restricted by penetration depth, it may fail for surgery to form a physical window [122]. However, the 690 nm and 860 nm range (laser light) is defined as the ideal range because of their penetration capability

[121, 123]. Actually, the laser light source generates electromagnetic radiation with a high degree of coherence rather than non-coherent LEDs, which is often monochromatic and directed, and is similar to a flat wave. Since laser light is amplified by stimulated emission, it has properties such as monochromic, collimation and coherence [124]. Moreover, red and near infrared ranges have healing features on cells where they can enhance energy production and regeneration so the laser light reaches deeper area of tissues [122].

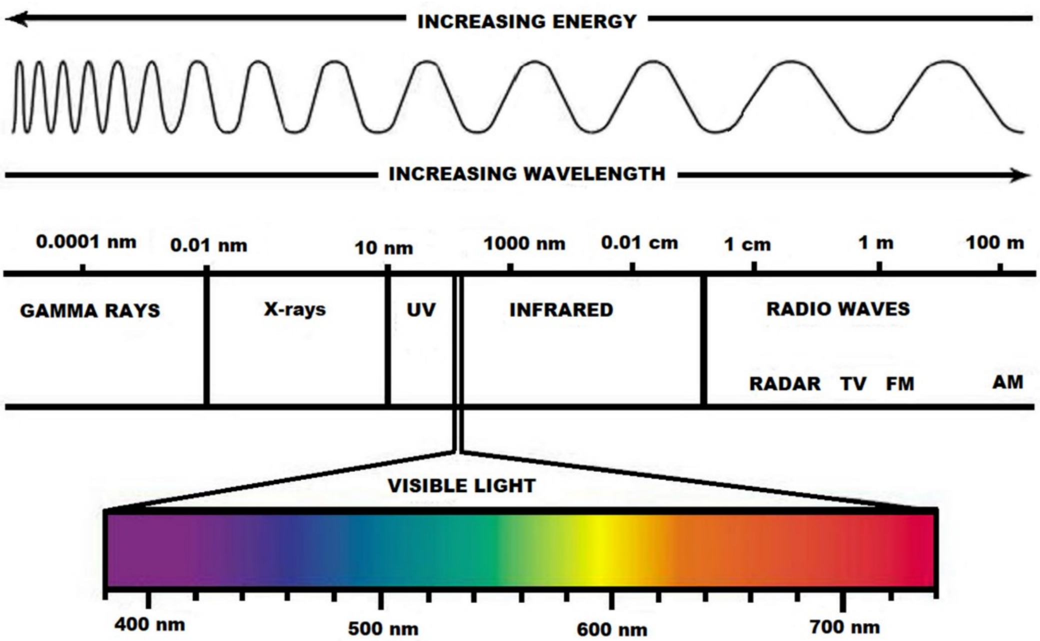

Figure 1.8: Electromagnetic spectrum for LLLT [120].

1.4.1 The Molecular Mechanism of LLLT

The LLLT influences the action of photoacceptors or chromophores for induction cell signalling in biological systems [119, 125]. Chromophores are absorption molecules for light. One of the main chromophores in LLLT is cytochrome c oxidase (CCO) which is unit IV of mitochondrial respiratory chain in living organisms [116, 118]. CCO specifically absorbs red and near-infrared lights which increase advancement in energy metabolism due to the ATP synthesis [126], production of reactive oxygen species (ROS), and releasing of nitric oxide (NO) [119, 127, 128]. As the biochemical results of mitochondrial activation, electron transport, calcium influx from mitochondrial membrane and oxygen consumption increase in cells [116]. Additionally, produced ATP, ROS and NO molecules trigger signal molecules in microenvironments of cells [129, 130]. The set of events accelerates cell division by increasing the synthesis of DNA and RNA, transcription factors, and proteins that play roles in the regulation of the cell cycle [130]. The biostimulatory molecules of LLLT provide DNA synthesis, cell proliferation, ECM synthesis, differentiation of stem cells, mineralization, wound healing even bone regeneration [116, 119].

1.4.2 Low Level Laser Therapy for Bone Regeneration

Bone is a complex tissue which has regeneration capability in case of damages, injury and fractures. However, large bone defects may show inadequate self-regeneration. Hence, LLLT presents an alternative way for bone regeneration particularly in large bone damages by using bone cell repair mechanism [131]. It triggers cell response mechanism without any thermal effect [132, 133]. LLLT supports cell proliferation [129], cell attachment and migration [134]. The degree of influence of LLLT on bone regeneration capacity depends on light parameters such as wavelength of light, energy density, output power, duration time, number of applications (single, double or triple treatment) and the size of the application area of the light beam on the target surface [133, 135]. Correct energy density and multiple treatment can increase cellular responses of cells so it can enhance cell migration, proliferation, viability [136]. Triplet treatment is especially more effective than single treatment due to stimulation capability [136, 137]. When cells are exposed lights during the triple treatment, the effectiveness of light on cells may increase step by step [136]. According to these parameters, cells create their own microenvironments, leading to either biomodulation or bioinhibition [138]. Thus, the identification of effective parameters is critically important for bone regeneration [117, 123, 139].

600-1000 nm ranges of wavelength are particularly more effective in BTE due to the their high penetration capacity [123, 140]. Around 600 nm of wavelength may promote ATP synthesis, osteogenic matrix protein expressions and even differentiation from stem cells to osteoblasts [133, 141]. Moreover, LLLT can increase proliferation of hBMSC [35] and endothelial cells [142] in bone structure. On the other hand, around 800 nm of wavelength also contributes to proliferation and differentiation of BMSC [135, 143]. Moreover, 808 nm of wavelength increased expressions of osteogenic genes [144], ECM mineralization and remodelling [135, 145]. LLLT supports calcium deposition and mineralization in bone [31, 144, 146]. 808 nm and 606 nm of wavelength promotes bone regeneration [147].

Chapter 2

2. Aim of The Study

BTE aims to increase the regeneration capacity of damaged and broken bones, which are enhancing day by day. However, due to the limited cellular responses and regeneration capacities of traditional in vitro models, the degree of effectiveness of many BTE applications is not fully understood and fails in clinical trials. The problems can be solved by development of 3D scaffold free microtissues (3D SFMs). 3D SFMs imitate natural bone tissue, aim to better connect among the cells of the bone tissue and behave like the natural in vivo environment. Stem cells are in close relationship with endothelial cells in natural bone tissue. The close relationship also triggers vascularization and osteogenesis process. Therefore, the study utilized hBMSC:HUVEC coculture on SFMs to take more natural cell responses. The study aimed examination of vasculogenic potential of hBMSC:HUVEC coculture on SFMs, the investigation of optimum concentration of integrin binding peptides on 3D SFMs, identification of the most effective energy densities of LLLT (at 655 nm and 808 nm of wavelength) both monolayer and 3D SFMs and examination of the combination of the most effective peptide concentration and LLLT groups.

Integrin binding peptides which are RGD, IKVAV and YIGSR are natural ECM protein fragments which may support stem cell proliferation, attachments, and differentiation. Although integrin dependent the most effective fragment and concentration in osteogenic differentiation have not been identified yet, it's known that there is critical important relationship between integrin binding and osteogenic differentiation. Taking into account all of these, integrin binding peptides may increase or decrease stem cell differentiation. Moreover, differentiation capacity of stem cell may depend on concentration of these peptide. While cells may be exposed to apoptosis in case of over dosage of needed concentration for differentiation, stem cells may not be differentiated because of inadequate concentration. The main goals of the study are (i) to define the most useful peptide among integrin binding peptides (RGD, IKVAV and YIGSR) in terms of viability and osteogenic differentiation capacity of SFMs, (ii) to find the most effective concentrations of them and (iii) compare ideal concentrations of these peptides in terms of osteogenic differentiation capacity.

LLLT or PBM support stem cell proliferation and differentiation. The ranges from 600 nm to 1200 nm of wavelength induce bone regeneration and healing by affecting CCO in mitochondria. The stimulation of CCO promotes ATP synthesis, ROS and NO releasing so bone healing is accelerated. The recovery capacity of bone depends on laser light parameters such as wavelength, single or multiple treatments of light, application time, energy density etc. Hence, identification of optimum energy densities at 655 nm and 808 nm of wavelength is desperately important for bone regeneration. The study targeted to (i) find optimum energy density at 655 nm of wavelength for stem cell differentiation both monolayer and SFMs, (ii) find optimum energy density at 808 nm of wavelength for stem cell differentiation both monolayer and SFMs, (iii) compare differentiation capacity of the most effective energy densities of both of them in both platforms, (iv) to light up underlying molecular mechanism of LLLT initiated with 655 nm and 808 nm of wavelength during osteogenesis both platforms.

BTE benefits from multiple combination of different strategies to improve quality of therapy. Both peptide and photobiomodulation therapies can be applied as multiple treatments. The combination may increase or decrease efficacy of therapeutic approach. Therefore, the study was designed by choosing the most effective energy densities at 655 nm and 808 nm of wavelength and the most successful concentration of integrin binding peptide which the best differentiation of stem cells was achieved The study aimed to examine the effects of the combination of both therapies in terms of stem cell differentiation on 3D SFMs.

The overall hypothesis is to mimic bone structure by combining hBMSC and HUVEC on 3D SFMs. The created the natural niches give in vivo mimicking results and support to find biological cues about peptide and LLLT for further therapy strategies in BTE. It is believed that these results will help researchers to take better results to be applied into the clinic to enhance bone regeneration.

Chapter 3

3. Examination of Vascular Capacity of Scaffold Free Human Microtissue During Osteogenesis

3.1 Introduction

Bone tissue engineering (BTE) aims to develop bone regeneration strategies for crucial level of bone fracture or damage [148, 149]. Recovery of bone damage depends on bone cell activity containing attachment, proliferation, migration and stem cell differentiation. Their environments conduct the activation of bone cells because the niche of bone cells regulates especially stem cell differentiation [148, 150]. Stem cells and endothelial cells contact each other in natural tissue. The relation supports vascularization of bone [151]. The vascularization phenomena is necessary to continue viability of stem cells [152]. Vascularization supports vitality of cells by supplying oxygen and nutrients into tissue. Additionally, vascular structure removes wastes of cell metabolism.

Vascularization is regulated by endothelial cells [152-154]. One of the most common used endothelial cell type is Human Umbilical Vein Endothelial Cells (HUVEC) because it is easy to obtain. HUVECs are located in inner layer of vein and closely contact with stem cells for initiation of vascularization. As HUVECs promote vascularization, they express some critical important markers such as Platelet Endothelial Cell Adhesion Molecule (PECAM), Ve-cadherin (Ve-cad), and Vascular Endothelial Growth Factor (VEGF). The molecular cues maintain viability and differentiation of stem cells. PECAM is an early vascular molecule that adhesion of endothelial cells. The adhesion of endothelial cells affects stem cells. PECAM may also trigger vascularization of HUVEC and Bone Mesenchymal Stem Cells (BMSCs) coculture during osteogenesis. Ve-cadherin is another vascular marker which plays fundamental role adhesions of endothelial junctions [155, 156]. The molecule regulates endothelial contacts for proliferation, apoptosis and growth [155, 157]. Signaling through VE-cadherin impacts endothelial cell by balancing action of growth factor receptors, intracellular messengers, and proteins [157]. VEGF, is also another vasculogenic marker, is synthesized by endothelial cells and needed for growth and viability of HUVECs during vasculogenesis [47, 158]. In addition, VEGF also supports stem cell viability in natural bone ECM. Furthermore, VEGF is an initiator for vascular growth during bone healing [158, 159]. In natural tissue, the relationship between osteoblasts and endothelial cells is controlled by VEGF releasing of osteoblasts, which forms vascular structure [153, 158]. Actually, the combination improved osteogenic markers such as alkaline phosphatase [158]. VEGF gets in closely contact not only PECAM [160, 161] but also Ve-cadherin [157, 161] for vasculogenesis.

The investigation of VEGF molecule is critically important for vasculogenesis of bone. There are many literature reports related with VEGF molecule expression fate of HUVECs in 2 dimensional (2D) monolayer culture system [152, 153, 158, 162, 163]. However, 2D system is limited in terms of transmission of signal molecules. 2D system is restricted gene and protein expression rate. The reason of limitations may depend on devoid of ECM. ECM is the primary network for cell behaviors. ECM is more presentable by 3D scaffold free microtissues (SFMs) rather than 2D system. This is because 3D SFMs are able to produce self ECM just as in vivo. The natural ECM production in in vitro mimics natural tissue from the point of high cellular connection. Gene and protein expression profile in 3D SFMs shows similarity to in vivo system. Moreover, 3D SFMs support coculture to mimic natural tissue structure (Figure 3.1).

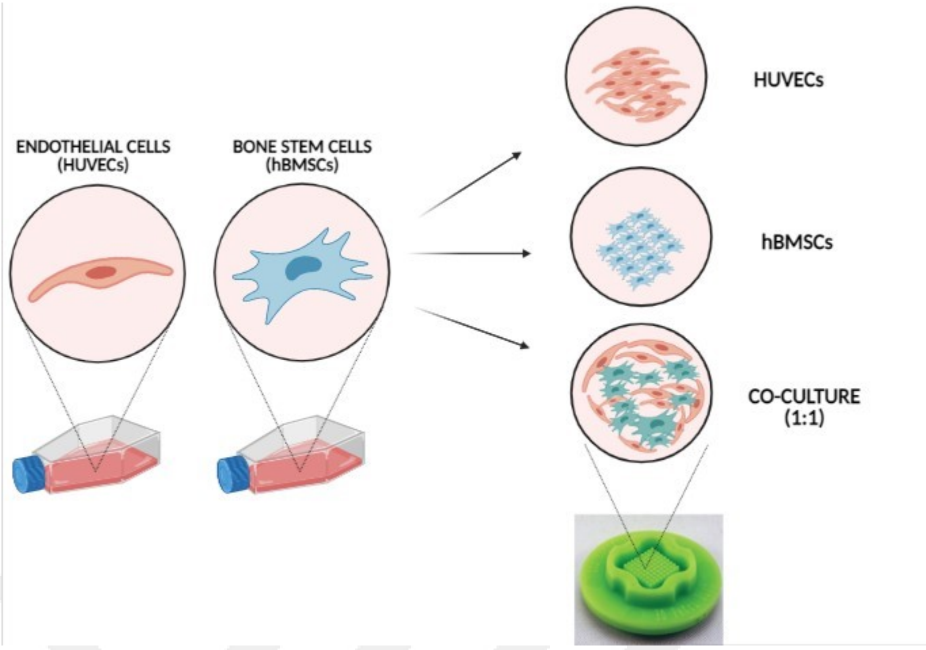

Figure 3.1: The fabrication of SFMs (only HUVEC, only hBMSC and coculture of hBMSC and HUVEC). (Created with BioRender.com).

In light of these information, the study aimed to investigate vasculogenic potential of hBMSC:HUVEC co-culture and examine interactions of vascular markers such as PECAM, Ve-cadherin and VEGF in 3D SFMs.

3.2 Materials and Methods

3.2.1 Materials

All materials were purchased from Sigma-Aldrich, St. Louis, Missouri, ABD such as DMEM:F12, L-Glutamine, Penicillin Streptomycin, Triton X-100, Paraformaldehyde, DAPI (D9542), Fetal Bovine Serum (FBS), Phosphate Buffer Saline (PBS), Bovine Serum Albumin (BSA). Endothelial Cell Growth Medium SingleQuots (EGM) media was purchased from Lonza, Basel, Switzerland. Live and Dead Kit (Cellstain) was taken by Dojindo, Munich, Germany. For qPCR, all materials were taken from invitrogen, Thermo, Waltham, Massachusetts, ABD. VEGF antibody was purchased by Santa Cruz Biotechnology Inc., Santa Cruz, California, USA. HUVECs were taken from Animal Cell Culture Laboratory of Bioengineering Department of Ege University. hBMSCs (300665-102) were taken from CLS Company, Eppelheim, Germany.

3.2.2 Cultivation of hBMSC and HUVEC

HUVEC and hBMSC were cultured with DMEM:F12 containing 10% FBS, 10 mM L-Glutamine, 1% penicillin/streptomycin [164]. For both cells, culture was humidified in incubator at 37 °C and 5% CO_2. The medias of cell were refreshed every 2 days. After cells reached nearly 90 % confluency, they prepared to construct SFMs.

3.2.3 Fabrication of SFMs with only hBMSC, only HUVEC and hBMSC:HUVEC coculture

To form SFMs, agarose molds were prepared by 3D petri dish. Then, agarose was incubated with media to ready for cell seeding [165]. SFMs of only hBMSC or only HUVEC were created with 100.000 cells. Co-cultured SFMs were also created totally 100.000 cells (1:1 ratio hBMSC:HUVEC). The SFMs were incubated with vascular EGM media (containing hydrocortisone, fibroblast growth factor (hFGF-B), insulin-like growth factor (R3-IGF-1), ascorbic acid, epidermal growth factor (hEGF), GA-1000 (gentamicin, amphotericin-B), heparin) supplemented with osteogenic compounds (100 nM dexamethasone, 50 µg/mL ascorbic acid, 10 mM ß-glycerophosphate).

3.2.4 Micrographs and Diameter Measurement of SFMs

Images of SFMs were taken to control under light microscope (Olympus, CKX41, Waltham, MA, USA) on days 1, 4 and 7. The diameter measurements of SFMs were analyzed on days 1, 4 and 7 by Image J (NIH, USA). Average diameters were calculated from triple repeated SFMs.

3.2.5 Viability of SFMs

To understand viability of SFMs of hBMSC, HUVEC, and coculture of them, live and dead assay was performed by Double Staining Kit (Dojindo Molecular Technologies, Inc., Kumamoto, Japan) [64]. While the vital cells were stained bv Calcein-AM/DMSO (green), dead cells were stained by propidium iodide/purified water (red). After 15 min incubation time, cells were observed under fluorescence microscope. Micrographs of live and dead cells of SFMs were separately captured and merged by using microscope software. Then, average color intensity was calculated for each experimental group. Green color intensity of HUVEC was measured and estimated as 100 % on day 1. The green intensities of only hBMSC and coculture were evaluated by comparing the HUVEC green intensity.

3.2.6 Relative mRNA expressions of Ve-cadherin, PECAM and VEGF on SFMs

The fold differences of Ve-cadherin, PECAM and VEGF were determined at the each time point descripted in previous studies [64, 166]. The sequences of the genes were given in Table 3.1 [64]. Firstly, total RNA was obtained from SFMs [64]. Then, extracted RNA was turned double stranded cDNA. 1 µg of cDNA was used to analyze fluorescence dye which is SYBR Green for qPCR (Step One Plus, Applied Biosystems, CA, USA). The fold differences of PECAM, Ve-cadherin and VEGF were calculated as $2^{(-\Delta\Delta CT)}$ formula.

Table 3.1: The forward and reverse primer sequences of vasculogenic markers [64].

GAPDH	F: GAAATCCCATCACCATCTTCC
	R: CCAGCATCGCCCCACTT
Ve-cadherin	F: TCACCTGGTCGCCAATCC
	R: AGGCCACATCTTGGGTTCCT
PECAM	F: GCTGACCCTTCTGCTCTGTT
	R: TGAGAGGTGGTGCTGACATC
VEGF	F: ATCTTCAAGCCATCCTGTGTGC
	R: GCTCACCGCCTCGGCTTGT

3.2.7 Immunofluorescence Staining of VEGF

To identify VEGF protein expression on SFMs, immunofluorescence staining was examined on day 7. All SFMs were washed two times with PBS and fixed with 4% paraformaldehyde [167-169]. After 30 min. incubation in room temperature, SFMs were lysed by 1% Triton X-100 in PBS for an hour. Then, they were blocked by 1.5% BSA for 2 hours. Primary mouse monoclonal anti-VEGF antibody (red) added into

SFMs. Then, DAPI (blue) was added into SFMs solution. After 20 min incubation time in room temperature, all SFMs were washed two-three times with PBS. Fluorescence dye was observed under the microscopy. All images were taken and merged by CellSense Entry software.

3.3 Results

3.3.1 Formation and viability of SFMs

To analyze formation and enlargements of the SFMs, SFMs images were taken on days 1, 4 and 7 as shown in Figure 3.2 during vasculogenesis. Changes in morphology of SFMs were well observed. All SFMs were greatly constructed after day 1. Additionally, the forms of all SFMs remained intact until the 7th day.

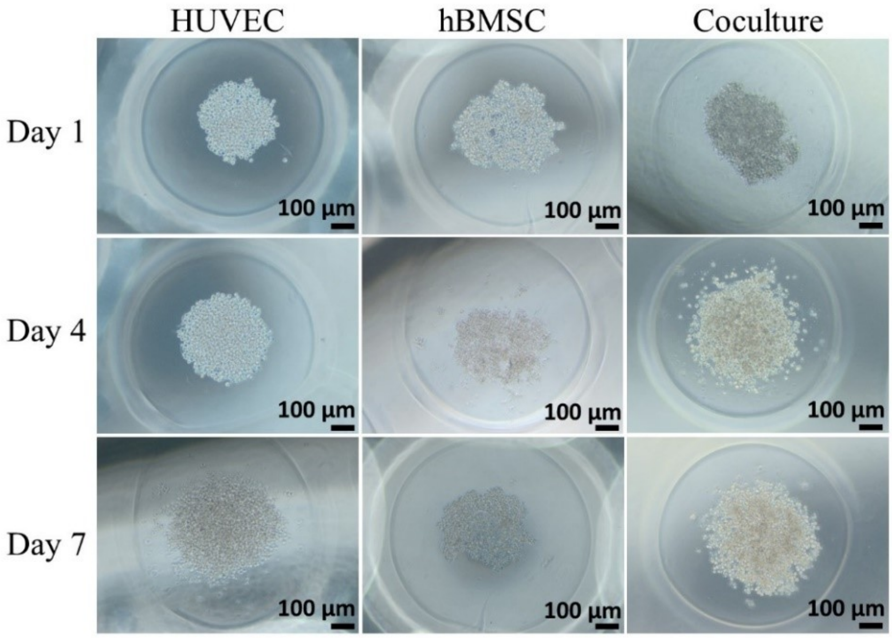

Figure 3.2: Images of HUVEC, hBMSC and coculture SFMs on days 1, 4 and 7 (Scale:100 µm)

The averages of SFMs were calculated from taken micrographs and given in Figure 3.3. Diameters of SFMs of only hBMSC, only HUVEC and coculture were measured as 310±17, 359±8, 444±17 µm, respectively on day 1. For day 4, diameters were calculated as 342±20, 435±14, 486±20 µm, respectively. In the end of the 7th day, diameters were 361±9, 469±11, 528±6 µm, respectively. The coculture SFMs showed statistically significant enlargement in each time point compared with only hBMSC and only HUVEC groups.

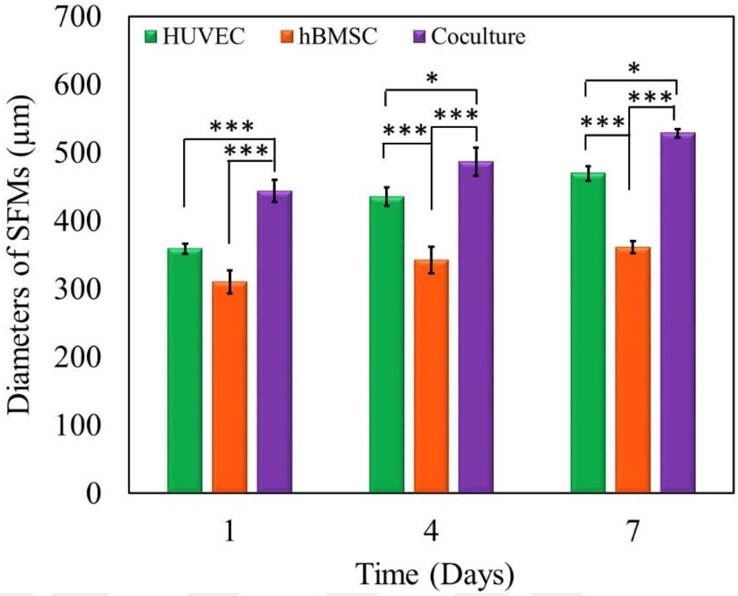

Figure 3.3: Diameter measurements of SFMs on days 1, 4 and 7. Results were analyzed by two way ANOVA and followed Tukey posthoc test (p*<0,05, p**<0,01 and p***<0,001).

Viability assay was also performed on days 1, 4, and 7 to compare experimental groups as shown in Figure 3.4. The viabilities of all SFMs were increased day by day. In the end of the 7^{th} day, the highest viable cell was observed in coculture.

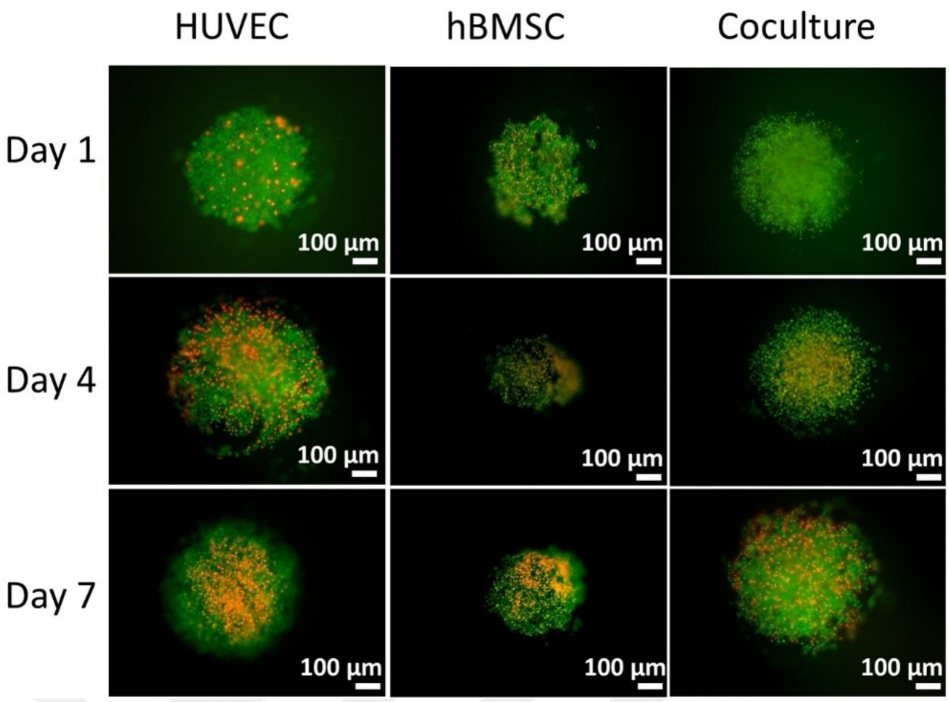

Figure 3.4: Viability analysis of SFMs on days 1, 4 and 7 (Scale:100 µm). While green colour represents live cells, red colour represents live cells.

Green color intensities of SFMs were measured and given in Figure 3.5. The green intensity of only HUVEC was estimated as 100%. Only hBMSC and coculture groups were compare with HUVEC intensity. The viable cell intensities of only hBMSC and co-culture were calculated as 89±6 and 124±2 %, respectively on day 1. For day 4, intensities of only HUVEC, only hBMSC and co-culture were 116±2, 104±7 and 139±2 %, respectively. Finally, viability ratios were 141±4, 128±14 and 169±0,4 %, respectively on day 7.

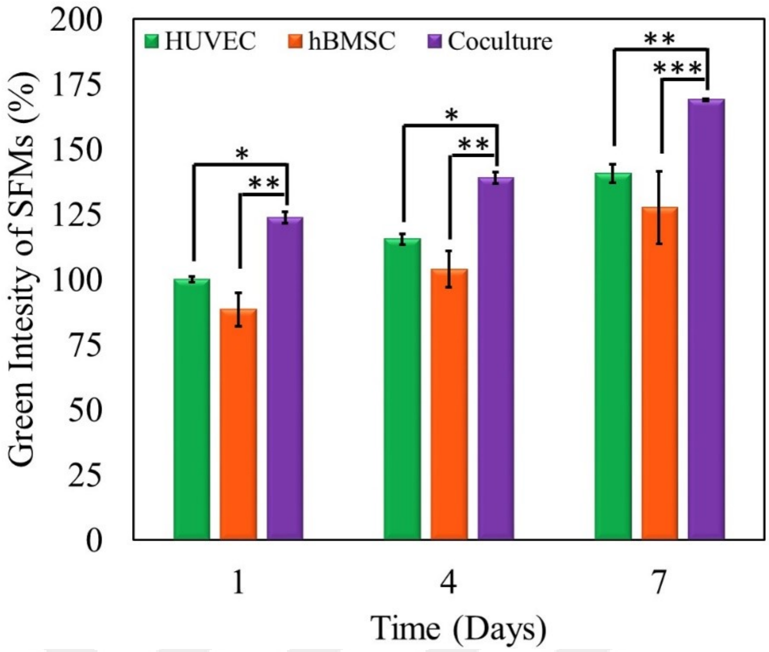

Figure 3.5: Green intensity measurement of SFMs. Results were analyzed by two way ANOVA and followed Tukey posthoc test (p*<0,05, p**<0,01 and p***<0,001).

3.3.2 Vascular marker expressions on SFMs

Fold differences of vascular genes such as Ve-cadherin, PECAM and VEGF were analyzed as shown in Figure 3.6. Fold differences of them were calculated according to expression profile of vascular markers of only HUVEC SFMs which was estimated as 1. Expression rate of SFMs of coculture significantly increased. In the first day, the Ve-cadherin relative mRNA fold differences of SFMs of only hBMSC and coculture were measured as 0,10±0,15 and 6,76±0,93, respectively. On day 4, Ve-cadherin gene expression rates were tested as 1,83±0,84 and 2,48±0,24, respectively. For day 7, the rates were 0,88±0,15 and 1,39±0,24, respectively. PECAM mRNA fold changes of only hBMSC and coculture were 0,44±0,04 and 9,91±0,68, respectively on day 1. Then, expression rates were 1,22±0,24 and 1,87±0,25, respectively on day 4. Finally, PECAM fold differences were calculated as 0,92±0,20 and 0,98±0,07, respectively. The expression rates of VEGF of only hBMSC and coculture groups were 0,32±0,03 and 3,10±0,32, respectively on day 1. Additionally, the VEGF changes were measured as 0,81±0,23 and 3,28±0,46, respectively on day 4. In the last day of vasculogenesis, VEGF fold differences were calculated as 0,40±0,06 and 1,82±0,33, respectively.

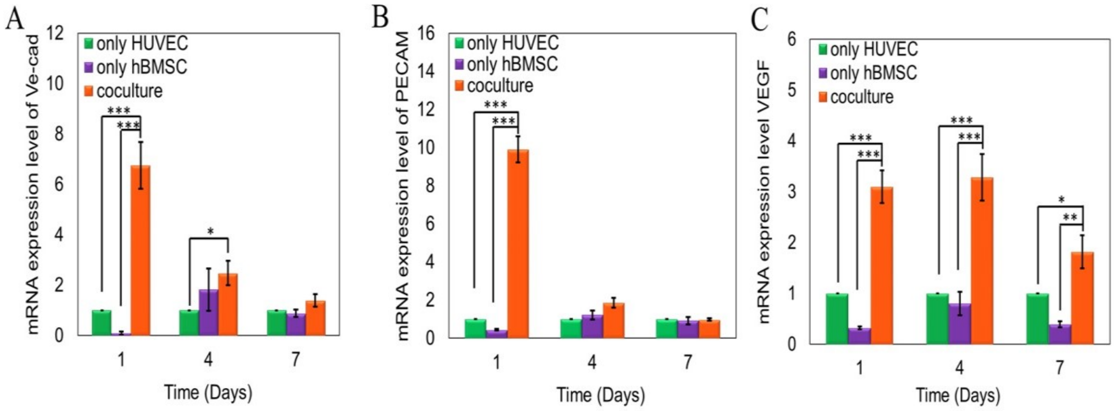

Figure 3.6: Vascular mRNA expression of SFMs on days 1, 4 and 7. A) Ve-cadherin B) PECAM C) VEGF. Only HUVEC gene expression was estimated as 1. Relative gene expressions of only hBMSC and coculture were calculated by 2-(ΔΔCT) method and compared with only HUVEC. Results were analyzed by two way ANOVA and followed Tukey postdoc test (p*<0,05, p**<0,01 and p***<0,001).

The confirmation of VEGF mRNA expression of coculture SFMs was performed by immunofluorescence staining on day 7 as given in **Figure 3.7** (A-C). According to DAPI staining, all SFMs showed nucleus forms but SFMs of coculture had more cell nucleus. VEGF the expression of vasculogenic maturation related proteins was dramatically higher than only HUVEC and only hBMSC groups. Only HUVEC group showed much more VEGF expression than only hBMSC SFMs.

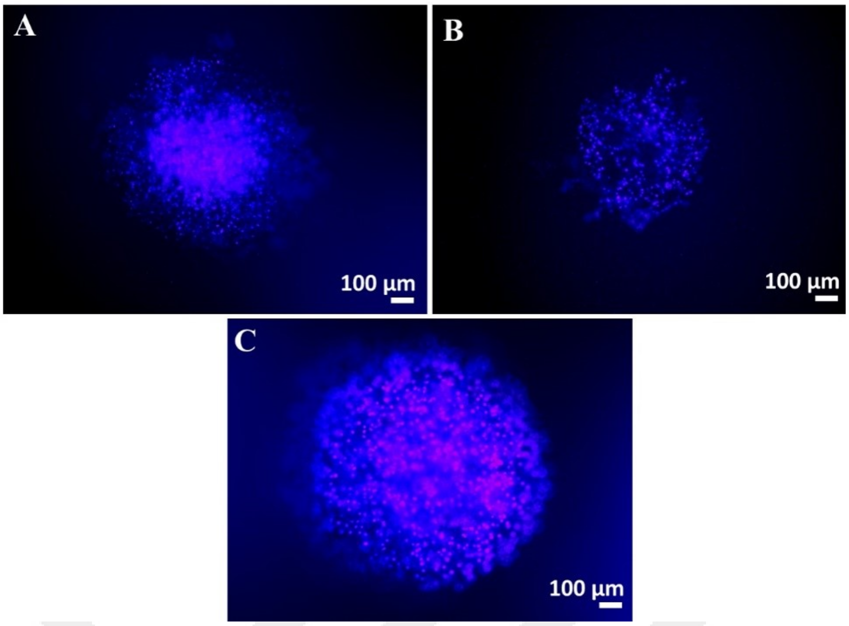

Figure 3.7: Images of VEGF immunofluorescence of (A) HUVEC, (B) hBMSC and (C) coculture SFMs on day 7 (Scale:100 µm). Nucleus on SFMs were dyed by DAPI (blue), VEGF protein was dyed antibody (red).

3.4 Discussions

In the study, cell proliferation, viability and vascular potential of hBMSC:HUVEC cocultivation were analyzed compared with only HUVEC and only hBMSC during osteogenesis. To take more natural cellular responses, SFMs were fabricated and evaluated by diameter measurement, viability assay, qPCR with Ve-cadherin, PECAM and VEGF vascular genes and VEGF immunostaining.

All SFMs were greatly constructed in each groups. Micrographs were followed day by day. Diameters of SFMs were measured on days 1, 4 and 7. Diameters of hBMSC:HUVEC SFMs were larger than only HUVEC and only hBMSC groups. The diameter enlargements of SFMs linked with proliferation rate of cell on SFMs [63, 64]. Thus, co-culture tends to enhance proliferation of cells on SFMs. On the other hand, a previous study showed that the combination of Adipose Derived MSC and endothelial cells promoted proliferation of endothelial cells [149]. Parallel to diameter results, the viability of co-culture was higher than only HUVEC and only hBMSC groups. The association of both cell line mutually increased viability. Endothelial cells are directly relevant in signal transduction with osteoprogenitor cells [170]. Previous studies also demonstrated that cells in coculture may enhance cell viability [149, 171].

Co-culture promotes not only endothelial cell proliferation both also vascularization. The highest Ve-cadherin expression was shown in the coculture group. In addition, bone like coculture may express osteogenic marker rather than only stem cell [170]. Ve-cadherin is a molecule which is found in endothelial junction point [157] and expressed in vascularization [155, 156]. The highest endothelial connection was observed in SFMs of coculture compared with only HUVEC. Previous study clarified that following interaction with endothelial cells, MSCs can restore endothelium balance, perhaps via aiding association of endothelial cell and VE-Cadherin [172]. Coculture, but not only endothelial or stem cells, increased Ve-cadherin expression [173]. Similar to VE-cadherin, PECAM is another fundamental vascular probe which is adhesion marker. PECAM may direct vascular fate of cells [174]. Thus, PECAM is closely related to VEGF in vascularization. In the study, coculture more expressed PECAM vascular marker than only HUVEC group. Actually, only HUVEC showed less vascular marker expression rate than control group. As it was expected, only hBMSC group didn't show Ve-cadherin or PECAM expression as much as only HUVEC. The connection of endothelial cells based on Ve-cadherin supports VEGF expression which is critically important factor for vasculogenesis [175]. VEGF is one of the major vascular marker which is regularly expressed during vascularization [168]. VEGF expression contributes to endothelial proliferation and maturation [47, 158]. Yu, J. et al. also showed that only Adipose Derived MSC (ADMSC) can even enhanced VEGF expression [176]. A study which conducted by Nguyen et al. concluded that mRNA expressions of PECAM and VEGF in coculture were higher compared to the only HUVEC expression in collagen hydrogel based scaffolds [177]. Moreover, VEGF mRNA fold expression of ADMSC spheroids was much more than monolayer ADMSC and ADMSC sheets [176] because spheroids support higher cell to cell interaction [61]. Additionally, ADMSC may trigger angiogenic potential of endothelial cells [168, 178]. Heidari-Moghadam A. et al. showed that coculture was better mimicking platform than single cell type [168]. In this study, it was observed that the highest VEGF fold change was shown in hBMSC:HUVEC coculture compared with only hBMSC and only HUVEC groups.

Parallel to relative mRNA fold change, immunofluorescence results of coculture also showed the highest VEGF protein expression compared with only HUVEC group. A previous study concluded that VEGF promotes endothelial cell proliferation and viability [168]. Additionally, Pons J. et al. showed that producing VEGF from endothelial cells enhances mesenchymal stem cell proliferation and viability [179]. Moreover, low VEGF expression rate limited regeneration capacity [154, 176]. Thus, the VEGF expression may induce both cell viabilities of stem cell and endothelial cells and also vascularization of bone like coculture in the study.

Consequently, results of the study were consistent with literature research concluded that co-culture of hBMSC:HUVEC could improve proliferation and viability both only stem cell and endothelial cells. It was clearly indicated that bone like coculture with hBMSC:HUVEC expressed highly vascular markers rather than only HUVEC. Moreover, VEGF is a key molecule not only endothelial cells but also stem cells. Thus, the expression of VEGF is critically important point to form vascular networks. VEGF can contribute to vascularization of bone like forms.

3.5 Conclusions

The study fabricated SFMs to compare proliferation, viability and vascular capacities of SFMs of only HUVEC, only hBMSC and bone like co-culture. It was concluded that coculture exhibited higher cell proliferation, viability and vascularization strategy than only HUVEC. To understand bone regeneration capacity in vitro SFMs, using coculture for further study may provide better vascular responses than only endothelial cell responses. The coculture of endothelial and stem cells may provide to take more natural responses for vascularized bone in BTE applications.

Chapter 4

4. Determination of Optimum Concentration of Integrin Binding Peptides on Scaffold Free Microtissues (SFMs) for Bone Regeneration

4.1 Introduction

Stem cell based therapy in bone tissue engineering aims to repair bone defects for bone regeneration [180, 181]. To mimic natural bone structure, stem cell based therapy can benefit from coculture strategy using together stem cell and endothelial cell [182]. The combination triggers osteogenic differentiation by affecting cell behaviours and responses [151]. The cellular responses and behaviours mostly depend on extracellular matrix (ECM) [182, 183]. ECM in bone regulates bone cells by facilitating the creation of sticky structures and activating signal pathways that control cell spreading, survival, and differentiation [184]. Thus, ECM is critically important platform for creation of microenvironment of cells [84, 87] which includes many different proteins such as fibronectin, collagen, and laminin. Integrins are the fundamental adhesion molecules that attach cells into the basal matrix [185]. Since natural ligands of integrin are located in cell membranes and ECM proteins [186], short integrin binding peptides are remarked their therapeutic potentials. As integrin binding peptides in ECM have osteogenic differentiation potential, determining certain sequences are also crucial for bone regeneration (Figure 4.1).

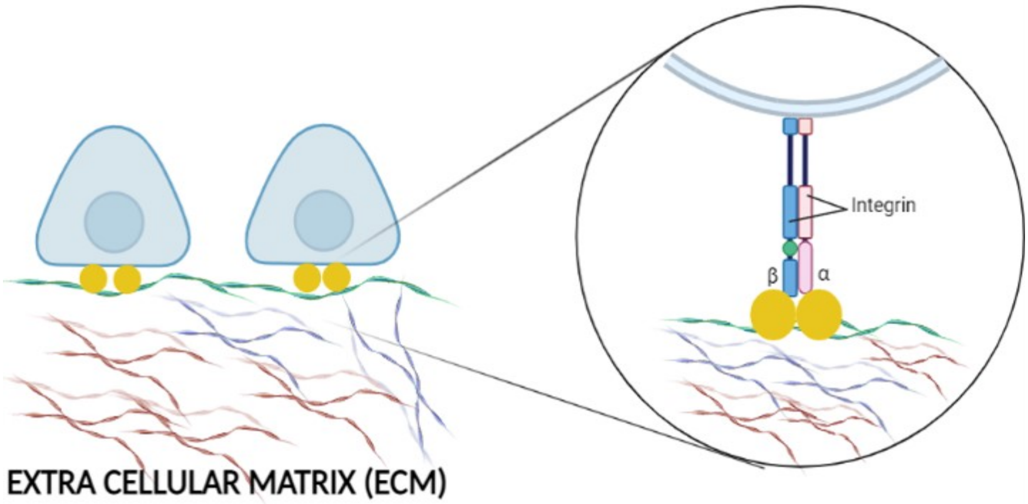

Figure 4.1: Interactions of integrin and ECM (Created with BioRender.com).

Integrin binding peptides, which are Ile-Lys-Val-Ala-Val (IKVAV), Arg-Gly-Asp (RGD), and Tyr-Ile-Gly-Ser-Asp (YIGSR), have a potential to induce osteogenic differentiation [102, 183, 184, 186]. Identifying optimum concentration of integrin binding peptides is another critical important point of osteogenic differentiation [186] because defined optimum concentration in monolayer may fail for further studies [64, 187, 188]. Limited ECM production of traditional monolayer culture may be inadequate for differentiation of stem cell [188-192]. Since the traditional methods have lack of intercellular connections, they may be failed in bone remodelling [193]. The challenge is needed natural and self ECM production for natural stem cell responses. Thus, new platforms which can mimic natural structure and niches of bone microenvironments are required. Therefore, 3 Dimensional scaffold free systems (3D SFMs) have been developed to overcome these in vitro challenges. Since SFMs have larger surface area and the higher cellular communication than traditional cell culture techniques [165, 181, 193, 194], they have greater potential in identification of the optimum concentration of peptide researches for bone tissue engineering. Moreover, 3D SFMs can mimic natural cell matrix and closely contact cell to cell interactions [64]. SFMs, which don't benefit from supporting material for cell growth in 3D, closely link between cell to cell or cell to matrix interaction [193, 194]. They support similar microenvironment conditions from the point of phenotypic properties, ECM production and tissue functions like in vivo. 3D SFMs allow similar expression profile of osteogenic genes and proteins and also differentiation capacity of stem cell with in vivo. In addition, cells in 3D SFMs synthesize self ECM matrix proteins. Since integrins directly bind ECM matrix proteins for stem cell proliferation and differentiation [102], the synthesis of self ECM proteins is crucial to control cell behaviours. Therefore, 3D SFMs also create a platform to determine the optimum concentration of integrins binding peptides for bone regeneration.

The study aimed to determine the integrin binding peptide sequence (RGD, IKVAV and YIGSR) that supports osteogenic differentiation and compare osteogenic differentiation capacities of them and to find the optimum concentrations of them in SFMs for osteogenic differentiation.

4.2 Materials and Methods

4.2.1 Materials

All cell culture materials were purchased from Sigma (MA, USA) except for special descripted kit and assays. All aminoacids, resin and reagent were taken from Aapptec (Louisville, KY). Cellstain double staining kit was taken from Dojindo (CS01-10, Japan). ALPase activity (ab83369) was conducted by Abcam (USA). Calcium mineralization was tested by (DICA 500, Quanthichrom, Wilhelm-Mauser, Germany). Total RNA Isolation Kit was performed by Thermo Scientific, USA. cDNA Synthesis was realized by Biomatik (MuLV First Strand, Ontario, Canada).

4.2.2 Cell Culture and Fabrication of Bone like 3D SFMs

HUVECs and hBMSCs were cultured with Dulbecco's Modified Eagle media:F12 (DMEM:F12) which includes 10 % FBS, 10,000 units/mL of penicillin, 10,000 µg/mL of streptomycin, 50 µg/mL gentamicin, 250 ng/mL fungizone, and 1% L-glutamine in % 5 CO_2, 95 % humidity, and 37°C. After tyrpsinization, 3D SFMs were created in agarose mold which is formed by 3D Petri Dish. Bone like 3D SFMs were constructed as coculture (1:1) and cultured with osteogenic media (contains 100 nM dexamethasone, 50 µg/mL ascorbic acid, and 10 mM ß-glycerophosphate [195].

4.2.3 Synthesis of Integrin Binding Peptides

Integrin binding peptides which are Ile-Lys-Val-Ala-Val (IKVAV), Gly-Arg-Gly-Asp-Ser (GRGDS), and Tyr-Ile-Gly-Ser-Asp (YIGSR) were synthesized by Focus XC peptide synthesizer [196, 197]. Amimoacids were respectively added into rink amide resin with 0.37 mM loading capacity. Then, peptides were lyophilized, after each sequence was cleaved from the resin. All peptides were mixed serum free osteogenic media in 0,5 mM, 1 mM and 2 mM concentrations. 0,5 mM, 1 mM and 2 mM concentrations of IKVAV was defined as I0, I1 and I2, respectively. 0,5 mM, 1 mM and 2 mM concentrations of GRGDS was defined as R0, R1 and R2, respectively. 0,5 mM, 1 mM and 2 mM concentrations of YIGSR was defined as Y0, Y1 and Y2, respectively. The control group (C) was constructed in only serum free osteogenic media without any peptide. The positive control group (PC) contained 10% FBS osteogenic media without any additional peptide. 3D SFMs were incubated prepared media on days 4, 7, 14, and 21.

4.2.4 Images and Diameters of 3D SFMs

Images and diameters of SFMs were followed on days 4, 7, 14, and 21. Images of 3D SFMs were taken under microscope (CKX41, Olympus, Japan) in the each time points. Diameter analysis was performed on three different SFMs by Image J (NIH, USA) (n=3) [165]. Average value of diameter calculations was measured. Statistical analysis was performed by Two way ANOVA (GraphPad Prism).

4.2.5 Viability Quantification of 3D SFMs

Viabilities of 3D SFMs were performed Double Staining Kit on days 4, 7, 14, and 21 [165]. After 3D SFMs were washed two times by Phosphate Buffer Salin (PBS), 11 mmol of L Calcein-AM / DMSO (green) and 1.5 mmol of L Propidium Iodide (red) were added. After 15 minutes at 37°C incubation, SFMs were washed 5 times with PBS again. Images were taken under fluoresence microscope (CKX41, Olympus, Japan). The green intensities were calculated quantitatively by Image-J. Average green intensity of control group was estimated as 100 %. The averages of the other experimental groups were compared with control.

4.2.6 Osteogenic Differentiation And Mineralization

3D SFMs were separately lysed with 10 mM Tris and 0.2% Triton. After the lysates were homogenized, 150 µL of kit reagent and 50 µL of samples were mixed into 96-well plate [198]. DNA amounts of 3D SFMs were quantified at excitation 360 nm and the emission 460 nm of wavelength. Then, ALP activity was tested according to previous study [199]. 10 µl of ALP enzyme and 50 µl of 5 mM para-nitrophenyl phosphate were mixed and incubated with sample for 60 min. Then, 20 µl of stop solution was added and read at 405 nm of wavelength. Calcium amount was measured to examine mineralization of 3D SFMs [200, 201]. Reagent A and B were added in equal volume (75 µl) and mixed with 50 µl of sample. After 45 min incubation, calcium absorbance was read at 612 nm on multimode spectrometer (Synergy™ HTX Multi-Mode Reader, BioTek, VT, USA). ALP and calcium amounts of each group were normalized with DNA amount of related experimental group. Osteogenic differentiation was evaluated with normalized results.

4.2.7 Osteogenic Differentiation in mRNA level

The gene expression of osteogenic bone markers was assessed using quantitative real time qPCR [64]. Total RNA of all 3D SFMs was isolated by using RNA extraction kit. Then, 1 µg of cDNA was generated by standard PCR. qPCR (Step One Plus, Applied Biosystems, Foster City, USA) was used to analyse mRNA profile for osteogenic markers. GAPDH was employed as a housekeeping gene. Osteogenic markers which are ALP, Collagen, and Osteopontin (OPN), were normalized by GAPDH. Relative mRNA fold difference was calculated according to the $2^{-(\Delta\Delta Ct)}$ formula. Table 4.1 shows the forward and reverse sequences of osteogenic primers and the housekeeping gene.

Table 4.1: The primer sequences of the osteogenic markers used in qPCR analysis.

GENE	Sequences
GAPDH	R: AACAGCGACACCCACTCCTC F: CATACCAGGAAATGAGCTTGACAA
Alkalin Phosphatase (ALP)	R: ACATTCCCACGTCTTCACATTT F: AGACATTCTCTCGTTCACCGCC
Collagen Type I	R: TGACGAGACCAAGAACTG F: TCAGCCTTAGACGCCTCAAT
Osteopontin (OPN)	R: ATGAGATTGGCAGTGATT F: TTCAATCAGAAACTGGAA

4.2.8 Statistical Analysis

All experiments were performed triple repeated (n=3). Averages were taken and graphically presented. Statistical analysis of assays was performed by Two way ANOVA (GraphPad Prism, CA, USA). The results were considered significant p*< 0.05, p**< 0.01 and p***< 0.001.

4.3 Results

4.3.1 Image and Diameter of 3D SFMs

Images of 3D SFMs were taken every time points as presented in Figure 4.2 for IKVAVs, Figure 4.3 for RGDs, and Figure 4.4 for YIGSRs.

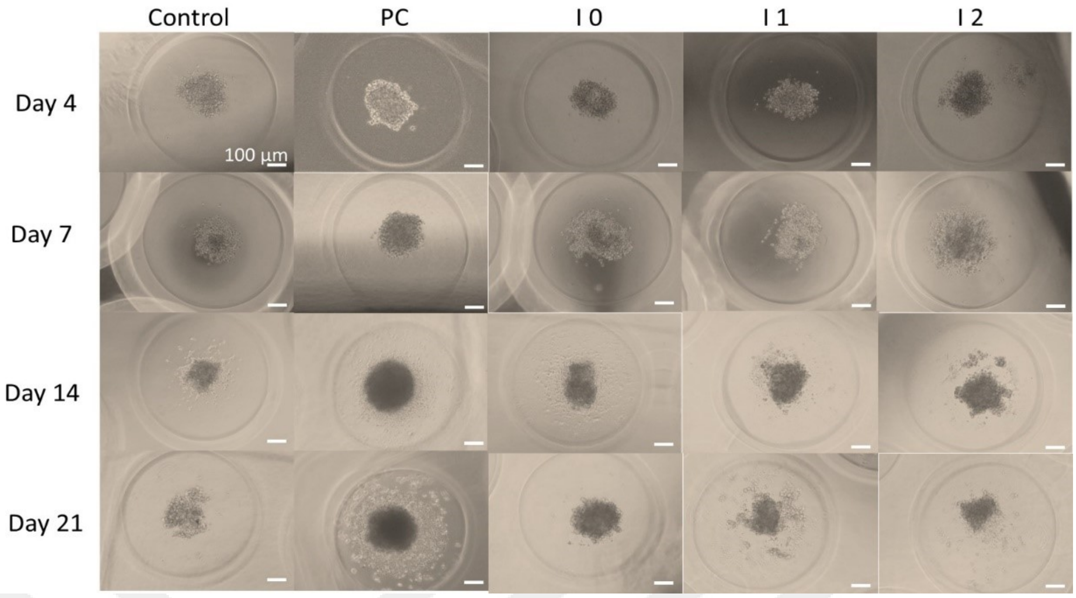

Figure 4.2: Images of bone like SFMs of control, PC, IKVAVs (I0, I1 and I2) on days 4, 7, 14, and 21. Scale bar 100 µm.

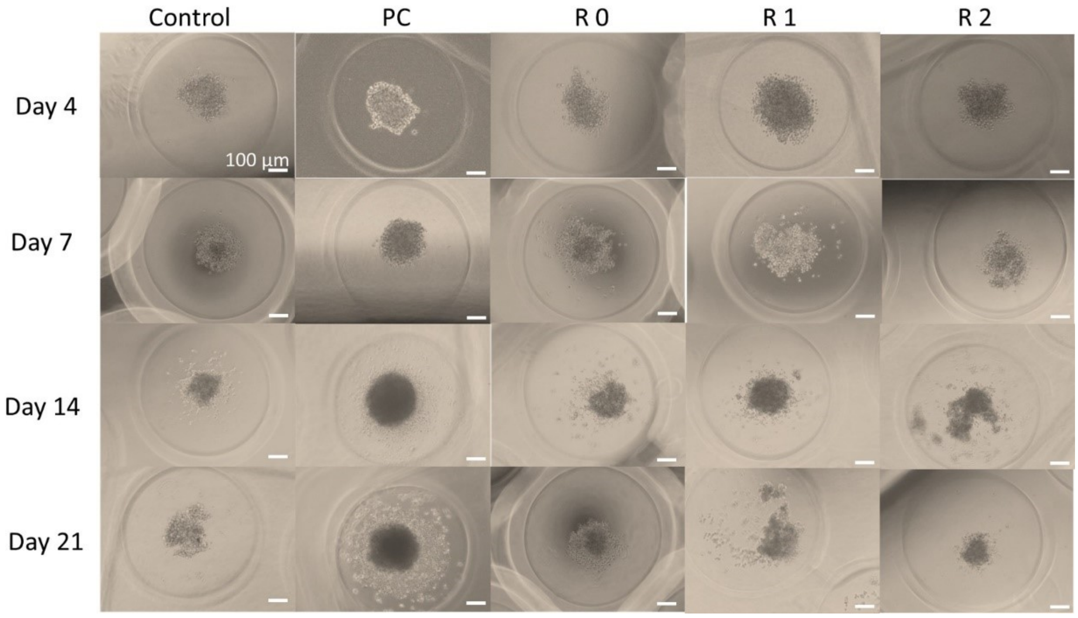

Figure 4.3: Images of bone like SFMs of control, PC, RGDs (R0, R1 and R2) on days 4, 7, 14, and 21. Scale bar 100 µm.

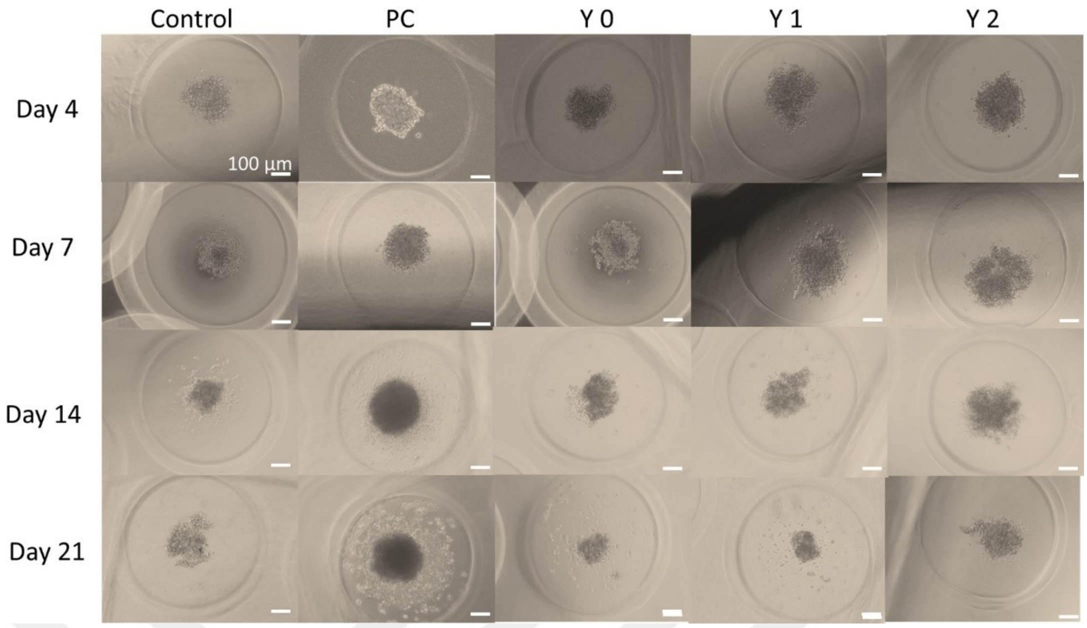

Figure 4.4: Images of bone like SFMs of control, PC, YIGSRs (Y0, Y1 and Y2) on days 4, 7, 14, and 21. Scale bar 100 µm.

All SFMs were greatly constructed on day 4. After 7th day, the diameters of control and the other experimental groups started shrinkage except for PC. However, the diameter of R1 group gradually diminished, not as sharply as the other experimental groups. The diameter of PC increased day by day. After 14th day, control and R2 groups especially showed diameter shrinkage. Diameter of control and R2 observed lower form than the other experimental groups in the end of the 21st day. The results of average diameter measurement promoted images of 3D SFMs. The diameters of SFMs of C, PC, IKVAVs (I0, I1 and I2), RGDs (R0, R1 and R2) and YIGSRs (Y0, Y1 and Y2) were measured on days 4, 7, 14 and 21 as shown in Figure 4.5. For 4th day, the measurements of C and PC groups were 198±18 and 328±20 µm. The I0, I1 and I2 groups were measured as 262±5, 222±2, 247±3 µm. The R0, R1 and R2 groups were 281±28, 366±1, 244±9 µm. The Y0, Y1 and Y2 groups were analysed as 297±8, 363±9, and 335±6 µm, respectively. While diameter of PC increased from 4th to 14th, the diameters of all SFMs decreased. On day 7, the highest diameter of all groups was R1 group which was measured as 406±19 µm. C and PC diameters were 251±18 and 400±14 µm, respectively. While the highest diameter increasing was shown in I2 group among IKVAV groups, Y2 was the highest enlargement group among YIGSR on day 7. In the 14th and 21st days, the diameter of R1 was higher than the other experimental groups but not PC. On day 21st, the diameter of PC was calculated as 474±44 µm.

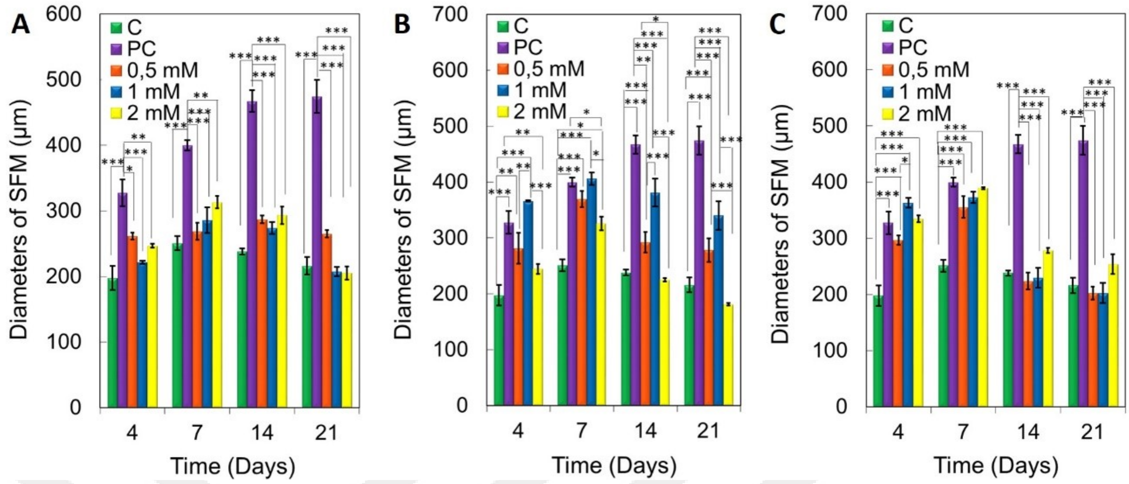

Figure 4.5: Diameter measurements of bone like SFMs (A) control, PC, IKVAVs (I0, I1 and I2) (B) control, PC, RGDs (R0, R1 and R2) (C) control, PC, YIGSRs (Y0, Y1 and Y2) on days 4, 7, 14, and 21.

4.3.2 Viabilities of 3D SFMs

Viabilities of SFMs were analysed to find efficacy of peptides and their concentrations on days 4, 7, 14, and 21 presented in Figure 4.6 for IKVAVs,

Figure 4.7 for RGDs, and Figure 4.8 for YIGSRs. All SFMs were greatly dyed by green and red. Until 4th day, all SFMs showed viable cells. However, nearly all groups started to show red color after 7th day. From 7th day to 21st day, dead cells increased in nearly all SFMs.

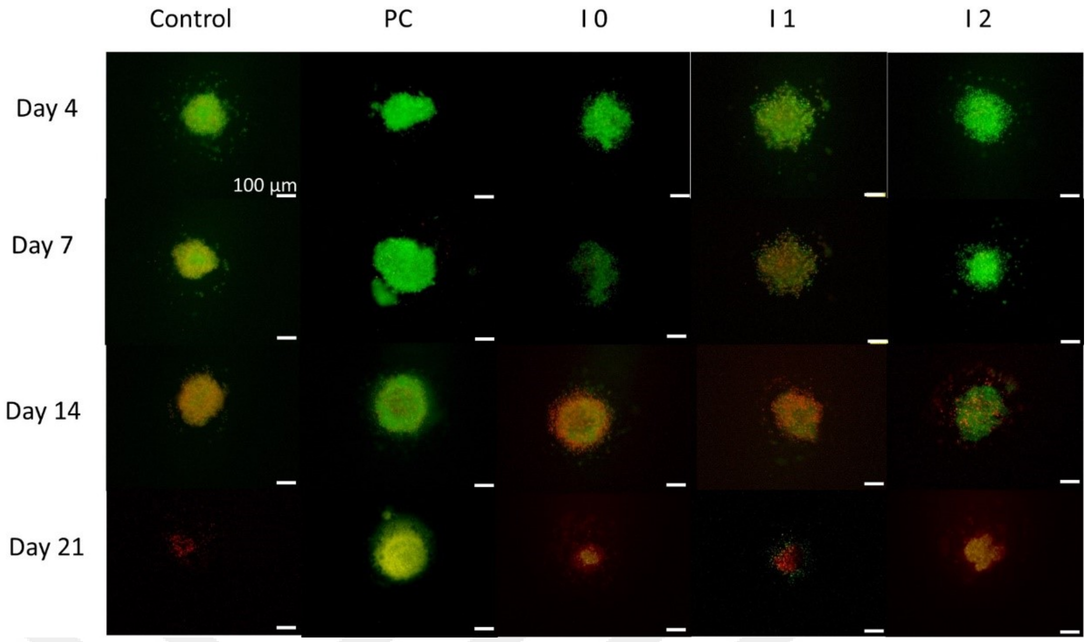

Figure 4.6: Viability images of control, PC, IKVAVs (I0, I1 and I2) on days 4, 7, 14, and 21. Scale bar 100 µm.

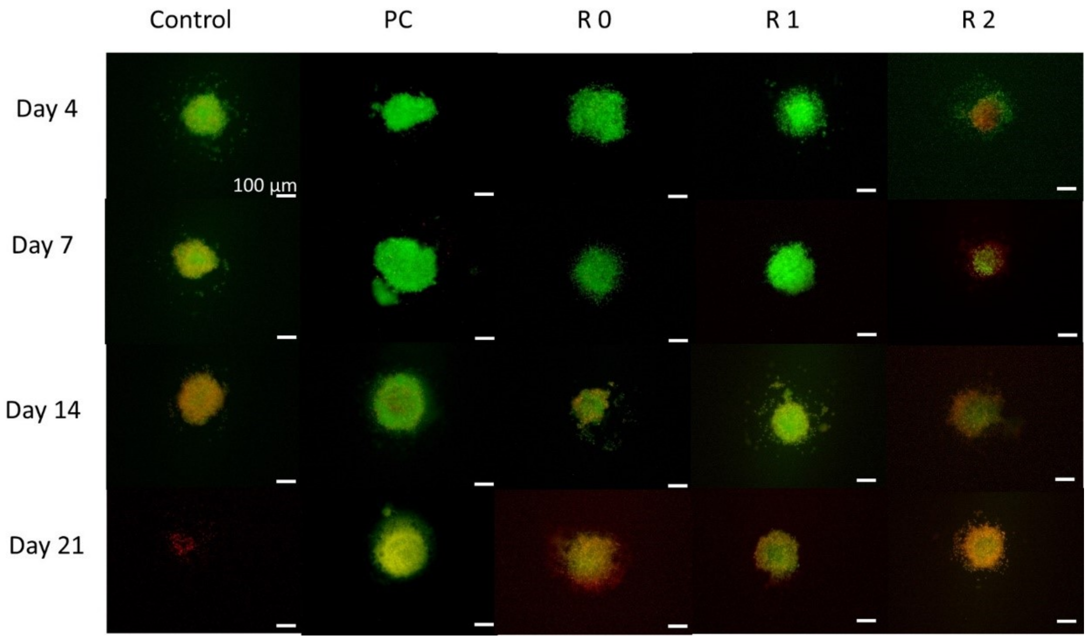

Figure 4.7: Viability images of control, PC, RGDs (R0, R1 and R2) on days 4, 7, 14, and 21. Scale bar 100 µm.

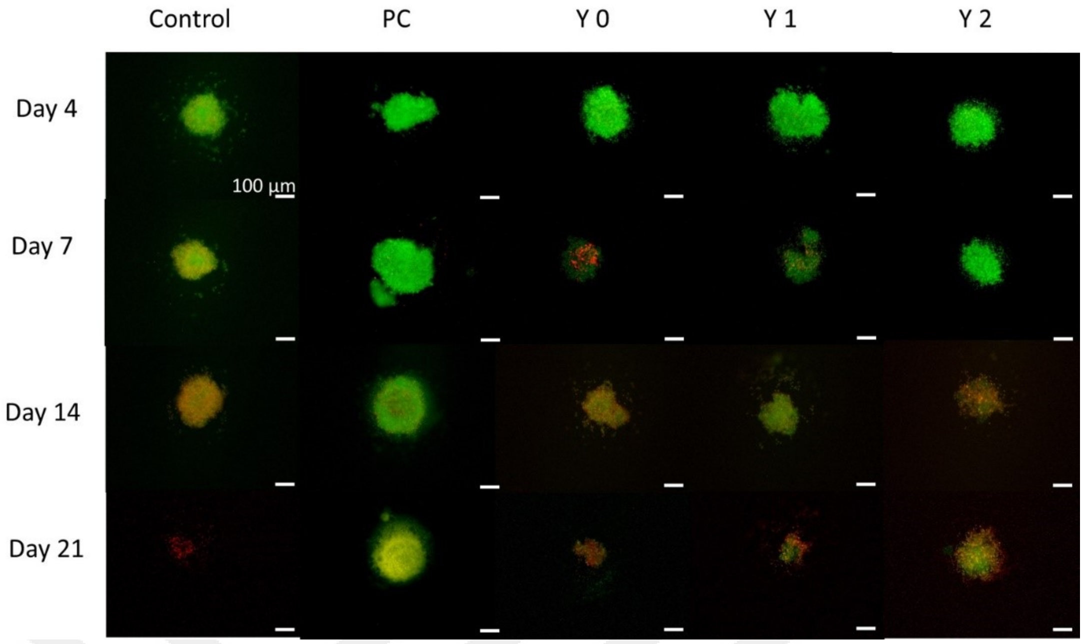

Figure 4.8: Viability images of control, PC, YIGSRs (Y0, Y1 and Y2) on days 4, 7, 14, and 21. Scale bar 100 µm.

To get quantitative information, the green colour intensities of SFMs were calculated. The green colour intensity of control group was measured and estimated as 100 % on day 4. Then, the green intensities of the other experimental groups were compared with control group and presented in Figure 4.9. The green intensities of C, PC, IKVAVs, RGDs and YIGSRs were measured 100±0, 111±3, 109±5, 109±6, 110±6, 110±3, 112±5, 92±5, 100±8, 109±4, and 100±8 % in the 4th day, respectively. Even in the 4th day, the highest green intensity was in R1 group compared with other experimental and PC group. Green intensities of all groups decreased from 4th to 21st day. However, the highest green intensity was observed in R1 group after PC. The ratio was measured as 115±15 %.

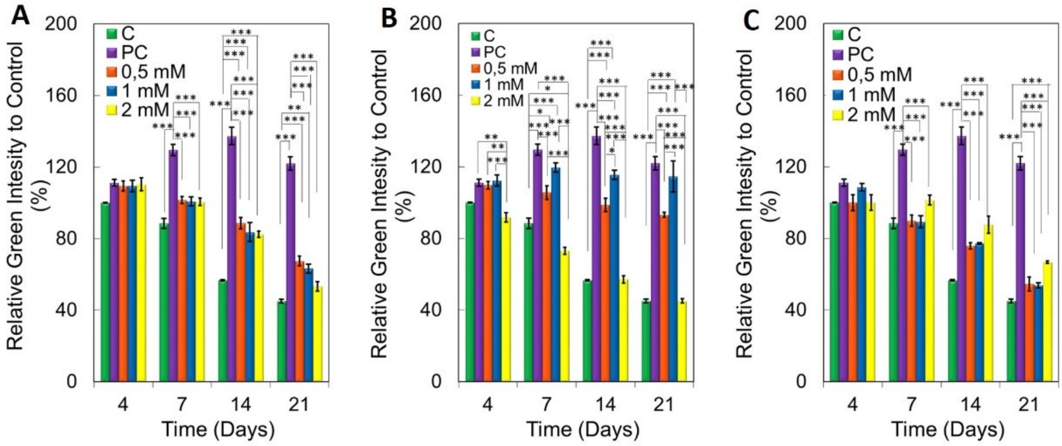

Figure 4.9: Green intensity measurements of bone like SFMs (A) control, PC, IKVAVs (I0, I1 and I2) (B) control, PC, RGDs (R0, R1 and R2) (C) control, PC, YIGSRs (Y0, Y1 and Y2) on days 4, 7, 14, and 21.

4.3.3 Osteogenic Differentiation of 3D SFMs

DNA quantification, ALPase activity and mineralization measurements were performed to compare osteogenic differentiation potential of integrin binding peptides. DNA amounts of all groups were measured as presented in Figure 4.10. ALP activity and mineralization results were normalized by DNA. Results of DNA amount of 3D SFMs were parallel to diameter and viability results. While the lowest DNA amount belonged to control group, the highest value was observed in positive control in all time points. R1 showed more proliferative effect than the other experimental groups.

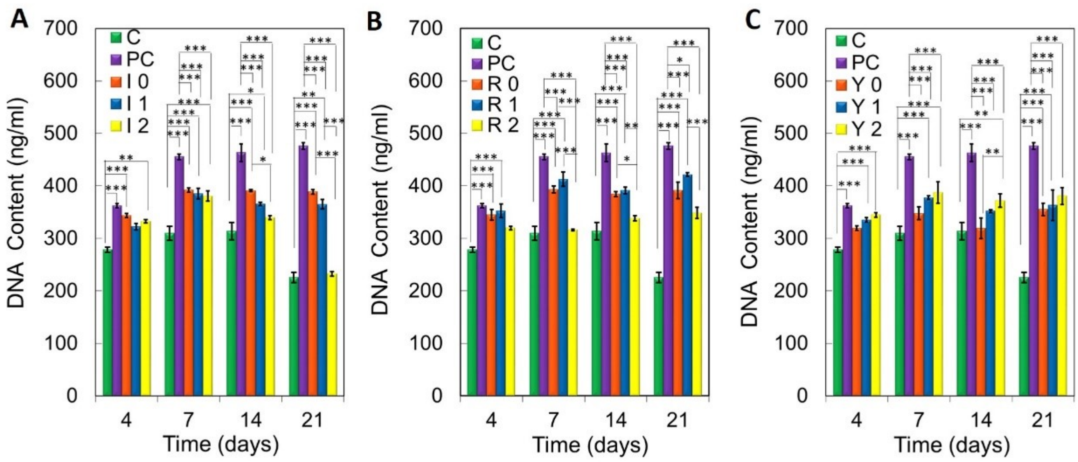

Figure 4.10: DNA Content Analysis of (A) control, PC, IKVAVs (I0, I1 and I2) (B) control, PC, RGDs (R0, R1 and R2) (C) control, PC, YIGSRs (Y0, Y1 and Y2) on days 4, 7, 14, and 21.

ALP activities of SFMs were calculated and presented in Figure 4.11. Nearly all groups showed ALP activity on day 14. ALP activities of all groups were found as 2081±99, 2237±89, 2436±24, 2280±23, 2226±34, 2621±26, 3094±40, 2158±37, 2147±140, 2208±51, and 2385±121 nmol/ng DNA on day 14, respectively. However, R1 exhibited the highest ALP activity. Moreover, R0 had also higher ALP activity than the all experimental groups. While I0 had the highest ALP among IKVAV groups, Y2 was higher than the other YIGSR groups. However, both of them were not statistically significant.

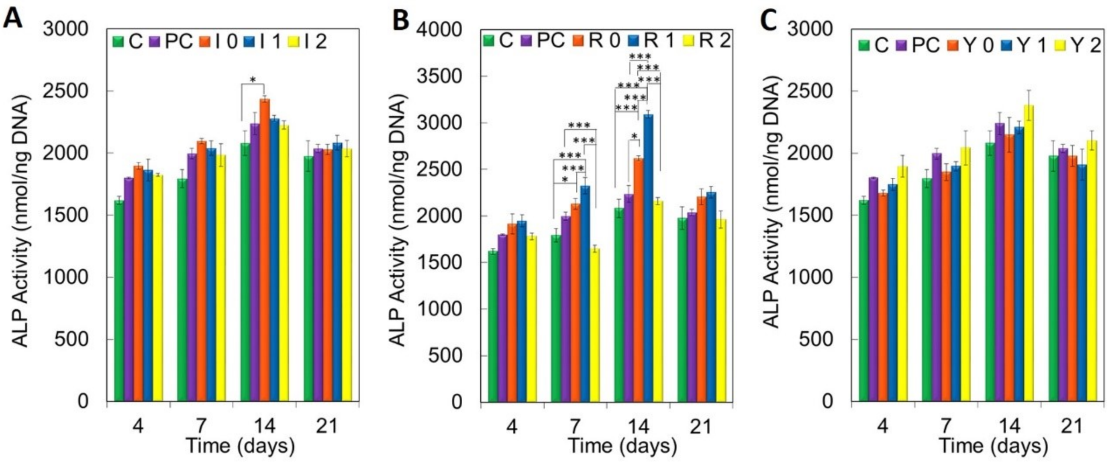

Figure 4.11: ALP activity measurements of (A) control, PC, IKVAVs (I0, I1 and I2) (B) control, PC, RGDs (R0, R1 and R2) (C) control, PC, YIGSRs (Y0, Y1 and Y2) on days 4, 7, 14, and 21.

Mineralization was also observed in all groups as shown in Figure 4.12. Calcium amounts of C, PC, IKVAVs, RGDs and YIGSRs were respectively found 3448±253, 4088±24, 5025±84, 4899±154, 3727±134, 5181±165, 5471±90, 3673±204, 3303±236, 3402±211, and 5000±178 IU/ng DNA on day 21. R1 group showed again the highest calcium mineralization compared with the other experimental groups. Calcium amounts of R0, I0 and Y2 followed calcium amount of R1 group.

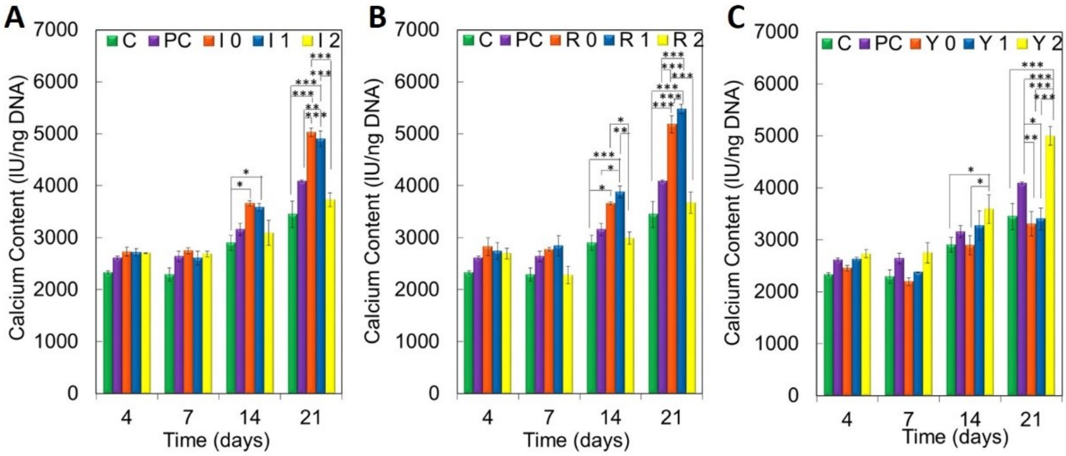

Figure 4.12: Mineralization of (A) control, PC, IKVAVs (I0, I1 and I2) (B) control, PC, RGDs (R0, R1 and R2) (C) control, PC, YIGSRs (Y0, Y1 and Y2) on days 4, 7, 14, and 21.

4.3.4 Relative Osteogenic Gene Expressions of SFMs

ALP, collagen and osteopontin osteogenic markers were analysed on days 4, 7, 14, and 21. The average expression of osteogenic markers in control group was estimated as 1 in each day. The fold differences of the other experimental groups were calculated as relative to control and served in Figure 4.13. Relative ALP expressions of Y1 and Y2 were 82±12 and 122±12 on day 4. On day 14, relative ALP fold differences of C, PC, IKVAVs, RGDs and YIGSRs were measured as 1±0, 14±3, 59±5, 13±4, 14±7, 73±21, 200±127, 3±1, 6±3, 2±1, and 58±9, respectively. ALP mRNA of R1 was expressed 200 times higher than control at 14^{th} day. Whereas I0 expressed higher ALP than the other IKVAV groups, Y2 showed higher ALP expression than the other YIGSR groups.

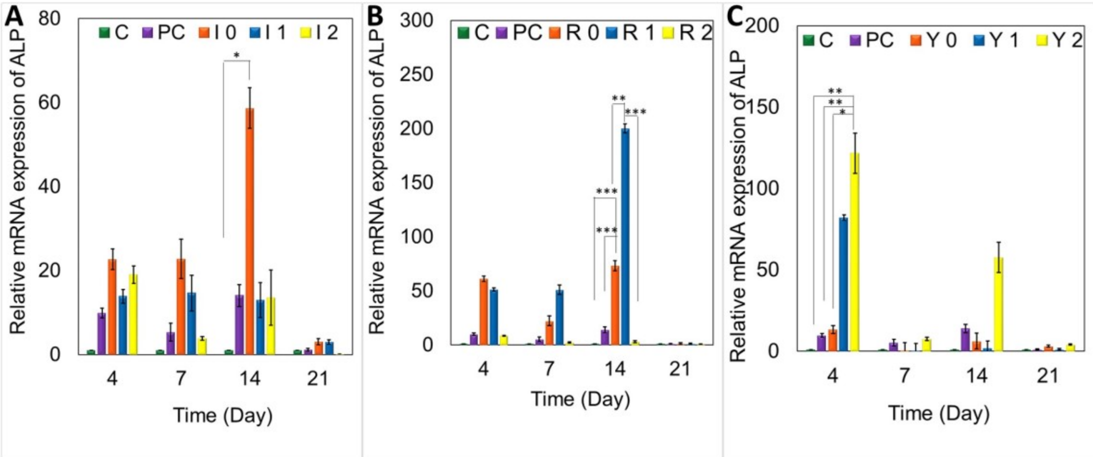

Figure 4.13: Relative ALP gene expression analysis (A) control, PC, IKVAVs (I0, I1 and I2) (B) control, PC, RGDs (R0, R1 and R2) (C) control, PC, YIGSRs (Y0, Y1 and Y2) on days 4, 7, 14, and 21.

Relative collagen mRNA expressions were given in Figure 4.14. Collagen was also expressed by nearly C, PC and peptide groups. The highest collagen expression was observed in R1 for all time points. Moreover, collagen fold difference of only R1 increased, the values were measured as 7±3, 14±1, 23±6, and 36±1 on days 4, 7, 14, and 21. While I0 was typically higher expressed collagen than the other IKVAV groups, Y2 group generally showed more collagen expression than the other YIGSR groups in all time points. However, they were not statistically significant.

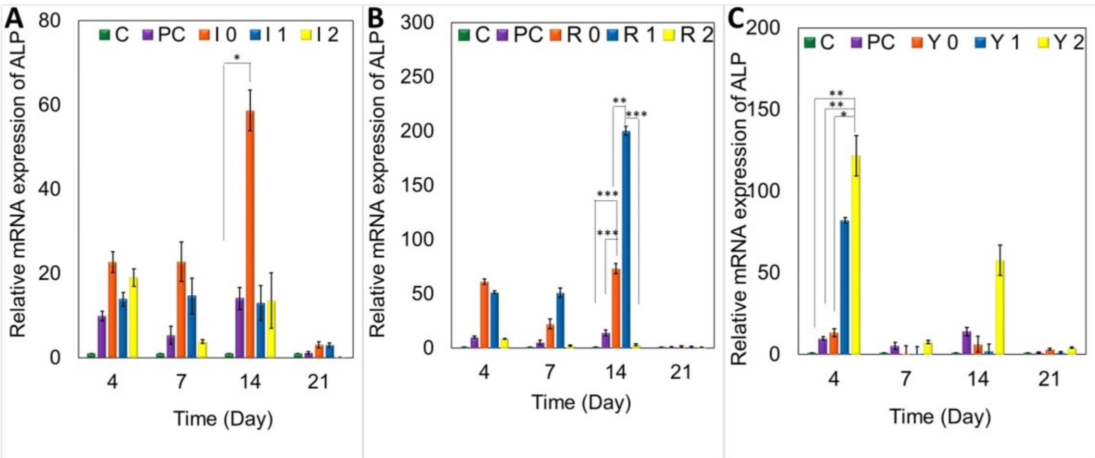

Figure 4.14: Relative collagen gene expression analysis (A) control, PC, IKVAVs (I0, I1 and I2) (B) control, PC, RGDs (R0, R1 and R2) (C) control, PC, YIGSRs (Y0, Y1 and Y2) on days 4, 7, 14, and 21.

Relative mRNA expressions of osteopontin were presented in Figure 4.15. Osteopontin expression rates of all groups were evaluated. In all time points, R1 and

R0 expressed osteopontin gene compared with the others. R1 group significantly expressed osteopontin on day 21. On day 21, osteopontin fold differences of C, PC, IKVAVs, RGDs and YIGSRs were measured as 1±0, 3±2, 8±1, 1±1, 2±0,4, 15±5, 390±29, 1±0,2, 1±1, 0,4±0,1, and 7±1, respectively. Similar to the other osteogenic marker expression rates, R1 was the highest osteopontin expressed group among all experimental groups. I0 was superior osteopontin expression than the other IKVAV. In addition, Y2 typically higher expressed osteopontin than the other YIGSR groups. However, I0 and Y2 did not find significant.

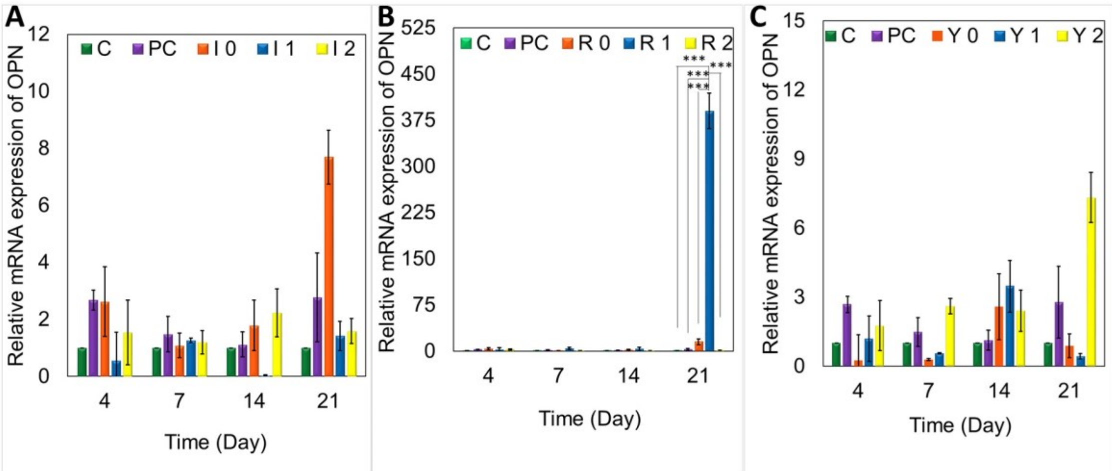

Figure 4.15: Relative osteopontin gene expression analysis (A) control, PC, IKVAVs (I0, I1 and I2) (B) control, PC, RGDs (R0, R1 and R2) (C) control, PC, YIGSRs (Y0, Y1 and Y2) on days 4, 7, 14, and 21.

4.4 Discussions

SFMs produced self ECM by allowing coculture just as in vivo [193]. Since SFMs coculture can imitate bone tissue, it can exhibit better expression of stemless markers during bone regeneration [202]. Microenvironments of bone play crucial role for cellular metabolism, repairing mechanism and regeneration [203]. The lack of complex microenvironment of traditional monolayer culture unfortunately causes limited matrix protein expression and restricted regenerative capacity [193]. 3D SFMs are beneficial platforms for evaluation efficacy of biomaterials in terms of production of natural ECM and higher cellular interaction than monolayer culture [64, 165, 193, 194]. Relations of cell to cell or ECM receptors are essential for the organization of cells into functional tissue. Thus, integrins as binding units of ECM proteins have essential roles for stem cell differentiation and bone regeneration. In the present study, abilities of proliferation, viability and osteogenic differentiation of integrins binding peptides were evaluated on 3D SFMs at 4^{th}, 7^{th}, 14^{th}, and 21^{st} days.

All SFMs were greatly constructed. The average diameter of R1 was larger than positive control on days 4 and 7. Diameters of all SFMs decreased after especially 14^{th} day. The reason of increasing diameter of PC day by day may depend on including 10% FBS which is effective components for cell viability and proliferation [165, 204]. Parallel to PC, R0 and R1 groups critically affected cell proliferation because of contribution to enlargement of SFMs. They preserved their diameters. Similar to RGD groups, YIGSR groups also increased diameters of SFMs. Viability values of SFMs also promoted to diameter results. R0 and R1 groups had the highest viability rates than the other integrins binding peptides. Green intensity of R1 group showed higher viable cell on day 21 than even 4^{th} day of control. Although categorization of peptides and their concentration is so hard, it can be seen that R1 group showed highly great proliferation, viability and osteogenic differentiation as well positive control. Kim J. et. al. declared that RGD had the highest cell proliferation and viability rate rather than IKVAV in chorion derived MSCs [204]. 0.5 mM concentrations of RGD and YIGSR showed that they didnt change ligand chemistry but ALP in RGD group was more expressed than YIGSR [205]. Frith et. al. predicted that YIGSR may enhance cellular interaction but not as much as RGD [102, 205]. A study declared that RGD decorated hyaluronate hydrogels remarkably contributed to fabrication of microtissues, enhanced cell proliferation and improved cell viability compared with IKVAV and YIGSR in salivary gland progenitor cells [206]. Although the diameter of I0 took part in the last rows of all groups, the diameters increased after 4^{th} day. In 7^{th}, 14^{th} and 21^{st} days, YIGSR groups were generally under the IKVAV groups in terms of diameter length and green color intensity. In the study, IKVAV concentrations exhibited higher SFMs enlargements than Y0 and Y1 groups. A study improved that IKVAV and YIGSR peptides may regulate cellular behaviours [207, 208]. While IKVAV mostly plays role in growth of cells, YIGSR generally supports adhesion and migration [207]. The greater enlargement capability may depend on growth and attachment properties of IKVAV.

Similarly, DNA quantification results also promoted enlargements of SFMs and viability results. The highest DNA amounts in each time points belonged to peptide free 10% FBS group. However, R1 was higher than the other IKVAV, RGD and YIGSR peptide concentrations. Ding et al. showed that encapsulated Mesenchymal Stem Cells (MSC) in RGD modified hydrogels (1:3 RGD-hydrogel concentration) improved cell to cell communication, cell to ECM adhesion, and influenced cell survival by using integrins binding signals [209]. Moreover, the 1:2 RGD-hydrogel concentration showed the highest cell viability in another study [210]. Thus, 0.5 mM of RGD was more effective peptide concentration not only among RGD concentrations but also IKVAV and YIGSR. RGD supported longer term viability than IKVAV groups as mentioned in the literature [211]. Rinker et al, showed that 1 mM Acryl-PEG-RGDS supported cell survival and differentiation for MSC and coculture with adipose and osteoblast cells [212]. Another study showed that IKVAVS sequence supported cellular attachments but not proliferation, nevertheless RGDS sequence demonstrated greater cell attachment, proliferation, and growth than IKVAVS sequences [213]. The study suggested that RGDS is attractive for multiple integrin receptors such as fibronectin receptor $\alpha 5\beta 1$ of MSCs, promotes cell spreading and organization of cytoskeleton of cells, and also cell proliferation. Moreover, the RGD sequence, which leads to the activation of adhesion proteins of ECM, regulates the adhesion dependent signal for cell survival [214]. ALP activities of all SFMs were evaluated to understand osteogenic differentiation capacity of integrins binding peptides. From the first time point to the last time point, ALP activity of R1 was the highest rate compared with the other experimental groups even positive control. After 14th day, ALP activities of nearly all group decreased as expected. However, the highest ALP activity was found in R1 group which was followed by R0. Thus, it was shown that RGD supported the highest ALP expressions for osteogenic differentiation. The result of ALP activity is proved by literature that RGD improves ALP activity [215-217]. A research indicated that higher ALP activity was found in the 0.5 mM RGD in comparison to the 0.5 mM YIGSR [205]. Even though I0 showed more ALP expression than Y2, the ALP expression differences between I0 and Y2 were not found statistically significant. IKVAV concentrations generally more expressed ALP than the YIGSR concentrations. However, I0 was not significant compared with the other experimental groups except for control. Although Y2 group showed ALP activity, it was not significant. Mineralization was observed in the late time point of osteogenic differentiation [218]. The matrix mineralization had also been proved by osteogenic gene expressions. A study indicated that RGD increased matrix mineralization [216, 218]. Chien et. al. reported that even 0.5 mM concentration of RGD supports mineralization of hBMSCs during osteogenic differentiation [219]. The results of this study were confirmed that R0 promoted calcification. However, R1 had more calcified matrix than 0.5 mM in this study. Wang et. al. showed that nearly 1 mM of chimeric RGD peptide also deposited calcium mineral to MC3T3-E1 cell on titanium discs [220]. The chimeric peptide also supported osteogenic differentiation. Moreover, Itoh et. al. used 0.5 mg/ml of IKVAV and YIGSR in HAp-coating on nerve regeneration [221]. Controversy, a study which contained RGD, YIGSR, and SIKVAV peptide therapy declared that only RGD and SIKVAV sequences displayed a critical expansion in calcium uptake [222]. In the case, however, all of them were engaged with adhesion of Sertoli cells to laminin, they might tie to various ECM proteins/integrins on the cell surface and trigger different signalling pathways. The present study also confirmed that 0.5 mM of IKVAV released higher calcium concentration than YIGSR groups.

Relative mRNA expressions of ALP, collagen and osteopontin genes were evaluated by qPCR on days 4, 7, 14, and 21. ALP, as an early marker, was mostly produced in R1 group compared with the other experimental groups. Relative mRNA expression of ALP endorsed results of ALP activity that R1 was followed by R0. Although, ALP mRNA expression of I0 was higher than Y2 group, the differences between them were not statistically significant. Similar to ALP results, R1 mostly expressed collagen. Actually, native collagen already contains RGD sequence [203]. On the other hand, nearly all IKVAV groups were higher expressed collagen than YIGSR groups. Previous study used collagen mimetic peptides with RGD and IKVAV. The results of the study showed that RGD sequence significantly increased proliferation rate and collagen stimulation [223]. However, a study showed that combination of YIGSR and a unit of collagen supports to bind collagen [224]. The reason of lower osteogenic differentiation of Y0 and Y1 groups may depend on inadequate of these concentrations in the main frame. On the other hand, the expression of osteopontin of R1 followed similar results with ALP and collagen mRNA expression. The overwhelming majority in osteopontin expression was observed in R1 group. A research already showed that the osteopontin binds to integrins to regulate ion transportation by utilizing RGD sequence [225]. Actually, RGD and osteopontin interaction occurs depending on concentration of RGD. It is already known that natural structure of osteopontin includes RGD sequence [226]. A study stated that RGD and YIGSR induced osteopontin expression in adipose derived MSCs [227].

Consequently, RGD and IKVAV may initiate osteogenic differentiation by multiple integrin ligands [215]. 50 % (w/v) of IKVAV can induce upregulation of osteogenic markers for regeneration of bone in MSCs [228]. 0.5 mM of IKVAV supported the higher differentiation than the 1 mM and 2 mM concentrations of IKVAV. On the other hand, 2 mM of YIGSR showed competitive properties with 0.5 mM of IKVAV group. 2 mM of YIGSR already exhibited the higher osteogenic differentiation than the other YIGSR groups. However, the 1 mM of RGD sequence was the most effective group and concentration in terms of osteogenic differentiation. The reason may depend that RGD is mostly recognized by hBMSC for differentiation [229].

The previous studies suggested that osteogenesis may be dependent upon the activation of β1 integrin [102, 230]. Moreover, RGD plays critical important role in stem cell differentiation by binding to collagen, αvβ3 and αvβ5 integrins so it mediates cell signalling and differentiation [231]. The interaction of RGD and integrin (particularly α5β1, α5βv) transfers the signal to proliferate cells by the integrin-mediated signalling [216, 232]. Moreover, another study suggested that α5β1 integrin and RGD peptide interaction comes from the aspartic acid (D) -154 residue in the α5 subunit [233, 234]. Calcium cation also plays fundamental role for ECM protein and integrin binding. Actually, the differentiation ability of RGD may depend on multiple integrin binding properties of RGD [102]. The success of RGD sequence may depend on more interaction with integrin mediated signalling than IKVAV and YIGSR.

4.5 Conclusions

The study supported the first comprehensive analysis of alternative integrin binding peptides and their different concentrations throughout differentiation of hBMSCs, showing that osteogenesis was characterized by SFMs diameter, viability, osteogenic differentiation and qPCR analysis of osteogenic genes. Understanding the role of integrin binding peptides in cellular responses is fundamental for the progression of stem cell based regenerative therapies. Although the molecular mechanism of integrin binding peptides has not been yet clarified, it has been observed in this study that RGD peptide is more effective than IKVAV and YIGSR peptides to get cellular responses of osteogenic differentiation. It was concluded that 1 mM concentration of RGD critically contributes to proliferation and viability of coculture of stem cell and endothelial cells on 3D SFMs. 1 mM of RGD peptide also improved bone regeneration by boosting osteogenic differentiation. The results may be evaluated by clinical researchers to repair of bone defects.

Chapter 5

5. Investigation of The Optimal Light Parameters for Photobiomodulation to Induce Osteogenic Differentiation of The Human Bone Marrow Stem Cell: Human Umbilical Vein Endothelial Cell Co-Culture

5.1 Introduction

Bone disorders are major health problems and are related to many chronic diseases in people over the age of 50 [235]. With the rapid growth of tissue engineering technologies, bone tissue engineering is now a promising strategy for therapeutic solutions to bone abnormalities in recent years. It benefits from multidisciplinary approaches which are used to improve or replace bone tissues [33]. Traditional *in vitro* cell culture aims to research the structure of the natural bone microenvironment for adhesion, proliferation, and differentiation of the cells by using the improvements in bone tissue engineering [236]. However, only one cell line usage can be insufficient to fabricate the natural bone structure in *in vitro* studies. Therefore, the co-culture system has been developed and utilized in the traditional monolayer cell culture model. The combination of more than one cell line, especially to mimic the bone microenvironment, supports the mutual interaction between cells and the matrix [237]. The major objective to create a co-culture is to enable cell-to-cell interaction and thus sustain the capacity of stem cells [237, 238]. Former studies indicated that the co-culture of Human Bone Marrow Stem Cells (hBMSC) and Human Umbilical Vein Endothelial Cells (HUVEC) influenced the proliferation of stem cells positively and improved their osteogenic differentiation [237, 239].

Besides the other promising tissue engineering strategies, photobiomodulation (PBM) therapy is an alternative application to promote cell differentiation and can also be used for osteogenic differentiation. PBM can be utilized for the modulation of cell functions that regulates cell growth, proliferation, and differentiation [240-244]. The red and near-infrared regime of the electromagnetic spectrum is mostly preferred to generate biomodulation effects through PBM because mitochondria have specific structures that act as a strong absorber for these wavelengths to initiate the mechanism of PBM [242, 245, 246]. The copper and heme group of cytochrome c oxidase in mitochondria are the chromophore molecules that strongly absorb the photon energy of red and near-infrared wavelengths. After the initiation of the chain of reactions in PBM, it continues with the synthesis of intracellular reactive oxygen species (ROS), ATP production, and NO release [242-244, 247-249]. These molecules act as signal molecules that induce the synthesis of transcription factors, genes, and protein expressions [240, 247]. Similar processes take place when PBM is used for osteogenic differentiation, bone regeneration, and bone healing [141] (Figure 5.1).

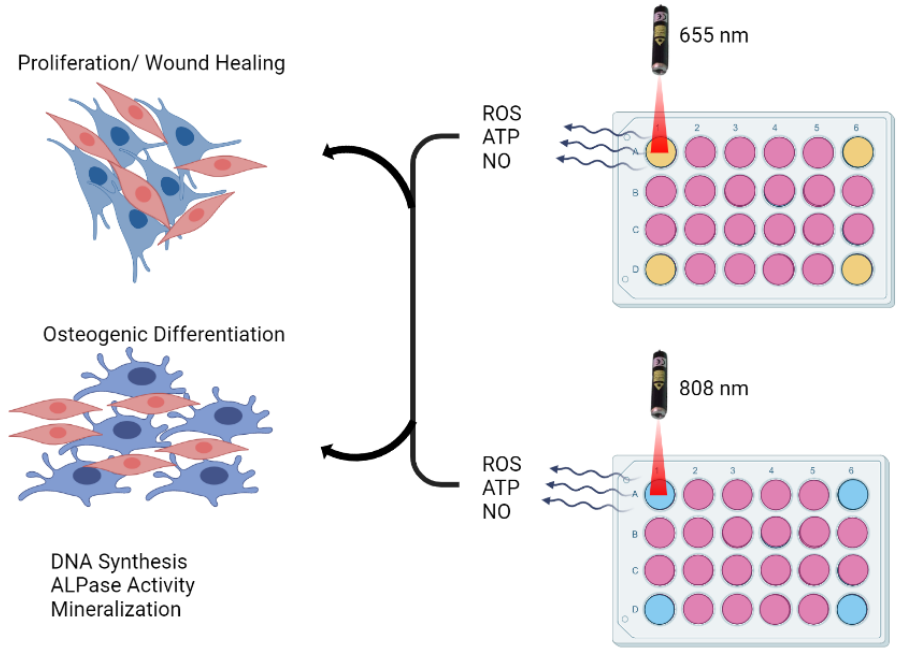

Figure 5.1: The induction of bone regeneration based on PBM. (Created with BioRender.com).

However, there is still a lack of information, which needs to be revealed, on the mechanism of PBM for osteogenic differentiation. Besides, determination of the specific wavelength and light parameters is great importance to increase the success of the light therapy. In addition to this, it is also known that successive light treatments provides more opportunistic outcomes in PBM, instead of single light treatment on the cells [248, 250, 251]. There are still unknowns about the underlying mechanism of osteogenic differentiation induced by PBM. The role of ROS, NO, and ATP levels in PBM has not yet been totally enlightened during osteogenic differentiation. Therefore, we aimed to reveal the molecular mechanism of PBM at 655 and 808 nm of wavelengths during the osteogenesis of the (hBMSC):(HUVEC) co-culture and identify the most effective energy densities of both wavelengths for the osteogenic differentiation.

5.2 Materials and Methods

5.2.1 Materials

All cell culture products (Dulbecco's modified eagle medium: F12 (DMEM: F12), Penicillin Streptomycin, L-glutamine, Phosphate buffered saline tablets, trypsin-EDTA, 2′,7′-dichlorofluorescein diacetate (DCFH-DA), gentamycin, FBS, B-glycerophosphate, dexamethasone, ascorbic acid were purchased from Sigma Aldrich (St. Louis, Missouri, USA). hBMSCs were supplied from CLS Company (300665-102, Eppelheim, Germany). HUVECs were kindly provided from the Bioengineering Department, Ege University (Izmir, Turkey). ATP was analyzed by CellTiter-Glo (G7570, Promega, US). NO release was analyzed by Griess Reagent (K544-200, CA, USA). ALPase activity was tested by Alkaline Phosphatase Assay Kit (ab83369, Abcam, USA). Ca^{+2} content was measured by Quanthichrom Calcium Assay Kit (DICA-5, Bioassay Systems, CA, USA).

5.2.2 Cell Culture and Osteogenic Media Preparation

DMEM: F12 was used as the culture medium together with 10% fetal bovine serum (FBS), 1% penicillin-streptomycin, 50 µg/mL gentamicin, 250 ng/mL fungizone, and 1% L-glutamine for hBMSCs and HUVECs. They were incubated in a humidified environment containing 5% CO_2 at 37°C. After the cells reached confluency of around 80%, they were trypsinized for assays. Co-culture was constructed by hBMSC and HUVEC cells with a ratio of 1:1. Basal medium containing 100 nM dexamethasone, 50 µg/mL ascorbic acid, and 10 mM ß-glycerophosphate was used for osteogenic differentiation. Co-culture was incubated with osteogenic media up to day 21 [166]. For the scratch assay, a total of $5x10^5$ cells were used in a single well of 24-well plates. For the other assays, a total of $5x10^3$ cells were used in a single well of 96 well plates [246].

5.2.3 Light Sources

PBM therapy for osteogenic differentiation was performed by a 655-nm Diode Laser (Changchum New Industries Optoelectronics Tech, China) and an 808-nm

Diode Laser (Omnibil, Turkey). The optical fibers of laser devices were perpendicularly installed on an optical table with an XYZ platform to expose light to the cell culture plates. The distances between the fiber tip and the target remained constant throughout the experiment. Each laser device uniformly irradiated a defined region on plates, and the applied energy densities were changed by changing the exposure times. The output power of both laser devices was adjusted to 0.2 Watt. For both wavelengths, 1, 3, and 5 J/cm^2 of energy densities were employed to irradiate the cells three times with a 24-hour time interval [246].

5.2.4 In-vitro Wound Healing Assay

For the analysis of the cell proliferation and migration after PBM applications, the scratch assay was performed as a wound healing analysis. After overnight culture of the cells seeded in 24-well plates, the cells that adhered to the bottom of the wells were scratched with a pipette tip in the middle of the cell population [252]. Then, PBM applications were performed at 1, 3, and 5 J/cm^2 of energy densities three times with a 24-hour time interval. The control group was not received any light irradiation. Starting from the first light application, the micrographs of the cells were obtained with an inverted microscope (CKX41, Olympus, Tokyo, Japan) until the wound area was closed for each sample. The wound area of each sample was examined by Image J software (NIH, USA).

5.2.5 Analysis of the Intracellular ROS Production

Before PBM application, the co-culture was incubated with 100 µl of 0.1 mM 2′,7′-dichlorofluorescein diacetate (DCFH-DA) solution for 45 minutes. DCFH-DA was used to evaluate the amount of intracellular ROS produced as a result of laser treatments. In the presence of ROS, DCFH-DA is turned into dichlorofluorescein (DCF) and the fluorescent intensity of DCF can be measured as an indication of the ROS available in the cells. After the incubation with DCFH-DA, the co-culture was rinsed twice with PBS. Then the specific experimental protocols were applied to each group. The fluorescent intensity was read after the applications were completed with a microplate reader (Synergy™ HTX, BioTek, VT, USA) using the 485/20 nm of excitation wavelength and 528/20 nm of emission wavelength [253].

5.2.6 Analysis of ATP Production

One main indication of PBM is to produce ATP after light irradiation [254, 255]. ATP production of each sample was analyzed to enlighten the PBM mechanism of co-culture according to the literature and prescription of the kit [254]. Briefly, the ATP levels of 2D cell culture were measured 30 minutes after light applications. 50 μL of CellTiter-Glo was added into the mediums of co-culture. After 2 minutes of incubation at room temperature, the luminescence value was obtained with the microplate reader.

5.2.7 Analysis of NO Release

NO molecules in mitochondria are released after the light absorption by the cytochrome c oxidase. Thus, its analysis is very important to understand the underlying mechanism of PBM [253]. Briefly, the Griess reagent which contains sulfanilic acid and N-(1-naphthyl)ethylenediamine was used to quantify the amount of NO release. Nitrite molecule is the breakdown product of NO and it reacts with sulfanilic acid and N-(1-naphthyl) ethylenediamine. After this reaction, a dye molecule is produced and it can be analyzed spectrophotometrically. The identical amount of Griess reagent and the supernatant of each sample were mixed. They were incubated for 30 minutes at room temperature. The absorbance values were obtained with the microplate reader at 548 nm of wavelength.

5.2.8 Analysis of Osteogenic Differentiation

Osteogenic differentiation was analyzed by DNA quantification, ALP activity, and Calcium Deposition analysis as described in the previous study [166]. On 4, 7, 14, and 21 days, cells were rinsed with PBS and then they were lysed with 10 mM Tris-0.2% triton solution. These samples were used for the analysis of DNA, ALP, and calcium content. The amount of DNA was analyzed by mixing 50 μL of the suspension of each sample with 150 μL of the DNA solution. ALP activity was measured by p-nitrophenyl phosphate (pNPP) at 405 nm of wavelength in an alkaline solution. Each lysed sample was incubated in the presence of 10 μl ALP enzyme mixed with 50 μl 5 mM para-nitrophenyl phosphate solution. They were incubated at 25°C for 60 min in the dark. Then the samples were mixed with 20 µl of stop solution. The absorbance values were obtained at 405 nm of wavelength by a microplate reader [256]. Calcium content was analyzed by mixing 50 µL of the suspension with 150 µL of the working solution which includes Reagent A and B (1:1 ratio) of calcium assay [166]. After incubation, absorbance values were obtained at 612 nm of wavelength. ALP activity and Calcium content were identified in each sample by normalizing them with the DNA content.

5.2.9 Temperature Measurement

Although PBM is a non-thermal therapy and the output power was adjusted to 0.2 W in the experiments, the absorption of the photon energy may increase the temperature of the target. Thus, light applications may cause irreversible damage which is an undesired outcome in these applications. Thus, temperature measurements were carried out simultaneously with the laser irradiations during PBM applications with a thermal camera (Testo 882, Melrose, USA) on a 2D co-culture. Temperature measurements were carried out at the beginning (t_1) and the end of the light application (t_0). Δt was calculated by taking differences between the first and the last temperature measurement ($\Delta t = t_1 - t_0$) to monitor the temperature increase.

5.2.10 Statistical Analysis

All applications were repeated triple and at least 3 samples were used in each application. The data of ROS, ATP, and NO assays obtained from the experimental groups were normalized with the data of the control group. While data of ROS, ATP, and NO assays were analyzed by one-way ANOVA, the data of Scratch assay, DNA, ALP, and Calcium analysis were analyzed by two-way ANOVA. Then, each experimental group was compared with the control group by the Student's t-test. The statistical differences were defined as $p^* < 0.05$, $p^{**} < 0.01$ and $p^{***} < 0.001$.

5.3 Results

5.3.1 Wound Closure

Scratch assay images for the PBM applications at 655 nm of wavelength were given in Figure 5.2 and for the PBM applications at 808 nm of wavelength were given in Figure 5.3. Before the experiments, the cells in each sample were scratched so that there was no remaining cell in the middle of the wells. It was observed that the rate of proliferation and migration of cells increased depending on energy densities. Especially, after the 48th hour, the rate of proliferation was at its maximum level and the cells migrated to the wound area in all laser groups.

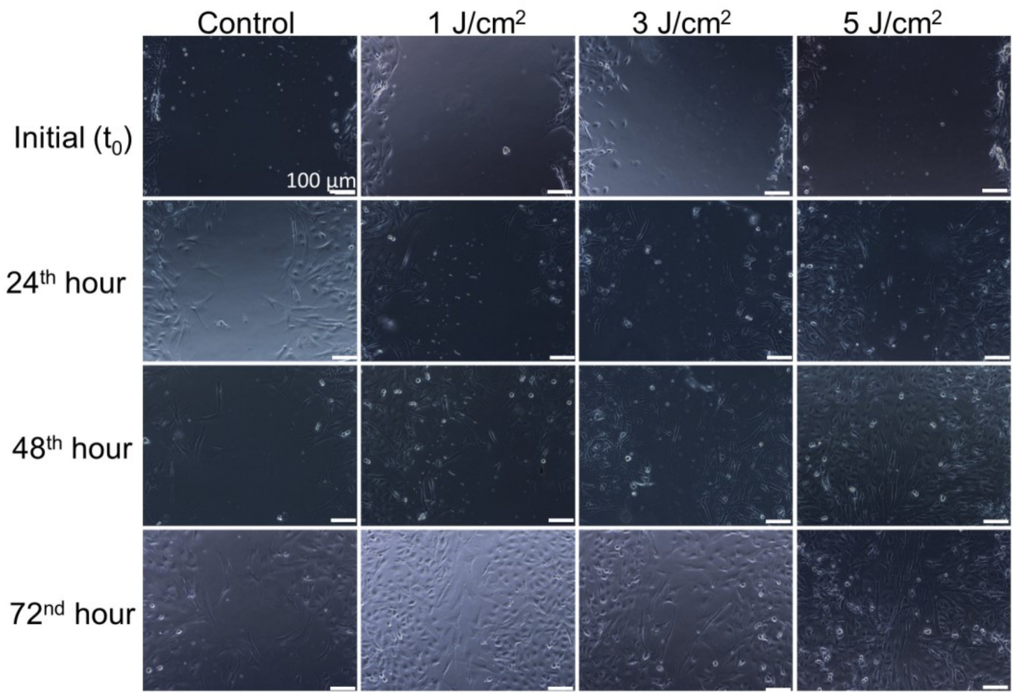

Figure 5.2: Microscopic images of the hBMSC: HUVEC co-culture obtained during *in vitro* wound-healing assay (Wavelength: 655 nm, Energy densities: 1, 3, and 5 J/cm^2, Scale bar is 100 µm)

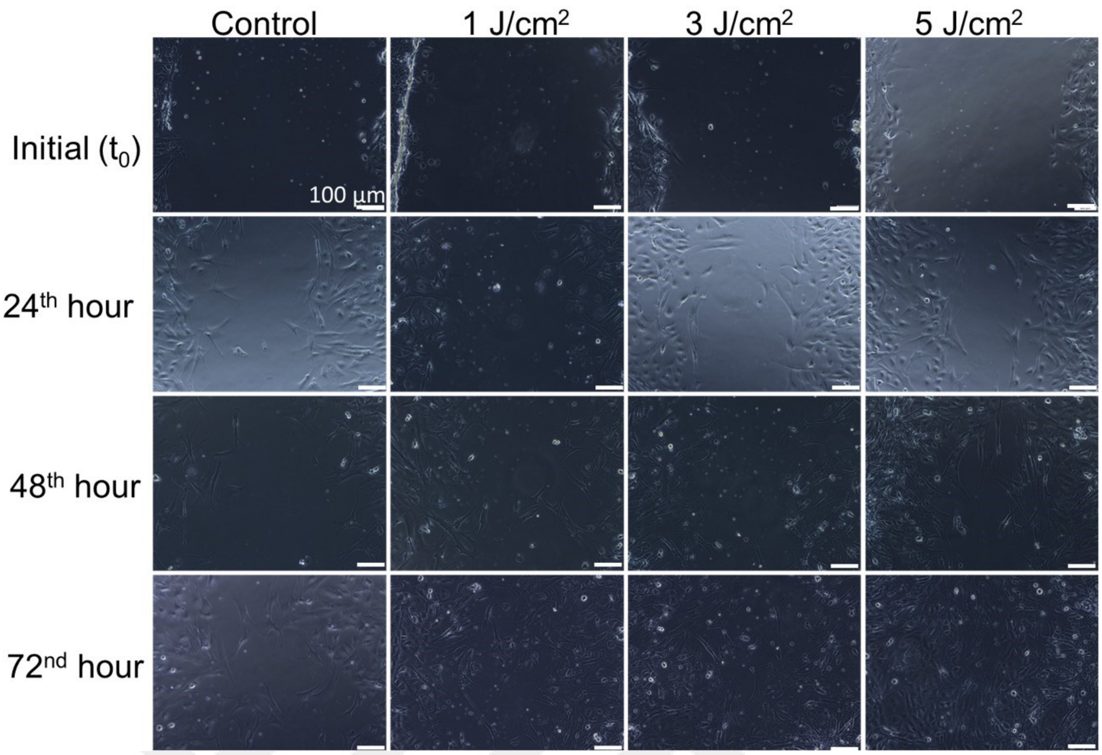

Figure 5.3: Microscopic images of the hBMSC: HUVEC co-culture obtained during *in vitro* wound-healing assay (Wavelength: 808 nm, Energy densities: 1, 3, and 5 J/cm^2, Scale bar is 100 µm)

The closed wound areas were represented in Figure 5.4 for the applications at 655 and 808 nm of wavelengths (A and B). For 655 nm of wavelength, wound closure measurements of control, 1, 3, and 5 J/cm^2 groups were calculated as 45±2.39%, 57±2.34% ($p^{*}<0.05$), 50±1.25%, and 96±1.81% ($p^{***}<0.001$) at the 48th hour, respectively. At the end of the 72nd hour, closed wound areas were 55±1.00%, 90±6.07% ($p^{***}<0.001$), 97±0.67% ($p^{***}<0.001$), 99±0.74% ($p^{***}<0.001$), respectively (Figure 5.4A). PBM application at 5 J/cm^2 energy density of 655 nm of wavelength provided the fastest wound healing process.

For 808 nm of wavelength, the closed wound area of the control, 1, 3, and 5 J/cm^2 groups were calculated as 45±2.39%, 56±1.09% ($p^{**}<0.01$), 51±5.12%, and 96±0.51% ($p^{***}<0.001$) at the 48th hour, respectively. At the end of the 72nd hour, measurements for the control, 1, 3, and 5 J/cm^2 groups were 55±1.00%, 97±1.12% ($p^{***}<0.001$), 96±2.82% ($p^{***}<0.001$), 100±0.05 ($p^{***}<0.001$), respectively (Figure

5.4 B). The application of 5 J/cm^2 energy density provided the fastest wound healing process at this wavelength, too.

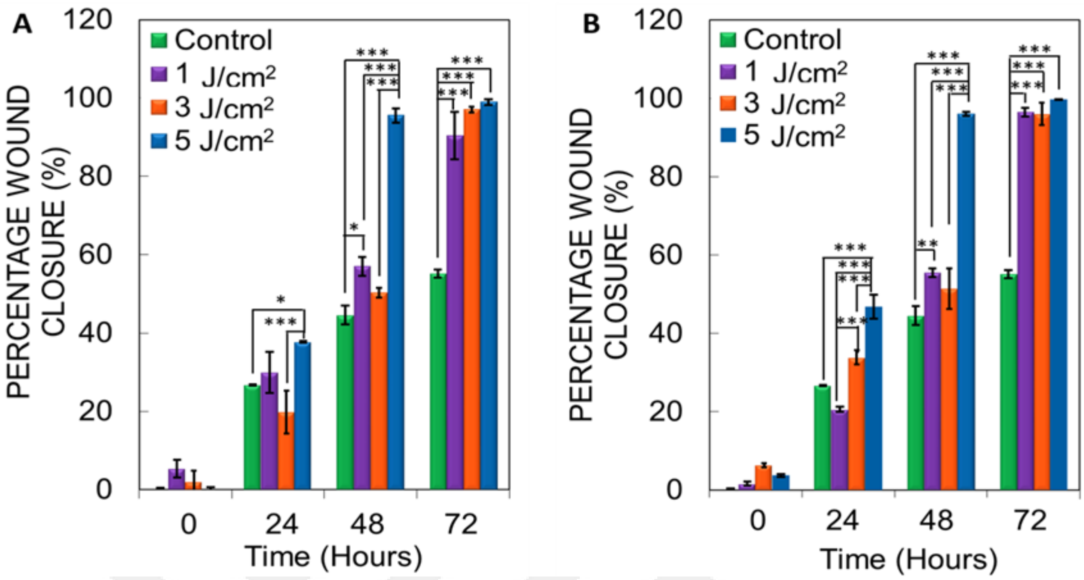

Figure 5.4: The percentages of the wound closures in *in vitro* wound healing assay of the hBMSC: HUVEC co-culture treated at a) 655 nm of wavelength b) 808 nm of wavelength (Energy densities: 1, 3, and 5 J/cm^2). Data were evaluated with two-way ANOVA followed by Student's t-test. $p^*<0.05$, $p^{**}<0.01$, and $p^{***}<0.001$

5.3.2 Intracellular ROS Production

The measurements for intracellular ROS production were presented in Figure 5.5. Even though there was not any statistically significant increase in ROS level compared to the control group, slight increases were observed with the 1 J/cm^2 application at 655 nm of wavelength and 3 J/cm^2 application at 808 nm of wavelength.

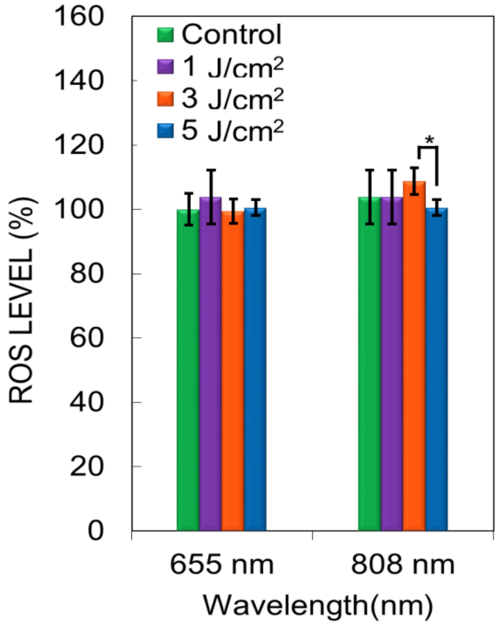

Figure 5.5: The percentages of the intracellular ROS level in the hBMSC: HUVEC co-culture treated at 655 and 808 nm of wavelengths (Energy densities: 1, 3, and 5 J/cm^2). Data were evaluated with one-way ANOVA followed by Student's t-test. p*<0.05, p**<0.01, and p***<0.001

5.3.3 ATP Synthesis

The levels of ATP production after each application were measured as they were presented in Figure 5.6. For the applications at 655 nm of wavelength, the levels of ATP productions in the control, 1, 3, and 5 J/cm^2 groups were 100±5%, 113±5% (p*<0.05), 73±3% (p***<0.001), and 118±4% (p***<0.001), respectively. For the applications at 808 nm of wavelength, the levels of ATP productions in the control, 1, 3, and 5 J/cm^2 groups were 100±5%, 125±0% (p***<0.001), 99±1%, and 122±6% (p***<0.001), respectively. The highest ATP production was observed in the 1 and 5 J/cm^2 groups for both wavelengths. They were also statistically significant compared to the control group. Interestingly, a decrease was observed in ATP level after the application at 3 J/cm^2 energy density for 655 nm of wavelength. Nevertheless, the increases in ATP level obtained in 5 J/cm^2 energy density application for both wavelengths were consistent with the increases in wound closures.

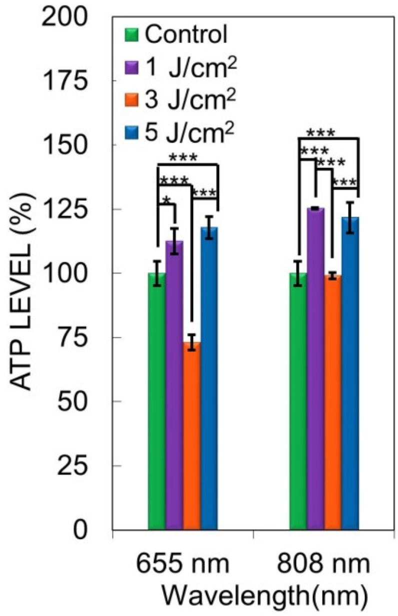

Figure 5.6: The percentages of the ATP level produced in the hBMSC: HUVEC co-culture treated at 655 and 808 nm of wavelengths (Energy densities: 1, 3, and 5 J/cm^2). Data were evaluated with one-way ANOVA followed by Student's t-test. p*<0.05, p**<0.01, and p***<0.001

5.3.4 NO Release

The levels of NO released after each application were shown in Figure 5.7. For 655 nm of wavelength, the maximum amount of NO was released with the application at 3 J/cm^2 energy density and it was measured as 156% which was statistically significant compared to the control group. 5 J/cm^2 energy density provided 20% more NO release compared to the control group, which was also statistically significant. For 808 nm of wavelength, the highest amount of NO was released after the application at 1 J/cm^2 energy density. It was 100% more than the control group. 3 J/cm^2 energy density provided 70% more NO release, and 5 J/cm^2 energy density provided 50% more NO release at this wavelength. All of these outcomes were statistically significant compared to the control group.

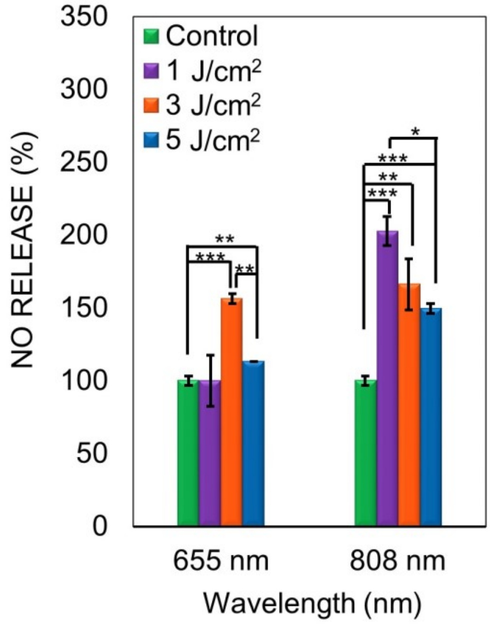

Figure 5.7: The percentages of the NO level released in the hBMSC: HUVEC co-culture treated at 655 and 808 nm of wavelengths (Energy densities: 1, 3, and 5 J/cm^2). Data were evaluated with one-way ANOVA followed by Student's t-test. p*<0.05, p**<0.01, and p***<0.001

5.3.5 DNA Content, ALPase Activity, and Calcium Level

To define the osteogenic differentiation capacity of the cells depending on the energy density and the wavelength, the analyses for DNA, ALPase, and Ca^{+2} content were performed after each application and their progress was followed until the 21st day. As shown in Figure 5.8, all energy densities at 655 nm of wavelength promoted the amount of double-stranded DNA day by day. The highest amount of DNA was achieved with the application at 5 J/cm^2 energy density, which was measured as 759±6 ng/ml. Similar outcomes were obtained at 808 nm of wavelength. All energy densities provided a day-by-day increase in DNA content in the cells and the application at 5 J/cm^2 energy density induced the highest amount of DNA production which was measured as 862±20 ng/ml at end of the last time point of osteogenic differentiation.

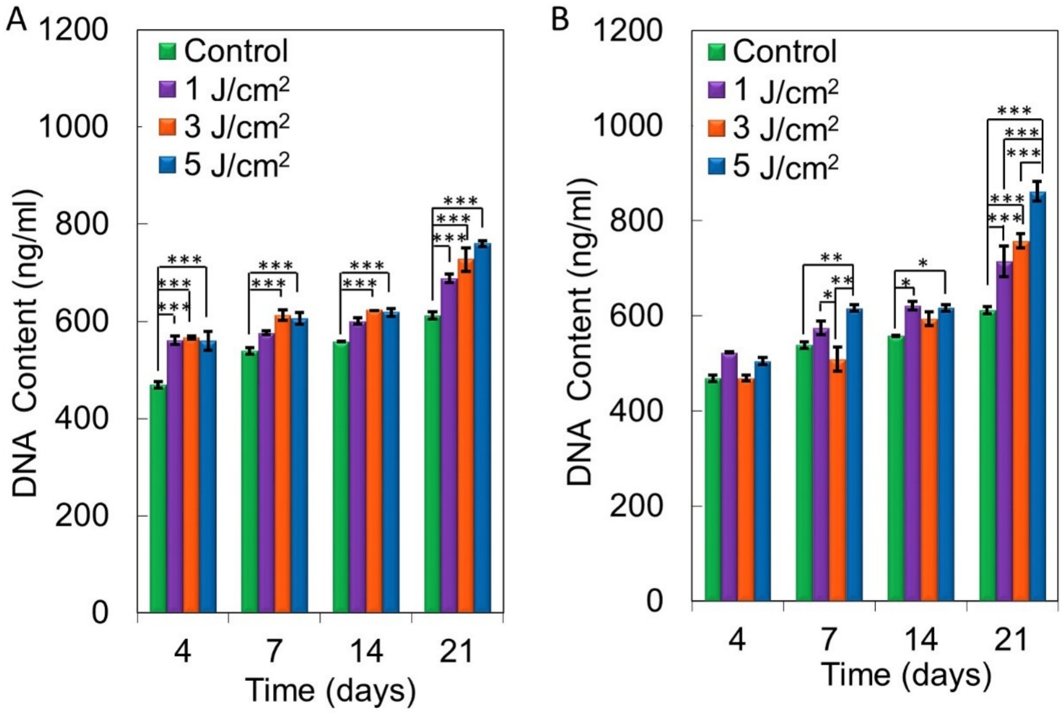

Figure 5.8: DNA content analysis in the hBMSC: HUVEC co-culture treated at a) 655 nm of wavelength b) 808 nm of wavelength (Energy densities: 1, 3, and 5 J/cm^2). Data were evaluated with two-way ANOVA followed by Student's t-test. p*<0.05, p**<0.01, and p***<0.001

Datas obtained from the analysis of ALPase activity were normalized with the DNA amount for each sample and presented in Figure 5.9. After the applications at 655 nm of wavelength, ALPase activities of control, 1, 3, and 5 J/cm^2 groups were measured as 3612±27, 3906±93, 3781±120, and 4154±58 IU/ng DNA on day 14, respectively. The highest ALPase activity was achieved with 5 J/cm^2 energy density at 655 nm of wavelength. Then, a decrease was observed in all experimental groups on the 21st day. After the applications at 808 nm of wavelength, ALPase activities of control, 1, 3, and 5 J/cm^2 groups were measured as 3612±27, 3741±62, 3921±26, and 4141±31 IU/ng DNA on day 14, respectively. The highest ALP activity at 808 nm of wavelength was measured as 4141±31 IU/ng DNA after the application at 5 J/cm^2 energy density on day 14. Similarly, a decrease was observed in all experimental groups on the 21st day.

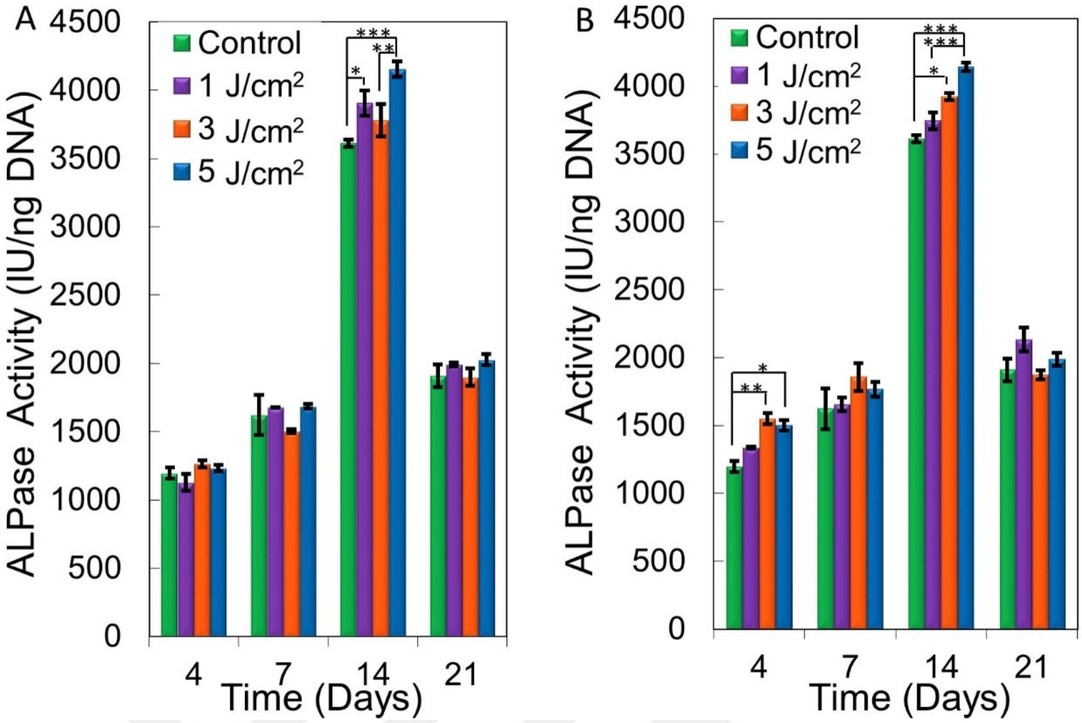

Figure 5.9: ALPase activity analysis in the hBMSC: HUVEC co-culture treated at a) 655 nm of wavelength b) 808 nm of wavelength (Energy densities: 1, 3, and 5 J/cm^2). Data were evaluated with two-way ANOVA followed by Student's t-test. p*<0.05, p**<0.01, and p***<0.001

The datas of the analysis for calcium content were normalized with the DNA amount for each sample and presented in Figure 5.10. For the applications at 655 nm of wavelength, the calcium contents in control, 1, 3, and 5 J/cm^2 groups were measured as 2437±68, 2798±43, 2491±188, and 3069±61 ng/ng DNA on day 21, respectively. For the applications at 808 nm of wavelength, the calcium contents in control, 1, 3, and 5 J/cm^2 groups were measured as 2437±68, 2706±124, 2516±46, and 2957±85 ng/ng DNA on day 21, respectively. The highest calcium content was obtained with the application at 5 J/cm^2 energy density for both wavelengths.

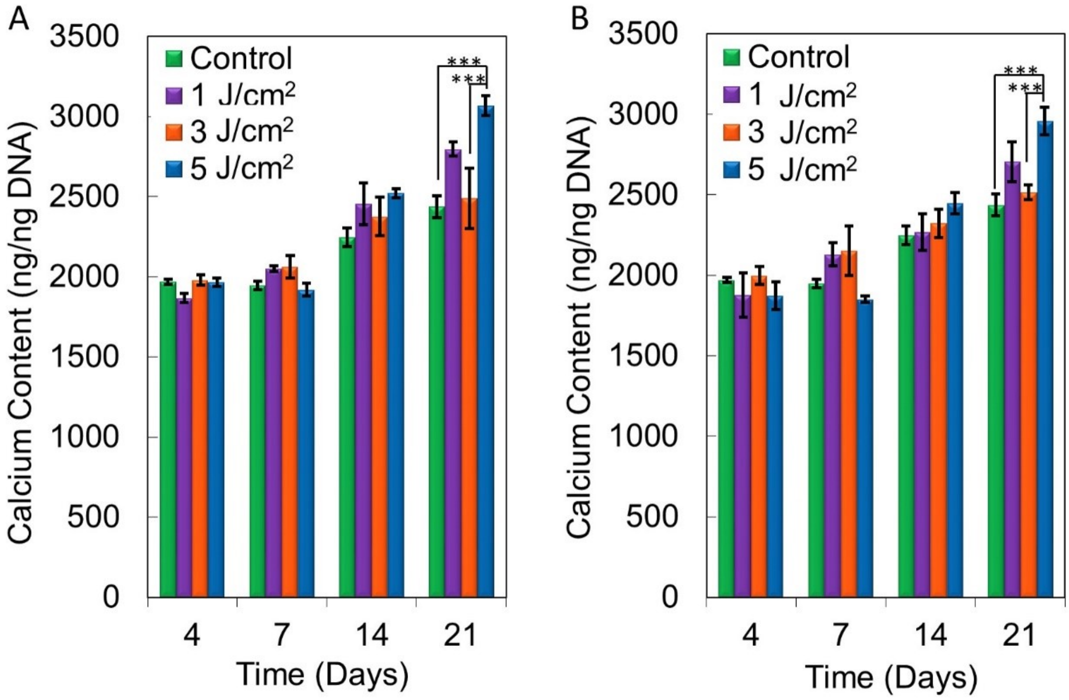

Figure 5.10: Calcium content analysis in the hBMSC: HUVEC co-culture treated at a) 655 nm of wavelength b) 808 nm of wavelength (Energy densities: 1, 3, and 5 J/cm^2). Data were evaluated with two-way ANOVA followed by Student's t-test. p*<0.05, p**<0.01, and p***<0.001

5.3.6 Temperature Changes

The temperature changes between the initial and final temperatures during the laser applications were measured with a thermal camera to monitor whether there was a photothermal effect on the cells. As it was shown in Table 5.1, the increase in temperature depended on the energy density and the wavelength. When the energy density increased, more temperature change was observed. Besides, 808 nm of wavelength induced more temperature increase in the cells. The highest temperature difference was 0.9°C and it was observed during the application at 5 J/cm^2 energy density for 808 nm of wavelength.

Table 5.1: Temperature measurements with a thermal camera during the laser applications

Temperature Measurements				
Wavelength	Energy Density (J/cm^2)	Initial (˚C)	Final (˚C)	Δt (˚C)
655 nm	1	24	24.2	0.2
	3	24.3	24.6	0.3
	5	24	24.7	0.7
808 nm	1	25	25.4	0.4
	3	25.3	25.9	0.6
	5	25	25.9	0.9

5.4 Discussions

In this study, the effects of 1, 3, and 5 J/cm^2 energy densities at 655 and 808 nm of wavelengths were investigated to induce osteogenic differentiation of the co-culture of Human Bone Marrow Stem Cell (hBMSC): Human Umbilical Vein Endothelial Cell (HUVEC). Mechanistic analyses for intracellular ROS production, NO release, and ATP synthesis were performed to understand their role in PBM therapy used for osteogenic differentiation. The changes in ROS, NO, and ATP levels were then correlated with the markers of osteogenesis, such as DNA, ALP, and calcium content.

The use of optimal dosimetry is critically important for PBM through the desired therapeutic outcome [257, 258]. Low-level light doses are used to induce PBM and especially red and near-infrared wavelengths are preferred because of the specific chromophores in the mitochondria that strongly absorb these wavelengths [243, 247, 251]. Nevertheless, near-infrared wavelengths have the possibility to cause photothermal reactions which may result in thermal side-effects on the target [257]. Even though low-level light parameters were investigated, temperature monitoring is crucial to be sure about the non-thermal mechanism of PBM. In this study, the maximum temperature change observed was 0.9°C which may be regarded as negligible and did not have the possibility to induce any thermal side-effect [259, 260]. Thus, the light parameters used in these experiments can be considered safe for PBM.

Wound closure depending on the proliferation and migration rate of the cells in hBMSC: HUVEC co-culture treated with laser light was compared with the non-treatment group. All energy densities at 655 and 808 nm of wavelength were quite effective after the 24th hour. Even though 5 J/cm^2 energy density was the most effective light parameter for both wavelengths in the 48th hour, all light-treated groups exhibited an effective proliferation rate than the control group. Previous studies have shown that red and near-infrared wavelengths support cell proliferation [245], especially the 5 J/cm^2 energy density of red wavelength contributed to the healing of the wounds [261-263]. Mokoena et al. showed that 5 J/cm^2 energy density at 660 nm of wavelength started to close the wounds after the 48th hour [264]. Topaloglu et al. also indicated that 5 J/cm^2 energy density at 808 nm of wavelength exhibited a faster wound healing process [246]. Thus, it can be seen that the outcomes of this study are compatible with the outcomes of the previous studies.

PBM is a non-thermal light application that triggers various cellular mechanisms via intracellular ROS production, ATP synthesis, NO release, etc. [242, 243]. Those signal molecules may induce osteogenic differentiation [245, 258]. Thus, the level and the role of these molecules were investigated in the hBMSC: HUVEC co-culture system after PBM. Surprisingly, the level of intracellular ROS did not change significantly in these experiments, only slight changes were observed after light applications. However, the rate of ATP synthesis significantly increased after light applications, especially at 1 and 5 J/cm^2 energy densities for both wavelengths. Similarly, previous studies have also reported that 5 J/cm^2 energy density at 632.8, 635, and 660 nm of wavelengths enhanced ATP production [249, 265]. Another study showed that 1 J/cm^2 energy density at 980 nm of wavelength was also effective for ATP synthesis [266]. Amaroli et al. showed in their study that 808 nm of wavelength induced ATP synthesis via mitochondria [258]. Therefore, it can be clearly stated that 1 and 5 J/cm^2 energy densities at red and near-infrared wavelengths have similar effects on hBMSC: HUVEC co-culture in terms of ATP production as in previous studies. Different from the energy densities that were effective for ATP synthesis, 3 J/cm^2 energy density at 655 nm of wavelength and 1 J/cm^2 energy density at 808 nm of wavelength were the most effective light parameters to induce more NO release. Nevertheless, 5 J/cm^2 energy density at both wavelengths exhibited significant NO release, which contributed PBM mechanism together with ATP synthesis. When light can trigger mitochondrial respiration by separating NO from cytochrome c oxidase, it is well known that its release is positively correlated with an increase in ATP and it indicates that mitochondrial metabolism and respiration have been activated [267].

While the proliferation and migration rates of the cells in the hBMSC: HUVEC co-culture increased, the measured DNA amount increased from the 4th to the 21st day, too. The highest DNA content was obtained from the cells treated with 5 J/cm^2 energy density for both wavelengths. Previous studies have also indicated that red and near-infrared wavelengths increase cell proliferation via PBM [261, 268, 269], thus it was not surprising to obtain a significant increase in DNA content. ALP is a critically important osteogenic marker that is expressed in the early time point of osteogenesis [166]. The ALP level was significantly increased after laser irradiation compared to untreated control groups. The highest expression rate of ALP was directly observed in the groups treated with 5 J/cm^2 energy density at 655 nm and 808 nm of wavelength. Biao et al. showed that the applications with 1 J/cm^2 energy density effectively expressed ALP levels at 630 and 810 of wavelength on day 14 [270]. In another study done by Bueno et al., the applications with 5 J/cm^2 energy density at 660 nm of wavelength promoted ALP activity on day 14 [271]. Previous studies already indicated that 5 J/cm^2 energy density augmented ALP activity and osteogenic differentiation of stem cells [271, 272] which supports our findings in this study. In general, a significant amount of calcium deposition occurs in late time points of osteogenic differentiation, indicating the mineralization of the bone matrix [166, 273]. Similar to the previous analysis, light application at 5 J/cm^2 energy density of both wavelengths deposited the highest calcium mineralization. A previous study indicated that both 630 and 810 nm of wavelengths in PBM can afford calcium deposition [270]. Ghidini et al. also showed that 5 J/cm^2 energy density at 645 nm of wavelength induced the highest cell proliferation and calcium deposition [274]. Karic et al. supported these findings with their study that 5 J/cm^2 energy density at 660 nm of wavelength provided osteogenic differentiation [249]. Other studies also showed that 808-810 nm of wavelengths increased the mineralization of stem cells [242, 270].

All of these findings supported that PBM is an effective therapeutic way for bone regeneration. In general, it is assumed that the PBM mechanism is supported by intracellular ROS, ATP, and NO release. However, we observed that the change in intracellular ROS was quite low and the changes in ATP and NO levels were significant. Thus, it should be stated that they have a more important role in osteogenic differentiation of the cells in the hBMSC: HUVEC co-culture through the PBM mechanism at red and near-infrared wavelengths. In previous studies, several energy densities ranging from 1 to 20 J/cm^2 of red and near-infrared wavelengths were assessed, 5 J/cm^2 energy density advanced MSCs proliferation, arrangements of bone factors, inflammation, and cell signalling pathways in the most striking way [271, 272, 275, 276]. Our findings also showed that 5 J/cm^2 energy density at 655 and 808 nm of wavelengths played the most effective role in cell proliferation and migration, ATP synthesis, NO release, ALPase activity, and mineralization.

5.5 Conclusions

It can be clearly stated that PBM enhanced osteogenic differentiation in the hBMSC: HUVEC co-culture, by influencing the mechanism of DNA synthesis, ALPase activity, and calcium content. Especially, ATP production and NO release had key roles in the proliferation, migration, and osteogenic differentiation through PBM therapy at red and near-infrared wavelengths. 5 J/cm^2 energy density at 655 and 808 nm of wavelength was the most successful light parameter on hBMSC: HUVEC co-culture for the osteogenic differentiation. It was understood that PBM therapy is an alternative and promising strategy for bone regeneration by determining the optimal light parameters that might be specific to certain types of cells.

Chapter 6

6. Photobiomodulation Therapy at Red And Near-Infrared Wavelengths for Osteogenic Differentiation in The Scaffold Free Microtissues

6.1 Introduction

One of the primary objectives of bone tissue engineering is to accelerate the bone regeneration using novel technologies that deal with stem cells, bone matrices, and bone cell signalling mechanisms. Especially, Human Bone Mesenchymal Stem Cells (hBMSCs) have shown high potency for the treatment of bone damage, bone loss, and fracture recently. hBMSCs produce cytokines and growth factors for the formation of extracellular matrix (ECM), promote wound repair, and induce bone regeneration [277]. The fate decision of hBMSCs can be regulated by their microenvironment which contains growth factors, cytokines, chemicals and, also mechanical forces [239]. hBMSCs are also affected by endothelial cells which they come into contact [239, 278]. The complex combination of these cells induces osteogenic differentiation [279]. Moreover, co-culture of stem cells and endothelial cells facilitates bone regeneration [280]. Besides, there are other technologies which are very promising and powerful for tissue regeneration, such as therapeutic light applications. Photobiomodulation (PBM) is an example of such therapeutic light applications, which are also capable to support the regeneration capacity of a co-culture formed by the stem and endothelial cells [253].

PBM, which is formerly defined as Low-Level Light Therapy (LLLT), is known to induce cell proliferation, differentiation, and wound healing [242, 281-285]. It may also support bone regeneration, and thereby the healing of large bone damages [286, 287]. It may have very effective roles in bone formation by inducing several physiological processes [242, 287]. PBM depends on photochemical interaction mechanism which is a non-thermal process and it directly affects the mitochondria [285, 288]. The wavelength range of 600 to 1200 nm is called therapeutic window and the light sources that operate in this region are commonly used to induce PBM [289, 290]. Especially, the wavelengths around 600 and 800 nm are strongly absorbed by the heme groups of cytochrome c oxidase in mitochondria and it is the onset of the mechanism of PBM [290]. Thus, cytochrome c oxidase works as a photoacceptor, which is found at the end of the mitochondrial respiratory chain [130]. Redox reactions in cytochrome c affect cell signalling molecules [282, 283, 291]. Biochemical reactions that are induced by these molecules result in the production of intracellular reactive oxygen species (ROS), Adenozine Triphosphate (ATP), and Nitric Oxide (NO) release at the end of the light absorption [242, 288, 292]. This set of events accelerates the cell division by increasing the synthesis of DNA and RNA, protein expressions, and supports the regulation of the cell cycle [242, 288]. PBM with these changes enhances the mitochondrial activity and as a result of this, it may induces osteogenic differentiation at the molecular level (Figure 6.1). Thus, it may support bone regeneration [242, 285, 288, 292].

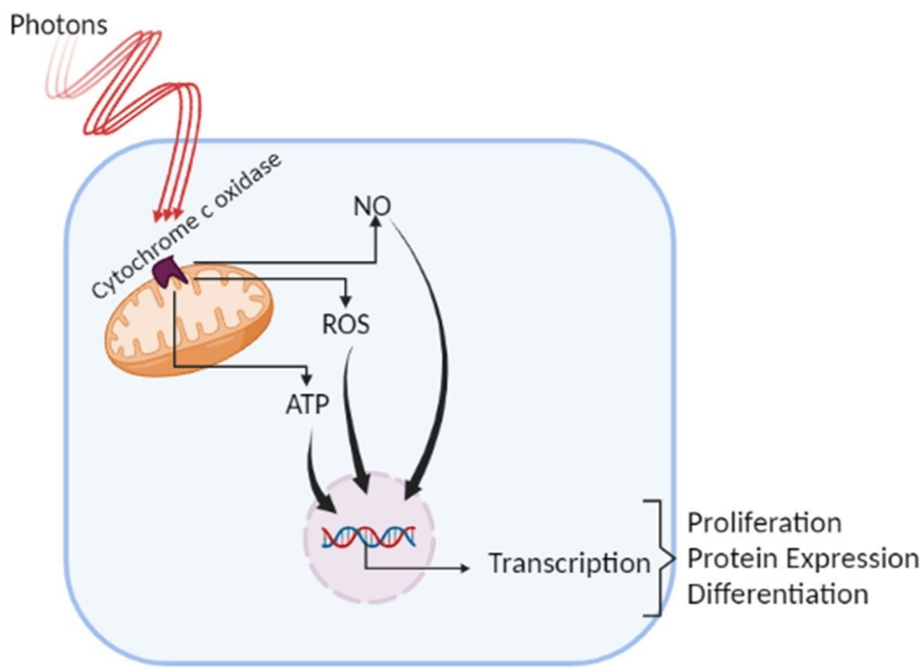

Figure 6.1: PBM induced bone regeneration. (Created with BioRender.com).

Along with this, the therapeutic success of PBM depends on several parameters such as the wavelength, energy density, output power, application time, the area of application, and the number of repetitions of the light applications [242, 293]. It is well known that PBM exhibits biphasic dose response of the cells and therefore it may induce biostimulation or bioinhibition depending on the light parameters that are used [289]. Thus, the use of optimal light parameters is very crucial for obtaining the desired photobiomodulative effect on the cells or tissue upon irradiation [242, 285, 286].

Recently, tissue engineering studies focuses on 3D *in vitro* models, instead of monolayer cell cultures, to observe the natural responses of the cells in their microenvironments [294]. The approach aims to ensure mimicking *in vivo* tissue regeneration. 3D Scaffold Free Microtissues (SFMs) can be a good candidate as a bridge between the traditional monolayer culture and *in vivo* systems [64, 294-296]. SFMs can produce a self-extracellular matrix (ECM) and they support obtaining more natural responses of cells in terms of cell proliferation, cellular communications, matrix production, and gene expression [64, 295, 297]. Therefore, SFMs may mimic natural niches of *in vivo* systems. 3D SFMs can also promote *in vivo* cellular responses during bone regeneration. Although the 3D SFMs have many advantages, 2D cell culture is the most well-known and the commonly used system in PBM studies [254, 269]. However, 2D cell culture may fail during the determination of the optimal light parameters [298-300], as well as the intracellular mechanisms that end up with cell proliferation, differentiation, and/or wound healing because of its limited matrix production and restricted cellular communication [64, 295, 296, 301, 302]. Therefore, the determination of the appropriate PBM parameters in 2D cell culture model may not be optimal methodology to investigate the mechanism of osteogenesis in complex organisms.

This study aimed to investigate the molecular mechanism of PBM on 3D SFMs formed by the coculture of hBMSCs and HUVECs. PBM was induced with two different wavelengths (655 and 808-nm) at three different energy densities (1, 3, and 5 J/cm^2). The optimal light parameters for bone tissue regeneration were evaluated with cell viability assays, mechanistic analysis (intracellular ROS production, ATP synthesis, and NO release), the determination of molecular mechanisms (DNA quantification, mineralization, and ALPase activity), and the gene expression analysis of the osteogenic markers via qRT-PCR.

6.2 Materials and Methods

6.2.1 Materials

hBMSC (300665-102) were purchased from, CLS Company, Eppelheim, Germany. HUVECs were kindly provided from the Department of Bioengineering, Ege University. All cell culture supplements (trypsin-EDTA, L-glutamine, DMEM:F12, Penicillin Streptomycin, Phosphate buffered saline tablets, 2′,7′-dichlorofluorescein diacetate (DCFH-DA), gentamycin, FBS, B-glycerophosphate, dexamethasone, ascorbic acid) were purchased from Sigma-Aldrich, MA, USA. Otherwise, the product information was descripted in below. CellTiter-Glo (G7570) was purchased from Promega, US for ATP activity analysis. Griess reagent was purchased, Biotium, CA, USA for NO assay. The cellstain double staining kit (CS01-10) was taken from Dojindo Molecular Technologies, Japan. ALPase activity (ab83369) was tested by Abcam, Alkaline Phosphatase Assay Kit (Colorimetric), USA was obtained from Abcam (ab83369), USA. Ca^{+2} content kit (DICA 500) was purchased from Quanthichrom, Wilhelm-Mauser, Germany. RNAqueous™ Total RNA Isolation Kit was purchased from Thermo, USA. MuLV First Strand cDNA Synthesis Kit was purchased from Biomatik (Ontario, Canada).

6.2.2 Cell Culture and Manufacture of 3D SFMs

hBMSCs were cultured in Dulbecco's Modified Eagle media: F12 (DMEM). They were grown within 10% fetal bovine serum (FBS), 1% antibiotics (contains 10,000 units/mL of penicillin and 10,000 µg/mL of streptomycin) under standard laboratory conditions (5% CO_2, 95% humidity, and 37°C). The medias of cells were refreshed every 2 days [64, 269, 303, 304]. When the cells covered the cell culture flasks with 90 %, they were incubated for 5 minutes with 0.25% Trypsin-EDTA solution to collect them. Then they were seeded for the fabrication of 3D SFMs with $1x10^5$ number of cells. hBMSC:HUVEC co-culture was constructed with a 1:1 ratio in 3D SFMs. For osteogenesis process, basal medium was supplemented with 100 nM dexamethasone, 50 µg/mL ascorbic acid, and 10 mM ß-glycerophosphate to prepare osteogenic media [305]. To construct 3D SFMs, melted agarose was added into 3D petri dish as descripted in previous studies [295, 306]. The agarose gel was incubated with osteogenic media for 30 minutes. Then, hBMSC and HUVEC were added to the agarose molds. After 1 day, co-culture SFMs were ready for PBM application.

6.2.3 Light Sources and PBM Applications

PBM was performed with 655 nm Diode Laser (Changchum New Industries Optoelectronics Tech, China) and 808-nm Diode Laser (Omnibil, Istanbul, Turkey). The optical fibers of the laser devices were fixed with an XYZ-platform on an optical table to illuminate the cell culture plates perpendicularly. The distances between the fiber tip and the target were kept a constant. Each laser irradiated a definite area homogenously on cell culture and the applied energy densities were determined by changing the exposure durations with a constant output power. The output power was set to 0.2 Watt for each light source. 1, 3, and 5 J/cm^2 of energy densities were used for both wavelengths (Table 6.1). The cells in 3D cell culture models were exposed to light irradiation three times with a 24-hour time interval to perform PBM applications in this study.

Table 6.1: Light Parameters used in PBM Applications.

	Output Power (W)	Exposure Durations (s)	Energy Density (J/cm^2)
655-nm diode laser	0.2	5	1
		14	3
		24	5
808-nm diode laser	0.2	11	1
		33	3
		55	5

6.2.4 Live and Dead Cell Assay

The effect of PBM applications on the cell viability of 3D SFMs, Cellstain double staining was used on days 4th,7th,14th and 21st. according to the protocols used in previous studies [64, 306]. After the PBM applications, the cell medium was removed and the agarose was washed 3 times with PBS. 11 mmol of L Calcein-AM / DMSO solution and 1.5 mmol of L Propidium Iodide / purified water solution which were prepared in PBS was added onto the agarose of SFMs and incubated for 15 minutes at 37°C. Then the agarose was washed 5 times with PBS and the SFMs were observed under the fluorescence microscopy (Olympus CKX41, Olympus Co. Ltd., Tokyo, Japan). The intensity values of green colors were calculated quantitatively by Image-J software as an indication of cell viability.

6.2.5 Measurements of the Diameters of SFMs

The micrographs of SFMs were obtained to follow the enlargement of SFMs during osteogenic period by using an inverted microscope (Olympus, CKX41, Tokyo, Japan) on days 4th, 7th, 14th, and 21st. The diameter measurements were performed as described in previous studies [64, 306]. The diameters of the SFMs were measured from 3 different angles with the Image J (NIH) program. The mean values and standard deviations of all datas were calculated to analyze the progression of the SFMs after PBM applications.

6.2.6 Analysis of the Intracellular ROS Production

Light irradiation during PBM applications induces intracellular ROS production after the absorption of light energy by cytochrome c oxidase and these products have a key role to induce some cellular pathways that result in cell proliferation/differentiation [277, 307]. DCFH-DA is a commonly used probe as an indicator for ROS, This probe is an indicator for ROS, can pass into the cell, and becomes a fluorescent agent (DCF) in the presence of ROS. After PBM applications, the mediums of SFMs were removed. Fresh PBS was added. Then, 100 µl of DCFH-DA solution was added to SFMs. This mixture was incubated at 37°C for 45 minutes in the dark. Then, the excess DCFH-DA that did not enter into the cells was washed with PBS twice. After washing steps, the amount of ROS formed in the cells was determined by measuring the fluorescence intensity with an excitation wavelength of 485 nm and an emission wavelength of 535 nm using a microplate reader (Synergy™ HTX Multi-Mode Microplate Reader, BioTek, Winooski, VT, USA).

6.2.7 ATP Production Assay

Another important outcome of PBM is an increase in ATP production [254]. Briefly, the ATP levels of 3D SFMs were measured 30 minutes after light applications. 50 µL of CellTiter-Glo was added into the mediums of 3D SFMs. The mixtures were incubated in a shaker for 2 minutes at room temperature. Then, it was further incubated for 10 minutes at room temperature to stabilize the luminescent dye. The luminescence value was read with the microplate reader.

6.2.8 Analysis of the NO Release

PBM also induces the release of NO molecules that are bound to mitochondria [281]. The amount of NO released after PBM was measured by Griess reagent as described in literature [253]. An hour after the applications were completed, the equal volume of Griess reagent and the cell medium of each sample were mixed. They were incubated for 30 minutes at room temperature. The amount of released NO in each sample was determined by measuring the absorbance at 548 nm of wavelength with the multimode reader. The NO levels of the experimental groups were normalized with the data of the control group.

6.2.9 DNA Quantification

The effect of PBM applications on SFMs was also evaluated with the DNA quantification on days 4th, 7th, 14th, and 21st. Briefly, SFMs were washed with cold PBS at first. Afterwards, SFMs were centrifuged at 4500 rpm for 15 min in PBS. The SFMs were lysed using a tissue shredder stick and then treated with 10 mM Tris and 0.2% Triton. 50 µl lysed samples and 150 bisbenzimide H 33258 were mixed for DNA quantification. After 4 minutes of incubation, fluorescent intensity was measured with the excitation wavelength of 360 nm and the emission wavelength of 460 nm for the determination of DNA quantity by multimode plate reader.

6.2.10 Analysis of ALPase Activity

The amount of ALPase, which plays an active role in osteogenesis [199], was measured on days 4th, 7th, 14th, and 21st. and then compared to experimental groups to observe the effect of PBM applications on ALPase activity. Briefly, 50 µL of Assay Buffer was used to homogenize the SFMs on ice, the mixture was centrifuged at 4500 rpm 4°C for 15 minutes. Then, the supernatant was mixed with 50 µl of pNPP solution and 10 µL of ALP enzyme. After incubation at 25°C for 60 minutes, 20 µL of stop solution was added to the mixture and absorbance was measured at 405 nm by multimode plate reader.

6.2.11 Calcium Quantification

In order to analyze the mineralization observed in the advanced stages of osteogenesis, the amount of Ca^{+2} was determined in each experimental group on days 4th, 7th, 14th , and 21st. Ca^{+2} determination was carried out as previous studies [305, 308]. Briefly, equal amounts of reagent A and B of Quanthichrom Calcium Kit were mixed. After the lysis of SFMs, 50 µl of samples were added to the mixture of reagents A and B. Then, the mixture was transferred into the wells of 96-well plate and incubated for 3 minutes at room temperature. The absorbance was measured at 612 nm by multimode plate reader.

6.2.12 qRT-PCR Analysis for the Gene Expressions of Osteogenic Bone Markers

The gene expressions of osteogenic bone markers were evaluated using quantitative real time PCR (qRT-PCR) analysis on days 4^{th}, 7^{th}, 14^{th} , and 21^{st} as shown in previous studies [64, 295]. Briefly, SFMs were lysed by tissue shredder stick. Total RNA of SFMs was purified by RNA isolation kit and then cDNA was synthesized by using random primers in buffer solution with Taq polymerase enzyme. qRT-PCR analysis was performed by using StepOne Plus Real-Time PCR System (Applied Biosystems, Foster City, USA). Glyceraldehyde 3-phosphate dehydrogenase (GAPDH) was used as a housekeeping gene and compared with osteogenic markers which were Alkaline Phosphatase (ALP), Collagen, and Osteopontin (OPN). mRNA levels of osteogenic markers were evaluated according to the $2^{-(\Delta\Delta Ct)}$ method. The forward and the reverse sequences of osteogenic primers and housekeeping gene were given in Table 6.2 [305, 309].

Table 6.2: The forward (F) and reverse (R) sequences of the osteogenic markers used in qRT-PCR analysis.

GENE	Sequences
GAPDH	R: AACAGCGACACCCACTCCTC F: CATACCAGGAAATGAGCTTGACAA
Osteopontin (OPN)	R: ATGAGATTGGCAGTGATT F: TTCAATCAGAAACTGGAA
Alkalin Phosphatase (ALP)	R: ACATTCCCACGTCTTCACATTT F: AGACATTCTCTCGTTCACCGCC

Collagen Type I	R: TGACGAGACCAAGAACTG F: TCAGCCTTAGACGCCTCAAT

6.2.13 Temperature Measurements during Light Irradiations

Even though PBM is defined as non-thermal light therapy [253], the absorption of near-infrared wavelengths may increase the temperature of the target during light applications and it may cause irreversible damage [310]. Thus, the temperature changes should be monitored especially during the light applications at near-infrared wavelengths. Temperature measurements were carried out simultaneously with the laser irradiations during PBM applications with a thermal camera (Testo 882, Melrose, USA) on 3D SFMs. The photothermal effect due to the temperature increase at the end of the light applications (t_1) was analyzed by making comparison with the initial temperature (t_0) measured before the applications ($\Delta t=t_1-t_0$).

6.2.14 Statistical Analysis

All experiments were performed with three samples and repeated at least three times. Averages of all datas and standard errors were calculated. Statistical analysis of one independent variable (ATP, ROS and NO) assays were assessed through one-way ANOVA, followed by Tukey’s post hoc test (GraphPad Prism 6, San Diego, CA, USA). Control group values were estimated as 100% and experimental groups were evaluated by comparing them with the data of the control group. The other assays were analyzed with two-way ANOVA, followed by Tukey’s Post hoc test. Significant differences between the experimental and control groups were determined as $p^* < 0.05$, $p^{**} < 0.01$, $p^{***} < 0.001$.

6.3 Results

6.3.1 Measurements of the Diameters of SFMs

The images of all SFMs were obtained on days 4, 7, 14, and 21 as presented in Figure 6.2 for the PBM applications at 655 nm and Figure 6.3 at 808 nm of wavelengths. On 14th day, cell scattering occurred around the SFMs. On 21st day, all SFMs preserved their form and no deterioration was observed in their structures.

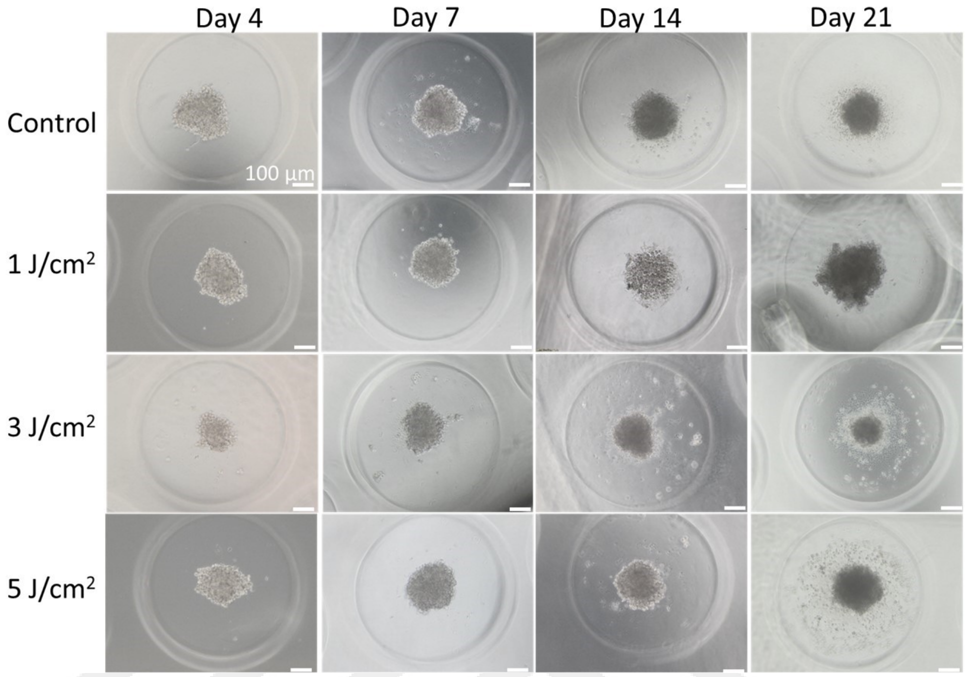

Figure 6.2: Microscopic images of tissue-engineered SFMs treated with 655-nm of wavelength on days 4, 7, 14, and 21 (Energy densities: 1, 3, and 5 J/cm2). Scale bar 100 µm.

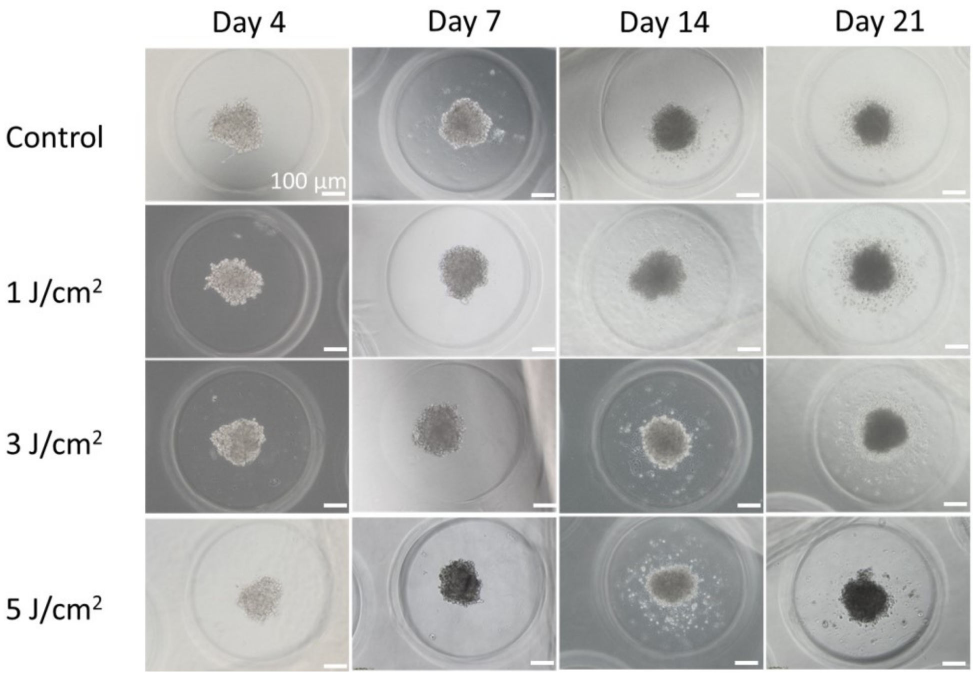

Figure 6.3: Microscopic images of tissue-engineered SFMs treated with 808-nm of wavelength on days 4, 7, 14, and 21 (Energy densities: 1, 3, and 5 J/cm^2). Scale bar 100 µm.

The diameters were measured on days 4, 7, 14, and 21 as shown in Figure 6.4. For 655-nm of wavelength at each energy density, the diameters of SFMs did not exhibit any statistically significant difference compared to control group on day 4. Nevertheless, 808 nm wavelength at 1 J/cm^2 and 5 J/cm^2 energy densities started to provide a statistically significant difference in SFM diameters compared to control on day 4. 808-nm of wavelength at the same energy densities maintained the similar outcome on 7th day, too.

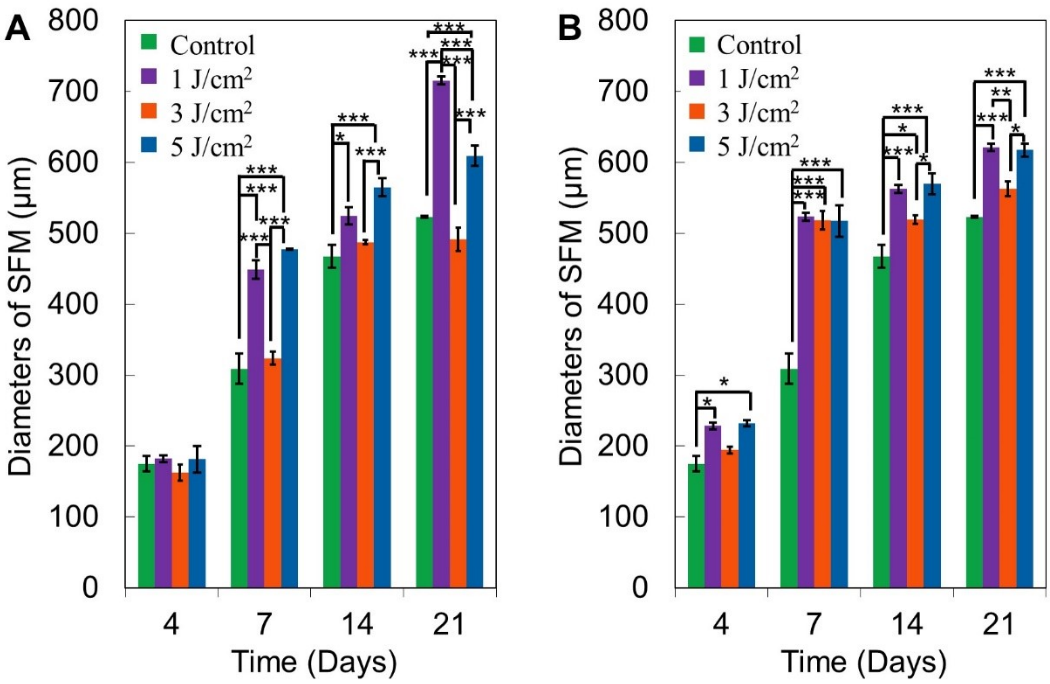

Figure 6.4: Diameter measurements of SFMs for (A) PBM applications at 655 nm of wavelength, (B) PBM applications at 808 nm of wavelength on days 4, 7, 14, and 21 (Energy densities: 1, 3, and 5 J/cm^2). Each column represented the average of the diameters ± SD. Statistically significant differences were determined by two-way ANOVA followed by Tukey's post hoc test (* for $p< 0.05$, ** for $p< 0.01$, *** for $p< 0.001$).

The diameters of SFM in control, 1, 3, and 5 J/cm^2 groups of the 655 nm of wavelength were measured as 523±1, 715±6 (p***<0.001), 491±17, and 609±14 (p***<0.001) μm on the 21st day, respectively. The diameters of SFM in control, 1, 3, and 5 J/cm^2 groups of the 808 nm of wavelength were 523±1, 621±5 (p***<0.001), 563±10, and 617±9 (p***<0.001) μm, respectively. The most effective energy densities of both wavelengths on the enlargement of SFM diameters were observed as 1 and 5 J/cm^2 when compared to the control group.

6.3.2 Cell Viability Analysis of SFMs

Cell viability in SFMs was analyzed on 4th, 7th, 14th, and 21st days to evaluate the effects of PBM. Obtained microscopic images were presented in Figure 6.5 and Figure 6.6 for the PBM applications at 655 nm and 808 nm of wavelengths, respectively.

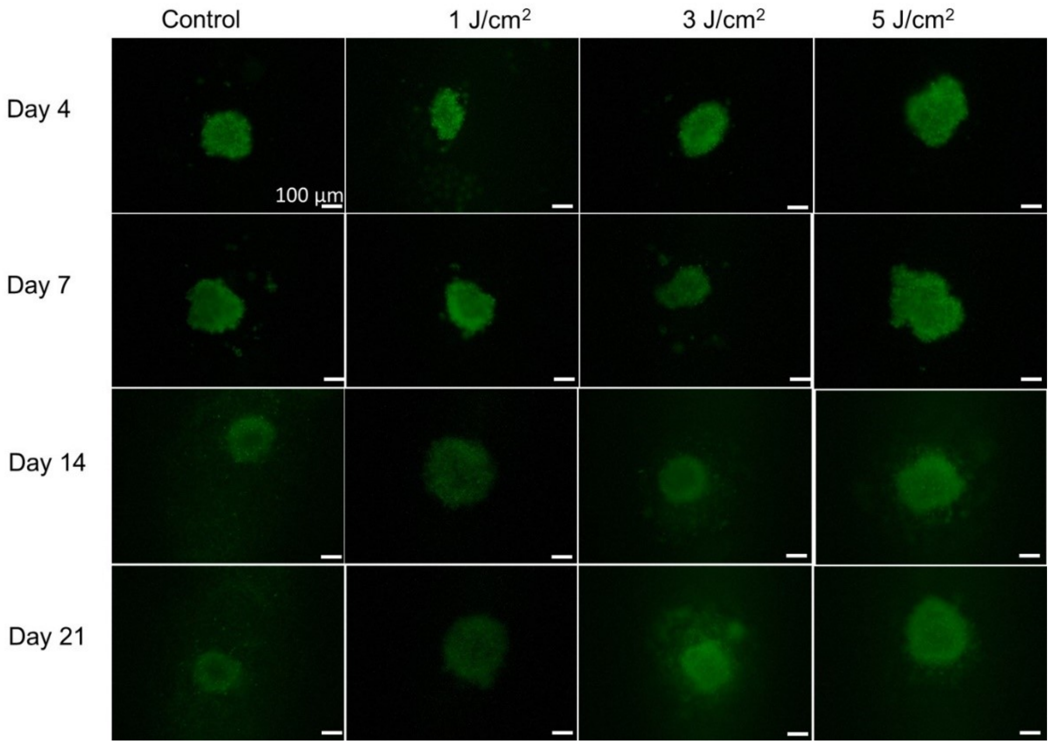

Figure 6.5: Cell viability images of SFMs treated with PBM applications at 655-nm of wavelength on days 4, 7, 14, and 21 (Energy densities: 1, 3, and 5 J/cm^2). Scale bar 100 µm.

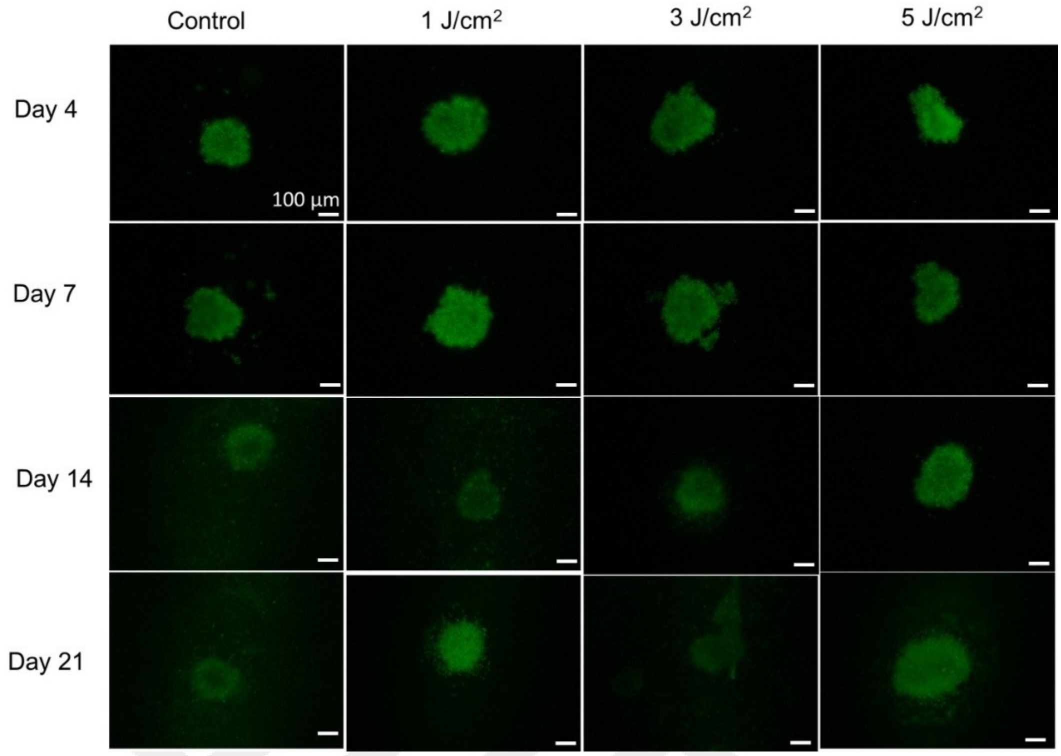

Figure 6.6: Cell viability images of SFMs treated with PBM applications at 808-nm of wavelength on days 4, 7, 14, and 21 (Energy densities: 1, 3, and 5 J/cm^2). Scale bar 100 µm.

Cell viability analyses were performed according to green color intensity as presented in Figure 6.7. Every SFM group had viable cells in all time points. The green color intensity of the control group was considered as 100 %. Then, the intensities of the other SFMs were calculated with respect to control.

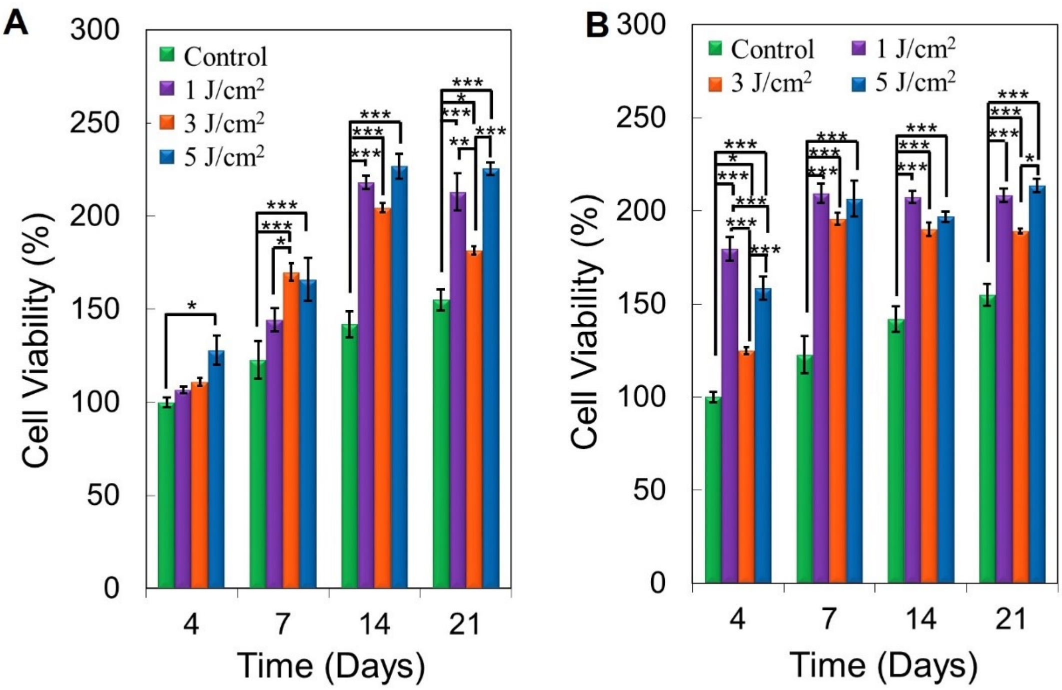

Figure 6.7: Percentage Cell Viability depending on the green intensity measurements in SFMs for (A) PBM applications at 655 nm of wavelength, (B) PBM applications at 808 nm of wavelength on days 4, 7, 14, and 21 (Energy densities: 1, 3, and 5 J/cm^2). Each column represented the average of the cell viability percentages ± SD. Statistically significant differences were determined by two-way ANOVA followed by Tukey's post hoc test (* for p< 0.05, ** for p< 0.01, *** for p< 0.001).

On the 4th day, the viability values of the control, 1, 3, and 5 J/cm^2 groups of the PBM applications at 655 nm of wavelength were measured as 100±3, 107±2, 111±2, and 128±8 (p*<0.05) %, respectively. On the 21st day, they were 155±6, 213±10 (p***<0.001), 181±2 (p*<0.05), and 225±3 % (p***<0.001). The cell viability in all SFMs increased day by day and the highest increase was obtained in 5 J/cm^2 group at this wavelength. In addition, there was no significant difference between the 1 and 5 J/cm^2 groups, even on the 21st day. When the green colour intensity was measured in SFMs treated with 808 nm of wavelength on the 4th day, the values of control, 1, 3, and 5 J/cm^2 groups were calculated as 100±3, 180±6 (p***<0.001), 125±2 (p*<0.05), and 159±6 % (p***<0.001), respectively. Additionally, on the 21st day the values were 155±6, 208±4 (p***<0.001), 189±1 (p***<0.001), and 214±4 (p***<0.001) %, respectively. The highest increase in cell viability was initially observed in 1 J/cm^2 group at 808-nm of wavelength. Then the value of 5 J/cm^2 group approached to the value of 1 J/cm^2 group on 21st day.

6.3.3 Intracellular ROS Production

The amount of intracellular ROS produced in 3D SFMs after light irradiations were presented in Figure 6.8. As it was shown, 1 J/cm^2 energy density produced the highest amount of intracellular ROS than the other experimental groups did. The intracellular ROS production in 1 J/cm^2 group at 655- nm of wavelength was measured as 226±13 % (p***<0.001). 5 J/cm^2 energy density was also quite successful, but not as much as 1 J/cm^2 group. However, PBM applied with 808 nm of wavelength showed that the efficiency of 1 and 5 J/cm^2 energy densities exhibited a similar outcome in terms of intracellular ROS production and the amount in SFMs were measured as 167±14 % (p***<0.001).

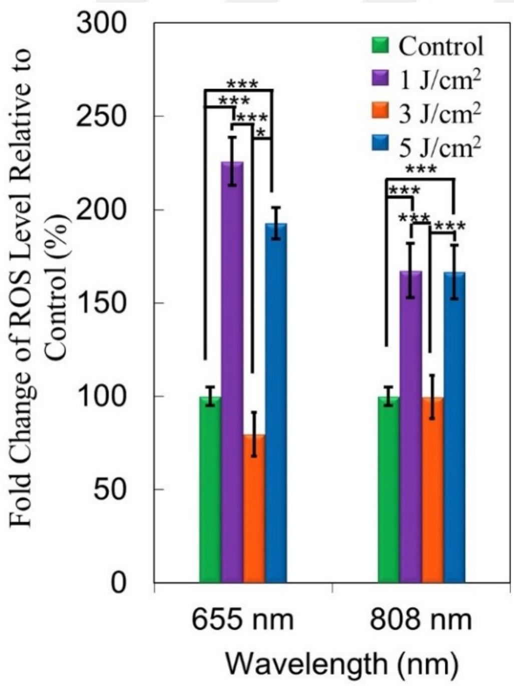

Figure 6.8: Intracellular ROS Production for PBM applications at 655 and 808 nm of wavelength (Energy densities: 1, 3, and 5 J/cm^2). Each column represented the average of the normalized ROS levels with respect to control ± SD. Statistically significant differences were determined by one-way ANOVA followed by Tukey's post hoc test (* for p< 0.05, *** for p< 0.001).

6.3.4 ATP Production

The level of ATP productions in the control, 1, 3, and 5 J/cm^2 groups at 655 nm of wavelength were measured as 100±8, 95±6, 67±8 (p*<0.05), and 129±10 (p*<0.05) % in 3D SFMs, respectively. For 808 nm of wavelength, the percentages for each group were determined as 100±8 for control, 106±6 for 1 J/cm^2, 127±17 ($p^*<0.05$) for 3 J/cm^2, and 144±7 % ($p^{**}<0.01$) for 5 J/cm^2. The highest ATP productions were obtained in the 5 J/cm^2 groups for both wavelengths (Figure 6.9).

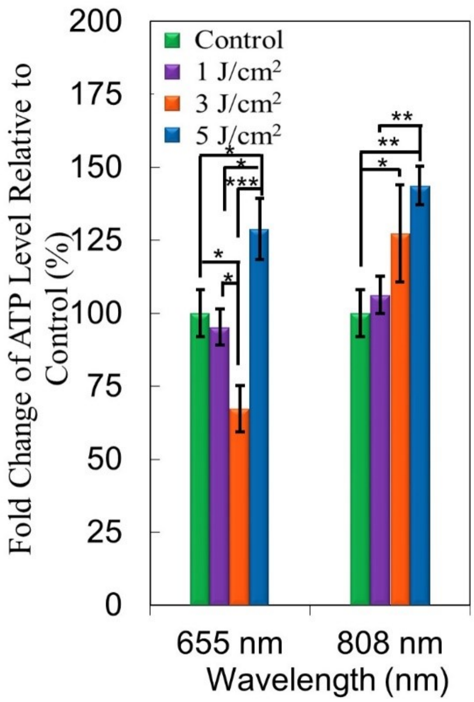

Figure 6.9: Adenosine Tri-Phosphate (ATP) Production for PBM applications at 655 and 808 nm of wavelength (Energy densities: 1, 3, and 5 J/cm^2). Each column represented the average of the normalized ATP levels with respect to control ± SD. Statistically significant differences were determined by one-way ANOVA followed by Tukey's post hoc test (* for p< 0.05, ** for p< 0.01, *** for p< 0.001).

6.3.5 NO Release

The outcome of the analysis for the determination of NO release via Griess reagent was shown in Figure 6.10. The highest amount of NO release was observed in 3 J/cm^2 group of 655 nm of wavelengths and 5 J/cm^2 group of 808 nm of wavelength. They were significantly different compared to the control group. The other experimental groups of each wavelength exhibited similar results as the control group.

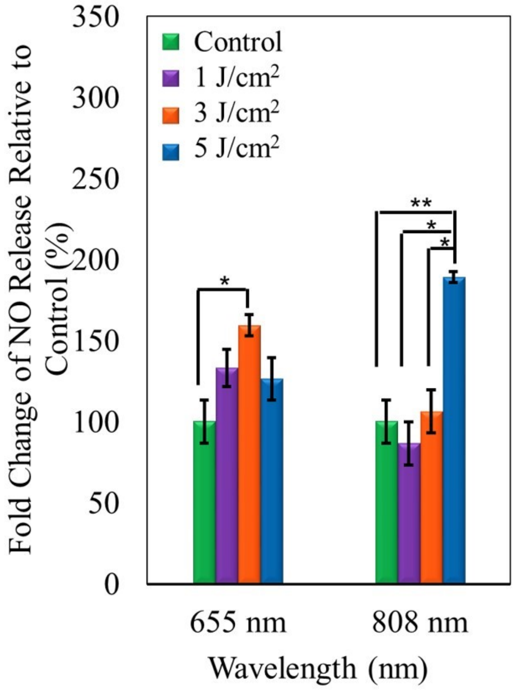

Figure 6.10: Nitric Oxide (NO) Release for PBM applications at 655 and 808 nm of wavelength (Energy densities: 1, 3, and 5 J/cm^2). Each column represented the average of the normalized NO levels with respect to control ± SD. Statistically significant differences were determined by one-way ANOVA followed by Tukey's post hoc test (* for $p< 0.05$, ** for $p< 0.01$).

6.3.6 DNA Quantification

The analysis of DNA Quantification was performed on days 4th, 7th, 14th, and 21st as shown in Figure 6.11. For PBM applications at 655 nm of wavelength, 5 J/cm^2 energy density enhanced DNA content day by day most remarkably. It was measured as 665.19±0.8 ng/ml at the end of the last time point and was significantly different compared to the control and other experimental groups (p***<0,001). For PBM applications at 808 nm of wavelength, the measured DNA amounts of all groups increased day by day, too. The DNA content in control, 1, 3, and 5 J/cm^2 groups were measured as 533.52±8.43, 603.91±14.49, 618.20±25.37, and 603.72±9.99 ng/ml on day 21, respectively. All energy densities at this wavelength resulted in significantly different outcomes compared to control group, (p***<0,001). However, they were not significantly different from each other.

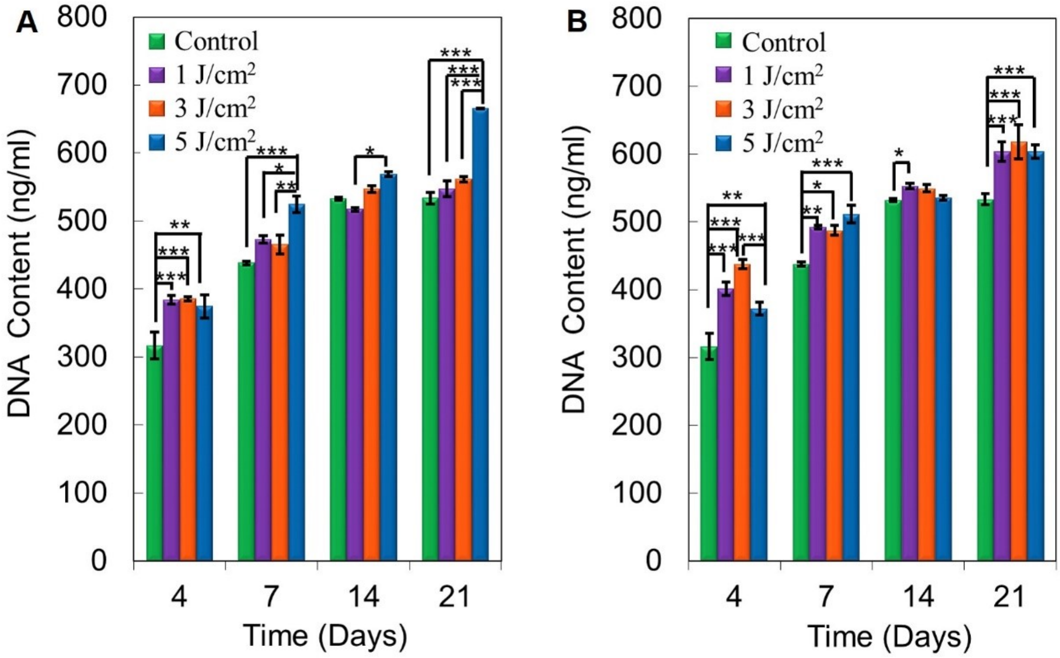

Figure 6.11: DNA Content Analysis for PBM applications at (A) 655 nm of wavelength, (B) 808 nm of wavelength (Energy densities: 1, 3, and 5 J/cm^2). Each column represented the average of the DNA amount ± SD. Statistically significant differences were determined by two-way ANOVA followed by Tukey's post hoc test (* for p< 0.05, ** for p< 0.01, *** for p< 0.001).

6.3.7 ALPase Activity

ALPase activity was measured on days 4th, 7th, 14th , and 21st for PBM applications at 655 nm and 808 nm of wavelengths and their results were presented in Figure 6.12. The ALPase measurements were normalized with the DNA content. All energy densities at both wavelengths enhanced the ALPase activity, especially on day 14. The ALPase levels of the control, 1, 3, and 5 J/cm^2 groups of the 655 nm of wavelengths were determined as 3497±39, 3763±19 (p*<0,05), 3572±51, and 3432±13 IU/ng DNA, respectively. The ALPase levels of the control, 1, 3, and 5 J/cm^2 groups of the 808 nm of wavelengths were determined as 3497±39, 3512±9, 3535±58, and 3816±25 (p**<0,01) IU/ng DNA, respectively. 1 J/cm^2 energy density of 655 nm of wavelength and 5 J/cm^2 energy density of 808 nm of wavelength induced the highest ALPase level. The ALPase levels of all experimental groups decreased on day 21.

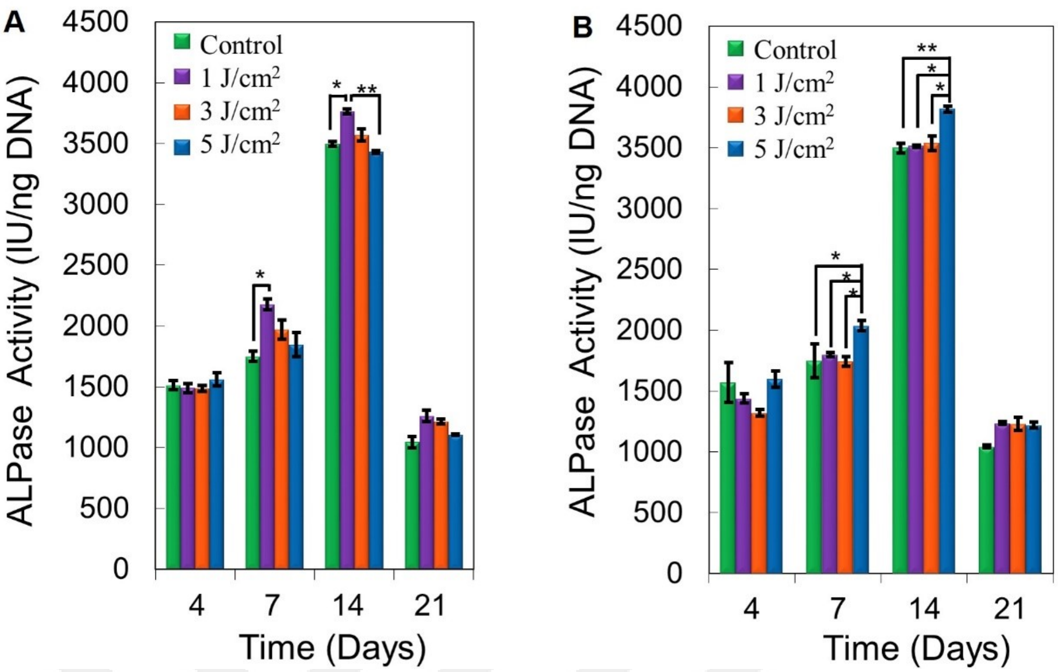

Figure 6.12: ALP activity measurements for PBM applications at (A) 655 nm of wavelength, (B) 808 nm of wavelength (Energy densities: 1, 3, and 5 J/cm^2). Each column represented the average of the ALPase amount ± SD. Statistically significant differences were determined by two-way ANOVA followed by Tukey's post hoc test (* for $p< 0.05$, ** for $p< 0.01$).

6.3.8 Mineralization of SFMs

The calcium amount which was normalized by the DNA content was shown in Figure 6.13 for 655 nm and 808 nm of wavelengths. The measured calcium amounts of the control, 1, 3, and 5 J/cm^2 groups of 655 nm of wavelength were 2946±96, 5168±232 (p***<0.001), 4655±188 (p***<0.001), and 4224±229 (p***<0.001) ng/ng DNA on day 21, respectively. The values of the control, 1, 3, and 5 J/cm^2 groups of 808 nm of wavelength were 2946±96, 3662±106 (p*<0.05), 4114±354 (p***<0.001), and 4700±12 (p***<0.001) ng/ng DNA on day 21, respectively. It was observed that 1 J/cm^2 energy density at 655 nm of wavelength and 5 J/cm^2 energy density at 808 nm of wavelength provided more calcium deposition than control and 3 J/cm^2 groups did on 21st day.

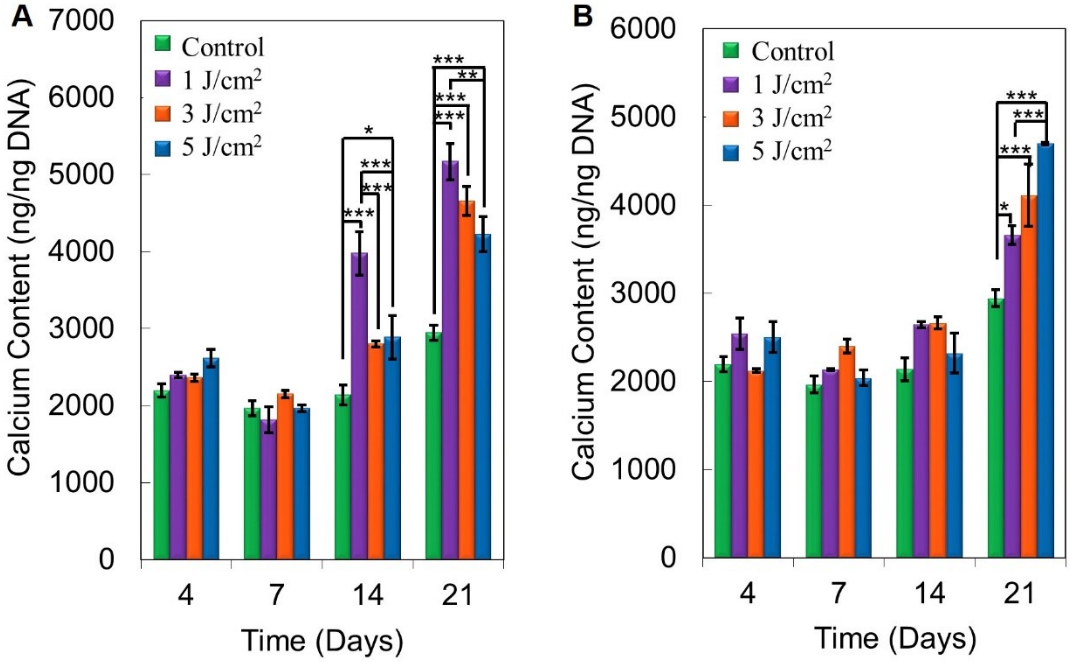

Figure 6.13: Analysis of Mineralization for PBM applications at (A) 655 nm of wavelength, (B) 808 nm of wavelength (Energy densities: 1, 3, and 5 J/cm^2). Each column represented the average of the calcium content ± SD. Statistically significant differences were determined by two-way ANOVA followed by Tukey's post hoc test (* for $p < 0.05$, ** for $p < 0.01$, *** for $p < 0.001$).

6.3.9 Relative Gene Expression Profiles of SFMs

The fold change in the mRNA level of ALP, Collagen (Col) and Osteopontin (OPN) genes in the control, 1, 3, and 5 J/cm^2 groups were represented in Figure 6.14 for 655 nm of wavelength and Figure 6.15 for 808 nm of wavelength. All energy densities at both wavelengths expressed a significant amount of ALP on the 4th, 7th, and 14th days compared to the control. The fold changes in the relative ALP gene expression of the control, 1, 3, and 5 J/cm^2 groups treated with 655 nm of wavelength were 1.00±0.00, 175.18±25.49 (p***<0.001), 68.52±24.00, and 175.29±38.81 (p***<0.001) on day 7, respectively. Additionally, on the 14th day, the gene expression levels of the same energy densities with same wavelength became 1.00±0.00, 212.02±25.36 (p***<0.001), 51.50±4.88, and 35.86±0.91, respectively. The highest ALP gene expression was observed with the PBM application at 655 nm of wavelength and 1 J/cm^2 energy density was the most successful application to induce it on day 14. The highest fold change of the relative Col gene expression was obtained in PBM applications applied with 1 J/cm^2 energy density of 655-nm of wavelength. The changes for 1 J/cm^2 energy density on days 4th, 7th, 14th, and 21st were calculated as 39.37±3.68 (p***<0.001), 47.50±2.24 (p***<0.001), 62.71±9.04 (p***<0.001), and 53.72±2.82 (p***<0.001), respectively. The fold changes of the relative OPN gene expression of the control, 1, 3, and 5 J/cm^2 groups treated with 655 nm of wavelength were 1.00±0.00, 53.72±2.82 (p***<0.001), 0.64±0.07, and 0.45±0.05 on day 21, respectively. The highest expression level was obtained with 1 J/cm^2 energy density among all experimental groups, especially on day 21.

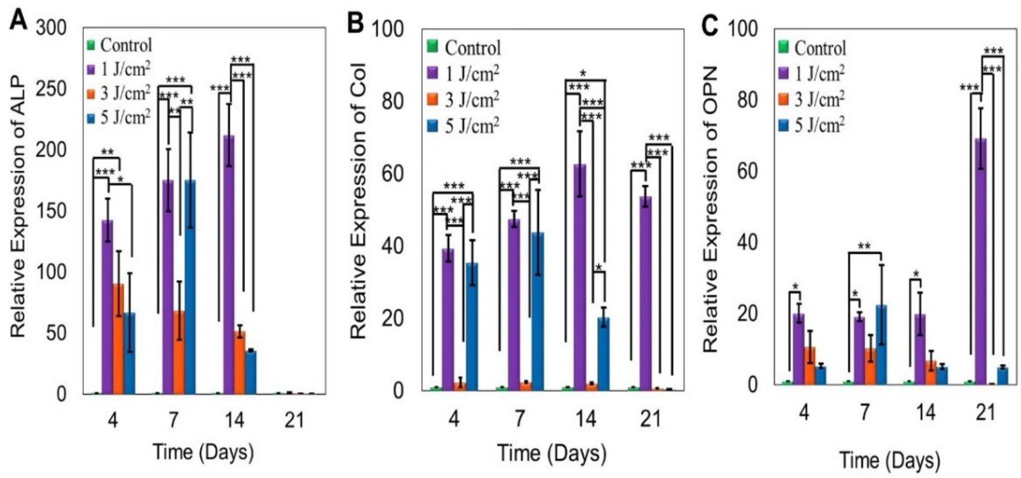

Figure 6.14: Relative gene expression analysis of osteogenic markers for PBM applications at 655 nm of wavelength (A) ALP, (B) Collagen, (C) Osteocalcin (Energy densities: 1, 3, and 5 J/cm^2). Each column represented the average of the relative gene expression normalized with the data of the control group ± SD. Statistically significant differences were determined by two-way ANOVA followed by Tukey's post hoc test (* for $p< 0.05$, ** for $p< 0.01$, *** for p< 0.001).

When the effect of PBM applications at 808 nm of wavelength was evaluated, the relative gene expression levels of ALP, Col and OPN which were shown in Figure 6.15 were obtained. ALP expression levels in control, 1, 3, and 5 J/cm^2 groups were found as 1.00±0.00, 60.31±14.58 (p**<0.01), 44.77±15.52 (p***<0.001), and 80.86±19.73 (p***<0.001) on the 7th day, while they were 1.00±0.00, 0.02±0.01, 0.17±0.02, and 144.39±2.61 (p***<0.001) on the 14th day, respectively. The 5 J/cm^2 group expressed higher ALP gene than the other groups on 4th, 7th and 14th days. Especially, on the 14th day, 5 J/cm^2 group showed the highest ALP gene expression rate, again. Collagen was specifically expressed in the 5 J/cm^2 energy density of 808 nm at each time point. Col mRNA fold changes of 5 J/cm^2 were calculated as 5.02± 2.71 (p***<0.001), 9.08±1.15 (p***<0.001), 2.45±0,71 (p***<0.001), and 1.79±0.23

(p***<0.001) on day 4, 7, 14 and 21, respectively. 5 J/cm^2 group of 808 nm expressed OPN gene with the highest rate among all experimental groups. The relative gene expression levels of OPN in the control, 1, 3, and 5 J/cm^2 at 808 nm of wavelength were observed as 1.00±0.00, 0.43±0.06, 0.05±0.00, and 118.68±12.56 (p***<0.001) on day 21, respectively.

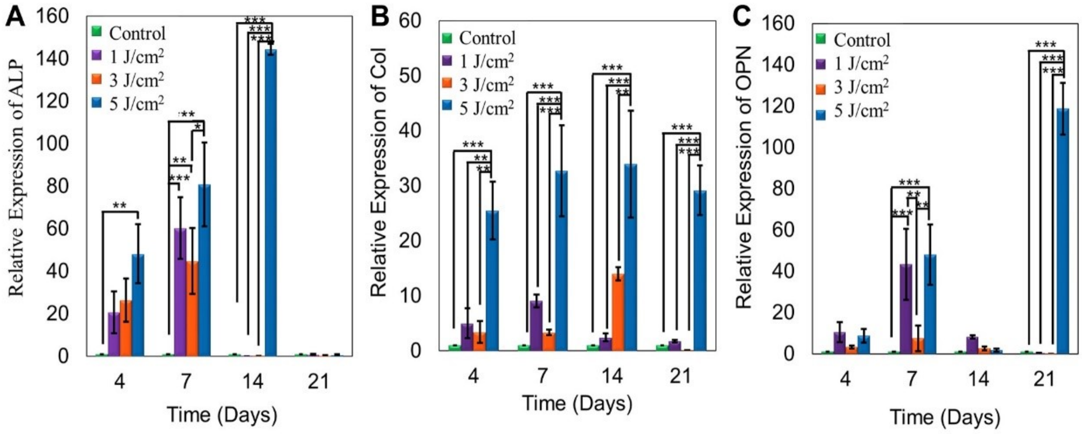

Figure 6.15: Relative gene expression analysis of osteogenic markers for PBM applications at 808 nm of wavelength (A) ALP, (B) Collagen, (C) Osteocalcin (Energy densities: 1, 3, and 5 J/cm^2). Each column represented the average of the relative gene expression normalized with the data of the control group ± SD. Statistically significant differences were determined by two-way ANOVA followed by Tukey's post hoc test (* for $p< 0.05$, ** for $p< 0.01$, *** for $p< 0.001$).

6.3.10 Temperature Changes during Light Irradiation

In order to observe the photothermal effect of light applications on 3D SFMs, especially because of the near-infrared light, the temperature values of SFMs were measured with a thermal camera (Testo 882, Melrose, USA) before, and at the end of the light applications. Δt was calculated by subtracting the first temperature measurement from the last temperature measurement ($\Delta t = t_{final} - t_{initial}$). The results were given in Table 6.3. Δt values increased, as the energy densities increased for each wavelength. The highest temperature change (0.7 ºC) was observed in 5 J/cm^2 energy density group at 808 nm of wavelength as expected. Nevertheless, these changes were quite low not capable to induce any phototermal effect on SFMs.

Table 6.3: Thermal Measurements of 3D SFMs Application.

Temperature Measurements				
Wavelengths	Energy Density (J/cm^2)	Initial Temperature (˚C)	Final Temperature (˚C)	Δt (˚C)
655 nm	1	24.9	25.1	0.2
	3	24.6	24.9	0.3
	5	24.9	25.4	0.5
808 nm	1	25.5	25.7	0.2
	3	25	25.3	0.3
	5	25.2	25.9	0.7

6.4 Discussions

It was previously reported that PBM can be an alternative strategy to support the regeneration of bone tissue [239, 242]. However, the tricky point is that the light parameters of PBM should be appropriately determined for *in vivo* systems to get more reliable approaches for the implementation of this therapy into the clinics. Mostly, the regeneration capacity of the tissue depends on those parameters [242]. It is well known that the cellular responses of 3D systems have similar tendency to the responses of *in vivo* systems [295]. Therefore, the determination of the cellular responses of 3D SFMs to PBM is important to clarify the molecular mechanism induced by PBM for bone tissue regeneration. Thus, the effects of 1, 3, and 5 J/cm^2 energy densities at 655 nm and 808 nm of wavelengths were investigated on 3D SFMs fabricated by the co-culture of hBMSC and HUVEC. After all light treatments at these energy densities and wavelengths, it has observed that all SFMs were successfully formed from day 1, including the control group. In previous studies, it has been shown that the diameters of SFMs correlate to the proliferation capabilities of the cells in SFMs [64, 296, 306]. The highest SFM diameters were achieved at 1 and 5 J/cm^2 energy densities of 655 nm or wavelength and 5 J/cm^2 energy density of 808 nm of wavelength. 3 J/cm^2 energy density of each wavelength was not as successful as the other energy densities and it exhibited similar outcome as observed in the control group. The SFMs of 1 and 5 J/cm^2 energy densities were more viable than control groups. Similarly, 1 and 5 J/cm^2 energy densities at 655 nm and 808 nm of wavelengths significantly increased the cell viability of fibroblasts and keratinocytes in previous studies [269, 311]. It has been already indicated that PBM applications especially at red and near-infrared wavelengths enhanced the proliferation and the metabolic activity of different cell types that conforms our results, too [281, 293, 312].

PBM is defined as a non-thermal therapy that stimulates various cellular mechanisms related to the production of intracellular ROS and ATP, NO release, etc. Optimal dosimetry at specific wavelengths gives better results [130, 242, 284]. Depending on the nature of biphasic dose response of cells/tissues, wrong intensities may result in thermal side effects [284]. Thus, temperature changes during applications should be monitored and possible thermal reactions should be prevented, especially with light irradiations at near-infrared wavelengths. In this study, temperature changes were monitored during any light irradiation. It was observed that increase in exposure duration causes an increase in temperature of the SFMs. As expected, the highest temperature increase was obtained with light application of 5 J/cm^2 at 808-nm of wavelength. Nevertheless, it was only 0.7ºC change and quite negligible. Therefore, it can safely be expressed that PBM applications in this study did not show any thermal effect on SFMs and the mechanism to induce osteogenesis mainly depended on the intracellular ROS, ATP production, and NO release [141, 285]. Thus, the roles of those molecules in SFMs were evaluated in each group and it was found out that especially 1 and 5 J/cm^2 energy densities created a statistically significant increase in the intracellular ROS production. Previous studies which also used similar energy densities at 677 nm and 830 nm of wavelength provided the same outcome in terms of ROS production [313, 314]. 3D SFMs mimic the *in vivo* system in terms of sensitivity to the outer influences to trigger the signal molecules [315], so the produced intracellular ROS level may have key role in the action mechanism of PBM during the osteogenesis.

Beside the production of intracellular ROS, a significant increase in ATP synthesis was observed, too. Especially 5 J/cm^2 energy density for both wavelengths triggered the most remarkable ATP production in SFMs. As stated in the literature, the production of ATP and ROS molecules is involved in the basic mechanism of PBM [254, 307, 310]. It has also been determined that 1 J/cm^2 energy density at 670 nm of wavelength was effective in the ATP production mechanism in previous study [316]. Abdalla et al. reported that 5 J/cm^2 energy density at 632.8 nm and 635 nm of wavelength increased ATP production by a rate of 70% [317]. Thus, it can be said that the results of ATP analysis in this study were consistent with the previous studies. NO release is another important change during PBM applications [254]. Moriyama et al. observed in their study that 655 nm of wavelength promoted NO release [318]. Although 1 and 5 J/cm^2 energy densities at 655 nm of wavelength triggered approximately 30% more NO release than the control, there were no significant differences between them. Interestingly, 3 J/cm^2 energy density at 655 nm of wavelength induced a significant amount of NO release which was not observed in other analysis at this energy density. However, in the light applications at 808-nm of wavelength, 5 J/cm^2 energy density stimulated more NO release just as it did in ROS and ATP production. Clearly, it can be said for this study that mainly similar energy densities in different analysis became responsible for stimulating the ROS and ATP production or NO release in significant amounts in terms of cell viability and mechanistic analysis. Each result obtained from different analysis confirms the others which make easy to determine the optimum energy density of PBM at red and near-infrared wavelengths on SFMs.

DNA contents in SFMs of all groups were evaluated and an increase was observed day by day. In particular, the energy density of 5 J/cm^2 at 655 nm of wavelength was the group with the highest number of DNA until the 21st day. For 808 nm of wavelength, all energy densities showed higher DNA content than control group. Similar to cell viability results, DNA amounts in all experimental groups were higher than in the control group.

ALP is important marker that is especially expressed in early osteogenesis. In the literature, it was stated that ALP reaches its highest level until the 14th day of osteogenesis and a quantitative decrease occurs on 21st day [242]. In this study, all groups expressed a significant amount of ALP on day 14. Similar to the previous analysis, 1 J/cm^2 at 655 nm of wavelength and 5 J/cm^2 of 808 nm of wavelength were the applications that induced the highest ALP expression. The expression rate of ALP at an early time point of osteogenesis showed that those groups had higher osteogenic differentiation capacity than other experimental groups.

Calcium ions, which are in the content of the bone tissue, play an important role in the cell proliferation [287] and the formation of a new bone tissue, which normally begin to be stored after the 15th day [242]. Studies in the literature clearly stated that PBM is effective in bone healing, cell proliferation, differentiation, collagen deposition, and calcium storage [242, 287, 291]. Calcium deposition promotes the maturation of osteoblast cells, so bone regeneration is accomplished [319]. While the 1 J/cm^2 group at the 655 nm of wavelength had the highest calcium content, the 5 J/cm^2 group at the 808 nm of wavelength had the highest calcium content. Again, similar intensities of those two different wavelengths properly deposited the calcium during osteogenesis of SFMs in this study.

To confirm the analysis of ALP enzyme activity analysis and osteogenesis induced by PBM, the relative gene expression levels of ALP, Collagen and osteopontin genes were examined by qRT-PCR analysis. The highest mRNA level of ALP was observed in 1 J/cm^2 group for the 655 nm of wavelength. Additionally, 5 J/cm^2 group for 808 nm of wavelength was also expressed the highest mRNA level of ALP on day 14. Both ALPase activity and the relative mRNA ALP level analysis confirmed each other. At the last time point of osteogenesis, all mRNA levels of ALP decreased on day 21. These outcomes were parallel to natural behaviours of ALP expression during osteogenesis [242, 305]. Collagen, one of the most important components of bone, contributes to the bone shape by providing mechanical support in the tissue [320]. Collagen creates the specific microenvironment for bone cells and increases the capacity of the cells to multiply, migrate, and differentiate [321]. In the PBM applications, 1 J/cm^2 energy density at 655 nm of wavelength expressed the highest collagen level in all time intervals. On the other hand, 5 J/cm^2 energy density at 808 nm of wavelength exhibited the highest collagen expression in all time intervals, too.

Osteopontin is a special protein that regulates the cells, takes part in mineralization, and has a very important role in osteogenesis [322]. It contributes to the formation of bone shape and the supports osteogenesis by holding the hydroxy hepatitis crystals in the bone structure. In the late stages of osteogenesis, it is expressed at the highest level and initiates mineralization [305, 322]. The osteopontin expression level induced by 1 J/cm^2 energy density at 655 nm of wavelength and 5 J/cm^2 energy density at 808 nm of wavelength were higher than the control group on the 4th, 7th, and 14th days of PBM application. In previous studies, it has been already indicated that PBM at 660 nm and 808 nm wavelengths may induce osteopontin expression [323]. The calcium content analysis showed that 1 J/cm^2 energy density at 655 nm of wavelength started the mineralization process and the highest calcium deposition rate was obtained in this group at 655 nm of wavelength was the highest deposition rate which correlated with the osteopontin expression level at 655 nm of wavelength. Moreover, 5 J/cm^2 energy density at 808 nm of wavelength expressed the osteopontin gene higher than the other groups at this wavelength on day 21. Again, the results of calcium deposition analysis supported the osteopontin gene expression rate obtained by qRT-PCR at the same energy density at 808 nm of wavelength.

As a result, energy densities of 1 J/cm^2 at 655 nm of wavelength and 5 J/cm^2 at 808 nm of wavelengths provided the most effective PBM not only for the production of intracellular ROS, ATP, and NO release but also for the ALPase activity, calcium deposition, and the gene expression levels of ALP, osteopontin, and collagen. Besides, all of these results were confirmed by the increase in cell viability and SFMs diameter. Thus, it can be concluded that 1 J/cm^2 energy density at 655 nm of wavelength and 5 J/cm^2 energy density at 808 nm of wavelength were the most effective energy densities to induce osteogenesis in microtissues and they may have the capacity to induce the similar mechanisms in *vivo* systems.

6.5 Conclusions

In conclusion, it was clearly stated that PBM enhanced osteogenesis in the 3D cell culture model. Intracellular ROS, ATP, and NO molecules play key roles in the proliferation, viability, and osteogenic differentiation of SFMs as expected. The changes in their levels after PBM applications were quite remarkable and depended on light parameters. Thus, this study proved the importance of light dosimetry in all biological processes once again and the physiological processes obtained with different parameters were consistent with the changes in the level of intracellular ROS, ATP, and NO molecules. Finally, it can be said that 1 J/cm^2 energy density at 655 nm of wavelength and 5 J/cm^2 energy density at 808 nm of wavelength were the most successful light parameters for the osteogenic differentiation in SFMs and they can be promising parameters for bone tissue engineering strategies.

Chapter 7

7. The Combination of Integrin Binding Peptide and Photobiomodulation Therapy to Improve Regeneration of Bone Like Microtissues

7.1 Introduction

Bone tissue engineering (BTE) targets to induce osteogenic differentiation by using biomaterials, stem cells, and different strategies including regenerative properties. Successful material fabrication for BTE is required an understanding of the composition and complex structure of native bone tissue, as well as an appropriate selection of biomimetic natural materials [324]. One of the bone mimetic peptides is tripeptide arginine-glycine-aspartic acid (RGD) which is found in structures of extracellular matrix (ECM) proteins such as fibronectin, laminin, collagen, and osteopontin [64, 325]. RGD is located on bone matrix proteins as integrin-binding site [102, 186]. Moreover, the RGD sequence of the adhesive proteins is distinguished by at least one member of structurally related receptors such as integrins [102, 325]. The structure of RGD in individual proteins may be a target for improvements of bone regeneration [102]. Integrin and RGD association triggers cell proliferation, adhesion, migration, osteogenic differentiation, and mineralization [325, 326]. Researches about RGD sequence gain a trend between researchers because of closely interaction of RGD in cell membrane. The combination of RGD peptide and different therapeutic strategy can improve quality of regeneration compared with only peptide therapy in BTE [327-

329]. The association of peptide therapy and phototherapy supported metabolic activity of cells [330]. RGD and light therapy at near infrared of wavelength were successfully combined to control tumor microenvironment [331]. Nanoparticles with RGD peptide and photothermal therapy produced oxygen species [332]. Moreover, peptide and phototherapy combination promoted therapeutic efficacy [333, 334]. Thus, it is possible to improve effectiveness of peptide therapy for osteogenic differentiation.

Light therapy is one of the therapeutic approach which is useful strategy to promote osteogenic differentiation [135]. The red and near-infrared spectrums of wavelength which are used in Low Level Laser Therapy (LLLT) or Photobiomodulation (PBM) directly induce chromophore molecule which is cytochrome c oxidase (CCO) in mitochondria of cells [134, 135]. Photon gradient is occurred in mitochondria by CCO which triggers promotion of ROS, ATP and NO releasing via the induction of mechanism of PBM. The signal molecules promote DNA duplication, adhesion, migration and differentiation [335-338]. Moreover, the signals support osteogenic gene and protein expressions [337, 339]. Particularly, from 1 J/cm^2 to 20 J/cm^2 energy densities at the 600-1200 nm ranges of wavelength, can be absorbed by mitochondria, trigger stem cells for proliferation and differentiation [340, 341]. However, traditional BTE techniques may not be sufficient to analyze efficacy of light therapy because of their non-sensitive features in terms of limited tissue depth [342, 343]. However, Scaffold Free Microtissues (SFMs) present more natural 3 Dimensional (3D) microenvironment of cells to analyze penetration and efficacy of wavelength [63, 64]. In addition, 3D SFMs present more complex shape and condition to evaluate stem cell behaviours [344, 345]. Moreover, 3D SFMs support closely cell to cell interaction [63, 345, 346] so stem cells may sense and constitute their natural cellular relations [347, 348]. The coculture of Human Bone Marrow Stem Cells (hBMSC) and Human Umbilical Vein Endothelial Cells (HUVEC) may form bone like structure by supporting the proliferation of each other during the bone healing and bone formation [349, 350].

The study aimed to investigate the effects of RGD peptide and 1 J/m^2 energy density at 655 nm of wavelength and RGD peptide and 5 J/cm^2 energy density at 808 nm of wavelength on hBMSC:HUVEC SFMs coculture during bone regeneration (as shown in Figure 7.1).

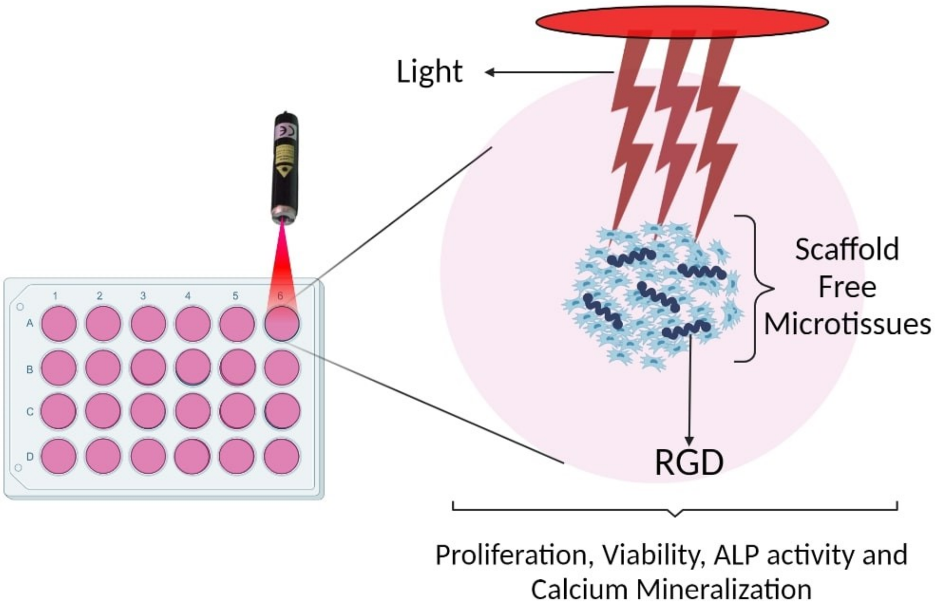

Figure 7.1: The combination of RGD and PBM therapy on bone like SFMs. (Created with BioRender.com)

7.2 Materials and Methods

7.2.1 Materials

All chemicals of peptide synthesis were taken from AAPPTEC (Louisville, KY, USA). hBMSC (300665-102) were purchased from, CLS Company, Germany. HUVECs were supported by the Department of Bioengineering, Ege University. All cell culture products (DMEM:F12 with L-Glutamine, Penicillin Streptomycin, 2′,7′-dichlorofluorescein diacetate (DCFH-DA), amphotericin, gentamycin, FBS, Β-glycerophosphate, dexamethasone, and ascorbic acid) were taken from Sigma-Aldrich, MA, USA. The others were specifically descripted. ATP assay which is CellTiter-Glo (G7570) was taken from Promega, US. NO releasing was measured by Griess reagent (K544-200, Biotium, CA, USA). Live and Dead Staining was performed by (Cellstain double staining kit, CS01-10, Dojindo Molecular Technologies, Japan). Alkaline Phosphatase Activity was tested by ALP Activity Kit (ab83369, Abcam, USA). Calcium amount was analyzed by DICA 500, Quanthichrom, Wilhelm-Mauser, Germany. Total RNA Isolation was performed by RNAqueous™, Thermo, USA. RNA was doubled by MuLV First Strand cDNA Synthesis Kit (Biomatik, Ontario, Canada).

7.2.2 Synthesis of Soluble RGD Peptide

RGD peptide, which consists of Gly-Arg-Gly-Asp-Ser aminoacids, was synthesized on having 9-fluorenylmethoxycarbonyl (Fmoc) 4-Methylbenzhydrylamine (MBHA) resin with 0.67 mmol/g loading capacity within automated peptide synthesizer (AAPPTEC Focus Xi, Louisville, KY, USA) [351]. According to loading capacity of resin, 2 equivalents (2 eq) aminoacid, O-Benzotriazole-N,N,N',N'-tetramethyluroniumhexafluoro-phosphate (HBTU; 2 eq), hydroxybenzotriazole (HOBt; 2 eq) and N,N-diisopropylethylamine (DIEA; 4 eq) HBTU in N,N-Dimethylformamide (DMF) were added into resin for 3 hours. After all sequences were completed, respectively, the RGD peptide was cleavaged from resin by using trifluoroacetic acid (TFA): triisopropylsilane (TIPS): H_2O solution (95:2.5:2.5) into cold ether. Then, the peptide was prepared to mix with serum free osteogenic media.

7.2.3 Cell Culture and SFMs Fabrication in Osteogenic Media Including RGD Peptide

hBMSCs and HUVECs were separately cultured with Dulbecco's Modified Eagle Media-F12 (DMEM- F12) with L-glutamin contained 10% FBS and 1% Penicillin-Streptomycin. The medias of cell culture were refreshed every 2 days up to 21st day. Cells were taken under incubator which includes 5% CO_2 and 37^{o}C temperature. Agarose mold was constructed by commercial 3D Petri Dish Plates as described in previous studies [63, 193]. Then the mold was incubated with osteogenic media containing 100 nM dexamethasone, 50 µg/mL ascorbic acid, and 10 mM ß-glycerophosphate and antibiotics (50 µg/mL gentamicin and 0.5 mg/mL amphotericin B) without serum [351-353]. The 1 mM concentration of RGD peptide was mixed with serum free osteogenic media except for positive control. hBMSC and HUVEC were seeded into agarose mold to fabricate SFMs by forming coculture in 1:1 ratio.

7.2.4 PBM Application on Bone like SFMs

PBM was performed with 1 J/cm^2 energy density at 655 nm Diode Laser (Changchum New Industries Optoelectronics Tech, China) and 5 J/cm^2 energy density at 808 nm Diode Laser (Omnibil, Istanbul, Turkey). The adjustment of optical fibers of the laser devices was fixed by an XYZ-platform on optical table to enlighten homogeneously the cell culture plates. The output power (0.2 Watt) was set for both light source. While 5 seconds were applied for 1 J/cm^2 energy density at 655 nm Diode Laser, 55 seconds were applied for 5 J/cm^2 energy density at 808 nm Diode Laser. 3D SFMs were exposed to light irradiation three times per 24 hour. To analyze the effects of association of RGD peptide and light applications, the experimental groups were prepared as control group, positive control, only RGD group, only PBM application with 1 J/cm^2 energy density at 655 nm of wavelength, the combination of 1 mM RGD peptide and PBM applications with1 J/cm^2 energy density at 655 nm of wavelength, only PBM application with 5 J/cm^2 energy density at 808 nm of wavelength and also the combination of 1 mM RGD and PBM application with 5 J/cm^2 energy density at 808 nm of wavelength. Positive control (PC) which contained 10 % FBS without any peptide and ligth application. The all results were compared with control group (C) which did not include RGD peptide and light application.

7.2.5 Micrographs and Diameter Calculation of SFMs

The micrographs of SFMs were taken under microscope (Olympus, CKX41, Tokyo, Japan) on days 4, 7, 14 and 21. Then, the diameters of at least three SFMs were measured by Image J (NIH, USA) in each time points. The averages of SFMs were measured.

7.2.6 Live and Dead Staining on SFMs

Live and Dead cell staining was performed to analyze cell viability of SFMs as descripted in previous studies [63, 64, 193]. After all SFMs were washed three times by PBS, 11 mmol of L Calcein-AM / DMSO and 1.5 mmol of L Propidium Iodide / purified water solution were mixed within PBS. Then, the mixture was added onto SFMs and incubated for 15 minutes. All SFMs washed again with PBS and observed under the fluorescence microscope. The green intensities of SFMs were calculated by Image-J.

7.2.7 Analysis of the Intracellular ROS Production

Since PBM promotes ROS production which has capacity of osteogenic differentiation [276, 354], the ROS production of SFMs was evaluated after the last light application by fluorescent agent DCF as descripted in literature [355, 356]. After PBM applications, 100 µl of DCFH-DA solution was added into SFMs at 37°C for 45 minutes in the dark. Over DCFH-DA solution was washed by PBS. After that, ROS was measured in multiplate spectrophotometer (Synergy™ HTX Multi-Mode Microplate Reader, BioTek, Winooski, VT, USA) according to fluorescence intensity (excitation: emission 485 nm: 535 nm).

7.2.8 Relative ATP Production of SFMs

One of the products of PBM is also ATP. ATP was measured after the last light application according to previous study [137, 357]. After light application, 50 µL of CellTiter-Glo was added into the medias of SFMs. Then, the luminescence values were measured by the microplate reader after 2 minutes incubation time at room temperature.

7.2.9 Analysis of NO Release

PBM based NO was measured after the last light application by the Griess reagent which includes sulfanilic acid and N-(1-naphthyl)ethylenediamine for quantification the NO releasing. Briefly, equal volume of Griess reagent and the medias of SFMs were mixed. Then, the mixture was incubated for 30 minutes. The absorbance of SFMs was obtained by the microplate reader at 548 nm [356, 357].

7.2.10 Osteogenic Differentiation Capacity of the Combined Therapy

Osteogenic differentiation capacity of the combined therapy on SFMs was evaluated with DNA amount, ALP Activity and Calcium Assay by following previous literature [199, 351, 358]. At the each time point (4, 7, 14, and 21 days), SFMs were washed by PBS. Samples were lysed by 10 mM Tris supplemented with 0.2% Triton in PBS. For DNA quantification, bisBenzimide H 33258 was added into each well and measured at the fluorescence (excitation: emission) 360 nm: 460 nm of wavelength. For ALP activity measurement, 10 µl of ALP enzyme and 50 µl of 5 mM para-nitrophenylphosphate (pNPP) were prepared to incubate sample for 1 hour. After added stop solution, the mixture was measured at 405 nm of wavelength. Calcium amounts of SFMs were measured by 50 µl calcium reagent mixture and 150 µl lysed sample at 612 nm of wavelength. The calculated ALP activities and calcium amounts were normalized according to DNA contents of SFMs at the each time point.

7.2.11 Relative Osteogenic Gene Expressions of Bone Like SFMs

The osteogenic gene expressions of bone like SFMs were assessed by quantitative real time PCR [64, 193, 351]. After 3D SFMs were lysed using a tissue shredder stick. Total RNA was isolated by using RNA extraction kit. At the last step, RNA of all SFMs was eluted by RNase-free water with final volume of 50 uL. 1 µg of RNA was doubled to cDNA in standart PCR. Real time PCR was evaluated by SYBR Green Mix by qPCR (Step One Plus, Applied Biosystems, Foster City, USA). All markers of SFMs were triple repeated in qPCR. GAPDH was utilized as endogenous control. The other osteogenic markers (ALP, Collagen, and Osteopontin) were normalized to GAPDH. The primer sequences of osteogenic markers were given in Table 7.1. Relative mRNA fold differences of the osteogenic markers were measured by $2^{-(\Delta\Delta Ct)}$ formula.

Table 7.1: The sequences of the osteogenic markers.

GENES	Sequences
GAPDH	R: AACAGCGACACCCACTCCTC F: CATACCAGGAAATGAGCTTGACAA
Alkalin Phosphatase (ALP)	R: ACATTCCCACGTCTTCACATTT F: AGACATTCTCTCGTTCACCGCC
Collagen Type I	R: TGACGAGACCAAGAACTG F: TCAGCCTTAGACGCCTCAAT

Osteopontin (OPN)	R: ATGAGATTGGCAGTGATT F: TTCAATCAGAAACTGGAA

7.2.12 Statistical Analysis

All experiments were repeated at least three times (n=3). Averages of all datas were calculated. Statistical analysis of all data was assessed by Two way ANOVA (GraphPad Prism, CA, USA), followed by Tukey's post hoc test. The values of control group were calculated and estimated as 100 % in ATP, ROS, NO datas. Moreover, qPCR values of control group were estimated as 1. The values of the other experimental groups were compared with the control group. The statistically significant results were determined as $p^* < 0.05$, $p^{**} < 0.01$ and $p^{***} < 0.001$.

7.3 Results

7.3.1 The formation and diameter analysis of SFMs

The formation and proliferation of SFMs were calculated following treatment with only PBM applications (at 655 nm and 808 nm of wavelength), and combination of RGD and PBM (at 655 nm and 808 nm of wavelength) and plotted as a percentage of untreated control and positive control (Figure 7.2 and Figure 7.3). All SFMs were greatly constructed and followed until day 21. Nearly all diameters of SFMs started to decrease after day 14. However, the highest diameter enlargement was observed in the combination of RGD and PBM applications at 655 nm of wavelength after PC on day 21. The diameters of C, PC, RGD, PBM at 655 nm, RGD+PBM at 655 nm, PBM at 808 nm, and RGD+ PBM at 808 nm groups were calculated 207±6, 429±10, 287±6, 256±20, 335±15, 247±10, and 332±23 μm on day 21, respectively. The diameter of RGD was larger than only PBM groups (at the 655 nm and 808 nm of wavelength) in the last time point.

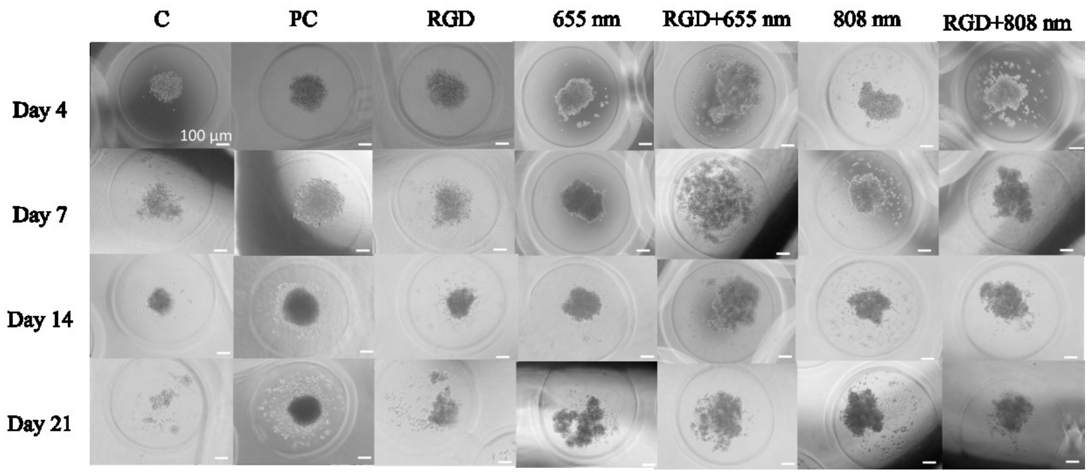

Figure 7.2: The formation of SFMs of control, positive control, RGD, PBM at 655 nm of wavelength, RGD+655 nm, PBM at 808 nm of wavelength, and RGD+808 nm on days 4, 7, 14, and 21.

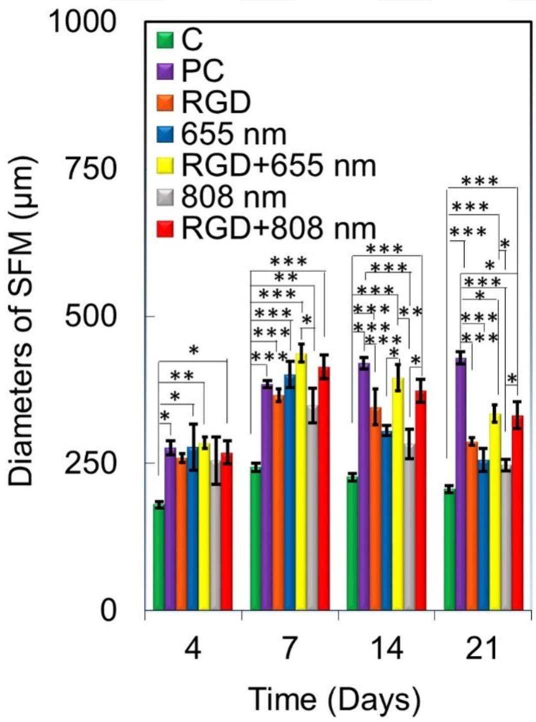

Figure 7.3: The average diameter changes of SFMs on days 4, 7, 14, and 21. Statistical Two way ANOVA analysis were marked as p*<0.05, p**<0.01 and p***<0.001

7.3.2 The viability analysis of SFMs

The viable and dead cells were dyed to understand the effects of experimental groups as shown in Figure 7.4.

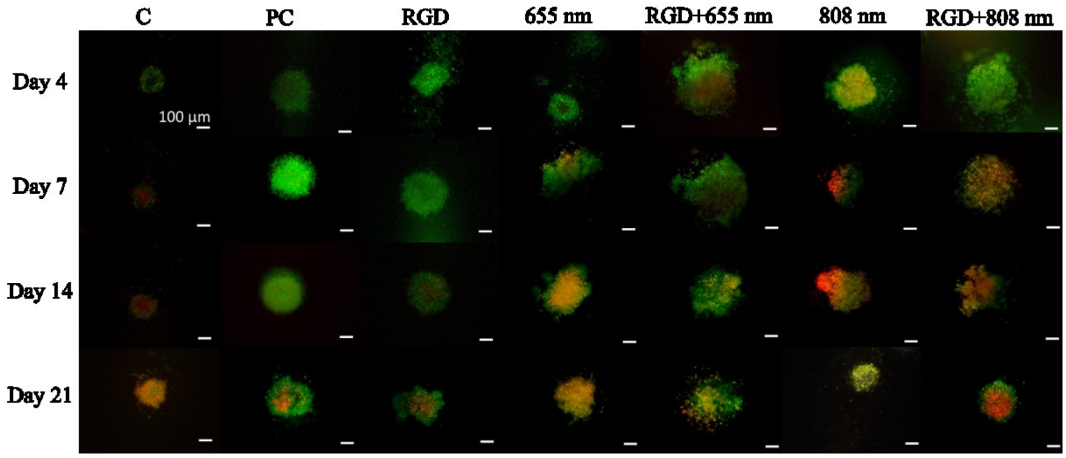

Figure 7.4: Viability of SFMs on days 4, 7, 14, and 21.

The viabilities of SFMs were evaluated according to green color intensity as presented in Figure 7.5. The average green intensity of control was estimated as 100 % at the 4th day. The other experimental groups were compared with the intensity of control. Parallel to diameter measurement, the viabilities of SFMs nearly initiated to shrink after day 14. The green intensities of C, PC, RGD, PBM at 655 nm, RGD+ PBM at 655 nm, PBM at 808 nm, and RGD+ PBM at 808 nm groups were measured as 61±0,2, 153±4, 120±4, 85±5, 118±3, 75±4, and 114±3 % on day 14, respectively. The diameter of RGD was larger than only PBM groups (at 655 nm and 808 nm of wavelength) on day 14. Even though the diameter of RGD was larger than the combined therapy, it was not statistically significant. The most diameter enlargement was observed in PC.

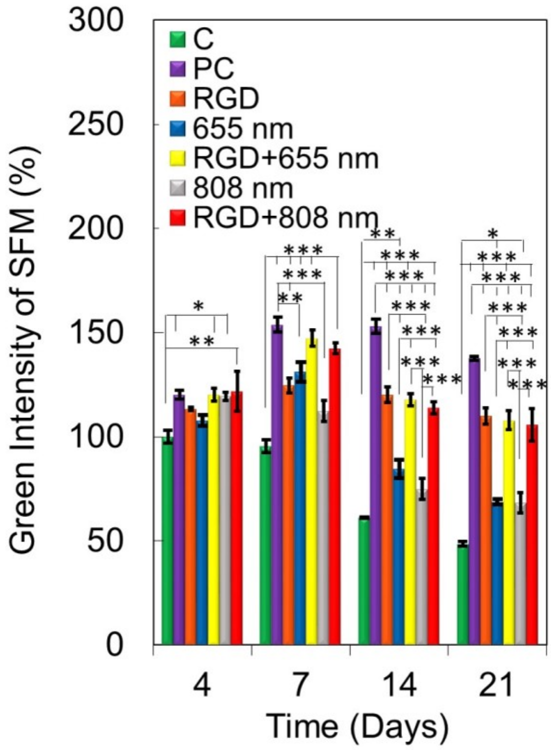

Figure 7.5: The averages of green intensities of SFMs depending on days 4, 7, 14, and 21. Statistical Two way ANOVA analysis were marked as p*<0.05, p**<0.01 and p***<0.001.

7.3.3 The relative ROS and ATP production and NO releasing for the combined therapy on SFMs

Production of ROS, synthesis of ATP and NO releasing were measured in all SFMs groups after triple light treatments as given in Figure 7.6.

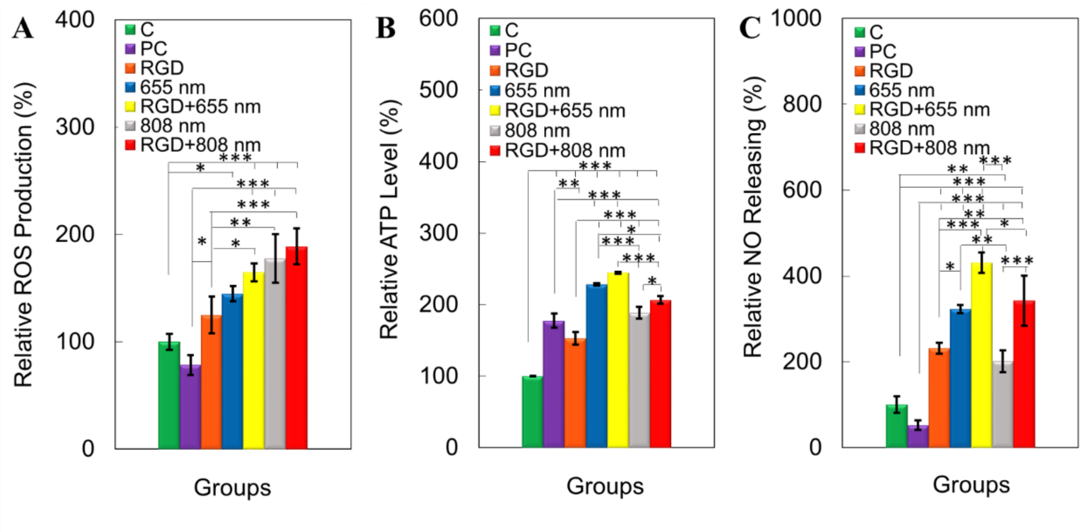

Figure 7.6: Percentage (A) ROS production, (B) ATP synthesis and (C) NO-releasing relative to control of SFMs after triple treatment. Statistical Two way ANOVA analysis were identified as p*<0.05, p**<0.01 and p***<0.001.

The ROS production of C, PC, RGD, PBM at 655 nm, RGD+ PBM at 655 nm, PBM at 808 nm, and RGD+PBM at 808 nm groups were measured 100±8, 78±9, 125±17, 145±7, 165±8, 178±23, and 189±17 %, respectively. All PBM groups produced more ROS than control group. Only RGD even propagated ROS production rather than control group. The lowest ROS production was observed in PC group among all experimental groups. ATP productions of SFMs were calculated by comparing with control group after triple PBM treatment. The ATP levels of C, PC, RGD, PBM at 655 nm, RGD+PBM at 655 nm, PBM at 808 nm, and RGD+ PBM at 808 nm groups were measured as 100±1, 178±10, 153±9, 228±2, 244±1, 188±8, and 207±5 %, respectively. The highest ATP production was observed in RGD+PBM at 655 nm group. The light treatment groups promoted ATP. However, only PBM at 655 nm of wavelength and the combination with PBM at 655 nm of wavelength showed higher effect than only 808 nm and the combination with 808 nm groups. Moreover, PBM at 655 nm of wavelength showed higher ATP production than positive control. One of the products of PBM is NO which was measured in all SFMs. The NO releasing results of C, PC, RGD, PBM at 655 nm, RGD+ PBM at 655 nm, PBM at 808 nm, and RGD+PBM at 808 nm groups were shown as 100±19, 53±11, 232±13, 323±10, 431±24, 201±25, and 342±59 %, respectively. While the highest NO releasing was observed in RGD+PBM at 655 nm group, the lowest NO releasing group was PC.

7.3.4 The osteogenic differentiation effects of the combination therapy for SFMs

Osteogenic differentiations of SFMs were evaluated by DNA amount, ALP activity and calcium deposition as shown in Figure 7.7.

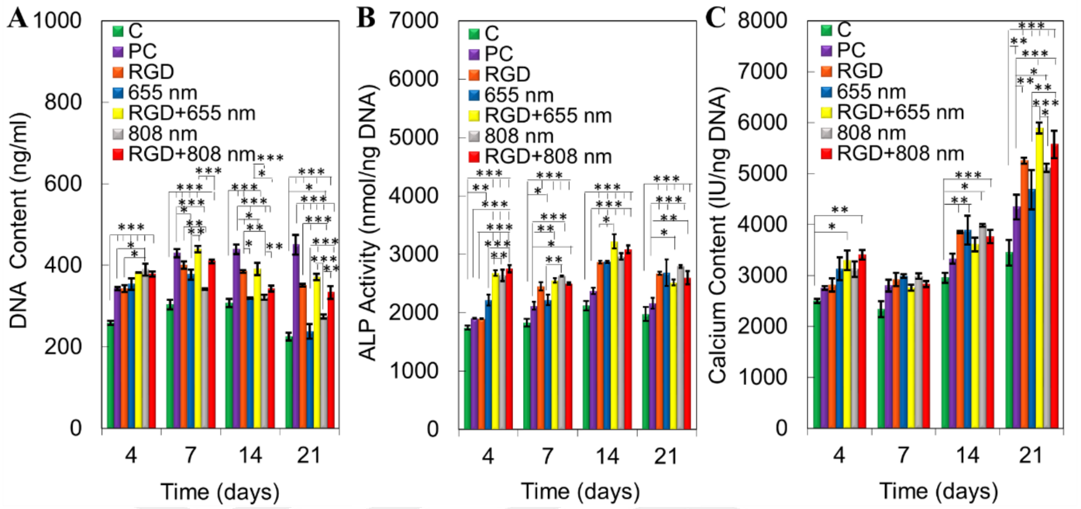

Figure 7.7: The osteogenic differentiation analysis of SFMs by (A) DNA quantification, (B) ALP Activity, (C) Calcium mineralization. Statistical Two way ANOVA analysis were identified as p*<0.05, p**<0.01 and p***<0.001.

DNA amount of SFMs showed parallel results with viability. Specifically, after day 14, DNA amounts of SFMs started to decrease. In the end of the last time point, DNA amounts of C, PC, RGD, PBM at 655 nm, RGD+PBM at 655 nm, PBM at 808 nm, and RGD+PBM at 808 nm groups were calculated as 225±10, 451±24, 351±3, 238±18, 371±8, 275±5, and 333±16 ng/ml, respectively. After PC, the highest DNA amount belonged to RGD+655 nm group. ALP activities of C, PC, RGD, PBM at 655 nm, RGD+PBM at 655 nm, PBM at 808 nm, and RGD+PBM at 808 nm SFMs were found 2120±84, 2374±58, 2866±26, 2871±21, 3220±121, 2962±57, and 3085±65 nmol/ng DNA on day 14, respectively. ALP activities of all SFMs were increased until day 14. The ALP activity of RGD+PBM at 655 nm of wavelength group reached in the highest point on day 14. Only RGD and only PBM at 655 nm of wavelength groups showed similar results each other. Calcium mineralization was evaluated in each time points. Although the combination therapy for both PBM groups enhanced in the first time point of osteogenic differentiation, the calcium amounts of combination were not statistically different than the only PBM groups. Calcification started after 21st day. The calcium amounts of C, PC, RGD, PBM at 655 nm, RGD+PBM at 655 nm, PBM at 808 nm, and RGD+PBM at 808 nm SFMs were tested as 3448±253, 4346±241, 5249±59, 4684±386, 5891±109, 5113±81 and 5574±270 IU/ng DNA in the last time point, respectively. Calcium amount of RGD+PBM at 655 nm of wavelength was higher than the other experimental groups, again.

Relative mRNA expressions of osteogenic markers (ALP, collagen and osteopontin) of C, PC, RGD, PBM at 655 nm, RGD+PBM at 655 nm, PBM at 808 nm, and RGD+PBM at 808 nm groups were evaluated by qPCR as presented in Figure 7.8.

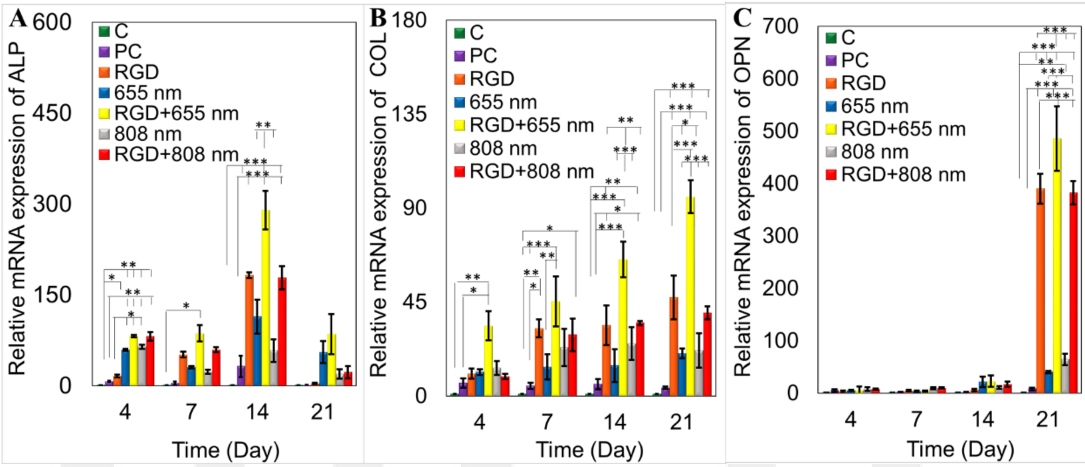

Figure 7.8: The osteogenic mRNA fold differences of SFMs relative to control: (A) ALP mRNA expression, (B) Collagen mRNA expression, (C) Osteopontin mRNA expression.

All genes were compared with control group which was estimated as 1. ALP expressions of PBM groups were effective from the first time point to 14th day. ALP expressions were reached on day 14 in the all groups. However, the highest ALP expression was observed in RGD+PBM at 655 nm of wavelength group. Relative ALP fold differences of C, PC, RGD, PBM at 655 nm, RGD+PBM at 655 nm, PBM at 808 nm, and RGD+PBM at 808 nm were calculated as 1±0, 32±18, 182±5, 114±28, 290±32, 58±20 and 178±22 on day 14, respectively. The combination therapies for both wavelengths were more effective than only peptide or only PBM groups. Although collagen mRNA was the highest expressed in RGD+PBM at 655 nm group, nearly all groups showed similar collagen expression in the first time point. In the last time point, the relative collagen expressions of C, PC, RGD, PBM at 655 nm, RGD+ PBM at 655 nm, PBM at 808 nm, and RGD+PBM at 808 nm were found as 1±0, 4±1, 47±10, 20±2, 95±8, 22±8, and 40±3, respectively. The highest collagen expression was found in RGD+ PBM at 655 nm of wavelength group in the last time point. All RGD and all PBM groups expressed more collagen than the control and positive control. The fold differences of osteopontin gene in C, PC, RGD, PBM at 655 nm, RGD+PBM at 655 nm, PBM at 808 nm, and RGD+PBM at 808 nm groups were found as 1±0, 8±3, 390±29, 40±2, 486±62, 64±11, and 382±22 in the last time point, respectively. From the first time point to last time point, all experimental groups expressed more osteopontin than control group. The highest osteopontin expression was observed in RGD+PBM at 655 nm of wavelength group again.

7.4 Discussions

In this study, we made out that the combination therapy with peptide and PBM supported more osteogenic differentiation capacity than only peptide or only PBM therapies. The results were indicated that 1 mM concentration of RGD and PBM at 655 nm of wavelength enhanced cell proliferation of SFMs, stem cell differentiation, and bone regeneration. The bone mimetic peptides like RGD peptide may be one of the most well-known integrin recognition sites in ECM proteins [328]. The sequence also regulates cellular attachment of bone cell into ECM [359]. The RGD sequence has critically important role in terms of proliferation and differentiation [328, 359]. On the other hand, LLLT or PBM has also improves stem cell differentiation [134]. The ranges of 600-1200 nm of wavelength are therapeutic window that directly affect mitochondria of cells to able to regulate cellular behaviours [360]. The state-of-the-art of BTE modalities are based upon supporting faster and easier tissue regeneration by controlling stem cell behaviours. Thus, the regenerative capacity can increase by combining biomaterials and PBM [361-363].

In all groups, SFMs were greatly constructed from day 4. The diameter analysis of 1 mM of RGD and PBM applications 1 J/cm^2 at 655 nm of wavelength and RGD+PBM at 808 nm of wavelength increased more proliferation than only single therapy groups and control group. The viability analysis of SFMs showed that the combination therapy with RGD+PBM at 655 nm of wavelength and RGD+PBM at 808 nm of wavelength showed higher viable cells compared with control and single therapy. The positive control showed higher diameter enlargement than the combination therapy in late time point because positive control included serum. The serum is vital components for metabolic activity of cells so it contributes to viability and proliferation of cells [63, 64]. However, minimum serum concentration is needed to analyze the real effect of tissue mimicking peptides [364]. Although the combination therapies with both light applications didn't have any serum concentration, both of them were increased the diameter and viability of SFMs. RGD+PBM at 655 nm of wavelength group was specifically enhanced the diameter of SFMs and proliferation of cells. Although single therapy promoted cell viability and proliferation, the combined therapy for both PBM application (at the 655 nm and 808 nm of wavelength) enhanced more cell proliferation and viability. Previous studies have been shown that the RGD peptide increases cell proliferation and cellular attachment to ECM because of its integrin binding capacity [325, 326]. At the 655 nm of wavelength also promoted the cell proliferation and migration [360, 365]. Similarly, 808 nm of wavelength can induce cell proliferation, migration and attachment [336, 366]. It is possible to promote cell proliferation by combining different therapies [226, 367].

The PBM made out different signal molecules such as ROS, ATP and NO [331, 339, 356]. The signal molecules directly take place in cell and contribute to synthesis of transcription factors [338, 360]. Although the highest ROS production was observed in RGD+PBM at 808 nm of wavelength group, the ROS production of RGD+PBM at 655 nm group of wavelength was higher than only RGD or only PBM at 655 nm of wavelength. Only RGD group also produced ROS but not significant. One of the output molecules of PBM is ROS. Although ROS was produced in single RGD therapy but not significant, the combined therapy may trigger more ROS production. The literature indicated that the interactions of integrin and ECM regulate critical adaptive stress response in cells and lead to amplification of ROS [329, 368, 369]. However, the combined therapy showed more ROS productivity than the other groups. The highest ATP was produced by RGD+PBM at 655 nm of wavelength. Actually, RGD induced ATP production and cell metabolism for viability. Similarly, 600-800 nm range of wavelength also promotes the synthesis of ATP because the range directly affects cytochrome-c oxidase in mitochondria [370]. The NO releasing occurs during light irradiation [134, 357, 366]. Moreover, RGD peptide may also release NO [329].

The highest NO releasing was observed in the combination of RGD+PBM at 655 nm of wavelength group. Moreover, RGD+PBM at 808 nm of wavelength group also released NO. Releasing NO stimulates proliferation and differentiation of MSCs so it is another strategy for bone tissue regeneration [329].

The differentiation capacity of combined therapies was evaluated by DNA, ALP activity, calcium mineralization and mRNA fold differences of osteogenic markers. The DNA amount of RGD+PBM at 655 nm of wavelength was higher than the other experimental groups as parallel with SFMs and viability results. The combination therapy (RGD peptide and PBM at the 655 nm of wavelength application) strongly proliferated cells which is critical important for bone regeneration. Although single therapy groups also expressed ALP, the highest ALP expression was observed in the combination of RGD+PBM at 655 nm of wavelength. ALP activity which is expressed bone cells in early time [351]. RGD and PBM at the 600-800 nm range of wavelength may promote to ALP activity for osteogenic differentiation [135, 326, 328, 337]. Even only RGD or only PBM groups deposited calcium in their matrix. Ji, B. et.al. exhibited that hydrogel-conjugated RGD peptide supported matrix mineralization [329]. On the other hand, PBM at the 600-800 nm range of wavelength also promoted calcium mineralization [135, 337, 371]. Calcium mineralization was also supported by combined therapy groups. The combination of RGD+PBM at 655 nm of wavelength group deposited calcium more than RGD+PBM at 808 nm of wavelength group.

mRNA fold differences of osteogenic markers were evaluated by qPCR analysis in all SFMs. The highest mRNA expressions of ALP were observed in the combination of RGD+PBM at 655 nm of wavelength group as parallel ALP activity results. Although the mRNA expression of ALP in only RGD group was more effective than only PBM application groups, the enzymatic results of ALP showed that the production of ALP was nearly same with light application groups. The literature already indicated that expression of ALP can be inducible in MSCs by RGD [359] or PBM [135, 276]. Actually, the promotion of ALP expression can be estimated in the combination of RGD and PBM (at the 655 nm and 808 nm of wavelength). The collagen mRNA fold difference in the combined therapies was overwhelmingly higher than the other experimental groups. However, only RGD group also highly expressed collagen rather than only PBM groups. Since RGD is a unit of some ECM proteins such as collagen [102, 203], the expression of collagen was promoted by even only RGD group. Even if PBM promoted collagen expression [371], PBM groups observed lower collagen production compared with RGD. However, the combination of RGD+PBM at 655 nm of wavelength group extensively expressed collagen rather than the other groups due to RGD concentration. Similarly, the highest mRNA expression of osteopontin was observed including RGD. Even though, only PBM groups showed low osteopontin mRNA expression rather than only RGD group, the combination of RGD+PBM at 655 nm of wavelength increased osteopontin expression. Actually, PBM at 660 and 808 nm of wavelength can contribute to osteopontin mRNA expression [323]. Similarly, the result of osteopontin mRNA fold differences of only PBM groups (at 655 nm and 808 nm of wavelength) exhibited more expression rather than control. However, the higher osteopontin expression was observed including RGD peptide. Since RGD sequence is located in osteopontin as one of the integrin binding sites [372]. Thus, it is possible to reach more expression rate by RGD including groups. The highest osteopontin was found in the combination of RGD+PBM at 655 nm of wavelength which supported osteogenic differentiation and even bone regeneration.

Consequently, it is discussed that the combination therapy of peptide and PBM (at 655 nm and 808 nm of wavelength) supported more cell proliferation, viability and differentiation than single therapy. 1 mM concentration of RGD and 1 J/cm^2 energy density at the 655 nm of wavelength combination promoted more cell proliferation, viability, differentiation and regeneration than 1 mM concentration of RGD and 5 J/cm^2 energy density at the 808 nm of wavelength combination.

7.5 Conclusions

Peptide or PBM therapy can be useful to increase osteogenic differentiation but the combination of them synergistically enhanced stem cell differentiation. The combination therapy promoted effectiveness of osteogenic differentiation rather than single RGD therapy or single PBM therapy. Although the combination of 1 mM concentration of RGD and 1 J/cm^2 energy density at the 655 nm of wavelength is the most effective group in terms of cell proliferation, viability and differentiation, both 1 mM concentration of RGD and 1 J/cm^2 energy density at the 655 nm of wavelength and 1 mM concentration of RGD and 5 J/cm^2 energy density at the 808 nm of wavelength may be a promising therapeutic window for clinical trials.

Chapter 8

8. Concluding Remarks

BTE aims to understand bone structure and formation and to induce regeneration capacity. Successfully bone regeneration is possible with knowledge of the bone biology. Thus, BTE targets to develop regenerative strategies by using cues of bone cell behaviours and microenvironment in vitro conditions. Since microenvironment is crucial for stem cell behaviours such as growth, viability, proliferation and differentiation, self-assembly ECM platforms are needed to investigate microenvironments of bone. SFMs can successfully mimic natural ECM, promote intracellular cross-talk of cells, and remodel like in vivo condition. Since mesenchymal stem cells closely contact with endothelial cells in bone, the study was benefited from the coculture of mesenchymal stem cell and endothelial cell to create bone like SFMs.

Biomimetic peptides are useful tools for direction cell behaviours in bone regeneration due to the advantages of their ECM mimicking, cell to cell and cell to ECM signalling properties. Integrin binding peptides (IKVAV, RGD, and YIGSR), are units of ECM proteins such as fibronectin, laminin, collagen and osteopontin, bind cell to matrix and initiate cell proliferation, adhesion, migration, and differentiation. Additionally, the bone regeneration can be influenced by external physical sources such as LLLT or PBM. Light in PBM is absorbed by chromophore molecules known as cytochrome c oxidase which is found in mitochondria of cells. After PBM therapy, ROS, ATP and NO are produced to induce cell proliferation, viability and osteogenic differentiation. To improve efficacy of PBM and peptide therapy, the combination of them can be used. The defined optimum concentration of integrin binding peptides and the most effective parameters of PBM can provide bone regeneration. For these purposes, the thesis performed five different studies on bone like SFMs. The first part included that the investigation of vascularization of coculture with mesenchymal stem cell and endothelial cell on SFMs. The part implied that endothelial cell mediated signaling molecules in the coculture improved vascular capacity of bone like structure. Moreover, the coculture also contributed to vascularization, growth, viability, and proliferation of stem cells. In the second part, the determination of osteogenic potential of integrin binding peptides (IKVAV, RGD and YIGSR) was examined in different concentrations (0.5 mM, 1 mM and 2 mM) on vascularized bone SFMs. 1 mM concentration of RGD peptide had more potential for inducing osteogenesis than the other concentrations of RGD and the other integrin binding peptide sequences. In the third part of the thesis, it brought into open the molecular mechanism of PBM at 655 and 808 nm of wavelength by determining role of production of ATP and releasing of NO in the proliferation, migration, and osteogenic differentiation. In addition, it was identified that 5 J/cm^2 energy density at 655 and 808 nm of wavelength was the most successful light parameter on monolayer co-culture in terms of osteogenic differentiation. In the fourth part, it was found that 1 J/cm^2 energy density at 655 nm of wavelength showed ROS and ATP production and NO releasing which were crucial signaling molecules in terms of cell proliferation, viability, and osteogenic differentiation on bone like SFMs. 5 J/cm^2 energy density at 808 nm of wavelength followed the 1 J/cm^2 energy density at 655 nm of wavelength on vascularized bone SFMs. In the last part, combined therapy was performed on vascularized bone SFMs by using the optimum concentration of integrin binding peptides and parameters of PBM therapy. Thus, the last part was designed by the combination of 1 mM RGD peptide and 1 J/cm^2 energy density at 655 nm of wavelength and the combination of 1 mM RGD peptide and 5 J/cm^2 energy density at 808 nm of wavelength on vascularized bone SFMs. The results indicated that 1 mM RGD peptide and 1 J/cm^2 energy density at 655 nm of wavelength, which showed ROS production, ATP synthesis and NO releasing, supported more cell proliferation, viability and osteogenic differentiation. In the sum of the thesis, only peptide therapy or only PBM therapy were even influential therapeutic way for bone regeneration, the combination therapy of them were actually more effective strategy to increase regenerative capacity of bone. According to indications, 1 mM RGD peptide and 1 J/cm^2 energy density at 655 nm of wavelength may be brilliant therapeutic window for clinical researches.

References

[1] Buck DW, Dumanian GA. Bone biology and physiology: Part I. The fundamentals. Plastic and reconstructive surgery 2012;129(6):1314-20.

[2] Topaloğlu U, Ketani MA, Saruhan BG. Kemik doku ve kemikleşme çeşitleri. Dicle Universitesi Veterinerlik Fakültesi dergisi 2017;10(1):62-71.

[3] Buckwalter J, Glimcher M, Cooper R, Recker R. Bone biology. Journal of Bone Joint Surgery Research 1995;77(8):1256-75.

[4] Black JDJ, Tadros BJ. Bone structure: from cortical to calcium. Orthopaedics and Trauma 2020;34(3):113-9.

[5] Carbonare LD, Giannini J. Bone microarchitecture as an important determinant of bone strength. Journal of Endocrinological Investigation 2004;27(1):99-105.

[6] Clarke B. Normal bone anatomy and physiology. Clinical Journal American Society Nephrology 2008;3 Suppl 3(Suppl 3):S131-S9.

[7] Fathi Kazerooni A, Pozo JM, McCloskey EV, Saligheh Rad H, Frangi AF. Diffusion MRI for assessment of bone quality; a review of findings in healthy aging and osteoporosis. Journal of Magnetic Resonance Imaging 2020;51(4):975-92.

[8] Hubbell JA, Massia SP, Desai NP, Drumheller PD. Endothelial cell-selective materials for tissue engineering in the vascular graft via a new receptor. Bio/technology (Nature Publishing Company) 1991;9(6):568-72.

[9] Ansari S, Ito K, Hofmann S. Cell Sources for Human In vitro Bone Models. Current Osteoporosis Reports 2021;19(1):88-100.

[10] Raja IS, Preeth DR, Vedhanayagam M, Hyon S-H, Lim D, Kim B, et al. Polyphenols-loaded electrospun nanofibers in bone tissue engineering and regeneration. Biomaterial Research 2021;25(1):29-.

[11] Zhou R, Guo Q, Xiao Y, Guo Q, Huang Y, Li C, et al. Endocrine role of bone in the regulation of energy metabolism. Bone Research 2021;9(1):25.

[12] Nahian A, Davis DD. Histology, Osteoprogenitor Cells. StatPearls. Treasure Island (FL): StatPearls Publishing Copyright © 2022, StatPearls Publishing LLC.; 2022.

[13] Dimitriou R, Jones E, McGonagle D, Giannoudis PV. Bone regeneration: current concepts and future directions. BMC Medicine 2011;9(1):66.

[14] Florencio-Silva R, Sasso GRdS, Sasso-Cerri E, Simões MJ, Cerri PS. Biology of Bone Tissue: Structure, Function, and Factors That Influence Bone Cells. BioMed Research International 2015;2015:421746.

[15] Setiawati R, Rahardjo PJO, Regeneration B. Bone Development and Growth. London: Intech Open; 2018; doi: 10.5772/intechopen.82452.

[16] Kini U, Nandeesh BN. Physiology of Bone Formation, Remodeling, and Metabolism. In: Fogelman I, Gnanasegaran G, van der Wall H, editors. Radionuclide and Hybrid Bone Imaging. Berlin, Heidelberg: Springer Berlin Heidelberg; 2012. p. 29-57.

[17] Bilezikian JP, Raisz LG, Martin TJ. Principles of bone biology: Academic press; 2008.

[18] García JR, García AJ. Biomaterial-mediated strategies targeting vascularization for bone repair. Drug delivery and translational research. 2016;6(2):77-95.

[19] Prisby RD. Bone Marrow Microvasculature. Comprehensive Physiology 2022. p. 1009-46.

[20] Zhao Y, Xie L. Unique bone marrow blood vessels couple angiogenesis and osteogenesis in bone homeostasis and diseases. Annals of the New York Academy of Sciences 2020;1474(1):5-14.

[21] Kolte D, McClung JA, Aronow WS. Chapter 6 - Vasculogenesis and Angiogenesis. In: Aronow WS, McClung JA, editors. Translational Research in Coronary Artery Disease. Boston: Academic Press; 2016. p. 49-65.

[22] Stegen S, van Gastel N, Carmeliet G. Bringing new life to damaged bone: The importance of angiogenesis in bone repair and regeneration. Bone 2015;70:19-27.

[23] Kalka C, Asahara T, Krone W, Isner JM. Angiogenesis and vasculogenesis. Therapeutic strategies for stimulation of postnatal neovascularization. Herz 2000;25(6):611-22.
[24] Habibovic P. Strategic directions in osteoinduction and biomimetics. Tissue Engineering Part A 2017;23(23-24):1295-6.
[25] Iaquinta MR, Mazzoni E, Bononi I, Rotondo JC, Mazziotta C, Montesi M, et al. Adult Stem Cells for Bone Regeneration and Repair. Frontiers cell and development biology 2019;7.
[26] Roseti L, Parisi V, Petretta M, Cavallo C, Desando G, Bartolotti I, et al. Scaffolds for Bone Tissue Engineering: State of the art and new perspectives. Materials science & engineering C, Materials for biological applications 2017;78:1246-62.
[27] Shin SY, Rios HF, Giannobile WV, Oh T-J. Chapter 36 - Periodontal Regeneration: Current Therapies. In: Vishwakarma A, Sharpe P, Shi S, Ramalingam M, editors. Stem Cell Biology and Tissue Engineering in Dental Sciences. Boston: Academic Press; 2015. p. 459-69.
[28] Roberts TT, Rosenbaum AJ. Bone grafts, bone substitutes and orthobiologics: the bridge between basic science and clinical advancements in fracture healing. Organogenesis 2012;8(4):114-24.
[29] Maia FR, Bastos AR, Oliveira JM, Correlo VM, Reis RL. Recent approaches towards bone tissue engineering. Bone 2022;154:116256.
[30] Perez JR, Kouroupis D, Li DJ, Best TM, Kaplan L, Correa D. Tissue Engineering and Cell-Based Therapies for Fractures and Bone Defects. Frontiers in Bioengineering and Biotechnology 2018;6.
[31] Park JY, Park SH, Kim MG, Park S-H, Yoo TH, Kim MS. Biomimetic Scaffolds for Bone Tissue Engineering. In: Noh I, editor. Biomimetic Medical Materials: From Nanotechnology to 3D Bioprinting. Singapore: Springer Singapore; 2018. p. 109-21.
[32] De Pieri A, Rochev Y, Zeugolis DI. Scaffold-free cell-based tissue engineering therapies: advances, shortfalls and forecast. Regenerative Medicine 2021;6(1):18.

[33] Amini AR, Laurencin CT, Nukavarapu SP. Bone tissue engineering: recent advances and challenges. Critical Reviews in Biomedical Engineering 2012;40(5):363-408.

[34] Walmsley GG, Ransom RC, Zielins ER, Leavitt T, Flacco JS, Hu MS, et al. Stem Cells in Bone Regeneration. Stem Cell Reviews and Reports 2016;12(5):524-9.

[35] Wang L, Wu F, Liu C, Song Y, Guo J, Yang Y, et al. Low-level laser irradiation modulates the proliferation and the osteogenic differentiation of bone marrow mesenchymal stem cells under healthy and inflammatory condition. Lasers in medical science 2019;34(1):169-78.

[36] Lin X, Patil S, Gao Y-G, Qian A. The Bone Extracellular Matrix in Bone Formation and Regeneration. Frontiers in Pharmacology 2020;11.

[37] Bicer M, Cottrell GS, Widera D. Impact of 3D cell culture on bone regeneration potential of mesenchymal stromal cells. Stem Cell Research & Therapy 2021;12(1):31.

[38] Szpalski C, Barbaro M, Sagebin F, Warren SM. Bone tissue engineering: current strategies and techniques--part II: Cell types. Tissue engineering Part B, Reviews 2012;18(4):258-69.

[39] Dixon DT, Gomillion CT. Conductive Scaffolds for Bone Tissue Engineering: Current State and Future Outlook. Journal of functional biomaterials 2021;13(1).

[40] Dang M, Saunders L, Niu X, Fan Y, Ma PX. Biomimetic delivery of signals for bone tissue engineering. Bone Research 2018;6(1):25.

[41] Gardin C, Ferroni L, Favero L, Stellini E, Stomaci D, Sivolella S, et al. Nanostructured biomaterials for tissue engineered bone tissue reconstruction. International Journal of Molecular Science 2012;13(1):737-57.

[42] Fernandez-Yague MA, Abbah SA, McNamara L, Zeugolis DI, Pandit A, Biggs MJ. Biomimetic approaches in bone tissue engineering: Integrating biological and physicomechanical strategies. Advanced Drug Delivery Reviews 2015;84:1-29.

[43] Albrektsson T, Johansson C. Osteoinduction, osteoconduction and osseointegration. European spine journal : official publication of the European

Spine Society, the European Spinal Deformity Society, and the European Section of the Cervical Spine Research Society 2001;10 Suppl 2(Suppl 2):S96-101.

[44] Garg T, Bilandi A, Kapoor B, Kumar S, Joshi R. Scaffold: Tissue engineering and regenerative medicine. International Research Journal Pharmacy 2011;2(12):37-42.

[45] Ovsianikov A, Khademhosseini A, Mironov V. The Synergy of Scaffold-Based and Scaffold-Free Tissue Engineering Strategies. Trends in biotechnology 2018;36(4):348-57.

[46] Law AMK, Rodriguez de la Fuente L, Grundy TJ, Fang G, Valdes-Mora F, Gallego-Ortega D. Advancements in 3D Cell Culture Systems for Personalizing Anti-Cancer Therapies. Frontiers in Oncology 2021;11.

[47] Tomás-Bort E, Kieler M, Sharma S, Candido JB, Loessner D. 3D approaches to model the tumor microenvironment of pancreatic cancer. Theranostics 2020;10(11):5074-89.

[48] Cortesi M, Giordano EJP. Non-destructive monitoring of 3D cell cultures: new technologies and applications. PeerJ 2022;10:e13338.

[49] Duval K, Grover H, Han LH, Mou Y, Pegoraro AF, Fredberg J, et al. Modeling Physiological Events in 2D vs. 3D Cell Culture. Physiology (Bethesda, Md) 2017;32(4):266-77.

[50] Hussey GS, Dziki JL, Badylak SF. Extracellular matrix-based materials for regenerative medicine. Nature Reviews Materials 2018;3(7):159-73.

[51] Edmondson R, Broglie JJ, Adcock AF, Yang L. Three-dimensional cell culture systems and their applications in drug discovery and cell-based biosensors. Assay and drug development technologies 2014;12(4):207-18.

[52] Gurski LA, Petrelli NJ, Jia X, Farach-Carson MC. 3D Matrices for Anti-Cancer Drug Testing and Development. Oncology Issues 2010;25(1):20-5.

[53] Van Zundert I, Fortuni B, Rocha S. From 2D to 3D Cancer Cell Models—The Enigmas of Drug Delivery Research 2020;10(11):2236.

[54] Dissanayaka WL, Zhu L, Hargreaves KM, Jin L, Zhang C. Scaffold-free Prevascularized Microtissue Spheroids for Pulp Regeneration. Journal of Dental Research 2014;93(12):1296-303.

[55] Ryu NE, Lee SH, Park H. Spheroid Culture System Methods and Applications for Mesenchymal Stem Cells. Cells 2019;8(12).

[56] Sumbal J, Budkova Z, Traustadóttir GÁ, Koledova Z. Mammary Organoids and 3D Cell Cultures: Old Dogs with New Tricks. Journal of Mammary Gland Biology and Neoplasia 2020;25(4):273-88.

[57] Lee S-J, Lee H-A. Trends in the development of human stem cell-based non-animal drug testing models. Korean J Physiol Pharmacol. 2020;24(6):441-52.

[58] Corrò C, Novellasdemunt L, Li VSW. A brief history of organoids. American journal of physiology Cell physiology 2020;319(1):C151-c65.

[59] Ashok A, Choudhury D, Fang Y, Hunziker W. Towards manufacturing of human organoids. Biotechnology advances 2020;39:107460.

[60] Langhans SA. Three-Dimensional in Vitro Cell Culture Models in Drug Discovery and Drug Repositioning. Frontiers in Pharmacology 2018;9.

[61] Han SJ, Kwon S, Kim KS. Challenges of applying multicellular tumor spheroids in preclinical phase. Cancer Cell International 2021;21(1):152.

[62] Yamato M, Okano T. Cell sheet engineering. Materials Today 2004;7(5):42-7.

[63] Çevik ZBY, Ördek A, Karaman O. Regulatory effects of laminin derived peptide on microtissue formation for tissue engineered scaffold-free constructs. The European Research Journal 2022.

[64] Yaralı ZB, Onak G, Karaman O. Effect of Integrin Binding Peptide on Vascularization of Scaffold-Free Microtissue Spheroids. Tissue Engineering and Regenerative Medicine 2020;17(5):595-605.

[65] Zanoni M, Cortesi M, Zamagni A, Arienti C, Pignatta S, Tesei A. Modeling neoplastic disease with spheroids and organoids. Journal of Hematology & Oncology 2020;13(1):97.

[66] Kloker LD, Yurttas C, Lauer UM. Three-dimensional tumor cell cultures employed in virotherapy research. Oncolytic Virotherapy 2018;7:79-93.

[67] Deka B, Kalita R, Bhatia D, Mishra A. Applications of paper as a support material in biomedical sciences: A decadal review. Sensors International 2020;1:100004.

[68] Müller L, Hatzfeld M, Keil R. Desmosomes as Signaling Hubs in the Regulation of Cell Behavior. Frontiers in Cell and Developmental Biology 2021;9.

[69] Talbot J, Lamora A, Stresing V, Verrecchia F. Chapter 8 - Gap junction in bone remodeling and in primary bone tumors: osteosarcoma and Ewing sarcoma. In: Heymann D, editor. Bone Cancer (Second Edition). San Diego: Academic Press; 2015. p. 83-9.

[70] Carvalho MP, Costa EC, Correia IJ. Assembly of breast cancer heterotypic spheroids on hyaluronic acid coated surfaces. Biotechnology progress 2017;33(5):1346-57.

[71] Xu J, Qi G, Wang W, Sun XS. Advances in 3D peptide hydrogel models in cancer research. Science of Food 2021;5(1):14.

[72] Cuevas-González MV, Suaste-Olmos F, Cuevas-González JC, Álvarez-Pérez MA. 3D spheroid cell cultures and their role in bone regeneration: a systematic review %J Odovtos International Journal of Dental Sciences 2022;24:44-57.

[73] Chauhan V, Kanwar SS. Chapter 4 - Bioactive peptides: Synthesis, functions and biotechnological applications. In: Verma ML, Chandel AK, editors. Biotechnological Production of Bioactive Compounds: Elsevier; 2020. p. 107-37.

[74] Nardo AE, Añón MC, Parisi G. Large-scale mapping of bioactive peptides in structural and sequence space. Plos One 2018;13(1):e0191063.

[75] Lorenzo J, Munekata PES, Gómez B, Barba FJ, Mora L, Pérez-Santaescolástica C, et al. Bioactive peptides as natural antioxidants in food products – A review. Trends in Food Science and Technology 2018.

[76] Bechaux J, Gatellier P, Le Page JF, Drillet Y, Sante-Lhoutellier V. A comprehensive review of bioactive peptides obtained from animal byproducts and their applications. Food & function 2019;10(10):6244-66.

[77] Wang L, Wang N, Zhang W, Cheng X, Yan Z, Shao G, et al. Therapeutic peptides: current applications and future directions. Signal Transduction and Targeted Therapy 2022;7(1):48.

[78] Wei J. How Wearables Intersect with the Cloud and the Internet of Things : Considerations for the developers of wearables. IEEE Consumer Electronics Magazine 2014;3(3):53-6.

[79] Thurman EM, Mills MS. Solid-phase extraction: principles and practice: Wiley New York; 1998.

[80] Isidro-Llobet A, Kenworthy MN, Mukherjee S, Kopach ME, Wegner K, Gallou F, et al. Sustainability Challenges in Peptide Synthesis and Purification: From R&D to Production. The Journal of Organic Chemistry 2019;84(8):4615-28.

[81] Palomo JM. Solid-phase peptide synthesis: an overview focused on the preparation of biologically relevant peptides. RSC Advances 2014;4(62):32658-72.

[82] Fields GB. Introduction to Peptide Synthesis. 2003;63(1):11.5.1-.5.9.

[83] Hou W, Zhang X, Liu C-F. Progress in Chemical Synthesis of Peptides and Proteins. Transactions of Tianjin University 2017;23(5):401-19.

[84] Barati M, Javanmardi F, Mousavi Jazayeri SMH, Jabbari M, Rahmani J, Barati F, et al. Techniques, perspectives, and challenges of bioactive peptide generation: A comprehensive systematic review 2020;19(4):1488-520.

[85] Shahidi F, Zhong Y. Bioactive peptides. Journal of AOAC International 2008;91(4):914-31.

[86] Recio C, Maione F, Iqbal AJ, Mascolo N, De Feo V. The Potential Therapeutic Application of Peptides and Peptidomimetics in Cardiovascular Disease. Frontiers in Pharmacology 2017;7:526-.

[87] Wang C, Liu Y, Fan Y, Li X. The use of bioactive peptides to modify materials for bone tissue repair. Regenerative biomaterials 2017;4(3):191-206.

[88] Boateng SY, Lateef SS, Mosley W, Hartman TJ, Hanley L, Russell B. RGD and YIGSR synthetic peptides facilitate cellular adhesion identical to that of laminin and fibronectin but alter the physiology of neonatal cardiac myocytes. American journal of physiology Cell physiology 2005;288(1):C30-8.

[89] Aguilar-Toalá JE, Quintanar-Guerrero D, Liceaga AM, Zambrano-Zaragoza ML. Encapsulation of bioactive peptides: a strategy to improve the stability,

protect the nutraceutical bioactivity and support their food applications. RSC Advances 2022;12(11):6449-58.
[90] Campbell ID, Humphries MJ. Integrin structure, activation, and interactions. Cold Spring Harbor Perspectives in Biology 2011;3(3):a004994.
[91] Yu D, Wang J, Qian K-J, Yu J, Zhu H-Y. Effects of nanofibers on mesenchymal stem cells: environmental factors affecting cell adhesion and osteogenic differentiation and their mechanisms. Journal of Zhejiang Universty Science B 2020;21(11):871-84.
[92] Shimaoka M, Kawamoto E, Gaowa A, Okamoto T, Park EJ. Connexins and Integrins in Exosomes. Cancers (Basel) 2019;11(1):106.
[93] Stanton AE, Tong X, Yang F. Extracellular matrix type modulates mechanotransduction of stem cells. Acta biomaterialia 2019;96:310-20.
[94] Alberts B. Molecular biology of the cell. WW Norton and Company; 2015.
[95] Visser R, Rico-Llanos GA, Pulkkinen H, Becerra J. Peptides for bone tissue engineering. Journal of controlled release: official journal of the Controlled Release Society 2016;244(Pt A):122-35.
[96] Marie PJ. Targeting integrins to promote bone formation and repair. Nature reviews Endocrinology 2013;9(5):288-95.
[97] Humphries JD, Byron A, Humphries MJ. Integrin ligands at a glance. Journal of cell science 2006;119(Pt 19):3901-3.
[98] Keselowsky BG, Collard DM, García AJ. Integrin binding specificity regulates biomaterial surface chemistry effects on cell differentiation. PNAS 2005;102(17):5953-7.
[99] Maeda T, Titani K, Sekiguchi K. Cell-adhesive activity and receptor-binding specificity of the laminin-derived YIGSR sequence grafted onto Staphylococcal protein A. Journal of biochemistry 1994;115(2):182-9.
[100] Yang Y, Ge S, Song Z, Zhao A, Zhao L, Hu Z, et al. A novel self-assembled epitope peptide nanoemulsion vaccine targeting nasal mucosal epithelial cell for reinvigorating CD8(+) T cell immune activity and inhibiting tumor progression. International journal of biological macromolecules 2021;183:1891-902.

[101] Davis-Hall D, Nguyen V, D'Ovidio TJ, Tsai E, Bilousova G, Magin CM. Peptide-Functionalized Hydrogels Modulate Integrin Expression and Stemness in Adult Human Epidermal Keratinocytes. Advanced biosystems 2019;3(10):e1900022.
[102] Frith JE, Mills RJ, Hudson JE, Cooper-White JJ. Tailored integrin-extracellular matrix interactions to direct human mesenchymal stem cell differentiation. Stem cells and development 2012;21(13):2442-56.
[103] Xiao G, Wang D, Benson MD, Karsenty G, Franceschi RT. Role of the alpha2-integrin in osteoblast-specific gene expression and activation of the Osf2 transcription factor. The Journal of biological chemistry 1998;273(49):32988-94.
[104] Adams JC, Watt FM. Regulation of development and differentiation by the extracellular matrix. Development (Cambridge, England) 1993;117(4):1183-98.
[105] Malcor J-D, Mallein-Gerin F. Biomaterial functionalization with triple-helical peptides for tissue engineering. Acta biomaterialia 2022.
[106] Susek KH, Korpos E, Huppert J, Wu C, Savelyeva I, Rosenbauer F, et al. Bone marrow laminins influence hematopoietic stem and progenitor cell cycling and homing to the bone marrow. Matrix Biology 2018;67:47-62.
[107] Lowin T, Straub RH. Integrins and their ligands in rheumatoid arthritis. Arthritis Research & Therapy 2011;13(5):244.
[108] Yamada M, Sekiguchi K. Molecular Basis of Laminin-Integrin Interactions. Current topics in membranes 2015;76:197-229.
[109] Timpl R. Macromolecular organization of basement membranes. Current opinion in cell biology 1996;8(5):618-24.
[110] Gu Y, Sorokin L, Durbeej M, Hjalt T, Jönsson J-I, Ekblom M. Characterization of Bone Marrow Laminins and Identification of α5-Containing Laminins as Adhesive Proteins for Multipotent Hematopoietic FDCP-Mix Cells. Blood 1999;93(8):2533-42.
[111] Vukicevic S, Luyten FP, Kleinman HK, Reddi AH. Differentiation of canalicular cell processes in bone cells by basement membrane matrix

components: Regulation by discrete domains of laminin. Cell 1990;63(2):437-45.

[112] Li B, Qiu T, Zhang P, Wang X, Yin Y, Li S. IKVAV regulates ERK1/2 and Akt signalling pathways in BMMSC population growth and proliferation. Cell Proliferation 2014;47(2):133-45.

[113] Nakai M, Mundy GR, Williams PJ, Boyce B, Yoneda T. A synthetic antagonist to laminin inhibits the formation of osteolytic metastases by human melanoma cells in nude mice. Cancer research 1992;52(19):5395-9.

[114] Li L, Liu W, Zhao Y, Ma P, Zha S, Chen P, et al. Dual-Peptide-Functionalized Nanofibrous Scaffolds Recruit Host Endothelial Progenitor Cells for Vasculogenesis to Repair Calvarial Defects. ACS Applied Materials & Interfaces 2020;12(3):3474-93.

[115] Perugini V, Meikle ST, Guildford AL, Santin M. Hyperbranched poly(ϵ-lysine) substrate presenting the laminin sequence YIGSR induces the formation of spheroids in adult bone marrow stem cells. Plos One 2017;12(12):e0187182.

[116] Hamblin MR, Pires de Sousa MV, Arany PR, Carroll J, Patthoff DD, editors. Low level laser (light) therapy and photobiomodulation: the path forward. Photonics West - Biomedical Optics; 2015.

[117] D'Amico A, Silva K, Rubero A, Dion S, Gillis J, Gallo J. The Influence of Phototherapy on Recovery From Exercise-Induced Muscle Damage. Internation Journal of Sports Physical Therapy 2022;17(4):658-68.

[118] Hamblin MR. Photobiomodulation or low-level laser therapy. Journal of Biophotonics 2016;9(11-12):1122-4.

[119] Fekrazad R, Asefi S, Allahdadi M, Kalhori KA. Effect of Photobiomodulation on Mesenchymal Stem Cells. Photomedicine and laser surgery 2016;34(11):533-42.

[120] Ailioaie LM, Litscher G. Molecular and Cellular Mechanisms of Arthritis in Children and Adults: New Perspectives on Applied Photobiomodulation 2020;21(18):6565.

[121] Dos Santos Mendes-Costa L, de Lima VG, Barbosa MPR, dos Santos LE, de Siqueira Rodrigues Fleury Rosa S, Tatmatsu-Rocha JC. Photobiomodulation:

systematic review and meta-analysis of the most used parameters in the resolution diabetic foot ulcers. Lasers in medical science 2021;36(6):1129-38.

[122] Huang LD. Brighten the Future: Photobiomodulation and Optogenetics. Focus (American Psychiatric Publishing) 2022;20(1):36-44.

[123] Gupta A, Dai T, Hamblin MR. Effect of red and near-infrared wavelengths on low-level laser (light) therapy-induced healing of partial-thickness dermal abrasion in mice. Lasers in medical science 2014;29(1):257-65.

[124] Najeeb S, Khurshid Z, Zafar MS, Ajlal S. Applications of Light Amplification by Stimulated Emission of Radiation (Lasers) for Restorative Dentistry. Medical principles and practice: international journal of the Kuwait University, Health Science Centre 2016;25(3):201-11.

[125] De Freitas LF, Hamblin MR. Proposed Mechanisms of Photobiomodulation or Low-Level Light Therapy. IEEE journal of selected topics in quantum electronics : a publication of the IEEE Lasers and Electro-optics Society 2016;22(3).

[126] Karu TI, Pyatibrat LV, Kolyakov SF, Afanasyeva NI. Absorption measurements of a cell monolayer relevant to phototherapy: reduction of cytochrome c oxidase under near IR radiation. Journal of photochemistry and photobiology B, Biology 2005;81(2):98-106.

[127] Cardoso FDS, Barrett DW, Wade Z, Gomes da Silva S, Gonzalez-Lima F. Photobiomodulation of Cytochrome c Oxidase by Chronic Transcranial Laser in Young and Aged Brains. Frontiers in neuroscience 2022;16:818005.

[128] Golovynska I, Golovynskyi S, Qu J. Comparing the Impact of NIR, Visible and UV Light on ROS Upregulation via Photoacceptors of Mitochondrial Complexes in Normal, Immune and Cancer Cells. Photochemistry and photobiology 2022.

[129] Giuliani A, Lorenzini L, Gallamini M, Massella A, Giardino L, Calzà L. Low infra red laser light irradiation on cultured neural cells: effects on mitochondria and cell viability after oxidative stress. BMC complementary and alternative medicine 2009;9:8.

[130] Karu TI. Cellular and Molecular Mechanisms of Photobiomodulation (Low-Power Laser Therapy). IEEE Journal of Selected Topics in Quantum Electronics 2014;20(2):143-8.
[131] Zaky AA, El Shenawy HMM, Harhsh TAH, Shalash M, Awad NMI. Can Low Level Laser Therapy Benefit Bone Regeneration in Localized Maxillary Cystic Defects? - A Prospective Randomized Control Trial. Open Access Macedonian Journal of Medical Science 2016;4(4):720-5.
[132] Alves AMM, de Miranda Fortaleza LM, Filho A, Ferreira DCL, da Costa CLS, Viana VGF, et al. Evaluation of bone repair after application of a norbixin membrane scaffold with and without laser photobiomodulation (λ 780 nm). Lasers in medical science 2018;33(7):1493-504.
[133] Wu JY, Chen CH, Yeh LY, Yeh ML, Ting CC, Wang YH. Low-power laser irradiation promotes the proliferation and osteogenic differentiation of human periodontal ligament cells via cyclic adenosine monophosphate. International journal of oral science 2013;5(2):85-91.
[134] Chen CH, Hung HS, Hsu SH. Low-energy laser irradiation increases endothelial cell proliferation, migration, and eNOS gene expression possibly via PI3K signal pathway. Lasers in surgery and medicine 2008;40(1):46-54.
[135] Amaroli A, Agas D, Laus F, Cuteri V, Hanna R, Sabbieti MG, et al. The Effects of Photobiomodulation of 808 nm Diode Laser Therapy at Higher Fluence on the in Vitro Osteogenic Differentiation of Bone Marrow Stromal Cells. Frontiers in physiology 2018;9:123.
[136] Brondon P, Stadler I, Lanzafame RJ. A study of the effects of phototherapy dose interval on photobiomodulation of cell cultures. Lasers in surgery and medicine 2005;36(5):409-13.
[137] Hawkins D, Abrahamse H. Effect of multiple exposures of low-level laser therapy on the cellular responses of wounded human skin fibroblasts. Photomedicine and laser surgery 2006;24(6):705-14.
[138] Atasoy KT, Korkmaz YT, Odaci E, Hanci H. The efficacy of low-level 940 nm laser therapy with different energy intensities on bone healing. Brazilian oral research 2017;31:e7.

[139] Huang YY, Chen AC, Carroll JD, Hamblin MR. Biphasic dose response in low level light therapy. Dose-response : a publication of International Hormesis Society 2009;7(4):358-83.
[140] Shinhmar H, Grewal M, Sivaprasad S, Hogg C, Chong V, Neveu M, et al. Optically Improved Mitochondrial Function Redeems Aged Human Visual Decline. The Journals of Gerontology: Series A 2020;75(9):e49-e52.
[141] Otremski I, Irga D, Edelstein S, Ornoy A, Newman R. Does laser irradiation effect fracture healing? Medical Laser Application 2004;19(3):146-9.
[142] Park IS, Chung PS, Ahn JC. Enhanced angiogenic effect of adipose-derived stromal cell spheroid with low-level light therapy in hind limb ischemia mice. Biomaterials 2014;35(34):9280-9.
[143] Mirza S, Sadiq MSK, Alqahtani A, Al-Saleh S, Alqutub MN, Almubarak AM, et al. The effect of 805 nm near-infrared photobiomodulation on proliferation and differentiation of bone marrow stem cells in murine rats. European review for medical and pharmacological sciences 2021;25(20):6319-25.
[144] Tim CR, Bossini PS, Kido HW, Malavazi I, von Zeska Kress MR, Carazzolle MF, et al. Effects of low-level laser therapy on the expression of osteogenic genes during the initial stages of bone healing in rats: a microarray analysis. Lasers in medical science 2015;30(9):2325-33.
[145] da Rocha EA, Alvarez MMP, Pelosine AM, Carrilho MRO, Tersariol ILS, Nascimento FD. Laser Photobiomodulation 808 nm: Effects on Gene Expression in Inflammatory and Osteogenic Biomarkers in Human Dental Pulp Stem Cells. Front Pharmacolology 2021;12:782095.
[146] Merigo E, Bouvet-Gerbettaz S, Boukhechba F, Rocca J-P, Fornaini C, Rochet N. Green laser light irradiation enhances differentiation and matrix mineralization of osteogenic cells. Journal of Photochemistry and Photobiology B: Biology 2016;155:130-6.
[147] R RP, Da Silva AL, Nacer RS, Vieira RP, de Oliveira LV, Santos de Faria Júnior N, et al. Evaluation of the osteogenic effect of low-level laser therapy (808 nm and 660 nm) on bone defects induced in the femurs of female rats submitted to ovariectomy. Lasers in medical science 2011;26(4):515-22.

[148] Roseti L, Parisi V, Petretta M, Cavallo C, Desando G, Bartolotti I, et al. Scaffolds for Bone Tissue Engineering: State of the art and new perspectives. Materials Science and Engineering: C 2017;78:1246-62.

[149] Sun Y, Ju Y, Fang B. Exosomes from human adipose-derived mesenchymal stromal/stem cells accelerate angiogenesis in wound healing: implication of the EGR-1/lncRNA-SENCR/DKC1/VEGF-A axis. Human Cell 2022.

[150] Xie C, Ye J, Liang R, Yao X, Wu X, Koh Y, et al. Advanced Strategies of Biomimetic Tissue-Engineered Grafts for Bone Regeneration 2021;10.

[151] Cipriano J, Lakshmikanthan A, Buckley C, Mai L, Patel H, Pellegrini M, et al. Characterization of a prevascularized biomimetic tissue engineered scaffold for bone regeneration. Journal of biomedical materials research Part B, Applied biomaterials 2020;108(4):1655-68.

[152] Mercado-Pagán ÁE, Stahl AM, Shanjani Y, Yang Y. Annals of Biomedical Engineering 2015;43(3):718-29.

[153] Santos MI, Reis RL. Vascularization in bone tissue engineering: physiology, current strategies, major hurdles and future challenges. Macromolecular bioscience 2010;10(1):12-27.

[154] Nguyen VT, Canciani B, Cirillo F, Anastasia L, Peretti GM, Mangiavini L. Effect of Chemically Induced Hypoxia on Osteogenic and Angiogenic Differentiation of Bone Marrow Mesenchymal Stem Cells and Human Umbilical Vein Endothelial Cells in Direct Coculture. Cells 2020;9(3):757.

[155] Vestweber D. VE-cadherin: the major endothelial adhesion molecule controlling cellular junctions and blood vessel formation. Arteriosclerosis, thrombosis, and vascular biology 2008;28(2):223-32.

[156] Duong CN, Vestweber D. Mechanisms Ensuring Endothelial Junction Integrity Beyond VE-Cadherin. Frontiers in physiology 2020;11.

[157] Harris ES, Nelson WJ. VE-cadherin: at the front, center, and sides of endothelial cell organization and function. Current opinion in cell biology 2010;22(5):651-8.

[158] Nguyen LH, Annabi N, Nikkhah M, Bae H, Binan L, Park S, et al. Vascularized bone tissue engineering: approaches for potential improvement. Tissue engineering Part B, Reviews 2012;18(5):363-82.

[159] Devescovi V, Leonardi E, Ciapetti G, Cenni E. Growth factors in bone repair. La Chirurgia degli organi di movimento 2008;92(3):161-8.

[160] DeLisser H, Liu Y, Desprez P-Y, Thor A, Briasouli P, Handumrongkul C, et al. Vascular endothelial platelet endothelial cell adhesion molecule 1 (PECAM-1) regulates advanced metastatic progression. Proceedings of the National Academy of Sciences 2010;107(43):18616-21.

[161] Woodfin A, Voisin M-B, Nourshargh S. PECAM-1: A Multi-Functional Molecule in Inflammation and Vascular Biology. Arteriosclerosis, Thrombosis, and Vascular Biology 2007;27(12):2514-23.

[162] Najdanović JG, Cvetković VJ, Stojanović ST, Vukelić-Nikolić MĐ, Živković JM, Najman SJ. Vascularization and osteogenesis in ectopically implanted bone tissue-engineered constructs with endothelial and osteogenic differentiated adipose-derived stem cells. World Journal of Stem Cells 2021;13(1):91-114.

[163] Genova T, Petrillo S, Zicola E, Roato I, Ferracini R, Tolosano E, et al. The Crosstalk Between Osteodifferentiating Stem Cells and Endothelial Cells Promotes Angiogenesis and Bone Formation. Frontiers in Physiology 2019;10.

[164] Bonanini F, Kurek D, Previdi S, Nicolas A, Hendriks D, de Ruiter S, et al. In vitro grafting of hepatic spheroids and organoids on a microfluidic vascular bed. Angiogenesis 2022.

[165] Karaman O, Yaralı ZB. Determination of minimum serum concentration to develop scaffold free micro-tissue. The European Research Journal 2018;4(3):145-51.

[166] Onak G, Şen M, Horzum N, Ercan UK, Yaralı ZB, Garipcan B, et al. Aspartic and Glutamic Acid Templated Peptides Conjugation on Plasma Modified Nanofibers for Osteogenic Differentiation of Human Mesenchymal Stem Cells: A Comparative Study. Scientific Reports 2018;8(1):17620.

[167] Onak G, Gökmen O, Yaralı ZB, Karaman O. Enhanced osteogenesis of human mesenchymal stem cells by self-assembled peptide hydrogel functionalized with glutamic acid templated peptides. Journal of tissue engineering and regenerative medicine 2020;14(9):1236-49.

[168] Heidari-Moghadam A, Bayati V, Orazizadeh M, Rashno M. Role of Vascular Endothelial Growth Factor and Human Umbilical Vein Endothelial Cells in Designing An In Vitro Vascular-Muscle Cellular Model Using Adipose-Derived Stem Cells. Cell journal 2020;22(Suppl 1):19-28.

[169] Jing H, Liao L, Su X, Shuai Y, Zhang X, Deng Z, et al. Declining histone acetyltransferase GCN5 represses BMSC-mediated angiogenesis during osteoporosis. The FASEB Journal 2017;31(10):4422-33.

[170] Steiner D, Mutschall H, Winkler S, Horch RE, Arkudas A. The Adipose-Derived Stem Cell and Endothelial Cell Coculture System-Role of Growth Factors? Cells 2021;10(8).

[171] Jiang M, Shen Q, Zhou Y, Ren W, Chai M, Zhou Y, et al. Fluid shear stress and endothelial cells synergistically promote osteogenesis of mesenchymal stem cells via integrin β1-FAK-ERK1/2 pathway. Turkish journal of biology = Turk biyoloji dergisi 2021;45(6):683-94.

[172] Menge T, Gerber M, Wataha K, Reid W, Guha S, Cox CS, Jr., et al. Human mesenchymal stem cells inhibit endothelial proliferation and angiogenesis via cell-cell contact through modulation of the VE-Cadherin/β-catenin signaling pathway. Stem cells and development 2013;22(1):148-57.

[173] Shibani Pati AYK, Jing Zhao, Fernando Jimenez, Michael H. Gerber, Matthew Harting, John B. Redell, Raymond Grill, Yoichi Matsuo, Sushovan Guha, Charles S. CoxJr., Marvin S. ReitzJr., John B. Holcomb, and Pramod K. Dash. Human Mesenchymal Stem Cells Inhibit Vascular Permeability by Modulating Vascular Endothelial Cadherin/β-Catenin Signaling. Stem cells and development 2011;20(1):89-101.

[174] Gama Sosa MA, De Gasperi R, Perez GM, Hof PR, Elder GA. Hemovasculogenic origin of blood vessels in the developing mouse brain. The Journal of comparative neurology 2021;529(2):340-66.

[175] Liu Z, Qi L, Li Y, Zhao X, Sun B. VEGFR2 regulates endothelial differentiation of colon cancer cells. BMC cancer 2017;17(1):593.

[176] Yu J, Hsu YC, Lee JK, Cheng NC. Enhanced angiogenic potential of adipose-derived stem cell sheets by integration with cell spheroids of the same source. Stem Cell Researcha and Therapy 2022;13(1):276.

[177] Nguyen BB, Moriarty RA, Kamalitdinov T, Etheridge JM, Fisher JP. Collagen hydrogel scaffold promotes mesenchymal stem cell and endothelial cell coculture for bone tissue engineering. Journal of biomedical materials research Part A 2017;105(4):1123-31.
[178] Lee SH, Jin SY, Song JS, Seo KK, Cho KH. Paracrine effects of adipose-derived stem cells on keratinocytes and dermal fibroblasts. Annals of dermatology 2012;24(2):136-43.
[179] Pons J, Huang Y, Arakawa-Hoyt J, Washko D, Takagawa J, Ye J, et al. VEGF improves survival of mesenchymal stem cells in infarcted hearts. Biochemical and Biophysical Research Communication 2008;376(2):419-22.
[180] Lin H, Chen H, Zhao X, Chen Z, Zhang P, Tian Y, et al. Advances in mesenchymal stem cell conditioned medium-mediated periodontal tissue regeneration. Journal of translational medicine 2021;19(1):456.
[181] Mendoza AH, Balzarini D, Alves T, Rovai ES, Holzhausen M. Potential of mesenchymal stem cell sheets on periodontal regeneration: A systematic review of pre-clinical studies. Current stem cell research & therapy 2022.
[182] Ma J, Wu S, Liu J, Liu C, Ni S, Dai T, et al. Synergistic effects of nanoattapulgite and hydroxyapatite on vascularization and bone formation in a rabbit tibia bone defect model. Biomaterials science 2022.
[183] Chen X, Yu B, Wang Z, Li Q, Dai C, Wei J. Progress of Periosteal Osteogenesis: The Prospect of In Vivo Bioreactor. Orthopaedic surgery 2022.
[184] Shekaran A, García AJ. Extracellular matrix-mimetic adhesive biomaterials for bone repair. Journal of biomedical materials research Part A 2011;96(1):261-72.
[185] Alberts B, Johnson A, Lewis J, Raff M, Roberts K, Walter P. Integrins. Molecular Biology of the Cell 4th edition: Garland Science; 2002.
[186] Zhao J, Santino F, Giacomini D, Gentilucci L. Integrin-Targeting Peptides for the Design of Functional Cell-Responsive Biomaterials. Biomedicines 2020;8(9).
[187] Lovitt CJ, Shelper TB, Avery VM. Miniaturized three-dimensional cancer model for drug evaluation. Assay and drug development technologies 2013;11(7):435-48.

[188] Sharipol A, Lesch ML, Soto CA, Frisch BJ. Bone Marrow Microenvironment-On-Chip for Culture of Functional Hematopoietic Stem Cells. Frontiers in bioengineering and biotechnology 2022;10:855777.

[189] Niu H, Xiao J, Lou X, Guo L, Zhang Y, Yang R, et al. Three-Dimensional Silk Fibroin/Chitosan Based Microscaffold for Anticancer Drug Screening. Frontiers in bioengineering and biotechnology 2022;10:800830.

[190] Samimi H, Sohi AN, Irani S, Arefian E, Mahdiannasser M, Fallah P, et al. Alginate-based 3D cell culture technique to evaluate the half-maximal inhibitory concentration: an in vitro model of anticancer drug study for anaplastic thyroid carcinoma. Thyroid research 2021;14(1):27.

[191] Xu J, Qi G, Sui C, Wang W, Sun X. 3D h9e peptide hydrogel: An advanced three-dimensional cell culture system for anticancer prescreening of chemopreventive phenolic agents. Toxicology in vitro 2019;61:104599.

[192] Cirigliano SM, Díaz Bessone MI, Berardi DE, Flumian C, Bal de Kier Joffé ED, Perea SE, et al. The synthetic peptide CIGB-300 modulates CK2-dependent signaling pathways affecting the survival and chemoresistance of non-small cell lung cancer cell lines. Cancer Cell International 2017;17:42.

[193] Dissanayaka WL, Zhu L, Hargreaves KM, Jin L, Zhang C. Scaffold-free Prevascularized Microtissue Spheroids for Pulp Regeneration. Journal of dental research 2014;93(12):1296-303.

[194] Dissanayaka WL, Zhu L, Hargreaves KM, Jin L, Zhang CJJoe. In vitro analysis of scaffold-free prevascularized microtissue spheroids containing human dental pulp cells and endothelial cells. Journal of Endodontics 2015;41(5):663-70.

[195] Yang H, Wang S, Bian H, Xing X, Yu J, Wu X, et al. Extracellular matrix-mimicking nanofibrous chitosan microspheres as cell micro-ark for tissue engineering. Carbohydrate Polymers 2022;292:119693.

[196] Kumar VA, Liu Q, Wickremasinghe NC, Shi S, Cornwright TT, Deng Y, et al. Treatment of hind limb ischemia using angiogenic peptide nanofibers. Biomaterials 2016;98:113-9.

[197] Conway RE, Rojas C, Alt J, Nováková Z, Richardson SM, Rodrick TC, et al. Prostate-specific membrane antigen (PSMA)-mediated laminin proteolysis generates a pro-angiogenic peptide. Angiogenesis 2016;19(4):487-500.

[198] Bohari SP, Grover LM, Hukins DW. Pulsed low-intensity ultrasound increases proliferation and extracelluar matrix production by human dermal fibroblasts in three-dimensional culture. Journal of Tissue Engineering 2015;6:2041731415615777.

[199] Xiang J, Bian Y. PWAR6 interacts with miR-106a-5p to regulate the osteogenic differentiation of human periodontal ligament stem cells. Molecular Medicine Reports 2021;23(4).

[200] Zhu X, Ma K, Zhou K, Voelkl J, Alesutan I, Leibrock C, et al. Reversal of phosphate-induced ORAI1 expression, store-operated Ca2+ entry and osteogenic signaling by MgCl2 in human aortic smooth muscle cells. Biochemical and Biophysical Research Communications 2020;523(1):18-24.

[201] Srinivasan A, Teo N, Poon KJ, Tiwari P, Ravichandran A, Wen F, et al. Comparative Craniofacial Bone Regeneration Capacities of Mesenchymal Stem Cells Derived from Human Neural Crest Stem Cells and Bone Marrow. ACS biomaterials science & engineering 2021;7(1):207-21.

[202] Cheng NC, Chen SY, Li JR, Young TH. Short-term spheroid formation enhances the regenerative capacity of adipose-derived stem cells by promoting stemness, angiogenesis, and chemotaxis. Stem cells translational medicine 2013;2(8):584-94.

[203] Ferreira AM, Gentile P, Chiono V, Ciardelli G. Collagen for bone tissue regeneration. Acta Biomaterialia 2012;8(9):3191-200.

[204] Kim JH, Jekarl DW, Kim M, Oh EJ, Kim Y, Park IY, et al. Effects of ECM protein mimetics on adhesion and proliferation of chorion derived mesenchymal stem cells. International journal of medical sciences 2014;11(3):298-308.

[205] Haugh MG, Vaughan TJ, Madl CM, Raftery RM, McNamara LM, O'Brien FJ, et al. Investigating the interplay between substrate stiffness and ligand chemistry in directing mesenchymal stem cell differentiation within 3D macro-porous substrates. Biomaterials 2018;171:23-33.

[206] Fowler EW, Ravikrishnan A, Witt RL, Pradhan-Bhatt S, Jia X. RGDSP-Decorated Hyaluronate Hydrogels Facilitate Rapid 3D Expansion of Amylase-Expressing Salivary Gland Progenitor Cells. ACS biomaterials science & engineering 2021;7(12):5749-61.

[207] Jain R, Roy S. Controlling Neuronal Cell Growth through Composite Laminin Supramolecular Hydrogels. ACS Biomaterials Science & Engineering 2020;6(5):2832-46.

[208] Zhao T, Sellers DL, Cheng Y, Horner PJ, Pun SH. Tunable, Injectable Hydrogels Based on Peptide-Cross-Linked, Cyclized Polymer Nanoparticles for Neural Progenitor Cell Delivery. Biomacromolecules 2017;18(9):2723-31.

[209] Ding J, Dun Y, He D, Shao Y, Liu F, Zhang L, et al. RGD-Hydrogel Improves the Therapeutic Effect of Bone Marrow-Derived Mesenchymal Stem Cells on Phosgene-Induced Acute Lung Injury in Rats. Computational intelligence and neuroscience 2022;2022:2743878.

[210] Wang F, Nan LP, Zhou SF, Liu Y, Wang ZY, Wang JC, et al. Injectable Hydrogel Combined with Nucleus Pulposus-Derived Mesenchymal Stem Cells for the Treatment of Degenerative Intervertebral Disc in Rats. Stem cells international 2019;2019:8496025.

[211] Dhillon J, Young SA, Sherman SE, Bell GI, Amsden BG, Hess DA, et al. Peptide-modified methacrylated glycol chitosan hydrogels as a cell-viability supporting pro-angiogenic cell delivery platform for human adipose-derived stem/stromal cells. Journal of biomedical materials research Part A 2019;107(3):571-85.

[212] Rinker TE, Hammoudi TM, Kemp ML, Lu H, Temenoff JS. Interactions between mesenchymal stem cells, adipocytes, and osteoblasts in a 3D tri-culture model of hyperglycemic conditions in the bone marrow microenvironment. Integrative biology : quantitative biosciences from nano to macro 2014;6(3):324-37.

[213] Macková H, Plichta Z, Proks V, Kotelnikov I, Kučka J, Hlídková H, et al. RGDS- and SIKVAVS-Modified Superporous Poly(2-hydroxyethyl methacrylate) Scaffolds for Tissue Engineering Applications 2016;16(11):1621-31.

[214] Manferdini C, Trucco D, Saleh Y, Gabusi E, Dolzani P, Lenzi E, et al. RGD-Functionalized Hydrogel Supports the Chondrogenic Commitment of Adipose Mesenchymal Stromal Cells. Gels (Basel, Switzerland) 2022;8(6).

[215] Luo K, Gao X, Gao Y, Li Y, Deng M, Tan J, et al. Multiple integrin ligands provide a highly adhesive and osteoinductive surface that improves selective cell retention technology. Acta Biomaterialia 2019;85:106-16.

[216] Shin YM, Jo SY, Park JS, Gwon HJ, Jeong SI, Lim YM. Synergistic effect of dual-functionalized fibrous scaffold with BCP and RGD containing peptide for improved osteogenic differentiation. Macromolecular bioscience 2014;14(8):1190-8.

[217] Amso Z, Cornish J, Brimble MA. Short Anabolic Peptides for Bone Growth. Medicinal research reviews 2016;36(4):579-640.

[218] Fraioli R, Dashnyam K, Kim JH, Perez RA, Kim HW, Gil J, et al. Surface guidance of stem cell behavior: Chemically tailored co-presentation of integrin-binding peptides stimulates osteogenic differentiation in vitro and bone formation in vivo. Acta biomaterialia 2016;43:269-81.

[219] Chien HW, Fu SW, Shih AY, Tsai WB. Modulation of the stemness and osteogenic differentiation of human mesenchymal stem cells by controlling RGD concentrations of poly(carboxybetaine) hydrogel. Biotechnology journal 2014;9(12):1613-23.

[220] Wang D, Liao X, Qin X, Shi W, Zhou B. A novel chimeric peptide binds MC3T3-E1 cells to titanium and enhances their proliferation and differentiation. Molecular Medicine Reports 2013;7(5):1437-41.

[221] Itoh S, Yamaguchi I, Suzuki M, Ichinose S, Takakuda K, Kobayashi H, et al. Hydroxyapatite-coated tendon chitosan tubes with adsorbed laminin peptides facilitate nerve regeneration in vivo. Brain Research 2003;993(1):111-23.

[222] Ravindranath N, Papadopoulos V, Brooker G, Dym M. Rat Sertoli cell calcium response to basement membrane and follicle-stimulating hormone. Biology of reproduction 1996;54(1):130-7.

[223] Balion Z, Sipailaite E, Stasyte G, Vailionyte A, Mazetyte-Godiene A, Seskeviciute I, et al. Investigation of Cancer Cell Migration and Proliferation

on Synthetic Extracellular Matrix Peptide Hydrogels. Frontiers in bioengineering and biotechnology 2020;8:773.

[224] Whalen MS, Daso RE, Thomas MF, Banerjee IA. Interactions of betainium and imidazolium-based ionic liquids with peptide amphiphiles and their implications in the formation of nanohybrid composite gels. Journal of Sol-Gel Science and Technology 2021;97(2):488-504.

[225] Wu G, Li X, Seo H, McLendon BA, Kramer AC, Bazer FW, et al. Osteopontin (OPN)/Secreted Phosphoprotein 1 (SPP1) Binds Integrins to Activate Transport of Ions Across the Porcine Placenta 2022;27(4).

[226] Zhou N, Ma X, Hu W, Ren P, Zhao Y, Zhang T. Effect of RGD content in poly(ethylene glycol)-crosslinked poly(methyl vinyl ether-alt-maleic acid) hydrogels on the expansion of ovarian cancer stem-like cells. Materials Science and Engineering: C 2021;118:111477.

[227] Zhang D, Kilian KA. Peptide microarrays for the discovery of bioactive surfaces that guide cellular processes: a single step azide-alkyne "click" chemistry approach. Journal of materials chemistry B 2014;2(27):4280-8.

[228] Dos Santos BP, Garbay B, Fenelon M, Rosselin M, Garanger E, Lecommandoux S, et al. Development of a cell-free and growth factor-free hydrogel capable of inducing angiogenesis and innervation after subcutaneous implantation. Acta biomaterialia 2019;99:154-67.

[229] Park JS, Yang HN, Jeon SY, Woo DG, Na K, Park K-H. Osteogenic differentiation of human mesenchymal stem cells using RGD-modified BMP-2 coated microspheres. Biomaterials 2010;31(24):6239-48.

[230] Gronthos S, Simmons PJ, Graves SE, Robey PG. Integrin-mediated interactions between human bone marrow stromal precursor cells and the extracellular matrix. Bone 2001;28(2):174-81.

[231] Carvalho MS, Cabral JMS, da Silva CL, Vashishth D. Bone Matrix Non-Collagenous Proteins in Tissue Engineering: Creating New Bone by Mimicking the Extracellular Matrix. Polymers 2021;13(7).

[232] Plow EF, Haas TA, Zhang L, Loftus J, Smith JW. Ligand binding to integrins. The Journal of biological chemistry 2000;275(29):21785-8.

[233] Schaffner F, Ray AM, Dontenwill M. Integrin α5β1, the Fibronectin Receptor, as a Pertinent Therapeutic Target in Solid Tumors. Cancers 2013;5(1):27-47.

[234] Nagae M, Re S, Mihara E, Nogi T, Sugita Y, Takagi JT. Crystal structure of α5β1 integrin ectodomain: Atomic details of the fibronectin receptor. The Journal of Cell Biology 2012;197(1):131-40.

[235] Qu H, Fu H, Han Z, Sun Y. Biomaterials for bone tissue engineering scaffolds: A review. RSC advances 2019;9(45):26252-62.

[236] Ciuffreda MC, Malpasso G, Musarò P, Turco V, Gnecchi M. Protocols for in vitro Differentiation of Human Mesenchymal Stem Cells into Osteogenic, Chondrogenic and Adipogenic Lineages. In: Gnecchi M, editor. Mesenchymal Stem Cells: Methods and Protocols. New York, NY: Springer New York; 2016. p. 149-58.

[237] Paschos NK, Brown WE, Eswaramoorthy R, Hu JC, Athanasiou KA. Advances in tissue engineering through stem cell-based co-culture. Journal of tissue engineering and regenerative medicine 2015;9(5):488-503.

[238] Meng X, Gao X, Chen X, Yu J. Umbilical cord-derived mesenchymal stem cells exert anti-fibrotic action on hypertrophic scar-derived fibroblasts in co-culture by inhibiting the activation of the TGF β1/Smad3 pathway. Experimental and Therapeutic Medicine 2021;21(3):1-.

[239] Bidarra SJ, Barrias CC, Barbosa MA, Soares R, Amédée J, Granja PL. Phenotypic and proliferative modulation of human mesenchymal stem cells via crosstalk with endothelial cells. Stem cell research 2011;7(3):186-97.

[240] Choi K, Kang BJ, Kim H, Lee S, Bae S, Kweon OK, et al. Low-level laser therapy promotes the osteogenic potential of adipose-derived mesenchymal stem cells seeded on an acellular dermal matrix. Journal of Biomedical Materials Research Part B: Applied Biomaterials 2013;101(6):919-28.

[241] Alves AMM, de Miranda Fortaleza LM, Ferreira DCL, da Costa CLS, Viana VGF, Santos JZLV, et al. Evaluation of bone repair after application of a norbixin membrane scaffold with and without laser photobiomodulation (λ 780 nm). Lasers in medical science 2018;33(7):1493-504.

[242] Amaroli A, Agas D, Laus F, Cuteri V, Hanna R, Sabbieti MG, et al. The effects of photobiomodulation of 808 nm diode laser therapy at higher fluence on the

in vitro osteogenic differentiation of bone marrow stromal cells. Frontiers in physiology 2018;9:123.

[243] Karu TI. Cellular and molecular mechanisms of photobiomodulation (low-power laser therapy). IEEE Journal of Selected Topics in Quantum Electronics 2013;20(2):143-8.

[244] Bai J, Li L, Kou N, Bai Y, Zhang Y, Lu Y, et al. Low level laser therapy promotes bone regeneration by coupling angiogenesis and osteogenesis. Stem Cell Research & Therapy 2021;12(1):432.

[245] Tani A, Chellini F, Giannelli M, Nosi D, Zecchi-Orlandini S, Sassoli C. Red (635 nm), Near-Infrared (808 nm) and Violet-Blue (405 nm) Photobiomodulation Potentiality on Human Osteoblasts and Mesenchymal Stromal Cells: A Morphological and Molecular In Vitro Study. International Journal of Molecular Science 2018;19(7).

[246] Topaloglu N, Özdemir M, Çevik ZBY. Comparative analysis of the light parameters of red and near-infrared diode lasers to induce photobiomodulation on fibroblasts and keratinocytes: An in vitro study. Photodermatology, photoimmunology & photomedicine 2021;37(3):253-62.

[247] Dompe C, Moncrieff L, Matys J, Grzech-Leśniak K, Kocherova I, Bryja A, et al. Photobiomodulation—underlying mechanism and clinical applications. Journal of clinical medicine 2020;9(6):1724.

[248] Hawkins D, Abrahamse H. Effect of multiple exposures of low-level laser therapy on the cellular responses of wounded human skin fibroblasts. Photomedicine and Laser Surgery 2006;24(6):705-14.

[249] Karic V, Chandran R, Abrahamse H, Medicine. Laser-Induced Differentiation of Human Adipose-Derived Stem Cells to Temporomandibular Joint Disc Cells. Lasers in Surgery and Medicine 2021;53(4):567-77.

[250] Brondon P, Stadler I, Lanzafame RJ. A study of the effects of phototherapy dose interval on photobiomodulation of cell cultures. Lasers in Surgery and Medicine 2005;36(5):409-13.

[251] Cronshaw M, Parker S, Anagnostaki E, Mylona V, Lynch E, Grootveld M. Photobiomodulation dose parameters in dentistry: a systematic review and meta-analysis. Dentistry Journal 2020;8(4):114.

[252] Liang CC, Park AY, Guan JL. In vitro scratch assay: a convenient and inexpensive method for analysis of cell migration in vitro. Nature protocols 2007;2(2):329-33.

[253] Topaloglu N, Bakay E. Mechanistic approaches to the light-induced neural cell differentiation: Photobiomodulation vs Low-Dose Photodynamic Therapy. Photodiagnosis and Photodynamic Therapy 2022;37:102702.

[254] Negri LB, Martins TJ, da Silva RS, Hamblin MR. Photobiomodulation combined with photodynamic therapy using ruthenium phthalocyanine complexes in A375 melanoma cells: Effects of nitric oxide generation and ATP production. Journal of Photochemistry and Photobiology B: Biology 2019;198:111564.

[255] Crous A, Jansen van Rensburg M, Abrahamse H. Single and consecutive application of near-infrared and green irradiation modulates adipose derived stem cell proliferation and affect differentiation factors. Biochimie 2022;196:225-33.

[256] Gerdes S, Mostafavi A, Ramesh S, Memic A, Rivero IV, Rao P, et al. Process-Structure-Quality Relationships of Three-Dimensional Printed Poly(Caprolactone)-Hydroxyapatite Scaffolds. Tissue engineering Part A 2020;26(5-6):279-91.

[257] Zecha JA, Raber-Durlacher JE, Nair RG, Epstein JB, Sonis ST, Elad S, et al. Low level laser therapy/photobiomodulation in the management of side effects of chemoradiation therapy in head and neck cancer: part 1: mechanisms of action, dosimetric, and safety considerations. Supportive care in cancer : official journal of the Multinational Association of Supportive Care in Cancer 2016;24(6):2781-92.

[258] Amaroli A, Ravera S, Parker S, Panfoli I, Benedicenti A, Benedicenti S, et al. An 808-nm diode laser with a flat-top handpiece positively photobiomodulates mitochondria activities. Photomedicine and Laser Surgery 2016;34(11):564-71.

[259] Stamborowski SF, de Oliveira Spinelli BM, Lima FPS, Costa DR, de Silveira Souza GA, Lima MO, et al. The influence of photobiomodulation on the

temperature of the brachial biceps during muscle fatigue protocol. Lasers in medical science 2021;36(8):1741-9.

[260] Wang X, Wanniarachchi H, Wu A, Gonzalez-Lima F, Liu H. Transcranial photobiomodulation and thermal stimulation induce distinct topographies of EEG alpha and beta power changes in healthy humans. Scientific reports 2021;11(1):18917-.

[261] Zein R, Selting W, Hamblin MR. Review of light parameters and photobiomodulation efficacy: dive into complexity. Journal of biomedical optics 2018;23(12):120901.

[262] Lanzafame RJ, Stadler I, Kurtz AF, Connelly R, A. Peter Sr. T, Brondon P, et al. Reciprocity of exposure time and irradiance on energy density during photoradiation on wound healing in a murine pressure ulcer model. Lasers in surgery and medicine 2007;39(6):534-42.

[263] Al-Watban FA, Zhang X. The comparison of effects between pulsed and CW lasers on wound healing. Journal of clinical laser medicine & surgery 2004;22(1):15-8.

[264] Mokoena DR, Houreld NN, Sathish S, Dhilip K, Abrahamse H. Photobiomodulation at 660 nm stimulates fibroblast differentiation. Lasers in Surgery and Medicine 2020;52(7):671-81.

[265] Abdalla M, Nagy A, Ye WN, Mussivand T, editors. Overview of photo-induced therapy for ATP production. Photonics North 2012; 2012: SPIE.

[266] Amaroli A, Pasquale C, Zekiy A, Utyuzh A, Benedicenti S, Signore A, et al. Photobiomodulation and oxidative stress: 980 nm diode laser light regulates mitochondrial activity and reactive oxygen species production. Hindawi: Oxidative Medicine and Cellular Longevity 2021; 6626286; p 11.

[267] Sharma SK, Kharkwal GB, Sajo M, Huang YY, De Taboada L, McCarthy T, et al. Dose response effects of 810 nm laser light on mouse primary cortical neurons. Lasers in Surgery and Medicine 2011;43(8):851-9.

[268] Basso FG, Soares DG, de Souza Costa CA, Hebling J. Low-level laser therapy in 3D cell culture model using gingival fibroblasts. Lasers in medical science 2016;31(5):973-8.

[269] Özdemir M, Çevik ZBY, Topaloğlu N, editors. The Effect of Photobiomodulation with Red and Near-Infrared Wavelengths on Keratinocyte Cells. 2020 Medical Technologies Congress (TIPTEKNO); IEEE 2020.

[270] Chang B, Qiu H, Zhao H, Yang X, Wang Y, Ji T, et al. The effects of photobiomodulation on MC3T3-E1 cells via 630 nm and 810 nm light-emitting diode. Medical Science Monitor 2019;25:8744.

[271] Bueno NP, Copete IN, Lopes HB, Arany PR, Marques MM, Ferraz EPJJoB. Recovering the osteoblastic differentiation potential of mesenchymal stem cells derived from diabetic rats by photobiomodulation therapy. Journal of biophotonics 2021;14(3):e202000393.

[272] Diniz IM, Carreira AC, Sipert CR, Uehara CM, Moreira MS, Freire L, et al. Photobiomodulation of mesenchymal stem cells encapsulated in an injectable rhBMP4-loaded hydrogel directs hard tissue bioengineering. Journal of Cellular Physiology 2018;233(6):4907-18.

[273] Mohamed-Ahmed S, Fristad I, Lie SA, Suliman S, Mustafa K, Vindenes H, et al. Adipose-derived and bone marrow mesenchymal stem cells: a donor-matched comparison. Stem Cell Research & Therapy 2018;9(1):168.

[274] Ghidini G, Mori D, Pulcini S, Vescovi P, Sala R. Photobiomodulation with a 645 nm Diode Laser of Saos-2 Cells and Platelet-Rich Plasma: The Potential for a New Mechanism of Action. Photobiomodulation, Photomedicine, and Laser Surgery 2021;39(2):86-93.

[275] Ferreira LS, Diniz IMA, Maranduba CMS, Miyagi SPH, Rodrigues M, Moura-Netto C, et al. Short-term evaluation of photobiomodulation therapy on the proliferation and undifferentiated status of dental pulp stem cells. Lasers in medical science 2019;34(4):659-66.

[276] Soleimani M, Abbasnia E, Fathi M, Sahraei H, Fathi Y, Kaka G. The effects of low-level laser irradiation on differentiation and proliferation of human bone marrow mesenchymal stem cells into neurons and osteoblasts--an in vitro study. Lasers in medical science 2012;27(2):423-30.

[277] Zhang X, Li J, Ye P, Gao G, Hubbell K, Cui X. Coculture of mesenchymal stem cells and endothelial cells enhances host tissue integration and epidermis

maturation through AKT activation in gelatin methacryloyl hydrogel-based skin model. Acta biomaterialia 2017;59:317-26.
[278] Ball SG, Shuttleworth AC, Kielty CM. Direct cell contact influences bone marrow mesenchymal stem cell fate. The international journal of biochemistry & cell biology 2004;36(4):714-27.
[279] Kaigler D, Krebsbach PH, West ER, Horger K, Huang YC, Mooney DJ. Endothelial cell modulation of bone marrow stromal cell osteogenic potential. FASEB journal: official publication of the Federation of American Societies for Experimental Biology 2005;19(6):665-7.
[280] He Y, Lin S, Ao Q, He X. The co-culture of ASCs and EPCs promotes vascularized bone regeneration in critical-sized bone defects of cranial bone in rats. Stem Cell Research & Therapy 2020;11(1):338.
[281] Chen CH, Hung HS, Hsu Sh. Low-energy laser irradiation increases endothelial cell proliferation, migration, and eNOS gene expression possibly via PI3K signal pathway. Lasers in Surgery and Medicine: The Official Journal of the American Society for Laser Medicine and Surgery 2008;40(1):46-54.
[282] Wang L, Wu F, Liu C, Song Y, Guo J, Yang Y, et al. Low-level laser irradiation modulates the proliferation and the osteogenic differentiation of bone marrow mesenchymal stem cells under healthy and inflammatory condition. Lasers in medical science 2019;34(1):169-78.
[283] Wang Y, Huang Y-Y, Wang Y, Lyu P, Hamblin MR. Photobiomodulation of human adipose-derived stem cells using 810 nm and 980 nm lasers operates via different mechanisms of action. Biochimica et Biophysica Acta (BBA)-General Subjects 2017;1861(2):441-9.
[284] Zecha JA, Raber-Durlacher JE, Nair RG, Epstein JB, Sonis ST, Elad S, et al. Low level laser therapy/photobiomodulation in the management of side effects of chemoradiation therapy in head and neck cancer: part 1: mechanisms of action, dosimetric, and safety considerations. Supportive Care in Cancer 2016;24(6):2781-92.
[285] Wu J-Y, Chen C-H, Yeh L-Y, Yeh M-L, Ting C-C, Wang Y-H. Low-power laser irradiation promotes the proliferation and osteogenic differentiation of

human periodontal ligament cells via cyclic adenosine monophosphate. International journal of oral science 2013;5(2):85-91.

[286] Zaky AA, El Shenawy HMM, Harhsh TAH, Shalash M, Awad NMI. Can low level laser therapy benefit bone regeneration in localized maxillary cystic defects?-a prospective randomized control trial. Open Access Macedonian Journal of Medical Science 2016;4(4):720.

[287] Alves AMM, de Miranda Fortaleza LM, Maia Filho ALM, Ferreira DCL, da Costa CLS, Viana VGF, et al. Evaluation of bone repair after application of a norbixin membrane scaffold with and without laser photobiomodulation (λ 780 nm). Lasers in medical science 2018;33(7):1493-504.

[288] Giuliani A, Lorenzini L, Gallamini M, Massella A, Giardino L, Calzà L. Low infra red laser light irradiation on cultured neural cells: effects on mitochondria and cell viability after oxidative stress. BMC complementary and alternative medicine 2009;9(1):1-10.

[289] Huang Y-Y, Chen ACH, Carroll JD, Hamblin MR. Biphasic dose response in low level light therapy. Dose-response : a publication of International Hormesis Society 2009;7(4):358-83.

[290] Niemz MH. Laser-tissue interactions: Springer; 2007.

[291] Tani A, Chellini F, Giannelli M, Nosi D, Zecchi-Orlandini S, Sassoli C. Red (635 nm), near-infrared (808 nm) and violet-blue (405 nm) photobiomodulation potentiality on human osteoblasts and mesenchymal stromal cells: a morphological and molecular in vitro study. International Journal of Molecular Science 2018;19(7):1946.

[292] Tim CR, Bossini PS, Kido HW, Malavazi I, von Zeska Kress MR, Carazzolle MF, et al. Effects of low-level laser therapy on the expression of osteogenic genes during the initial stages of bone healing in rats: a microarray analysis. Lasers in medical science 2015;30(9):2325-33.

[293] Atasoy KT, Korkmaz YT, Odaci E, Hanci H. The efficacy of low-level 940 nm laser therapy with different energy intensities on bone healing. Brazilian oral research 2017;31.

[294] Futrega K, Mosaad E, Chambers K, Lott W, Clements J, Doran M. Bone marrow-derived stem/stromal cells (BMSC) 3D microtissues cultured in BMP-

2 supplemented osteogenic induction medium are prone to adipogenesis. Cell and tissue research 2018;374(3):541-53.

[295] Dissanayaka W, Zhu L, Hargreaves K, Jin L, Zhang C. Scaffold-free prevascularized microtissue spheroids for pulp regeneration. Journal of Dental Research 2014;93(12):1296-303.

[296] Yarali ZB, Uzun A, Karaman DŞ, Karaman O, editors. Feasibility Study of Mesoporous Silica Nanoparticles Permeability through the Cancer Microtissues. 2018 Medical Technologies National Congress (TIPTEKNO); IEEE 2018.

[297] Walmsley GG, Ransom RC, Zielins ER, Leavitt T, Flacco JS, Hu MS, et al. Stem Cells in Bone Regeneration. Stem cell reviews and reports 2016;12(5):524-9.

[298] Jensen C, Teng Y. Is It Time to Start Transitioning From 2D to 3D Cell Culture? Frontiers in Molecular Bioscience 2020;7(33).

[299] Imamura Y, Mukohara T, Shimono Y, Funakoshi Y, Chayahara N, Toyoda M, et al. Comparison of 2D- and 3D-culture models as drug-testing platforms in breast cancer. Oncology Reports 2015;33(4):1837-43.

[300] Kapałczyńska M, Kolenda T, Przybyła W, Zajączkowska M, Teresiak A, Filas V, et al. 2D and 3D cell cultures - a comparison of different types of cancer cell cultures. Archives of Medical Science 2018;14(4):910-9.

[301] Saleh F, Whyte M, Genever P. Effects of endothelial cells on human mesenchymal stem cell activity in a three-dimensional in vitro model. European Cells & Materials 2011;22(242):e57.

[302] Wolint P, Bopp A, Woloszyk A, Tian Y, Evrova O, Hilbe M, et al. Cellular self-assembly into 3D microtissues enhances the angiogenic activity and functional neovascularization capacity of human cardiopoietic stem cells. Angiogenesis 2019;22(1):37-52.

[303] Topaloglu N, Özdemir M, Çevik ZBY. Comparative analysis of the light parameters of red and near-infrared diode lasers to induce photobiomodulation on fibroblasts and keratinocytes: An in vitro study. Photodermatology, Photoimmunology & Photomedicine 2021;37(3):253-62.

[304] Ren L, Ma D, Liu B, Li J, Chen J, Yang D, et al. Preparation of Three-Dimensional Vascularized MSC Cell Sheet Constructs for Tissue Regeneration. BioMed Research International 2014;2014:301279.

[305] Onak G, Şen M, Horzum N, Ercan UK, Yaralı ZB, Garipcan B, et al. Aspartic and Glutamic Acid Templated Peptides Conjugation on Plasma Modified Nanofibers for Osteogenic Differentiation of Human Mesenchymal Stem Cells: A Comparative Study. Scientific Reports 2018;8(1):17620.

[306] Karaman O, Yaralı ZB. Determination of minimum serum concentration to develop scaffold free micro-tissue. The European Research Journal 2018;4(3):145-51.

[307] Sun L, Jiang W, Zhang H, Guo Y, Chen W, Jin Y, et al. Photosensitizer-Loaded Multifunctional Chitosan Nanoparticles for Simultaneous in Situ Imaging, Highly Efficient Bacterial Biofilm Eradication, and Tumor Ablation. ACS Applied Materials & Interfaces 2019;11(2):2302-16.

[308] Srinivasan A, Teo N, Poon KJ, Tiwari P, Ravichandran A, Wen F, et al. Comparative Craniofacial Bone Regeneration Capacities of Mesenchymal Stem Cells Derived from Human Neural Crest Stem Cells and Bone Marrow. ACS Biomaterials Science & Engineering 2021;7(1):207-21.

[309] Kang Y, Kim S, Fahrenholtz M, Khademhosseini A, Yang Y. Osteogenic and angiogenic potentials of monocultured and co-cultured human-bone-marrow-derived mesenchymal stem cells and human-umbilical-vein endothelial cells on three-dimensional porous beta-tricalcium phosphate scaffold. Acta biomaterialia 2013;9(1):4906-15.

[310] Topaloglu N, Güney M, Yuksel S, Gülsoy M. Antibacterial photodynamic therapy with 808-nm laser and indocyanine green on abrasion wound models. Journal of biomedical optics 2015;20(2):28003.

[311] Szezerbaty SKF, de Oliveira RF, Pires-Oliveira DA, Soares CP, Sartori D, Poli-Frederico RCJLims. The effect of low-level laser therapy (660 nm) on the gene expression involved in tissue repair. Lasers in medical science 2018;33(2):315-21.

[312] Soleimani M, Abbasnia E, Fathi M, Sahraei H, Fathi Y, Kaka G. The effects of low-level laser irradiation on differentiation and proliferation of human bone

marrow mesenchymal stem cells into neurons and osteoblasts—an in vitro study. Lasers in medical science 2012;27(2):423-30.

[313] Osaki T, Sakata I, Uto Y, Yamashita M, Murahata Y, Azuma K, et al. Effects of TONS504-photodynamic therapy on mouse mammary tumor cells. Oncology Letters 2018;16(2):2078-84.

[314] Yang J, Wang L, Wu MX. 830 nm photobiomodulation therapy promotes engraftment of human umbilical cord blood-derived hematopoietic stem cells. Scientific Reports 2020;10(1):19671.

[315] Edmondson R, Broglie JJ, Adcock AF, Yang L. Three-dimensional cell culture systems and their applications in drug discovery and cell-based biosensors. Assay and drug development technologies 2014;12(4):207-18.

[316] Stein E, Koehn J, Sutter W, Wendtlandt G, Wanschitz F, Thurnher D, et al. Initial effects of low-level laser therapy on growth and differentiation of human osteoblast-like cells. Wien Klinche Wochenschrift 2008;120(3):112-7.

[317] Abdalla M, Nagy A, Ye WN, Mussivand T, editors. Overview of photo-induced therapy for ATP production. Photonics North 2012; 2012: International Society for Optics and Photonics.

[318] Moriyama Y, Moriyama EH, Blackmore K, Akens MK, Lilge L. In vivo study of the inflammatory modulating effects of low-level laser therapy on iNOS expression using bioluminescence imaging. Photochemistry and photobiology 2005;81(6):1351-5.

[319] Modi PK, Prabhu A, Bhandary YP, Shenoy P S, Hegde A, Es SP, et al. Effect of calcium glucoheptonate on proliferation and osteogenesis of osteoblast-like cells in vitro. Plos One 2019;14(9):e0222240.

[320] Ricard-Blum SJCSHpib. The collagen family. Cold Spring Harbor Perspectives Biology 2011;3(1):a004978.

[321] Ferreira AM, Gentile P, Chiono V, Ciardelli GJAb. Collagen for bone tissue regeneration. Acta Biomaterials 2012;8(9):3191-200.

[322] Sodek J, Ganss B, McKee MJ. Osteopontin. Critical Review Oral Biology Medicine 2000;11(3):279-303.

[323] de Oliveira VT, Ferrara-Jr JI, Matielo HA, da Silva Alves A, Britto LR, Aranha ACC, et al. Involvement of substance P, osteopontin and satellite glial cells on

photobiomodulation-induced antinociceptive effect in an experimental model of dentin hypersensitivity. Lasers in medical science 2021;36(6):1297-305.

[324] Koons GL, Diba M, Mikos AG. Materials design for bone-tissue engineering. Nature Reviews Materials 2020;5(8):584-603.

[325] Ruoslahti E, Pierschbacher MD. New Perspectives in Cell Adhesion: RGD and Integrins. Science 1987;238(4826):491-7.

[326] Nagasaki K, Chavez MB, Nagasaki A, Taylor JM, Tan MH, Ma M, et al. The Bone Sialoprotein RGD Domain Modulates and Maintains Periodontal Development. Journal of Dental Research 2022;0(0):00220345221100794.

[327] Karamat-Ullah N, Demidov Y, Schramm M, Grumme D, Auer J, Bohr C, et al. 3D Printing of Antibacterial, Biocompatible, and Biomimetic Hybrid Aerogel-Based Scaffolds with Hierarchical Porosities via Integrating Antibacterial Peptide-Modified Silk Fibroin with Silica Nanostructure. ACS biomaterials science & engineering 2021;7(9):4545-56.

[328] Kim HJ, You SJ, Yang DH, Eun J, Park HK, Kim MS, et al. Injectable hydrogels based on MPEG-PCL-RGD and BMSCs for bone tissue engineering. Biomaterials science 2020;8(15):4334-45.

[329] Najafi H, Abolmaali SS, Heidari R, Valizadeh H, Tamaddon AM, Azarpira N. Integrin receptor-binding nanofibrous peptide hydrogel for combined mesenchymal stem cell therapy and nitric oxide delivery in renal ischemia/reperfusion injury. Stem Cell Reseach & Therapy 2022;13(1):344.

[330] Zwiri AM, Ahmad W, Asif JA, Phaik KS, Husein A, Kassim NK, et al. A Randomized Controlled Trial Evaluating the Levels of the Biomarkers hs-CRP, IL-6, and IL-8 in Patients with Temporomandibular Disorder Treated with LLLT, Traditional Conservative Treatment, and a Combination of Both. International journal of environmental research and public health 2022;19(15).

[331] Zhang P, Wang C, Zhao J, Xiao A, Shen Q, Li L, et al. Near Infrared-Guided Smart Nanocarriers for MicroRNA-Controlled Release of Doxorubicin/siRNA with Intracellular ATP as Fuel. ACS Nanotechnology 2016;10(3):3637-47.

[332] Yu M, Zeng W, Ouyang Y, Liang S, Yi Y, Hao H, et al. ATP-exhausted nanocomplexes for intratumoral metabolic intervention and photoimmunotherapy. Biomaterials 2022;284:121503.

[333] Wu X, Wang L, Xu YN, Chen JL, Luo KQ, Yuan MH, et al. Chemo-Phototherapy with Carfilzomib-Encapsulated TiN Nanoshells Suppressing Tumor Growth and Lymphatic Metastasis. Small (Weinheim an der Bergstrasse, Germany) 2022;18(29):e2200522.

[334] Silva SK, Plepis AMG, Martins V, Horn MM, Buchaim DV, Buchaim RL, et al. Suitability of Chitosan Scaffolds with Carbon Nanotubes for Bone Defects Treated with Photobiomodulation. International Journal of Molecular Science 2022;23(12).

[335] Lee JH, Kim KH, Kwon OH, Kwon OK, Uyama H, Kim YJ. Photodynamic Activity of Protoporphyrin IX-Immobilized Cellulose Monolith for Nerve Tissue Regeneration. International Journal of Molecular Science 2022;23(3).

[336] Cai W, Hamushan M, Zhang Y, Xu Z, Ren Z, Du J, et al. Synergistic Effects of Photobiomodulation Therapy with Combined Wavelength on Diabetic Wound Healing In Vitro and In Vivo. Photobiomodulation & Photomedicine in Laser Surgery 2022;40(1):13-24.

[337] Choi K, Kang BJ, Kim H, Lee S, Bae S, Kweon OK, et al. Low-level laser therapy promotes the osteogenic potential of adipose-derived mesenchymal stem cells seeded on an acellular dermal matrix. Journal of biomedical materials research Part B, Applied biomaterials 2013;101(6):919-28.

[338] AlGhamdi KM, Kumar A, Moussa NA. Low-level laser therapy: a useful technique for enhancing the proliferation of various cultured cells. Lasers in medical science 2012;27(1):237-49.

[339] Gutiérrez D, Rouabhia M, Ortiz J, Gaviria D, Alfonso C, Muñoz A, et al. Low-Level Laser Irradiation Promotes Proliferation and Differentiation on Apical Papilla Stem Cells. Journal of lasers in medical sciences 2021;12:e75.

[340] Kim H, Kim MJ, Kwon YW, Jeon S, Lee SY, Kim CS, et al. Benefits of a Skull-Interfaced Flexible and Implantable Multilight Emitting Diode Array for Photobiomodulation in Ischemic Stroke. Advanced science (Weinheim, Baden-Wurttemberg, Germany) 2022;9(11):e2104629.

[341] Ji B, Guo Z, Wang M, Yang B, Wang X, Li W, et al. Flexible polyimide-based hybrid opto-electric neural interface with 16 channels of micro-LEDs and electrodes. Microsystems & Nanoengineering 2018;4(1):27.

[342] Kim W, Gwon Y, Park S, Kim H, Kim J. Therapeutic strategies of three-dimensional stem cell spheroids and organoids for tissue repair and regeneration. Bioactive Materials 2023;19:50-74.
[343] Lotsberg ML, Røsland GV, Rayford AJ, Dyrstad SE, Ekanger CT, Lu N, et al. Intrinsic Differences in Spatiotemporal Organization and Stromal Cell Interactions Between Isogenic Lung Cancer Cells of Epithelial and Mesenchymal Phenotypes Revealed by High-Dimensional Single-Cell Analysis of Heterotypic 3D Spheroid Models. Frontiers in oncology 2022;12:818437.
[344] Beauchamp P, Jackson CB, Ozhathil LC, Agarkova I, Galindo CL, Sawyer DB, et al. 3D Co-culture of hiPSC-Derived Cardiomyocytes With Cardiac Fibroblasts Improves Tissue-Like Features of Cardiac Spheroids. Frontiers in molecular biosciences 2020;7:14.
[345] Tidwell TR, Røsland GV, Tronstad KJ, Søreide K, Hagland HR. Metabolic flux analysis of 3D spheroids reveals significant differences in glucose metabolism from matched 2D cultures of colorectal cancer and pancreatic ductal adenocarcinoma cell lines. Cancer & metabolism 2022;10(1):9.
[346] Mokhtari RB, Qorri B, Sambi M, Baluch N, Kumar S, Das B, et al. 3D Multicellular Stem-Like Human Breast Tumor Spheroids Enhance Tumorigenicity of Orthotopic Xenografts in Athymic Nude Rat Model. Cancers (Basel) 2021;13(11).
[347] Luo L, Zhang W, Wang J, Zhao M, Shen K, Jia Y, et al. A Novel 3D Culture Model of Human ASCs Reduces Cell Death in Spheroid Cores and Maintains Inner Cell Proliferation Compared With a Nonadherent 3D Culture. Frontiers in cell and developmental biology 2021;9:737275.
[348] Kargozar S, Mozafari M, Hamzehlou S, Brouki Milan P, Kim HW, Baino FJAS. Bone Tissue Engineering Using Human Cells: A Comprehensive Review on Recent Trends, Current Prospects, and Recommendations 2019.
[349] Lopes D, Martins-Cruz C, Oliveira MB, Mano JF. Bone physiology as inspiration for tissue regenerative therapies. Biomaterials 2018;185:240-75.

[350] Shafiee S, Shariatzadeh S, Zafari A, Majd A, Niknejad H. Recent Advances on Cell-Based Co-Culture Strategies for Prevascularization in Tissue Engineering. Frontiers in bioengineering and biotechnology 2021;9:745314.

[351] Onak G, Gökmen O, Yaralı ZB, Karaman O. Enhanced osteogenesis of human mesenchymal stem cells by self-assembled peptide hydrogel functionalized with glutamic acid templated peptides. Journal of tissue engineering and regenerative medicine 2020;14(9):1236-49.

[352] Wang Y, Xia C, Chen Y, Jiang T, Hu Y, Gao Y. Resveratrol Synergistically Promotes BMP9-Induced Osteogenic Differentiation of Mesenchymal Stem Cells. Stem cells international 2022;2022:8124085.

[353] Rovai ES, Alves T, Gasparoni LM, França BN, Sipert CR, Kantarci A, et al. Protease-activated receptor type 1 (PAR1) increases CEMP1 gene expression through MAPK/ERK pathway. Brazilian oral research 2022;36:e048.

[354] Sun L, Jiang W, Zhang H, Guo Y, Chen W, Jin Y, et al. Photosensitizer-Loaded Multifunctional Chitosan Nanoparticles for Simultaneous in Situ Imaging, Highly Efficient Bacterial Biofilm Eradication, and Tumor Ablation. ACS Applied Materials Interfaces 2019;11(2):2302-16.

[355] Minz AP, Das B, Mohapatra D, Suresh V, Mishra S, Senapati S. Gemcitabine induces polarization of mouse peritoneal macrophages towards M1-like and confers antitumor property by inducing ROS production. Clinical & Experimental Metastasis 2022.

[356] Ghidini G, Mori D, Pulcini S, Vescovi P, Sala R. Photobiomodulation with a 645 nm Diode Laser of Saos-2 Cells and Platelet-Rich Plasma: The Potential for a New Mechanism of Action. Photobiomodulation Photomedicine in Laser Surgery 2021;39(2):86-93.

[357] Negri LB, Martins TJ, da Silva RS, Hamblin MR. Photobiomodulation combined with photodynamic therapy using ruthenium phthalocyanine complexes in A375 melanoma cells: Effects of nitric oxide generation and ATP production. Journal of photochemistry and photobiology B, Biology 2019;198:111564.

[358] Choe G, Lee M, Oh S, Seok JM, Kim J, Im S, et al. Three-dimensional bioprinting of mesenchymal stem cells using an osteoinductive bioink

containing alginate and BMP-2-loaded PLGA nanoparticles for bone tissue engineering. Biomaterials Advances 2022;136:212789.

[359] Ma S, Li X, Hu H, Ma X, Zhao Z, Deng S, et al. Synergetic osteogenesis of extracellular vesicles and loading RGD colonized on 3D-printed titanium implants. Biomaterials science 2022.

[360] Sert G, Kucukguven A, Zırh EB, Demirtaş TT, Çakar AN, Gümüşderelioğlu M, et al. Photobiomodulation with polychromatic light (600-1200 nm) improves fat graft survival by increasing adipocyte viability, neovascularization, and reducing inflammation in a rat model. Lasers in surgery and medicine 2022;54(2):268-80.

[361] Kamarehei F. The effects of combination therapy by solid lipid nanoparticle and dental stem cells on different degenerative diseases. American journal of translational research 2022;14(5):3327-43.

[362] Zaccaron RP, Barbieri RT, Mendes C, Venturini LM, Alves N, Mariano SS, et al. Photobiomodulation associated with lipid nanoparticles and hyaluronic acid accelerate the healing of excisional wounds. Journal of biomaterials applications 2022:8853282221109344.

[363] Mendes C, Dos Santos Haupenthal DP, Zaccaron RP, de Bem Silveira G, Corrêa M, de Roch Casagrande L, et al. Effects of the Association between Photobiomodulation and Hyaluronic Acid Linked Gold Nanoparticles in Wound Healing. ACS biomaterials science & engineering 2020;6(9):5132-44.

[364] Karaman O, Yaralı ZB. Determination of minimum serum concentration to develop scaffold free micro-tissue. The European Research Journal 4(3):145-51.

[365] Zhang Y, Su J, Ma K, Li H, Fu X, Zhang C. Photobiomodulation promotes hair regeneration in injured skin by enhancing migration and exosome secretion of dermal papilla cells. Wound repair and regeneration : official publication of the Wound Healing Society and the European Tissue Repair Society 2022;30(2):245-57.

[366] Yokomizo S, Roessing M, Morita A, Kopp T, Ogawa E, Katagiri W, et al. Near-infrared II photobiomodulation augments nitric oxide bioavailability via phosphorylation of endothelial nitric oxide synthase. FASEB journal : official

publication of the Federation of American Societies for Experimental Biology 2022;36(9):e22490.
[367] Karadağ Köse Ö, Borlu M. Efficacy of the combination of Q-switched Nd:YAG laser and microneedling for melasma. Journal of cosmetic dermatology 2021;20(3):769-75.
[368] Mlih M, Karpac J. Integrin-ECM interactions and membrane-associated Catalase cooperate to promote resilience of the Drosophila intestinal epithelium. PLoS biology 2022;20(5):e3001635.
[369] Fang D, Li T, Wu Z, Wang Q, Wan M, Zhou M, et al. Dual drive mode polydopamine nanomotors for continuous treatment of an inferior vena cava thrombus. Journal of materials chemistry B 2021;9(41):8659-66.
[370] Tang J, Wang L, Loredo A, Cole C, Xiao H. Single-atom replacement as a general approach towards visible-light/near-infrared heavy-atom-free photosensitizers for photodynamic therapy. Chemical science 2020;11(26):6701-8.
[371] Bourouni I, Kyriakidou K, Fourmousis I, Vrotsos IA, Karoussis IK. Low Level Laser Therapy With an 810-nm Diode Laser Affects the Proliferation and Differentiation of Premature Osteoblasts and Human Gingival Fibroblasts In Vitro. Journal of lasers in medical sciences 2021;12:e33.
[372] Kim ID, Lee H, Jin YC, Lee JK. Osteopontin Peptide Icosamer Containing RGD and SLAYGLR Motifs Enhances the Motility and Phagocytic Activity of Microglia. Experimental neurobiology 2017;26(6):339-49.

CURRICULUM VITAE

EDUCATION

- **BSc.** **:** Ataturk University, Science Faculty, Department of Molecular Biology and Genetics
- **MSc.** **:** Izmir Katip Çelebi University, Institute of Science, Department of Biomedical Technologies

PROFESSIONAL EXPERIENCE

- 2016- Lecturer- Izmir Katip Celebi University at the Biomedical Test, Calibration, Application and Research Center

EXPERIENCES

- Biomaterials
- Cell Cultures
- Tissue Engineering
- Regenerative Medicine
- Photo Therapy

LIST OF PUBLICATIONS

- **Çevik Z. B.**, Ördek A., Karaman O., Regulatory effects of laminin derived peptide on microtissue formation for tissue engineered scaffold-free constructs, The European Research Journal, 18 Feb 2022, DOI: 10.18621/eurj.874472. (Research Article).
- Küçük D., Savran L., Ercan U.K., **Yaralı Z.B.**, Karaman O., Kantarci A., Sağlam M., Köseoğlu S. Evaluation efficacy of non-thermal atmospheric pressure plasma in treatment of periodontitis: a randomized controlled clinical trial,Clinical Oral Investigations, 2 Jan 2020, Doi: 10.1007/s00784-019-03187-2 (Research Article).
- Topaloglu Avsar N., Özdemir M., **Çevik Z.B.**, Comparative Analysis Of The Light Parameters Of Red And Near-Infrared Diode Lasers To Induce Photobiomodulation On Fibroblasts And Keratinocytes: An In Vitro Study,

Photodermatology, Photoimmunology Amp Photomedicine, 2020, 0905-4383,1600-0781 (Research Article).

- **Çevik Z. B.**, Pulat G., Karaman O., Effect of Integrin Binding Peptide on Vascularization of Scaffold-Free Microtissue Spheroids, Tissue Engineering and Regenerative Medicine, 2020, 1738-2696, 17, 5, 595-605 (Research Article).
- Pulat G., Gökmen O., **Çevik Z. B.**, Karaman O., Enhanced Osteogenesis Of Human Mesenchymal Stem Cells By Self assembled Peptide Hydrogel Functionalized With Glutamic Acid Templated Peptides, Journal Of Tissue Engineering And Regenerative Medicine, 2020, 1932-6254, 14, 9, 1236-1249 (Research Article).
- Seven F., Gölcez T., Pulat G., **Çevik Z. B.**, Karaman O., Sen M., Guiding neural extensions of PC12 cells on carbon nanotube tracks dielectrophoretically formed in poly(ethylene glycol) dimethacrylate, RSC Advances, 2020, 10, 44, 26120-26125 (Research Article).
- Ozdemir M., **Yaralı Çevik Z.B.**, Topaloğlu N., The Effect Of Photobiomodulation With Red And Near-Infrared Wavelengths On Keratinocyte Cells, 2020 Medical Technologies Congress (TIPTEKNO), 25 Dec, 1-4, 2020 doi: 10.1109/TIPTEKNO50054.2020.9299214 (Conference Proceedings-IEEE Indexing).
- Olcay B., **Çevik Z.B.**, Karaman O. Determination Of Optimum Concentration Of The NGR Peptide with Anticancer Effect On Breast Cancer Microtissue 2020 Medical Technologies Congress (TIPTEKNO), 2020, 25 Dec, 1-3, doi: 10.1109/TIPTEKNO50054.2020.9299303 (Confrence Proceeding-IEEE Indexing).
- Utar B., **Yaralı Z. B.**, Karaman O., "The Effect of RGD Peptide on Vascular Bone Micro-Tissue Formation," 2019 Medical Technologies Congress (TIPTEKNO), 2019, pp. 1-3, doi: 10.1109/TIPTEKNO.2019.8895236 (Conference Proceedings-IEEE Indexing).
- Onak G., Şen M., Horzum N., Ercan U.K., **Yaralı Z.B.**, Garipcan B., Karaman O. Aspartic and Glutamic Acid Templated Peptides Conjugation on Plasma Modified Nanofibers for Osteogenic Differentiation of Human Mesenchymal Stem Cells: A

Comparative Study Scientific Reports, 04 Dec 2018, Doi: https://doi.org/10.1038/s41598-018-36109-5, (Research Article)

- **Yaralı Z. B.** and Karaman O., "The effect of RGD peptide on pre vascularization of scaffold-free microtissue," 2017 Medical Technologies National Congress (TIPTEKNO), 2017, pp. 1-3, doi: 10.1109/TIPTEKNO.2017.8238098 (Conference Proceedings-IEEE Indexing).
- Karaman O. and **Yaralı Z.B.** The Effect Of Serum Concentrations On Scaffold-free Micro-Tissue Formation, Dec, The European Research Journal, 17, Doi: 10.18621/eurj.342109 (Research Article)

CONFERENCE PAPERS

- **Çevik Z. B.**, Korkmaz A., Topaloglu Avsar N., Karaman O., Evaluation of ATP production of low level laser therapy in monolayer and 3 dimensional cell culture, 2021 Medical Technologies National Congress, Oct, Antalya, Turkey 4-6 (Oral Presentation)
- **Çevik Z. B.**, Korkmaz A., Karaman O., Effects of laminin derived peptides on hbmsc-huvec coculture, 2021 Medical Technologies National Congress, Oct, Antalya, Turkey 4-6 (Oral Presentation)
- Ozdemir M., **Yaralı Çevik Z.B.**, Topaloğlu N., The Effect Of Photobiomodulation With Red And Near-Infrared Wavelengths On Keratinocyte Cells, 2020 Medical Technologies National Congress, Noc, Online, Turkey, 12-14 (Oral Presentation)
- Olcay B., **Çevik Z.B.**, Karaman O. Determination Of Optimum Concentration Of The NGR Peptide with Anticancer Effect On Breast Cancer Microtissue 2020 Medical Technologies National Congress, Noc, Online, Turkey, 12-14 (Oral Presentation).
- Utar B., **Yaralı Z.B.**, Karaman O., The Effects of RGD Peptide on Vascular Bone Formation, 2019 Medical Technologies National Congress, Oct, Kuşadası, Aydın, 3-5 (Oral Presentation)
- Bardak M., **Yaralı Z.B.**, Kaya A., Karaman O. Research On The Effect Of Wound Healing On Pulsed Electromagnetic Field And Pulsed Radiofrequency Applications With Sensor Technologies, 1st International Health Sciences and Life Congress, 02-05 May 2018 Burdur/TURKEY (Oral Presentation)

- **Yaralı Z.B.**, Uzun A., Karaman Şen D., Karaman O. Feasibility Study Of Mesoporous Silica Nanoparticles Permeaility Through The Cancer Microtissues 2018 Medical Technologies National Congress, Nov, Gazi Magosa, Cyprus, 8-10 (Oral Presentation)
- Ördek A., **Yaralı Z.B.**, Karaman O. Evaluation of the Effect of Laminin-Derived YIGSR Peptide on HUVEC Micro-Tissue Formation 2018 Medical Technologies National Congress, Nov, Gazi Magosa, Cyprus, 8-10 (Oral Presentation)
- Köken B., **Yaralı Z.B.**, Karaman O. Efficacy of IKVAV Peptide on HUVEC Microtissue Growth 2018 Medical Technologies National Congress, Nov, Gazi Magosa, Cyprus, 8-10 (Oral Presentation)
- Kaya F., Genç S., **Yaralı Z.B.**, Karaman O., Sağlam M., Köseoğlu S. Kronik Periodontitis Hastalarında Cerrahi Olmayan Periodontal Tedaviye Ek Olarak LANAP ve DDLT Uygulamalarının Klinik, Biyokimyasal ve Radyografik Parametreler Üzerine Etkisi, Türk Periodontoloji Derneği 48. ULuslararası Bilimsel Kongresi, 26 Oct 2018, İstanbul/ Turkey (Oral Presentation).
- **Yaralı Z.B.** and Karaman O., The Effect of Different RGD Peptide Concentrations on 3D (Human Umbilical Vein Endothelial Cell) HUVEC Microtissue, 2. International Postgraduate Congress, May, Manisa, Turkey, 12-14 2017 (Oral Presentation)
- **Yaralı Z.B.** and Karaman O., The Effect Of Serum Concentrations On Scaffold-Free Micro-Tissue Formation, 2. International Postgraduate Congress, May, Manisa, Turkey, 12-14 2017 (Oral Presentation)
- **Yaralı Z.B.** and Karaman O., The Effect of RGD Peptide on Pre-Vascularization of Scaffold-free Microtissue, 2017 Medical Technologies National Congress, Oct, Trabzon, Turkey, 12-14 (Oral Presentation)
- **Yaralı Z.B.** and Karaman O., Effect of Soluble RGD Peptide on Vasculogenesis of Scaffold-Free Micro-Tissues, Tissue Engineering & Regenerative Medicine, Dec, North Caroline, America, 3-6 2017 (Poster)
- **Yaralı Z.B.** and Karaman O., Effect of Soluble RGD Peptide on Vasculogenesis of Scaffold-Free Micro-Tissues, Tissue Engineering Part A, Volume 23, 2017 (Poster Abstract)

- Kahraman E., Demirci A., Tanyolaç Zeynep, **Yaralı Z.B.** and Karaman O., The efficacy of using RGD Peptide Sequence on in vitro Wound Healing, 20th National Biomedical Engineering Meeting, November, Izmir, Turkey, 3-5 2016 (Poster Presentation)

PROJECTS

- Investigation of Biostimulatory and Differentiation Efficacy of Red and Near Infrared Wavelengths on Bone-Like Microtissue, 2020-1002 TUBITAK 220S280 (Scholarship)
- Development of Anti-Microbial Peptide Conjugated Alginate Gel For Management of Infected Wounds, 2018-ODL-MUMF-0014 (Researcher)
- The Effect of Serum Concentrations On Scaffold-Free Micro-Tissue Formation, 2017-TYL-FEBE-0044 (Researcher)
- The Effect of RGD Peptide On Cell-Cell Interactions, Cell Proliferation And Vasculogenesis During Micro Tissue Formation, 2016-ODL-MUMF-0008 (Researcher)

PRESENTS

- IKCU 2020 Year Academical Encouragement Award
- Küçük D., Savran L., Ercan U., **Yaralı Z.,** Karaman O., Kantarcı A., Sağlam M. and Köseoğlu S., Kronik Peridontitis Hastalarında Cerrahisiz periodontal Tedaviye İlave Atmosferik Basınçlı Soğuk Plazma Kullanmının Klinik, Biyokimyasal ve Mikrobiyolojik Parametreler Üzerine Etkileri, Turkish Society of Peridontology 47th InternationalScientific Congress and 26th Symposium, Nov, Istanbul, Turkey, 17-18 (Oral Presentation and The best oral presentation present)